School of Chemical and Petroleum Engineering

Novel ceramic membranes for gas separation in enabling the clean energy delivery

Chi Zhang

This thesis is presented for the Degree of
Doctor of Philosophy
of
Curtin University

February 2016

Declaration

To the best of my knowledge and belief this thesis contains no material previously published by any other person except where due acknowledgement has been made.

This thesis contains no material which has been accepted for the award of any other degree or diploma in any university.

Signature:………………………………………

Date:………………………...

Abstract

The ceramic membranes with excellent oxygen ionic conductivity have shown great potential in gas separation, especially oxygen separation, clean energy delivery such as oxyfuel combustion, integrated gasification combined cycle (IGCC) plant and catalytic membrane reactors. In oxyfuel combustion and clean coal energy delivery, CO_2-resistant membrane materials enable direct oxygen separation from air (feed side) to the recirculated flue gas (permeate side) that contains mostly CO_2. In catalytic membrane reactors, CO_2-resistant membrane materials allow the reactor to be operated for thousands of hours in CO_2 containing atmosphere. In solid oxide fuel cells, CO_2-resistant MIEC materials allow single chamber operation for more portable applications. Therefore, it is obvious that CO_2-resistance is the most essential issue in developing novel ceramic membranes for practical applications. The overall aim of this thesis is to study and develop novel CO_2-resistant ceramic membranes for oxygen separation under CO_2 atmosphere. It is believed that if the CO_2-resistant ceramic membranes can exhibit excellent oxygen permeability under CO_2-containing atmosphere, they will have the potential to be applied further for clean energy delivery.

Fluorite materials, despite their inherent CO_2 resistance, typically have low O_2 permeability but can be improved *via* different approaches such as thin film technology and the recently developed minimum internal electronic short-circuit second phase and external electronic short-circuit decoration. In this thesis, we explored the use of different external electronic short-circuit decoration on the surface of the gadolinium doped ceria (GDC) membrane. The external electronic short-circuit concept has been proved its feasibility by decorating silver or platinum paste on the fluorite membrane surface in previous research. Herein, we first investigated to apply perovskite oxide instead of silver or platinum as the external electronic short-circuit decoration on a GDC membrane. The membrane coated with perovskite oxide improved the flux of oxygen compared with the membranes coated with pure Ag. The maximum oxygen flux reached 0.13 mL min^{-1} cm^{-2} at 850 °C for a GDC membrane with thickness of 0.8 mm. The membrane with the perovskite oxide decoration on the feed side and an Ag coating exposed to a CO_2-containing sweep side was stable during a long-term permeation test, indicating that this design is suitable for clean energy delivery such as the oxyfuel combustion. In this case, we explained the improvement in oxygen flux using a triple-

phase boundary theory.

Furthermore, inspired by the triple-phase boundary theory, we developed dual-phase surface decoration to simultaneously provide external electronic short-circuit and create more triple-phase boundary area on the membrane surface. A dual-phase mixture of GDC (50 wt.%)–Ag (50 wt.%) was applied as the surface decoration on a GDC membrane. Such design not only improved the oxygen flux by providing more triple-phase boundary area for oxygen exchange reaction, but also reduced the cost by using less Ag. The maximum oxygen flux 0.128 mL min^{-1} cm^{-2} was obtained for a 1-mm thick GDC membrane at 850 °C. The as-decorated GDC membrane retained a stable flux for at least 130 h under CO_2-containing atmosphere.

To further explore the use of fluorite oxide as CO_2-resistant membrane, we investigated to mix GDC with a minor amount ($\leq$ 5mol.%) of transition metal oxide (Co-O, Fe-O and Cu-O). Generally, the addition of transition metal oxide in fluorite oxide can reduce the sintering temperature of the membranes, which is known as the sintering aid. Moreover, the sintering aid improves the electronic conductivity of fluorite ceramic membranes as well as enabling their use as CO_2-resistant membranes without any electronic conducting phase or external short-circuit decoration. Oxygen permeation test clearly proved that with 2 mol.% Co sintering aid in the GDC membrane, the oxygen flux boosted twice compared with pure GDC. The electronic conductivity improved up to 3.5 times at 900 °C, as calculated from a modified EMF method. The stable oxygen flux achieved during the long-term oxygen permeation test using 100% CO_2 as the sweep gas demonstrates the potential of the prepared membrane to realize clean energy delivery.

In addition to robust fluorite oxide membranes, cobalt-free perovskite oxides are an alternative to CO_2-resistant membranes. We synthesized the cobalt-free $SrFeO_{3-\delta}$ (SF) with tantalum (Ta) dopant and studied its enhanced CO_2-resistance. It was found that a minor amount of Ta doping ($SrFe_{0.95}Ta_{0.05}O_{3-\delta}$) induced the phase transition from orthorhombic to cubic perovskite. The better CO_2-resistance of Ta-doped SF originated from the higher binding energy of lattice oxygen (O1s) in contrast to the undoped SF compound. At 950 °C, a 1.0 mm-thick $SrFe_{0.95}Ta_{0.05}O_{3-\delta}$ membrane showed a stable oxygen flux of 0.85 mL min^{-1} cm^{-2} when exposed to CO_2-containing atmosphere. The Ta-doped SF demonstrated its potential for applications in gas separation, and clean energy delivery such as oxyfuel combustion and membrane reactor for chemical synthesis.

The thesis presents and discusses several methods to fabricate CO_2-resistant membranes that will be potentially applied in gas separation and clean energy delivery. It provides general knowledge on CO_2-resistance mechanisms, material selection and future direction for design of CO_2-resistant membranes.

Acknowledgement

The past three and half years witnessed the most important periods in my life. I would like to take this opportunity to thank all of you who have been encouraging me, helping me, inspiring me and criticizing me.

I would like to express my sincere gratitude to my supervisor Prof. Shaomin Liu, for providing me this precious opportunity for my PhD research and for his continuous guidance, patience, inspiration, hands-on help and constructive criticism during this research. He is my role model both in science and life. Without him, completion of this thesis would have been impossible and my entire academic life would be different.

Equally, I am deeply grateful to my co-supervisor, Prof. Shaobin Wang, for his advice and assistance on my research and personal life. I am also very grateful to Prof. Zongping Shao and Dr. Jian Liu for the support of using their equipment during this work. Special thanks are given to Dr. Jaka Sunarso, for his innovative ideas and his help on revising my manuscripts.

I would like to thank the staff members from the Department of Chemical Engineering: Dr. Lihong Liu, Dr. Guanliang Zhou, Dr. Kun Zhang, Anja Werner, Roshanak Doroushi, Jason Wright, Araya Abera, Yu Long, Xiao Hua and Andrew Chan. I am also grateful to staff from Department of Applied Physics, for their assistance in XRD and SEM training, and to the staff from Department of Physics of UWA, for their training and assistance in TEM.

Special thanks go to my friends, Zhangfeng Shen, Hao Tian, Long Li, Xiaochen Guo, Jinglong Gao, Mingming Zhang, Xin Pang, Wenran Gao, Huayang Zhang, Wenjie Tian, Yuxian Wang, Xiaoguang Duan, Chen Wang, Yu Liu, Wei Wang, Jian Kang, Yilin Liu, Jijiang He, Yazi Liu, Meiwen Wang, Tingting Li, Min Ao, Bing Song, Chao Feng, Sui Boon Liaw, Chow, Lee, Pae and many others. They are all wonderful people and true friends.

I also sincerely acknowledge the financial support for my PhD study from Australian Research Council via its Future Fellow Program (FT12100178) and the Curtin International Postgraduate Research Scholarship.

Most of all, I express my deepest gratitude to my family — my parents, my wife and my parents-in-law, for their support, tolerance, love and devotion in my life. Special

List of Publications

1. **C. Zhang**, J. Sunarso, S. Liu, Designing CO_2-resistant oxygen-selective mixed ionic-electronic conducting membranes: guidelines, recent advances and forward directions, Chem. Soc. Rev. 46 (2017) 2941-3005.

2. **C. Zhang**, H. Tian, J. Sunarso, J. Liu, S. Liu, Enhanced oxygen permeability and electronic conductivity of $Ce_{0.8}Gd_{0.2}O_{2-\delta}$ membrane *via* the addition of transition metal oxide sintering aids, J. Am. Ceram. Soc, under review.

3. **C. Zhang**, H. Tian, D. Yang, J. Sunarso, J. Liu, S. Liu, Enhanced CO_2 resistance for robust oxygen separation through Ta-doped $SrFeO_{3-\delta}$ membranes, ChemSusChem 9 (2016) 505-512.

4. **C. Zhang**, X. Meng, J. Sunarso, L. Liu, R. Xu, Z. Shao, S. Liu, Oxygen permeation behaviour through $Ce_{0.9}Gd_{0.1}O_{2-\delta}$ membranes electronically short-circuited by dual-phase $Ce_{0.9}Gd_{0.1}O_{2-\delta}$-Ag decoration, J. Mater. Chem. A 3 (2015) 19033-19041.

5. **C. Zhang**, R. Ran, G. H. Pham, K. Zhang, J. Liu, S. Liu, $Ce_{0.9}Gd_{0.1}O_{2-\delta}$ membrane coated with porous $Ba_{0.5}Sr_{0.5}Co_{0.8}Fe_{0.2}O_{3-\delta}$ for oxygen separation, RSC Adv. 5 (2014) 5379-5386.

6. P. Liang, **C. Zhang**, H. Sun, S. Liu, M. Tade, S. Wang, Solar photocatalytic water oxidation and purification on ZIF-8 derived C-N-ZnO composites, Energy Fuels 31 (2017) 2138-2143.

7. P. Liang, **C. Zhang**, H. Sun, S. Liu, M. Tade, S. Wang, Photocatalysis of C, N doped ZnO derived from ZIF 8 for dye degradation and water oxidation, RSC Adv. 6 (2016) 95903-95909.

8. P. Liang, **C. Zhang**, X. Duan, H. Sun, S. Liu, M. Tade, S. Wang, An insight to N doped graphene evolution from metal organic frameworks and peroxymonosulfate activation towards excellent degradation of persistent contaminants, Environ. Sci.: Nano 4 (2017) 315-324.

9. P. Liang, **C. Zhang**, X. Duan, H. Sun, S. Liu, M. Tade, S. Wang, Catalytic oxidation of p hydroxylbenzoic acid on N doped graphene via peroxymonosulfate activation: N functionality and mechanism, ACS Sustain. Chem. Eng. 5 (2017) 2693-2701.

10. K. Zhang, **C. Zhang**, L. Zhao, B. Meng, J. Liu, S. Liu, Enhanced oxygen permeation behavior of BSCF membranes in CO_2–containing atmosphere with SDC functional shell, Energy Fuels 30 (2016) 1829-1834.

11. J. Y. Chan, K. Zhang, **C. Zhang**, H. Tian, S. Liu, Novel tungsten stabilizing $SrCo_{1-x}W_xO_{3-\delta}$ membranes for oxygen production, Ceram. Int. 41 (2015) 14935-14940.

12. R. An, J. Song, Y. Li, X. Tan, J. Sunarso, **C. Zhang**, S. Wang, S. Liu, Bundling strategy to simultaneously improve the mechanical strength and oxygen permeation flux of the individual perovskite hollow fiber membranes, J. Membr. Sci. 527 (2017) 137-142.

Awards

Chinese Government Award for Outstanding Self-financed Students Abroad, 2016.

Table of Contents

List of Figures

List of Tables

Chapter 1: Introduction

1.1 Background

The continual growth of fossil fuels combustion leads to the increase of global CO_2 emission, which has become a severe environmental threat to human society. The CO_2 concentration in atmosphere has been increased by 19 % from 315 ppm in 1958 to 380 ppm in 2016.[1] One of the approaches to decrease CO_2 emission is oxyfuel combustion technology. Oxyfuel combustion delivers clean energy from combusting fossil fuels using pure O_2 or O_2/CO_2 mixtures instead of air. This process generates N_2-absent flue gas, which allows the highly concentrated CO_2 in the flue gas to be captured, compressed and separated easily.[1] The O_2 required in oxyfuel system is generally supplied from oxygen production plants. However, traditional oxygen production technology such as cryogenic distillation is costly and accounts for almost half of the overall CO_2 capture cost.[2] Oxygen permeation from an ionic transport membrane (ITM) can be a cost-effective alternative approach to supply oxygen to oxyfuel systems. However, additional devices such as an oxygen compressor are still required resulting in extra capital investment. Instead of simply supplying O_2 into the oxyfuel systems, a combination of ITM with combustion system is a more cost- and energy-effective choice. In such a system, the assembled ITM in the air separation unit would enable oxygen permeation from air in the feed side directly into the flue gas (containing mostly CO_2) on the permeate side.

Within the oxyfuel combustion context, the direct contact of highly concentrated CO_2 with membranes requires excellent CO_2-resistance of the ITM. In addition to oxyfuel combustion, other applications such as membrane reactors for green chemical synthesis[3-7] and single-chamber solid oxide fuel cells[8-10] represents other areas using CO_2-resistant membranes. In the green chemical synthesis area, CO_2, CO, H_2 and CH_4 are inevitably involved, requiring the membranes to be tolerant against CO_2. The single-chamber solid oxide fuel cells require the anode and cathode assembled in a single gas chamber, where the presence of CO_2 is unavoidable. Thus CO_2-resistance membrane materials are urgently required to ensure the stable operation of the fuel cells.

The development of CO_2-resistant oxygen-selective MIEC membranes is based on the two most promising materials, i.e., perovskite and dual-phase materials. The CO_2-resistant perovskite materials have three major features: (1) rare earth metal in A-

site cation; (2) minor amount of cobalt in B-site cation; (3) partial substitution of original B-site metal with more stable (high valence state and high acidity) transition metals.[11] The CO_2-resistant dual-phase membranes contain one chemical stable fluorite phase to conduct oxygen ions and one electronic conducting phase. The fluorite oxide generally features in low electronic conductivity, which can be overcome through mixing with one electronic conducting phase, or by using internal/external electronic short-circuit design. Numerous studies have been carried out to address these CO_2-resistant membrane concepts. For example, major efforts have been made to reveal the approaches and mechanisms to enhance the CO_2-resistance of perovskite membranes.[11-14] Our group has carried out several research projects on using internal/external electronic short-circuits on fluorite membranes.[15-17] Despite the great improvements demonstrated within the last decades, there are still undiscovered areas and opportunities to be pursued. These areas inspire the research objectives of this thesis.

1.2 Objectives

The major objective of this thesis is to develop novel CO_2-resistant membranes for gas separation and clean energy delivery. Ceramic membranes with high oxygen permeability and excellent stability in CO_2-containing atmosphere are investigated. To this end, following studies have been included:

1. Summarizing the current research status of CO_2-resistant oxygen-selective ceramic membranes.

2. Developing gadolinium doped ceria (GDC) membranes with single perovskite decorations to form external short-circuit to realize enhanced oxygen permeation flux and CO_2-resistance.

3. Exploring dual-phase surface decoration on GDC membranes to further demonstrate the applicability of the external short-circuit concept.

4. Using a transition metal sintering aid in GDC membranes to enhance the oxygen permeability and decrease the sintering temperature of GDC.

5. Applying tantalum doping into cobalt-free $SrFeO_{3-\delta}$ membranes and probing the CO_2-resistance enhancement mechanism of tantalum doping, through the chemistry perspective.

1.3 Thesis outline

This thesis consists of seven chapters. The first chapter is the introduction and the thesis outline. Chapter 2 summarizes the recent literature related to the topic of this thesis. Chapters 3-6 are the results and discussions of the experimental studies, which have been published or will be submitted for publication. The conclusions of this thesis as well as future directions are presented in Chapter 7.

Chapter 1: Introduction

This section explains the significance of CO_2-resistant oxygen-selective mixed ionic-electronic conducting (MIEC) membrane technology and justifies the need for further development in this topic. This chapter also lists the objectives and outline of this thesis.

Chapter 2: Literature review

This chapter presents an overall review and understanding of the reported CO_2-resistant membrane materials for the last two decades, and searches out a reliable strategy to further design new stable oxygen selective membranes with improved performance. This literature review will feature such underlying guidelines and relate them to the state of the art in the field.

Chapter 3: $Ce_{0.9}Gd_{0.1}O_{2-\delta}$ membrane coated with porous $Ba_{0.5}Sr_{0.5}Co_{0.8}Fe_{0.2}O_{3-\delta}$ for oxygen separation

A perovskite-structured $Ba_{0.5}Sr_{0.5}Co_{0.8}Fe_{0.2}O_{3-\delta}$ (BSCF) oxide is decorated onto a $Ce_{0.9}Gd_{0.1}O_{2-\delta}$ (GDC) membrane surface to form an external electronic short-circuit. The oxygen permeation behavior of as-prepared GDC membranes is compared with those decorated with silver paste. The GDC membrane with BSCF decorated on feed side and silver paste decorated on sweep side is demonstrated to be CO_2-resistant, proving its potential for clean energy applications.

Chapter 4: Oxygen permeation behavior through $Ce_{0.9}Gd_{0.1}O_{2-\delta}$ membranes electronically short-circuited by dual-phase $Ce_{0.9}Gd_{0.1}O_{2-\delta}$-Ag decoration

The chapter continues the study of an external short-circuit on GDC membranes. Instead of using perovskite oxide or pure silver paste decorations, this study tries to use dual-phase GDC-Ag decoration on GDC bulk membranes. Such a method not only forms an electronic conducting path over the GDC membrane, but also provides more triple-phase boundary areas to enhance the O_2 surface exchange rate.

Chapter 5: Enhanced oxygen permeability and electronic conductivity of Ce$_{0.8}$Gd$_{0.2}$O$_{2-\delta}$ membrane via the addition of transition metal oxide sintering aids

This chapter presents another approach to apply GDC as a CO$_2$-resistant membrane by using a sintering aid. In this work, we use a transition metal (Co, Fe and Cu) oxide as sintering aids in fluorite Ce$_{0.8}$Gd$_{0.2}$O$_{2-\delta}$ (GDC) to improve the electronic conductivity and sinterability. GDC with 2 mol.% Co is found to be the most effective sintering aid through oxygen permeation tests and the modified EMF method.

Chapter 6: Enhanced CO$_2$ resistance for robust oxygen separation through Ta-doped SrFeO$_{3-\delta}$ membranes

The chapter describes another material choice of fabricating CO$_2$-resistant oxygen-selective membranes. It is demonstrated that by doping Ta into SrFeO$_{3-\delta}$ (e.g. SrFe$_{0.95}$Ta$_{0.05}$O$_{3-\delta}$), the CO$_2$-resistance is enhanced due to the lower basicity and higher binding energy of lattice oxygen (O1s). The Ta-doped SrFeO$_{3-\delta}$ membrane enables its application in the oxyfuel process to deliver clean energy.

Chapter 7: Conclusions and perspectives

The chapter summarizes the achievements of this thesis and it also gives the future directions for this area.

1.4 References

1. R. Kneer, D. Toporov, M. Förster, D. Christ, C. Broeckmann, E. Pfaff, M. Zwick, S. Engels, M. Modigell, Energy Environ. Sci., 3 (2010) 198-207.

2. A.F. Sarofim, Challenges facing the use of coal in a carbon constrained world: What the biologists should be thinking about, GCEP and I-CARES biological capture and utilization workshop, Washington University, September 1, 2009.

3. S. Engels, F. Beggel, M. Modigell, H. Stadler, J. Membr. Sci., 359 (2010) 93-101.

4. A. Thursfield, I.S. Metcalfe, J. Mater. Chem., 14 (2004) 2475-2485.

5. X. Dong, W. Jin, N. Xu, K. Li, Chem. Commun., 47 (2011) 10886-10902.

6. W. Yang, H. Wang, X. Zhu, L. Lin, Top. Catal., 35 (2005) 155-167.

7. Y. Liu, X. Tan, K. Li, Catal. Rev. Sci. Eng., 48 (2006) 145-198.

8. T. Hibino, A. Hashimoto, T. Inoue, J.-i. Tokuno, S.-i. Yoshida, M. Sano, Science,

288 (2000) 2031-2033.

9. M. Yano, A. Tomita, M. Sano, T. Hibino, Solid State Ionics, 177 (2007) 3351-3359.

10. I. Riess, J. Power Sources, 175 (2008) 325-337.

11. J. Yi, M. Schroeder, M. Martin, Chem. Mater., 25 (2013) 815-817.

12. A. Brandão, J.F. Monteiro, A.V. Kovalevsky, D.P. Fagg, V.V. Kharton, J.R. Frade, Solid State Ionics, 192 (2011) 16-20.

13. W. Chen, C. Chen, L. Winnubst, Solid State Ionics, 196 (2011) 30-33.

14. J. Yi, M. Schroeder, T. Weirich, J. Mayer, Chem. Mater., 22 (2010) 6246-6253.

15. K. Zhang, Z. Shao, C. Li, S. Liu, Energy Environ. Sci., 5 (2012) 5257-5264.

16. K. Zhang, Y. Zou, C. Su, Z. Shao, L. Liu, S. Wang, S. Liu, J. Membr. Sci., 427 (2013) 168-175.

17. K. Zhang, L.H. Liu, Z.P. Shao, R. Xu, J.C.D. da Costa, S.B. Wang, S.M. Liu, J. Mater. Chem. A, 1 (2013) 9150-9156.

Chapter 2: Literature Review

Abstract

CO_2 resistance is an enabling property for the wide scale implementation of oxygen-selective mixed ionic-electronic conducting (MIEC) membrane in clean energy technologies, *i.e.*, oxyfuel combustion, clean coal energy delivery, and catalytic membrane reactors for greener chemical synthesis. The significant rise in the number of works over the past decade and the major progress in CO_2-resistant MIEC materials warrant the systematic guidelines on this topic. To this end, this review features the pertaining aspects in addition to the recent status and advances of the two most promising membrane materials, *i.e.*, perovskite and fluorite-based dual-phase materials. We explain how to quantify and design CO_2 resistant membranes using Lewis acid-base reaction concept and thermodynamics perspective and highlight the relevant characterization techniques. For perovskite materials, a trade-off generally exists between CO_2 resistance and O_2 permeability. Fluorite materials, despite their inherent CO_2 resistance, typically have low O_2 permeability but can be improved *via* different approaches such as thin film technology and the recently developed minimum internal electronic short-circuit second phase and external electronic short-circuit decoration. We then elaborate the two main future directions that are centralized around the development of new oxide compositions capable of featuring simultaneously high CO_2 resistance and O_2 permeability and the exploitation of phase reaction to create new conductive phase along the grain boundaries of dual-phase materials. The final part of the review discusses various complimentary characterization techniques and the relevant works that can provide insights into the degradation mechanism of oxide-based materials upon exposure to CO_2.

2.1 Background

The perpetual growth of energy demand leads to the continual consumption of fossil

fuels which is projected to increase by ~27 % over the 24 year-period, leading to the parallel increase in United States CO_2 emission from 6000 million tons per year (in 2006) to 8000 million tons per year (by 2030) according to the Energy Information Administration (EIA) within United States Department of Energy (U.S. D.O.E.).[1] Hydrocarbons in particular will still form a substantial part of the fuel to supply more than 60 % of the world's energy demand over the next 20 years.[2] These would contribute to the significant increase of anthropogenic carbon dioxide (CO_2) emission. The global atmospheric CO_2 concentration itself has increased from about 315 ppm (in 1958) to 375 ppm (at the end of 2005).[3]

One of the potential approaches is oxyfuel technology, primarily on pulverized coal combustion in a CO_2/O_2 atmosphere which offers facile CO_2 recovery, low NO_x emissions, and high desulfurization efficiency. There are several different oxyfuel power cycles, *e.g.*, advanced zero-emission power plant (AZEPP), Graz and water cycle, MATIANT and Feher supercritical CO_2 cycles, zero-emission power plant (ZEPP), zero-emission ITM oxyfuel plant, *etc*; the details of which can be found in another review paper.[2] In oxyfuel process, fuel (*e.g.*, coal, oil, gas and other hydrocarbons) is burned in a mixture of oxygen and recirculated flue gas (which comprise mainly of CO_2 and water vapor as well as traces of N_2, O_2, SO_2 and NO_x).[3] This is since fuel combustion using pure O_2 leads to extremely high combustion temperature.[2] The boilers in the currently existing power plants can be retrofitted to oxyfuel configuration given the matching between their maximum temperature ranges which would not otherwise be possible in the case of combustion using pure O_2. Furthermore, the absence of nitrogen in the flue gas allows easy processing of CO_2, *i.e.*, its purification up to 96-99 % which can then be compressed and condensed into liquid CO_2 for sequestration or use in other processes.[3] The required oxygen can be supplied by cryogenic distillation or ceramic-based ionic transport membrane; both of which will incur extra energy and capital penalties from additional devices such as compressor relative to the conventional air-fired power plant.

The latter technology, specifically known as oxygen ionic transport membrane (ITM), has rapidly become one of the key technologies within clean combustion based energy generation as demonstrated by substantial investment from developed countries such as US$90 million from Department of Energy on Ionic Transport Membrane Oxygen Development Program in U.S. and OXYCOAL-AC in Germany.[3,4] Compared to cryogenic process, ITM technology provides up to 48 % capital saving and up to 69 %

power saving for applications such as integrated gasification combined cycle (IGCC), decarbonized fuel, enrichment, oxyfuel, and gas to liquid.[3] For oxyfuel process, ITM, due to its reduced auxiliary power requirement, is more efficient in terms of cost and energy. Moreover, if good combustion performance can be achieved at low oxygen concentrations in CO_2/O_2 mixture, the capital and operational costs of ITM based oxyfuel plant can be reduced further.[3] Within the oxyfuel context, the availability of CO_2-resistant membrane materials would enable oxygen separation from air in the feed side of air separation unit directly into the recirculated flue gas (which contains mostly CO_2) on the other side. This would simplify the configuration and provide lower demand on membrane area as well as higher thermal efficiency relative to the case where direct contact between membrane and CO_2 is not allowed.[5]

Another important application for CO_2-resistant membrane lies in the area of membrane reactor for greener chemical synthesis, including partial oxidation of methane (CH_4) to syngas (H_2 and CO), oxidative coupling of CH_4 to C2 (ethylene and/or ethane), oxidative dehydrogenation of light alkanes to olefins, CO_2 thermal conversion to CO and water splitting to hydrogen (H_2).[6-10] In these important reactions, CO_2, H_2, and CH_4 are inevitably involved as the feed or product gases, requiring the membrane to be at least CO_2-tolerant. The best performance of such membrane reactor needs the matched properties of oxygen flux and catalytic efficiency to consume the permeated oxygen. The intermediate value of oxygen flux for CO_2-resistant membranes also perfectly fits within the membrane reactors context to optimize the product yields; since otherwise, too high oxygen concentration in the permeate side will highly oxidize the products; leading to low product selectivity. Single-chamber solid oxide fuel cells (SC-SOFC) represents another application area using CO_2-resistant membranes. In the SC-SOFC system, the anode and cathode are assembled in one gas chamber filled with fuel, oxidant gases, and reaction products. The presence of CO_2 is unavoidable in SC-SOFC reaction product stream, thus CO_2-resistant electrode materials are required in this fuel cell system.[11-14]

The emerging hundreds of publications on ITM topic highlights substantial interest on this technology which has manifested into several excellent review papers that cover the background, related technologies and applications, materials structures and compositions, transport mechanisms and theories, materials synthesis and characterization, oxygen permeation performances overviews, and/or future directions.[6,9,10,15-19] Zhang *et al.*, for example, overview the structure of perovskite-

related compounds, the oxygen permeation rate determining factors, and the materials selection guidelines.[16] Sunarso *et al.* provide comprehensive account on all aspects of mixed ionic-electronic conducting (MIEC) ceramic-based membranes with emphasis on the fluorite and perovskite-based structures, defect theory, transport mechanisms, and preparation methods.[15] Still, CO_2 resistance aspect of ITM technology has been rather overlooked despite its significance to realize the wide applications of this technology within oxyfuel combustion, clean coal energy delivery, and catalytic membrane reactors. This review thus aims to address this gap by featuring the current status and advances on CO_2-resistant MIEC membranes as well as the underlying concepts and approaches. The emphasis has been placed on perovskite and dual-phase materials. The review is outlined into five sections. This first section justifies the technology significance and its context. The second section features the pertaining aspects to develop CO_2-resistant MIEC membranes according to four major categories, *i.e.*, perovskite materials, dual-phase materials, other materials, and engineering approaches. The third section provides comparative insights into the performances of perovskite and dual-phase membranes. The fourth section, in turn, overviews the two latest directions for the development of CO_2-resistant MIEC membranes. Finally, the fifth section discusses the membrane degradation behavior in CO_2 atmosphere, mostly for the CO_2-prone perovskite materials.

2.2 CO_2-resistant oxygen-selective mixed ionic-electronic conducting membranes: materials perspective

Perovskite compounds have drawn major attention for application as mixed ionic-electronic conducting (MIEC) membranes due to their high oxygen flux determined by their inherently high ionic/electronic conductivities and surface oxygen exchange reaction kinetics. Perovskite MIEC compounds generally have overwhelming higher electronic conductivity than the ionic conductivity. Compared to perovskite, fluorite materials have lower ionic conductivity and substantially lower electronic conductivity but possess high chemical stability to tolerate these acidic or reducing gases. Thereby, fluorite material is usually designed as the novel robust membranes but accompanied with the second electronic conducting phase to compensate its low electronic conductivity limitation. The properties difference between these compounds can be

9

understood by inspecting their specific structures as schematized in **Figure 2.1**.

2.2.1 Perovskite materials

2.2.1.1 Structure and basic concepts
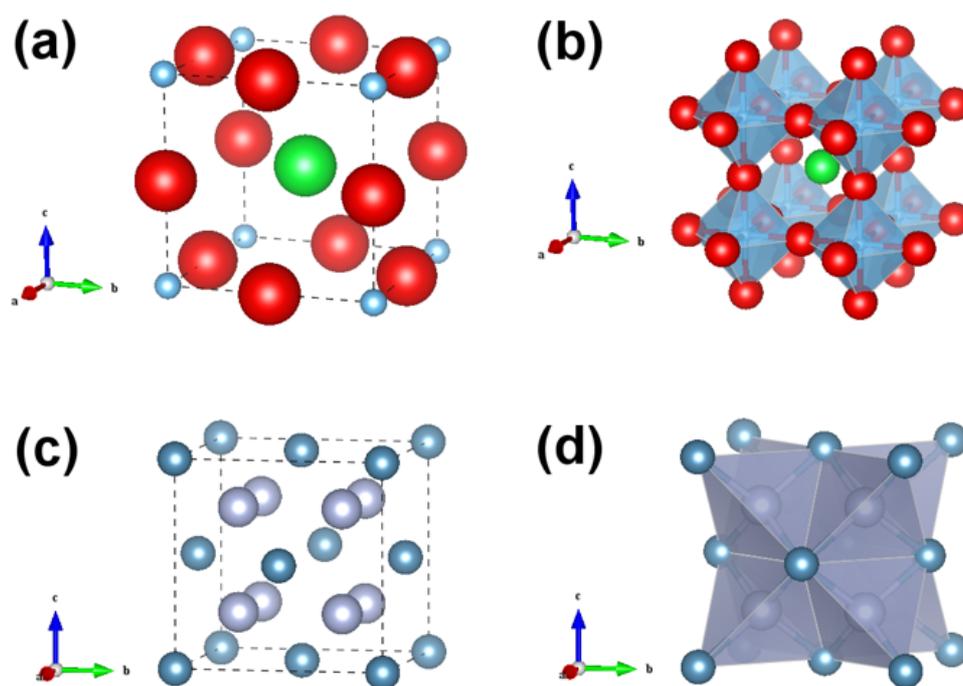
Figure 2.1 Ideal structure and the packing arrangement for: (a, b) perovskite ABO_3 compounds represented by $SrTiO_3$ (Green atoms – A (Sr), Light blue atoms – B (Ti), Red atoms – O (O)); and (c, d) fluorite AO_2 compounds represented by CaF_2 (Blue atoms – A (Ca), Grey atoms – O (F)).

Figure 2.1(a) and (b) depicts the ideal perovskite structure and its packing arrangement. Perovskite compounds are defined as those having ABO_3 formula. A and B here are two different metal cations with different size. Size limitation dictates the ionic radius range of A and B where generally A cation and B cation have ionic radius between 1.1-1.8 Å and 0.62-1 Å, respectively.[20] As such, A-site cation is normally from lanthanides, *e.g.*, Gd, Pr, and La or alkaline earth metals, *e.g.*, Sr and Ba while B-site cation can be transition metals, *e.g.*, Mn, Co, Fe, Cr and Zn or non-transition metals, *e.g.*, Al, Sn and Ga.[15] $SrTiO_3$ serves as the typical example. Perovskite structure consists essentially of a framework of corner-shared BO_6 octahedra where a large A cation sits in a cavity

between octahedra.[21] Each B cation is coordinated by 6 O anions creating 6 equidistant B-O bonds while each A cation is coordinated by 12 O anions creating 12 equidistant A-O bonds. A and B cations may have different oxidation state as represented by the formula of $A^{2+}B^{4+}O_3$ or $A^{1+}B^{5+}O_3$ or $A^{3+}B^{3+}O_3$.

The framework dimensions are fixed by the B-O bond length which in order for the cube shown in **Figure 2.1(a)** to form, the cube edge should be equal to twice the sum of ionic radius of B cation and O anion while the face diagonal should be equal to twice the sum of ionic radius of A cation and O anion; assuming that A cation is in complete contact with all its neighboring ions. By using Pythagorean theorem, it becomes apparent that:

$$(R_A + R_O)^2 = 2(R_B + R_O)^2 \qquad \text{(Eq. 2.1)}$$

$$R_A + R_O = \sqrt{2}(R_B + R_O) \qquad \text{(Eq. 2.2)}$$

$$1 = \frac{R_A + R_O}{\sqrt{2}(R_B + R_O)} \qquad \text{(Eq. 2.3)}$$

$$t = \frac{R_A + R_O}{\sqrt{2}(R_B + R_O)} \qquad \text{(Eq. 2.4)}$$

Therefore, **Eq. (2.3)** determines the relationship between the ionic radius values for A, B and O. The ratio of the sum of ionic radius of A and O to root square of 2 multiplied by the sum of ionic radius of B and O should ideally be equal to 1 for the cubic structure to form. This ratio was generalized as Goldschmidt tolerance factor (**Eq. (2.4)**), a simple predictor variable which have been widely used to design specific perovskite structure from numerous metal components.[21,22] The empirical ionic radius values for various metal cations have been listed by Shannon.[23]

Most perovskite compounds actually exist in their "non-stoichiometric" analogues, *i.e.*, as $ABO_{3-\delta}$ compounds where some oxygen anions are missing from the lattice. The δ here represents the non-stoichiometry parameter created upon incorporating A and B cations with total oxidation state of less than 6, *e.g.*, 5 from A^{2+} and B^{3+} or A^{1+} and B^{4+}. In fact, the presence of such "oxygen vacancies" defects is beneficial to provide a pathway for conductivity of oxygen ion (for oxygen ions hopping from one empty site to another empty site) and is the primary contributing

factor for the oxygen ionic conductivity. Moreover, the electronic conductivity can also be created in perovskite by choosing transition metals as the B-site metal component. It is well-known that transition metals can afford more than one oxidation state during reduction and oxidation reaction. Oxygen vacancies are often formed at increasing temperatures in conjunction with the reduction of transition metal components which are simultaneously accompanied by electron transfer reactions.[24,25] The presence of this simultaneous ionic and electronic conductivity characterizes its "mixed ionic-electronic conducting" definition.[15]

Another main advantage of using perovskite MIEC is its capability to host different metal oxides as represented by $A_{1-x-y}A'_xA''_yB_{1-x-y}B'_xB''_yO_{3-\delta}$. To this end, the structure and properties of the resultant perovskite can be tuned by tailing compositions to fit particular applications, *e.g.*, high ionic conductivity, electronic conductivity or catalytic activity. As an example, if electronic conductivity is not required, non-transition metal such as Ga can be incorporated into the B-site. Such perovskite compound, *e.g.*, $LaGaO_3$ serves as an excellent ionic conductor.[26]

2.2.1.2 Quantifying the extent of reaction with CO_2

Highly permeable oxygen-selective MIEC perovskite materials normally have alkaline earth metal constituents in their A-site which readily react with acidic CO_2. In the perspective of obtaining larger lattice size and higher oxygen permeability, Ba that has a large ionic radius of 1.61 Å (at coordination number of 12) becomes an attractive A-site component.[23] CO_2 exposure on such alkaline earth metal containing perovskite generally leads to the deterioration of the original structure and the resultant degradation of the oxygen permeation performance. For example, the O_2 flux of $Ba_{0.5}Sr_{0.5}Co_{0.8}Fe_{0.2}O_{3-\delta}$ membrane, when exposed to CO_2, decreases to zero rapidly, *i.e.*, within several minutes.[27-29] Identical degradation was also observed on $BaCo_{0.4}Fe_{0.4}Nb_{0.2}O_{3-\delta}$ membrane during exposure to CO_2.[30] Post characterization of CO_2-exposed membrane has been used to evaluate the extent of the structure decomposition which will be elaborated in more detail in the last section. Generally, the decomposed part on the surface is comprised of a carbonate layer and a decomposed zone.[27,29]

2.2.1.2.1 Thermodynamics perspective

The susceptibility of perovskite oxide to form carbonates upon contact with CO_2 can be assessed from thermodynamics point of view. Perovskite oxide, *i.e.*, ABO_3 can be considered as one among many possible phases in the binary mixture of $AO-BO_2$.[31] Its interaction and equilibrium with the gaseous species like CO_2 can be determined using thermodynamics relationship. To simplify, the oxygen nonstoichiometry (δ) of perovskite oxide is normally assumed to be negligible so that the effect of oxygen partial pressure can be neglected. The formation of different intermediate phases at
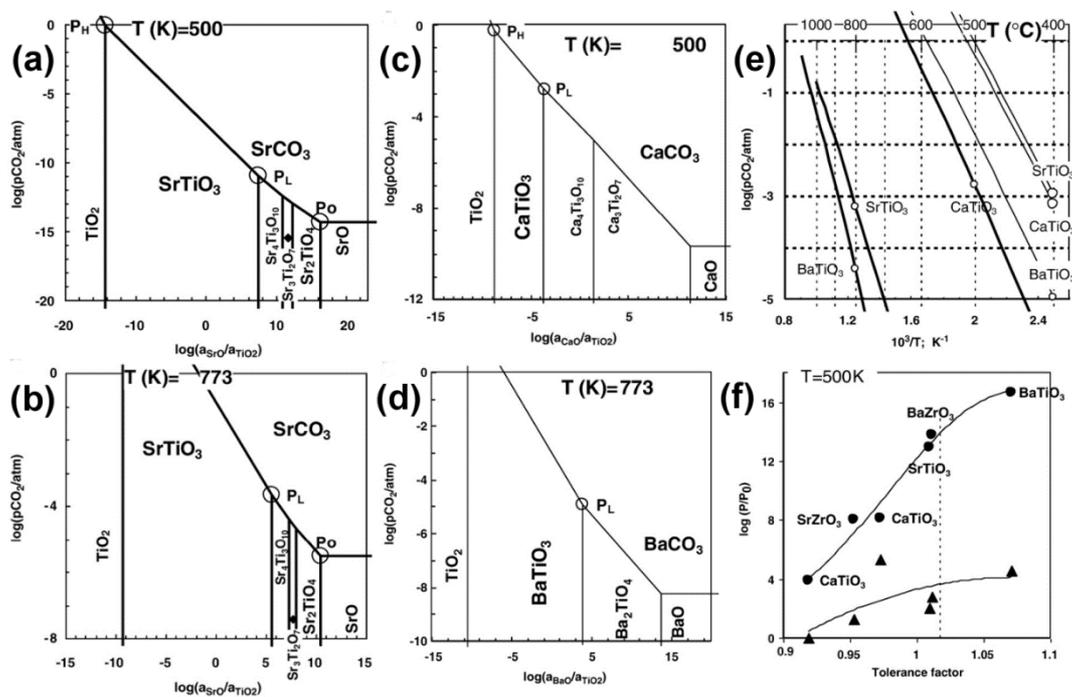
Figure 2.2 Stability diagrams for $SrO-TiO_2-CO_2$ system at (a) 500 K and (b) 773 K; Stability diagrams for (c) $CaO-TiO_2-CO_2$ system at 500 K and (d) $BaO-TiO_2-CO_2$ system at 773 K; (e) Lower and upper tolerance limits for alkaline earth titanates; and (f) Relative gains in CO_2 resistance for titanium and zirconium-based perovskites (Reproduced from ref. 31 with permission from Elsevier).

different ratio of AO to BO_2 depends on the reaction between AO and BO_2 and eventually, the activity ratio of AO to BO_2. In the presence of CO_2, another variable, *i.e.*, CO_2 partial pressure comes into play. For example, for the binary system of $SrO-TiO_2$, the stability diagram of $SrO-TiO_2-CO_2$ can be developed which correlates different phases as a function of the activity ratio of SrO to TiO_2 and CO_2 partial

13

pressure as illustrated in **Figure 2.2(a) and (b)**. The detailed calculations to generate such stability diagrams will not be discussed here since it is available on the work of Frade and co-workers and Yokokawa *et al.*.[31-33]

The stability diagrams are useful to determine the tolerance range to CO_2 as well as to compare the stability between different perovskite oxides.[31] **Figure 2.2(a)** for example shows that at 500 K (227 ^{o}C), $SrTiO_3$ is more stable to carbonation relative to SrO since $SrCO_3$ is formed from reaction with $SrTiO_3$ at higher CO_2 partial pressure. It is worth noting that the presence of excess TiO_2 actually increases the stability of $SrTiO_3$ (**Figure 2.2(a)**). Within this context, the composition (its heterogeneity) may have substantial effect on the CO_2 tolerance; the variation of which can be minimized using solution route rather than solid-state route which requires a higher temperature for a prolonged sintering time. Upon comparing **Figure 2.2(a) and (c)**, it becomes clear that at 500 K, $CaTiO_3$ is more stable than $SrTiO_3$ given the higher low and high pressure (P_L and P_H) for $CaCO_3$ formation from $CaTiO_3$ (relative to $SrTiO_3$ case). Likewise, $SrTiO_3$ is more stable than $BaTiO_3$ at 773 K (500 ^{o}C) when comparing **Figure 2.2(b) and (d)**. The low and high pressure limits for particular carbonate formation can also be summarized to correlate these limits with the temperature as shown in **Figure 2.2(e)** for different titanium-based perovskite oxides. Furthermore, the relative gains in CO_2 resistance of ABO_3 perovskite oxide with respect to the AO metal oxide appear to be connected to the Goldschmidt tolerance factor with higher factor favors higher resistance (**Figure 2.2(f)**).[31] The correlation between relative gains and tolerance factor for titanium based perovskite oxides implies general validity of the plot given the clear established trend between the experimental points and regression line (**Figure 2.2(f)**). If such relationship indeed exists and is extendable to every other perovskite oxide system, stability can be predicted using such plot for those systems where the thermodynamics data are absent.

The stabilization energy of the perovskite oxides may also be taken into consideration to analyze the carbonate formation tendency.[34] The stabilization energy of perovskite oxides is defined as the enthalpy change for perovskite formation from the constituent oxides (AO and BO_2), which can be written as:

$$\delta(ABO_3) = \left[\Delta_f H^0(ABO_3) - \left\{ \Delta_f H^0(AO_n) + \Delta_f H^0(BO_m) \right\} \right] \qquad \text{(Eq. 2.5)}$$

The chemical stability of the perovskite oxides against reactions with a particular chemical constituent such as CO_2 is associated with the stabilization energy of the perovskites from their constituent oxides (AO and BO_2). Moreover, the stabilization energy correlates with the Goldschmidt tolerance factor t with the ideal t value ($t = 1$) indicates the highest stabilization, while smaller t ($t < 1$) leads to lower stability.[33,35,36]

A typical ABO_3 perovskite reacts with CO_2 to form ACO_3 as follows:

$$ABO_3 + CO_2 \rightleftharpoons ACO_3 + BO_2 \tag{Eq. 2.6}$$

The reaction can be resolved into the following two reactions energetically:

$$ABO_3 \rightleftharpoons AO + BO_2 \tag{Eq. 2.7}$$

$$AO + CO_2 \rightleftharpoons ACO_3 \tag{Eq. 2.8}$$
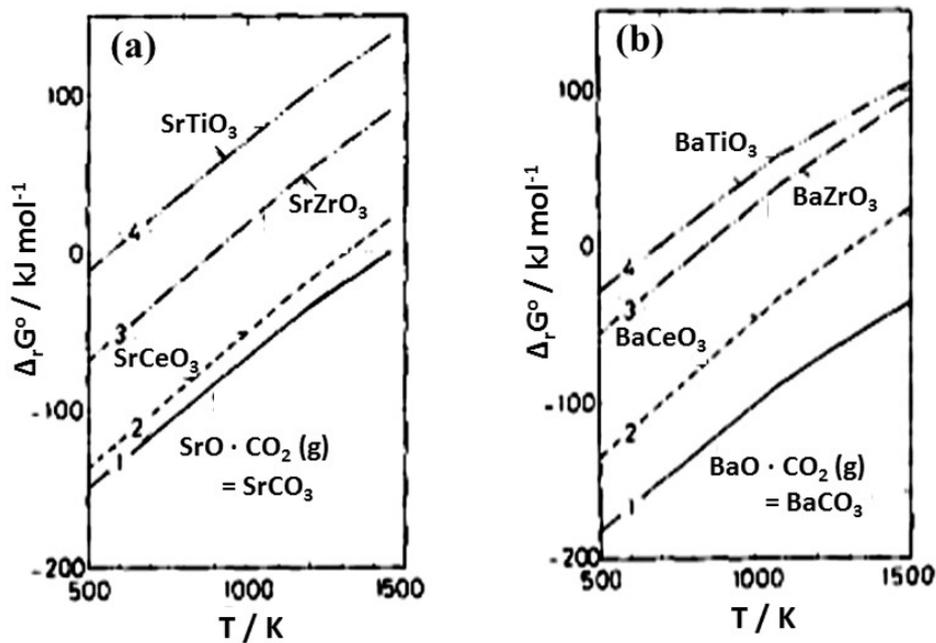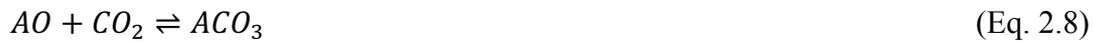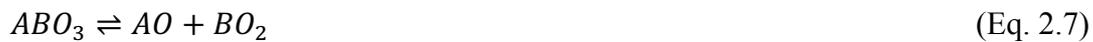
Figure 2.3 Gibbs energy change for carbonate formation for (a) strontium-based perovskites; and (b) barium-based perovskites; 1. AO + CO_2 (g) = ACO_3; 2. $ACeO_3$ + CO_2 (g) = ACO_3 + CeO_2; 3. $AZrO_3$ + CO_2 (g) = ACO_3 + ZrO_2; 4. $ATiO_3$ + CO_2 (g) = ACO_3 + TiO_2 (A = Sr or Ba) (Reproduced from ref. 34 with permission from Elsevier).

Figure 2.3 displays the Gibbs energy change for carbonate formation for some typical strontium and barium perovskite oxides. For each oxide, the stability against carbonate formation is a function of temperatures. With decreasing temperature, the Gibbs energy change becomes lower, indicating stronger tendency to form carbonates.

15
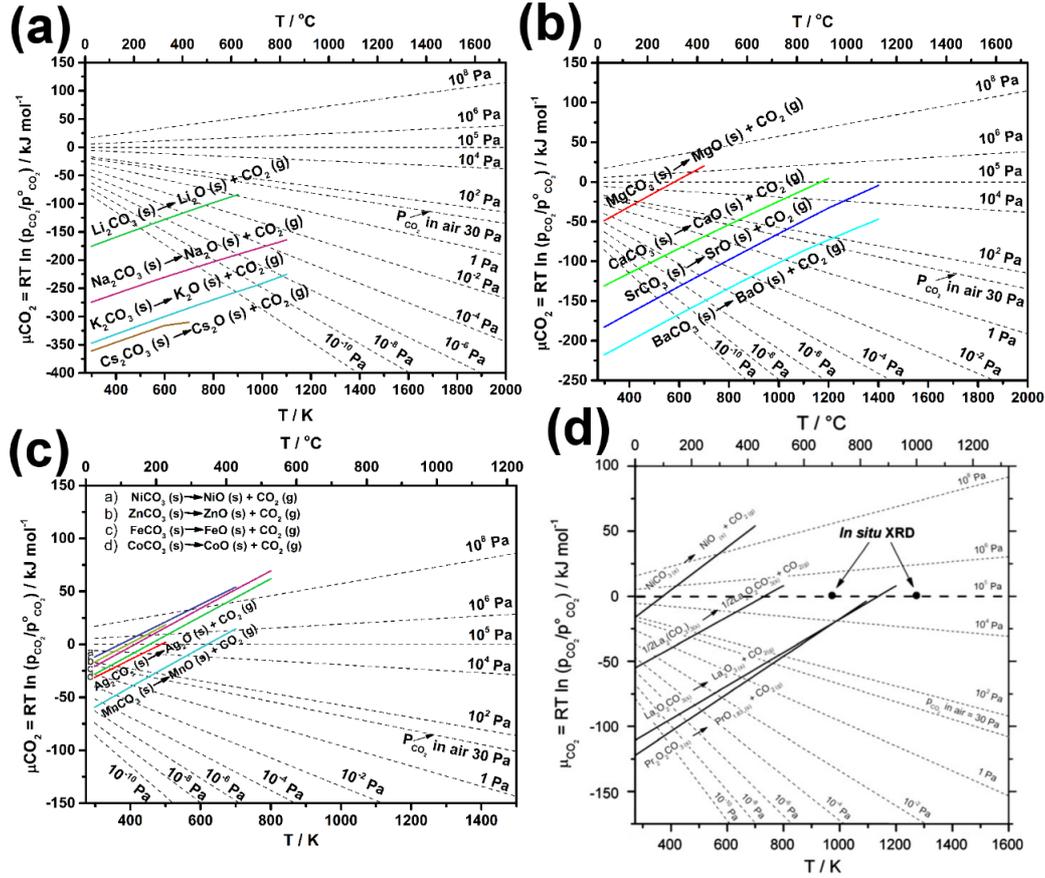
Figure 2.4 Ellingham diagrams for carbonates decomposition at different CO_2 partial pressure; (a) Li_2CO_3, Na_2CO_3, K_2CO_3 and Cs_2CO_3; (b) $MgCO_3$, $CaCO_3$, $SrCO_3$ and $BaCO_3$; (c) $NiCO_3$, $ZnCO_3$, $FeCO_3$, $CoCO_3$, Ag_2CO_3 and $MnCO_3$; and (d) $La_2(CO_3)_3$, $La_2O_2CO_3$ and $Pr_2O_2CO_3$ The dashed lines represent the chemical potential of CO_2 at a particular CO_2 partial pressure while the bold continuous lines represent the chemical potential of CO_2 for decomposition of a particular carbonate; both are functions of temperature (**Figure 2.4(a), (b), and (c)** were replotted based on the Ellingham diagrams from ref. 39-42; The thermodynamic data are taken from ref. 43; **Figure 2.4(d)** was reproduced from ref. 42 with permission from Elsevier).

For strontium and barium perovskite oxides, the stabilization energy increases (becomes negatively larger) with decreasing B^{4+} ion radius (0.87 Å > 0.72 Å > 0.605 Å for Ce, Zr, and Ti, respectively); manifesting into higher Gibbs energy change and lower tendency for carbonate formation.[23,34] The stability of the perovskite oxides was mainly determined by the less stable metal oxide constituent like SrO in the Sr-doped lanthanum perovskite oxide.[33] Comparing strontium and barium, although the tendency of carbonate formation is stronger for barium oxide, the stabilization energy of barium perovskite is (negatively) larger, resulting in the relatively similar stability against carbonate formation for strontium and barium perovskites.[34] This theory was

summarized and discussed in Martynczuk's paper.[37] This stabilization energy concept was applied by Klande *et al.* to explain the better CO_2 stability of $La_{0.6}Sr_{0.4}Co_{0.8}Fe_{0.2}O_{3-\delta}$ compared with $SrCo_{0.8}Fe_{0.2}O_{3-\delta}$.[38] They have proposed that the perovskite stabilization energies increase with increasing lanthanum content, leading to the higher stabilization effect for $La_{0.6}Sr_{0.4}Co_{0.8}Fe_{0.2}O_{3-\delta}$ compared to $SrCo_{0.8}Fe_{0.2}O_{3-\delta}$, which prohibits reactions on **Eq. (2.7) and (2.8)**. It is worth noting that the stabilization energy is just one of the possible aspects affecting the stability of perovskite against CO_2. Other parameters may need to be accounted for.

Another popular way is to estimate CO_2 resistance of a perovskite oxide based on its carbonate formation at a specific temperature and CO_2 partial pressure.[39-42] **Figure 2.4(a), (b), (c)** and **(d)** represent the typical Ellingham diagrams for evaluation of carbonates formation. Ellingham diagram has been utilized and disseminated by Feldhoff's group to estimate the stability of metal oxides in the CO_2-containing atmosphere at different CO_2 partial pressure.[39-42] To show its reproducibility, we re-calculated and re-plotted the Ellingham diagrams for alkaline metal carbonates (Li_2CO_3, Na_2CO_3, K_2CO_3, and Cs_2CO_3 in **Figure 2.4(a)**), alkaline-earth metal carbonates ($MgCO_3$, $CaCO_3$, $SrCO_3$, and $BaCO_3$ in **Figure 2.4(b)**), and transition metal carbonates ($NiCO_3$, $ZnCO_3$, $FeCO_3$, $CoCO_3$, Ag_2CO_3, and $MnCO_3$ in **Figure 2.4(c)**). The thermodynamic data from the data compilation of Barin *et al.* were used to obtain these three Ellingham diagrams.[43] The absence of the thermodynamic data for lanthanide carbonates ($La_2(CO_3)_3$, $La_2O_2CO_3$, and $Pr_2O_2CO_3$) requires their experimental measurements as performed by Feldhoff's group to obtain these compounds' diagrams (**Figure 2.4(d)**).[42] In Ellingham diagrams, the dashed lines represent the chemical potential of CO_2 at a particular CO_2 partial pressure while the bold continuous lines represent the chemical potential of CO_2 for decomposition of a particular carbonate; both are functions of temperature. The stability of a particular carbonate is evaluated by comparing the CO_2 chemical potential at a particular CO_2 partial pressure and temperature against the decomposition chemical potential at the same temperature. If the former is lower than the latter, the carbonate is thermodynamically unstable. In other words, the carbonate would form if the former is higher than the latter. For example, at 800 K (527 °C) and 1 Pa, the chemical potential of CO_2 is -75 kJ mol^{-1} while the chemical potential of decomposition of $BaCO_3$ and $CaCO_3$ is -130 kJ mol^{-1} and -53 kJ mol^{-1}, respectively (**Figure 2.4(a)**). At this condition, $BaCO_3$ may form whereas $CaCO_3$ is not likely to form.

17

Here, we only provide Ellingham diagrams for carbonates whose thermodynamic data are available. Diagrams for other carbonates can be identically constructed using the following procedure. First, the CO_2 chemical potential at different CO_2 partial pressures is calculated using $\mu_{CO_2} = RT \ln (p_{CO_2}/p_{CO_2}^o)$ (kJ mol^{-1}) and is plotted as y-axis with temperature and T as x-axis. Second, the Gibbs free energy change, ΔG_r for carbonate decomposition reaction is calculated using thermodynamic data and all of the reactions are normalized to generate one mole of CO_2. Taking $BaCO_3$ as an example, the Gibbs energy for the formation of $BaCO_3$ ($\Delta G_{f,BaCO_3}$), BaO ($\Delta G_{f,BaO}$), and CO_2 ($\Delta G_{f,CO_2}$) can be collected from the data compilation of Barin et $al.$.[43] The Gibbs free energy change ΔG_r for the carbonate decomposition reaction of $BaCO_3$ (s) → BaO (s) + CO_2 (g) is calculated using the formula of $\Delta G_r = \Delta G_{f,BaCO_3} - \Delta G_{f,BaO} - \Delta G_{f,CO_2}$. For each individual temperature, there is one corresponding ΔG_r. The ΔG_r values are then plotted in the diagram as the function of temperatures; forming a line with positive slope. Accordingly, at a certain temperature, if ΔG_r is higher than the chemical potential of CO_2 (μ_{CO_2}) at a given CO_2 partial pressure, the carbonate will decompose. For example, at 1000 K, the Gibbs free energy change ΔG_r for $BaCO_3$ (s) → BaO (s) + CO_2 (g) is -101.85 kJ mol^{-1}, which is higher than the CO_2 chemical potential of -134.11 kJ mol^{-1} at CO_2 partial pressure of 10^{-2} Pa. It indicates that $BaCO_3$ is not stable at 1000 K when the surrounding CO_2 partial pressure is 10^{-2} Pa. Ellingham diagram should be viewed as an approximate thermodynamic predictor for the carbonate stability. Other factors such as the stabilization energy of the perovskites and the kinetic of the carbonate decomposition may play role.

In most carbonate cases, there is also a correlation between the stability and the carbonate size where larger ionic radius normally leads to larger crystal energy for the respective metal carbonate and thus, higher stability. For instance, **Figure 2.4(b)** implies increasing stability from $CaCO_3$ to $SrCO_3$ and to $BaCO_3$, in parallel with increasing ionic radius of the metal cations, $i.e.$, 1.34 Å (Ca^{2+}), 1.44 Å (Sr^{2+}), and 1.61 Å (Ba^{2+}) (all with coordination number of 12).[23,41] Again, smaller ionic radius for Ni^{2+} (0.69 Å – coordination number of 6) compared to La^{3+} (1.36 Å – coordination number of 12) and Pr^{3+} (1.179 Å – coordination number of 9) is in accord with lower stability for $NiCO_3$ with respect to $La_2(CO_3)_3$, $La_2O_2CO_3$, and $Pr_2(CO_3)_3$ (**Figure 2.4(d)**).[23,42] Charge (or oxidation state) of the metal cation, on the other hand has reciprocal relationship to the stability of the carbonate with lower charge favors higher stability.[44]

2.2.1.2.2 Chemistry perspective

Although the thermodynamic analysis may provide a glimpse on the chemical stability of perovskite oxides, it requires the presence of thermodynamic data which are not always readily available for all compounds. The extent of reaction between perovskite oxide and CO_2 can also be rationalized using Lewis acid-base concept to address this shortcoming.[30,45-47] In this context, perovskite oxide is a base (or electron pair donor) while CO_2 is an acid (or electron pair acceptor). The basicity of perovskite oxide, *i.e.*, the tendency to give up (or donate) electrons to the adsorbed CO_2 molecule which varies at different temperature and oxygen partial pressure, becomes the determining variable. Higher basicity translates to intensified reaction. Sanderson's electronegativity and the oxidation state of the cations are the two parameters that reflect the relative basicity of the metal oxides.[48] Higher oxidation state generally signifies lower basicity (higher acidity) and accordingly, higher CO_2 resistance.
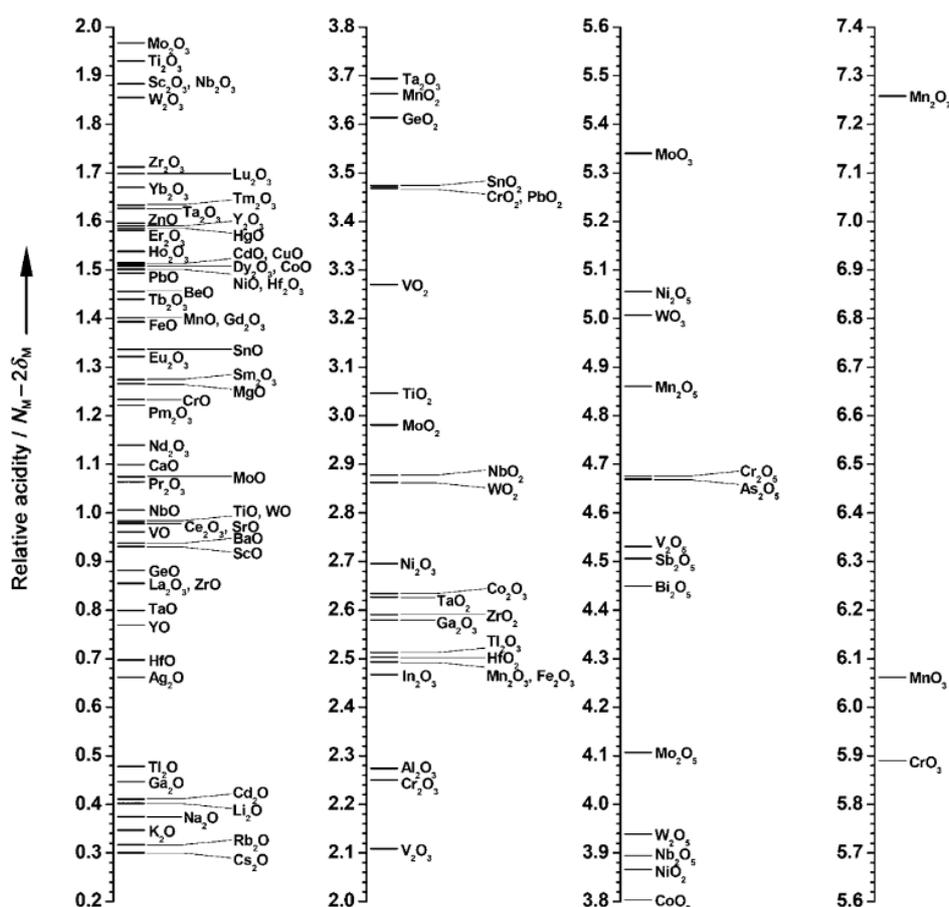
Figure 2.5 Comparison of the relative acidity of various oxides (Reproduced from ref. 48 with permission from Wiley).
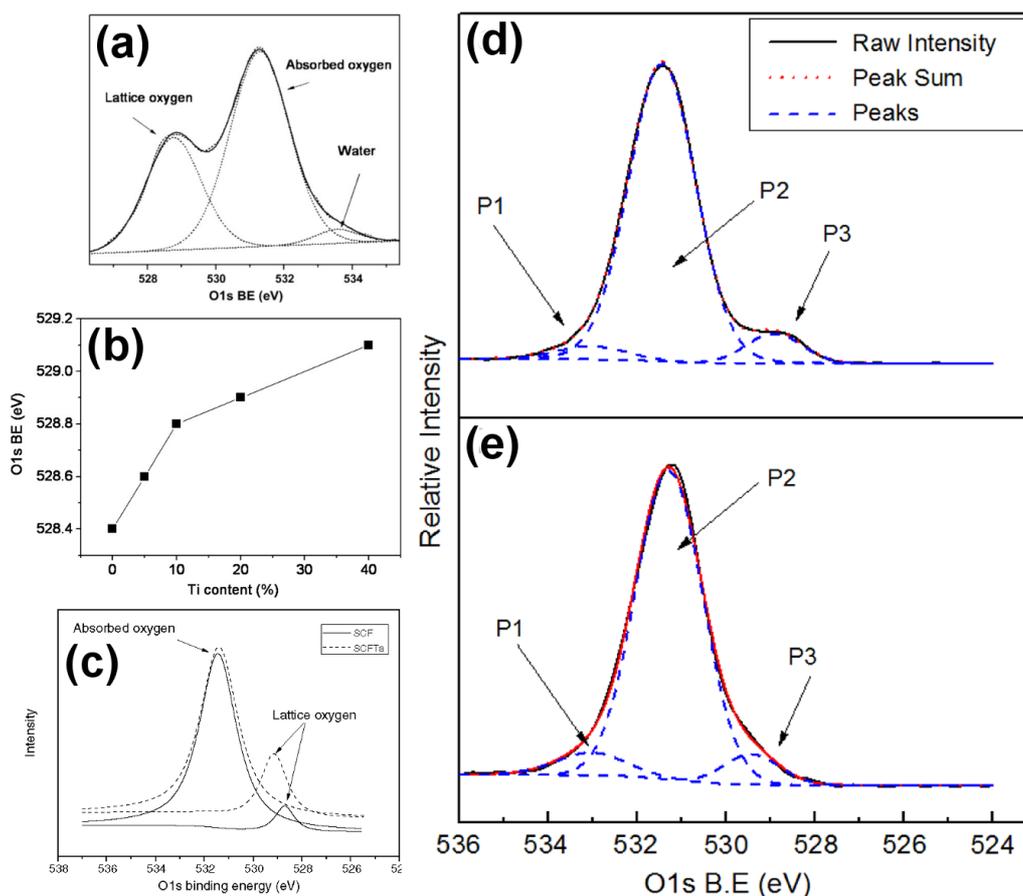
Figure 2.6 (a) X-ray photoelectron spectroscopy (XPS) spectrum of O1s binding energy (BE) for $Sr(Co_{0.8}Fe_{0.2})_{0.9}Ti_{0.1}O_{3-\delta}$; (b) The O1s BE of lattice oxygen as a function of Ti content (x) on $Sr(Co_{0.8}Fe_{0.2})_{1-x}Ti_xO_{3-\delta}$; (c) The O1s BE of adsorbed oxygen and lattice oxygen on $SrCo_{0.8}Fe_{0.2}O_{3-\delta}$ and $Sr(Co_{0.8}Fe_{0.2})_{0.9}Ta_{0.1}O_{3-\delta}$; and XPS spectrum of $SrCo_{0.8}Fe_{0.2}O_{3-\delta}$ quenched from 20-hour annealing at 950 °C in oxygen partial pressure of (d) 10^{-4} bar and (e) 1 bar (Reproduced from ref. 45-47 with permission from Elsevier).

The descriptor variable that indicates the relative acidity of metal oxide has been given by Jeong *et al.* in the form of N_M-$2\delta_M$ value where N_M represents the formal oxidation of the metal in compound and δ_M represents the partial charges of the metal ions.[48] **Figure 2.5** depicts such N_M-$2\delta_M$ values for 101 metal oxides where higher value reflects higher acidity. Moreover, the data in **Figure 2.5** clearly indicates that the surface acidity of a metal is a function of oxidation state of the cation, the electronegativity of the cation, and the electronegativity of the anion. Given the explicit acidity value, **Figure 2.5** becomes an invaluable reference for the design of new CO_2-resistant oxides compositions. To obtain this comprehensive correlation, Jeong *et al.* measured the intramolecular charge-transfer (ICMT) energies for adsorption of two

different dyes, *i.e.*, alizarin and 4-methoxyalizarin onto various metal oxides and sulfides by diffuse reflectance spectroscopy. They found correlations between the ICMT energies and N_M-$2\delta_M$ values which allowed them to calculate the Sanderson's electronegativity values for all tested samples including those for lanthanides (Ln_2O_3) and CeO_2 which were not available before their work.[48]

Since the reactions occur effectively only at the basic sites or sites with negative charge, *i.e.*, on oxide ions, the basicity of perovskite oxide can also be measured using the O1s binding energy (BE) from X-ray photoelectron spectroscopy (XPS) which reflects the electron density (or oxidation state) of oxide ions.[49] Higher O1s binding energy implies lower electron density (or higher oxidation state) and consequently, lower basicity.[49] The O1s peak on XPS data generally consists of contributions from 3 oxygen components, *i.e.*, oxygen in adsorbed water (at the highest BE), adsorbed oxygen (at the medium BE), and lattice oxygen (at the lowest BE) (**Figure 2.6(a), (d) and (e)**). The binding energy for lattice oxygen in most cases can be taken as an accurate measure for basicity. For example, Ti-doped $SrCo_{0.8}Fe_{0.2}O_{3-\delta}$ was reported to be more stable to CO_2 than $SrCo_{0.8}Fe_{0.2}O_{3-\delta}$; consistent with the fact that when the Ti content (x) in $Sr(Co_{0.8}Fe_{0.2})_{1-x}Ti_xO_{3-\delta}$ was increased from 0 to 0.4, the O1s BE of lattice oxygen increased from 528.4 eV to 529.1 eV (**Figure 2.6(a) and (b)**).[45] Partial substitution of Co and Fe in $SrCo_{0.8}Fe_{0.2}O_{3-\delta}$ with Ta (*i.e.*, $Sr(Co_{0.8}Fe_{0.2})_{0.9}Ta_{0.1}O_{3-\delta}$) also led to the shifting of lattice oxygen peak to a higher binding energy value, *i.e.*, by 0.4 eV from 528.7 eV (for $SrCo_{0.8}Fe_{0.2}O_{3-\delta}$) to 529.1 eV (for Ta-doped $SrCo_{0.8}Fe_{0.2}O_{3-\delta}$) (**Figure 2.6(c)**).[46] Accordingly, Ta-doped $SrCo_{0.8}Fe_{0.2}O_{3-\delta}$ showed enhanced stability to CO_2 with respect to $SrCo_{0.8}Fe_{0.2}O_{3-\delta}$. Moreover, exposing $SrCo_{0.8}Fe_{0.2}O_{3-\delta}$ to higher oxygen partial pressure, *e.g.*, 1 bar relative to 10^{-4} bar increased the CO_2 resistance in agreement with increased O1s BE for lattice oxygen at higher oxygen partial pressure, *i.e.*, 529.5 eV relative to 528.9 eV (**Figure 2.6(d) and (e)**).[47]

An effective way to reduce the basicity of the perovskite oxide is by decreasing the electron density of oxide ions. This can be achieved using metal elements whose cations strongly attract the electron cloud away from oxygen anion, *i.e.*, metal cations with high oxidation state, *e.g.*, Ta^{5+} and Ti^{4+} as demonstrated for Ta and Ti-doped $SrCo_{0.8}Fe_{0.2}O_{3-\delta}$ compounds.[45,46] The bonding between such metal cation and oxygen anion (*e.g.*, bonding energy of Ta–O and Ti–O is 799.1 kJ mol^{-1} and 672.4 kJ mol^{-1}, respectively) is substantially stronger than the bonding between common metal cation

and oxygen anion such as Co and Fe (*e.g.*, bonding energy of Co–O and Fe–O is 384.5 kJ mol^{-1} and 390.4 kJ mol^{-1}, respectively). Such strong bond however suppresses the oxygen loss from the lattice which affects negatively the oxygen permeability. Therefore, a trade-off exists between the oxygen permeability and the CO_2 resistance. The average metal-oxygen bond energy (ABE) provides a simple quantitative predictor in this regard to assess the CO_2 resistance.[50] This parameter can be calculated as shown below for $A_{1-x}A'_xB_{1-y-z}B'_yB''_zO_{3-\delta}$ -type perovskite oxide (**Eq. (2.9) – (2.13)**) and thus far has been exclusively used to determine the oxygen ionic diffusion in perovskite oxides.[51,52]

$$< ABE > = < A - O > + < B - O > \qquad \text{(Eq. 2.9)}$$

$$< A - O > = \Delta(A - O) + \Delta(A' - O) \qquad \text{(Eq. 2.10)}$$

$$< B - O > = \Delta(B - O) + \Delta(B' - O) + \Delta(B'' - O) \qquad \text{(Eq. 2.11)}$$

$$\Delta(A - O) = (x_A/(CN_A \cdot m)) \cdot (\Delta H_{A_mO_n} - m \cdot \Delta H_A - \frac{n}{2} \cdot D_{O_2}) \qquad \text{(Eq. 2.12)}$$

$$\Delta(B - O) = (y_B/(CN_B \cdot m)) \cdot (\Delta H_{B_mO_n} - m \cdot \Delta H_B - \frac{n}{2} \cdot D_{O_2}) \qquad \text{(Eq. 2.13)}$$

Where x_A and y_B represents the mole fraction of A and B; $\Delta H_{A(B)_mO_n}$ and $\Delta H_{A(B)}$ represents the enthalpy of formation of one mole of $A(B)_mO_n$ and the sublimation energy of *A(B)* metal at 25 °C, available from thermodynamics database; $CN_{A(B)}$ represents the coordination number of A and B site cations ($CN_A = 12$, $CN_B = 6$); and D_{O_2} represents the dissociation energy of O_2 (*i.e.*, 500.2 kJ mol^{-1}).

2.2.1.2.3 Other factors like chemical adsorption

In general, two subsequent processes manifest over the course of interaction between CO_2 and oxide-based membranes, *i.e.*, the CO_2 adsorption on the membrane surface and the carbonate formation. In most cases, the significant poisoning effect of CO_2 as reflected by the considerable deterioration of original flux is mainly attributed to the chemical adsorption of CO_2 onto membrane surface since the carbonate formation does

not occur instantaneously.[53] Three progressive steps are involved in the oxygen transport through MIEC membranes, *i.e.*, (1) the surface-exchange reaction of oxygen gas molecules and oxygen vacancies; (2) bulk-diffusions of lattice oxygen ions and electrons/electron holes across the bulk membrane; and (3) the surface-exchange reaction of lattice oxygen and electrons.[54,55] The oxygen transport rate is thus closely associated with the surface oxygen vacancies. To this end, when CO_2 is used as the sweep gas, oxygen ions on CO_2 may be adsorbed chemically on the oxygen vacancies of the membrane.[56,57] This leads to the decrease in oxygen permeation rate with increasing time. Such CO_2 adsorption effect is responsible for the rapid deterioration of O_2 flux after CO_2 is introduced and also the fast recovery of O_2 flux to larger value after CO_2 is removed.[53]

Using temperature programmed desorption, Yan *et al.* showed the competitive adsorption of O_2 and CO_2 on $Ba_{0.5}Sr_{0.5}Co_{0.8}Fe_{0.2}O_{3-\delta}$ (BSCF5582) surface.[58] They studied CO_2 adsorption effect on BSCF5582 in the presence of O_2 and H_2O; highlighting CO_2 adsorption as one of the factors reflecting the CO_2 tolerance of perovskite. The reactivity of CO_2 and Sr^{2+} and/or Ba^{2+} on BSCF5582 surface increased with increasing temperature when only CO_2 was adsorbed onto the surface. However, when CO_2 and O_2 were co-adsorbed on the surface, CO_2 adsorption was restrained, especially when O_2 adsorption became dominant at 700 °C. Furthermore, the presence of water led to more severe CO_2 poisoning effect due to the bicarbonate formation. Winnubst and co-workers showed that the addition of a low amount O_2 to CO_2 atmosphere enhanced the CO_2 tolerance of $SrCo_{0.8}Fe_{0.2}O_{3-\delta}$ membrane.[47] They found that when pure CO_2 was used as a sweep gas, the oxygen flux of $SrCo_{0.8}Fe_{0.2}O_{3-\delta}$ reduced to zero within 25 hours. When 5 vol. % O_2 was introduced into predominantly CO_2 sweep gas, the oxygen flux decreased by 34 % over the first 10-hour period before slowly increased to 90 % of its initial flux value within the following 50-hour period and then stabilized around this value.

Fang *et al.* proposed another factor that influences the CO_2 tolerance of fluorite-perovskite-based composite membrane, *i.e.*, 80 wt. % $Ce_{0.8}Gd_{0.15}Cu_{0.05}O_{2-\delta}$-20 wt. % $SrFeO_{3-\delta}$ (CGC-SF) dual-phase membrane. This factor is related to the chemical potential of oxygen (μ_{O_2}) across the membrane.[59] When O_2-enriched air was used as the feed gas (*i.e.*, the chemical potential of O_2 is increased), the membrane exhibited significantly enhanced CO_2-resistance when exposed to pure CO_2 sweep gas. They

hypothesized that the carbonates formation is thermodynamically and kinetically limited. Therefore, higher μ_{O_2} can suppress the adsorption of CO_2 significantly by generating faster O_2 releasing rate and lower oxygen vacancy concentration on the permeate side, contributing to the less carbonates formation during the long-term exposure to CO_2.[58] Nonetheless, another research work on $Ba(Co,Fe,Nb)O_{3-\delta}$ indicates that the increase of the oxygen partial pressure significantly promotes the $BaCO_3$ formation, which suggests that oxygen molecular probably becomes the oxygen source for the carbonation formation. However, they recommended further investigation to reveal the real oxygen source for the carbonate formation.[30]

Yi *et al.* investigated the oxygen permeability and stability of $Sr_{0.95}Co_{0.8}Fe_{0.2}O_{3-\delta}$ membrane in an atmosphere containing CO_2 and H_2O in the feed side.[60] Compared with applying CO_2 or H_2O alone in feed side, the combined presence of CO_2 and H_2O provides more negative effect on microstructure, phase composition, and oxygen permeation performance of $Sr_{0.95}Co_{0.8}Fe_{0.2}O_{3-\delta}$ membrane. This is identical with what was observed by Yan *et al.* on BSCF5582.[58] Such phenomena were caused by the formation of bicarbonate on the membrane surface which is enabled by the existence by both CO_2 and H_2O. The membrane degradation additionally correlates with the applied oxygen partial pressure and temperatures. Higher oxygen partial pressure and lower temperature (*i.e.*, 810 ^oC) enhanced the degradation effect. The bicarbonate formation was associated with the entropy reduction which is favored at lower temperature.

2.2.1.3 Recent status and advances

In this section, the recent works on CO_2-resistant perovskite membranes are summarized. For comparison purpose, the performances of some typical perovskite membranes are listed in **Table 2.1**.[30,39,41,45-47,53,61-73]

Alkaline-earth metals containing perovskite oxides such as $(Ba,Sr)(Co,Fe)O_{3-\delta}$ are among the best candidates for oxygen permeation membranes due to their high mixed ionic and electronic conductivity.[15] However, they have poor stability under CO_2 atmosphere. BSCF5582 disk, for example, have high oxygen fluxes that normally can reach more than 1 mL min^{-1} cm^{-2} at 950 ^oC, or even reach to 12.2 mL min^{-1} cm^{-2} at 1000 ^oC for an ultrathin BSCF5582 membrane with porous substate.[74-88] The low chemical

24

stability of BSCF5582 nevertheless resulted in the formation of barium or strontium carbonates as the surface layer and oxygen flux deterioration, upon exposure to CO_2.[27-29,81] As little as 300 ppm of CO_2, less than the content in air (380 ppm), was sufficient to damage BSCF5582 membrane.[89] The carbonate particles could form on the surface even after a short annealing time of 3 minutes at 800 ^{o}C in CO_2 atmosphere. With prolonged treatment time, the carbonate particles grew into compact carbonate layer.[29] Such degradation was also observed on the performance of the solid oxide fuel cell (SOFC) using BSCF5582 as the cathode component in CO_2 containing atmosphere.[90-93] Strong CO_2 adsorption on the BSCF5582 surface and the formed carbonate layer contributed to the decrease of the oxygen surface exchange reaction that impaired the cell performance. Small quantities of CO_2 (*i.e.*, 0.28-3.01 vol. %) negatively affected the SOFC performance at 450 ^{o}C.[90] To this end, several attempts have been performed to enhance CO_2 resistance of BSCF5582 membrane such as reducing the amount of alkaline earth elements and/or the amount of cobalt and incorporating fixed-valence metal elements in B-site.

As mentioned above, the stability of carbonates increases with increasing ionic radius of alkaline earth elements.[41,94,95] The stability increases in the order of Ca (1.34 Å), Sr (1.44 Å), and Ba (1.61 Å). Although Ca-containing perovskites show better stability towards CO_2 than Ba- and Sr-containing ones, carbonates still formed during exposure to CO_2 atmosphere.[57,96] Partial substitution of alkaline-earth cations in A-site with rare-earth cations has been adopted to enhance the CO_2 resistance of alkaline-earth elements containing perovskite oxides. For example, partial substitution of Ba with rare-earth cations, *i.e.*, La or Pr can substantially enhance the stability against CO_2.[53,69,72,97] Waindich *et al.* compared the CO_2 corrosion behavior of BSCF5582, $Ba_{0.3}Sr_{0.7}Co_{0.2}Fe_{0.8}O_{3-\delta}$ (BSCF3728), and $La_{0.3}Ba_{0.7}Co_{0.2}Fe_{0.8}O_{3-\delta}$ (LBCF3728). They found that BSCF3728 and LBCF3728 exhibit better chemical stability against CO_2 corrosion relative to BSCF5582.[98] The enhancement of stability against CO_2 can be understood from thermodynamics perspective as discussed above. Using Ellingham diagram, Partovi *et al.* predicted that the decomposition temperature is above 1100 ^{o}C for pure $SrCO_3$ and even higher (above 1400 ^{o}C) for $BaCO_3$ under an atmospheric pressure (101.3 kPa) of CO_2,[97] while the rare-earth cation carbonates decompose at lower temperatures.[15,41,42] Partial substitution of La in $LaFeO_{3-\delta}$ and $LaCo_{0.8}Fe_{0.2}O_{3-\delta}$ with Ca was performed to take advantage of higher Ca and La stability in CO_2 atmosphere. $(La_{1-x}Ca_x)FeO_{3-\delta}$ and $(La_{1-x}Ca_x)(Co_{0.8}Fe_{0.2})O_{3-\delta}$ compounds with x = 0.4-

0.6 were synthesized where only x = 0.4 compounds showed almost pure perovskite phases.[41]

In general, the complete substitution of Ba in A-site with rare-earth cations leads to substantially lower oxygen permeation flux (than that obtained in Ba-containing perovskites). For example, at 800 $^{\circ}$C, $La_{0.58}Sr_{0.4}Co_{0.2}Fe_{0.8}O_{3-\delta}$ membrane in 1-mm-thickness displayed oxygen flux of only around 0.15 mL min^{-1} cm^{-2} or an even lower flux value for $La_{0.6}Sr_{0.4}Co_{0.2}Fe_{0.8}O_{3-\delta}$ (LSCF6428).[99-101] The lower oxygen permeation flux was a consequence of two factors. Firstly, replacing low valence cations (*i.e.*, Ba^{2+} or Sr^{2+}) with higher valance cations (*i.e.*, La^{3+}) led into lower oxygen non-stoichiometry and also lower concentration of oxygen vacancies (relative to $SrCo_{0.2}Fe_{0.8}O_{3-\delta}$ or BSCF5582).[38,97] Secondly, reduced lattice parameter manifested from such replacement given the smaller ionic radius of La^{3+} (1.36 Å) compared with Sr^{2+} (1.44 Å).[23,97] CO_2 stability of $La_{0.6}Sr_{0.4}Co_{0.8}Fe_{0.2}O_{3-\delta}$ (LSCF6482) nonetheless increases following such substitution (relative to $SrCo_{0.2}Fe_{0.8}O_{3-\delta}$ and BSCF5582).[38] Besides the rare earth metal substitution strategy, the chemical and structural stability of perovskites can also be related to their A-site cation stoichiometry.[60,102-106] Shao *et al.* observed that the oxygen permeation of BSCF5582 increased slightly, *i.e.*, from 1.1 to 1.2 mL min^{-1} cm^{-2} during a long-term test for more than 1000 h at 850 $^{\circ}$C.[107] Such increment in permeation flux is associated to the A-site cation diffusion.[108] The resultant A-site cation deficiency caused by diffusion was charge compensated by the creation of additional oxygen vacancies which increased oxygen permeation flux. For $Sr_{1-y}Fe_{1-x}Ti_xO_{3-\delta}$ compounds, creation of A-site deficiency suppressed the oxygen-vacancy ordering and increased the structure disorder; leading to the stability of the cubic perovskite structure. In the case of A-site stoichiometric $SrFe_{0.8}Ti_{0.2}O_{3-\delta}$, exposure to CO_2 for 40 hours at 200 $^{\circ}$C led to the formation of $SrCO_3$ as revealed by the infrared (IR) absorption spectroscopy result. $SrCO_3$, on the other hand, did not form in case of A-site deficient $Sr_{1-y}Fe_{0.8}Ti_{0.2}O_{3-\delta}$ (y = 0.03-0.06). This observation indicates that structure and oxygen permeation flux stability may, in specific cases, be enhanced *via* the creation of A-site deficiency.[105] Another representative example is A-site deficient $Sr_{0.95}Nb_{0.1}Co_{0.9}O_{3-\delta}$ in the application context of cathode for SOFCs. After introducing CO_2-containing air, the increase in the area specific resistance (ASR) of the $Sr_{0.95}Nb_{0.1}Co_{0.9}O_{3-\delta}$ cathode was less than that of the $SrNb_{0.1}Co_{0.9}O_{3-\delta}$ cathode. The lower oxygen reduction reaction performance degradation for the former compound indicates that the A-site deficiency minimized CO_2 poisoning on the surface of the

cathode.[109] In addition, for the dual-phase (composite) membrane of $SrFe(Al)O_{3-\delta}$ - $SrAl_2O_4$, partial dissolution of $SrAl_2O_4$ in $SrFe(Al)O_{3-\delta}$ perovskite phase generated A-site deficiency in this phase. The resultant strontium deficiency contributed towards the improved composite stability against reaction with CO_2.[110] The mechanism behind the enhanced CO_2 resistance from A-site deficiency is still elusive. Generally speaking, the additional oxygen vacancies generated from A-site deficiency is likely to increase the oxygen permeation flux and the structure stability. Such higher concentration of oxygen vacancies tends to promote CO_2 surface adsorption and eventually, the formation of carbonates.

From the perspective of Lewis acid-base concept, partial substitution of B-site elements with fixed valence cation serves as an alternative option to improve the stability of perovskite membranes. The work of Czuprat *et al.* was among the earliest works to report the effect of exposing perovskite to CO_2 atmosphere.[39] For $BaCo_xFe_yZr_zO_{3-\delta}$ compound, exposure to 50 vol. % CO_2 in He for 5-10 hours led to the decomposition of perovskite structure up to a depth of 25 μm. Scanning electron microscopy indicates the formation of up to 10 μm $BaCO_3$-enriched layer followed by up to 15 μm Ba-depleted zone on top of the original perovskite layer. They also showed that the original microstructure and oxygen fluxes can be recovered in CO_2-free atmosphere (*i.e.*, He). Similar results were obtained on $BaCo_{0.7}Fe_{0.3-x}Zr_xO_{3-\delta}$ membrane of which a corrosion layer with an average thickness of 12 μm for x = 0.04 and 8 μm for x = 0.10 appeared.[65] CO_2 resistance enhances by increasing the amount of Zr dopant although with inevitable reduction of oxygen permeation flux. Doping with other high valence metal cations such as Ta, Nb, and Ce gives the identical effect towards the oxygen permeation, methane partial oxidation, and chemical stability behaviors of Ba fully-occupied A-site $BaCoFeO_{3-\delta}$ membranes.[30,111-117] Nb, in particular, is an effective dopant to enhance the stability of perovskite while maintaining high oxygen permeability.[30,118] Yi *et al.* studied the oxygen permeation behavior and the degradation mechanism of $Ba(Co,Fe,Nb)O_{3-\delta}$ perovskite in CO_2 atmosphere.[30] Partial substitution of Fe and Co by Nb leads to the higher CO_2 resistance (relative to the original compound) and the stability enhancement mechanism are explored using Lewis acid-base perspective as discussed above. Upon relating this observation with the acidity trend reported by Jeong *et al.*, (in increasing acidity order), *i.e.*, Fe^{2+}, Co^{2+}, Fe^{3+}, Co^{3+}, Co^{4+}, and Nb^{5+}; such acidity increase appears to correlate with the increasing oxidation

state.[48] Increasing content of Nb^{5+} or Fe^{3+} contributes towards higher acidity relative to the case of B-site cation fully occupied by Co^{2+}. The high valence metal doping approach manifested in several other compounds such as $BaCo_{0.7}Fe_{0.2}Sn_{0.1}O_{3-\delta}$, $BaCo_{0.7}Fe_{0.3-x}In_xO_{3-\delta}$, $BaTi_{0.2}Co_{0.5}Fe_{0.3}O_{3-\delta}$, and $BaBi_xCo_{0.2}Fe_{0.8-x}O_{3-\delta}$ which were tested as oxygen permeation membranes but without evaluating their stability in the presence of CO_2.[119-122] Despite the stability enhancement obtained *via* such doping, Ba-containing perovskites nonetheless show performance deterioration over time in CO_2-containing atmosphere as observed in the case of tantalum and bismuth co-doped perovskite $BaBi_{0.05}Co_{0.8}Ta_{0.15}O_{3-\delta}$.[67] $BaBi_{0.05}Co_{0.8}Ta_{0.15}O_{3-\delta}$ indeed demonstrated higher stability than BSCF5582 but the oxygen flux still declined under the long-term operation with CO_2-containing atmosphere as sweep gas. With the exception of $BaCo_{1-x}Fe_xO_{3-\delta}$ system, other compositions of B-site doping have mostly been performed. By substituting as low as 2 mole % of tungsten into BSCF5582, the phase transition and O_2 permeation performance degradation in CO_2 atmosphere was effectively suppressed on such $Ba_{0.5}Sr_{0.5}Co_{0.78}Fe_{0.2}W_{0.02}O_{3-\delta}$ membrane,[66] which exhibited higher stability under sweep gas containing 20 vol. % CO_2 within 1.5 hour-test period and 100 vol. % CO_2 within 0.25 hour-test period, compared with BSCF5582 without tungsten doping. Chen and co-workers developed Ti-doped $SrCo_{0.8}Fe_{0.2}O_{3-\delta}$, *i.e.*, $Sr(Co_{0.8}Fe_{0.2})_{1-x}Ti_xO_{3-\delta}$ (x = 0.05, 0.1, 0.2 and 0.4) to enhance the CO_2 resistance of $SrCo_{0.8}Fe_{0.2}O_{3-\delta}$.[45] Upon exposure to CO_2, the oxygen permeation flux of $SrCo_{0.8}Fe_{0.2}O_{3-\delta}$ was reduced to only 30 % of the initial flux after 70 hour-period. For $Sr(Co_{0.8}Fe_{0.2})_{0.95}Ti_{0.05}O_{3-\delta}$ after the same period of exposure, up to 43 % of the initial flux was retained. In the case of $Sr(Co_{0.8}Fe_{0.2})_{0.9}Ti_{0.1}O_{3-\delta}$ and $Sr(Co_{0.8}Fe_{0.2})_{0.8}Ti_{0.2}O_{3-\delta}$, on the other hand, CO_2 exposure did not affect the oxygen flux. Ta-doped $SrCo_{0.8}Fe_{0.2}O_{3-\delta}$, *i.e.*, $Sr(Co_{0.8}Fe_{0.2})_{0.9}Ta_{0.1}O_{3-\delta}$ was also demonstrated to be stable to CO_2 where only 5.3 % (from 1.32 mL min^{-1} cm^{-2} to 1.25 mL min^{-1} cm^{-2}) drop in oxygen flux was observed on switching the sweep gas from helium to CO_2. The flux stabilized at 1.14 mL min^{-1} cm^{-2} after 50 hours exposure to CO_2.[46]

Although partial substitution of B-site cations with more acidic (less basic) metal cation can enhance CO_2 resistance, the formation of alkaline-earth carbonate layer is unavoidable after prolonged exposure to pure CO_2. Ta-doped $SrFeO_{3-\delta}$ membrane, for example, in spite of its higher CO_2 resistance than non-doped $SrFeO_{3-\delta}$, *i.e.*, capability to retain its oxygen permeation flux for at least 71 hours under 10 vol. % CO_2 atmosphere, showed 33.9 % decay in oxygen flux within 26 hours when pure CO_2

was used as the sweep gas.[123] Zhu *et al.* evaluated CO_2 reaction mechanisms on $SrCo_{0.9-x}Fe_xNb_{0.1}O_{3-\delta}$ (SNCFx) cathodes.[50] No carbonate phase was detected on powder X-ray diffraction patterns for all perovskite compositions after one hour of CO_2 exposure at 600 $^{\circ}$C. Fourier Transform Infra-Red spectra nonetheless displayed the presence of carbonate functional groups on SNCF0.1, SNCF0.2, and SNCF0.3 which was absent on SNC, SNCF0.5, and SNF. In the cases of SNCF0.1, SNCF0.2, and SNCF0.3, Zhu *et al.* hypothesized the simultaneous occurrence of CO_2 adsorption and strontium carbonate formation whereas for the other compositions, only CO_2 adsorption occurred. These distinct behaviors appeared to correlate with the oxygen non-stoichiometries of the perovskites. Reducing Co content in B-site of the perovskite can enhance CO_2 resistance albeit the resultant reduction in O_2 permeability as discussed in detail by Partovi *et al.*.[72] The oxygen permeation properties and the chemical stabilities of cobalt-free $SrFe_{0.8}M_{0.2}O_{3-\delta}$ perovskites ($SrFe_{0.8}Zr_{0.2}O_{3-\delta}$, $SrFe_{0.8}Mo_{0.2}O_{3-\delta}$, and $SrFe_{0.8}W_{0.2}O_{3-\delta}$) were probed under CO_2-containing atmosphere.[64] Powder X-ray diffraction measurements combined with Rietveld analyses showed that the dominant phase for CO_2-exposed $SrFe_{0.8}M_{0.2}O_{3-\delta}$ is cubic perovskite. A very small peak emerged near the (110) plane peak that can be attributed to the pyrochlore phase or single oxide phase. When 10 vol. % CO_2 was introduced into the sweep gas, $SrFe_{0.8}Mo_{0.2}O_{3-\delta}$ and $SrFe_{0.8}W_{0.2}O_{3-\delta}$ displayed stable oxygen fluxes (0.15 and 0.17 mL min^{-1} cm^{-2}, respectively) for 10 hours whereas the oxygen flux of $SrFe_{0.8}Zr_{0.2}O_{3-\delta}$ gradually decreased. The latter deterioration was related to the presence of Zr^{3+} in CO_2-exposed $SrFe_{0.8}Zr_{0.2}O_{3-\delta}$ as evidenced by X-ray photoelectron spectroscopy results.[64] The stabilizing effect of divalent zinc-doped $(Ba,Sr)FeO_{3-\delta}$ (BSFZ) was investigated under CO_2 atmosphere.[37] Even when the cobalt was totally substituted by zinc, O_2 flux of BSFZ still decreased to almost zero when pure CO_2 was used as sweep gas. Martynczuk *et al.* found that the formation of 8 % carbonate phase on BSFZ surface was sufficient to induce the oxygen permeability degradation at 750 $^{\circ}$C.[37] Powder X-ray diffraction, scanning electron microscopy, and transmission electron microscopy results evidenced the co-existence of cubic, hexagonal, and tetragonal perovskites phases as well as a carbonate layer at the surface after CO_2 treatment. The tetragonal and cubic phases were found to be favorable for oxygen permeation while the hexagonal and carbonate phases were not. Furthermore, they also showed that the original O_2 permeability can be partially recovered by sintering CO_2-exposed membrane at high temperature, *i.e.*, 950 $^{\circ}$C under helium for a short time.

Yi *et al.* discussed the strategy to choose metal elements in CO_2-resistant perovskite ceramics.[62] In terms of A-site cation candidates from alkaline earth metals, the presence of large ionic radius cation such as Ba^{2+} usually leads to high oxygen permeability but has tendency to form carbonate with CO_2. Incorporating Ca^{2+}, on the other hand, would provide CO_2 tolerance although with the anticipated decrease of oxygen flux. Sr^{2+} that is located between those two metals in the same column in the periodic table, is expected to balance the oxygen permeability and CO_2 stability. For the B-site cation, Co and Fe have been extensively used with the former has poor stability under CO_2 while the latter shows better stability and is thus preferred. The inclusion of a low amount of metal with high valence such Nb^{5+} is beneficial to stabilize the perovskite framework and improve its resistance to CO_2. These considerations lead to the development of $Sr(Fe,Nb)O_{3-\delta}$ perovskite membrane processing good oxygen permeability and CO_2 tolerance. Zhang *et al.* evaluated the doping effect on the phase structure, chemical stability, sintering behavior, conductivity, and oxygen permeability of $SrFe_{0.8}M_{0.2}O_{3-\delta}$ (M = Ti^{4+}, Nb^{5+}, and Cr^{6+}) perovskites.[124] They found that the dopants with different oxidation states affect the oxidation state of Fe ions in the perovskite, *i.e.*, higher oxidation state for the dopants resulted in lower average oxidation state of Fe ions and also lower concentration of oxygen vacancies. CO_2 resistances of these compounds were correlated to the average metal-oxygen bond energy (ABE) in the perovskite where higher ABE value increases CO_2 resistance.

Based on these aforementioned works, we can delineate several major approaches that have been undertaken to enhance the stability of perovskite-based membranes to CO_2, *i.e.*, (1) Adopting rare earth metal cation as A-site cation; (2) Reduction in the Co content in B-site; and (3) Partial substitution of the original transition metals components in B-site with more acidic (less basic) or more stable transition metal components. In doing these approaches, the Goldschmidt tolerance factor consideration (**Eq. 2.4**) becomes crucial to ensure that a suitable perovskite structure (*i.e.*, cubic) with sufficiently high oxygen permeability can be obtained. Still, these approaches inevitably involve trade-off between the CO_2 resistance and O_2 permeability. The other option that does not induce such trade-off represents the engineering approach that can be attained *via* optimizing the membrane configuration (*i.e.*, area to volume ratio) and/or reducing the effective membrane transport thickness.

A more practical membrane configuration such as hollow fiber with thinner wall thickness can improve the oxygen permeation fluxes. To increase the oxygen

permeation fluxes achieved by the $SrFe_{0.8}Nb_{0.2}O_{3-\delta}$ (SFN) disk-shaped membrane, Zhu *et al.* developed SFN hollow fiber that demonstrated up to 1.12 mL min^{-1} cm^{-2} oxygen flux under air to CO_2 gradient and stable operation for more than 500 hours.[63] Likewise, Zhu *et al.* obtained approximately quadruple O_2 flux enhancement for $SrFe_{0.9}Ta_{0.1}O_{3-\delta}$ and $SrFe_{0.8}Sb_{0.2}O_{3-\delta}$ at 900 °C *via* modification of membranes geometries from disk to hollow fiber form.[71] Tan's group contributed numerous works on the morphological evolution and the associated oxygen permeation properties of LSCF6428 hollow fibers.[53,125-130] They also studied the influence of CO_2 on the oxygen permeation behavior of LSCF6428 hollow fiber.[53] CO_2 chemical adsorption on the LSCF6428 surface was the main poisoning effect of CO_2 for the short term. The adsorbed CO_2 occupied the oxygen vacancies sites, thus suppressing the oxygen flux of the fiber. After operation under CO_2 for more than 100 hours at 900 °C, the carbonates were gradually formed due to the reaction of Sr with the adsorbed CO_2 causing Sr segregation on the surface. However, such CO_2-induced corrosion on the surface did not lead to the membrane collapse given that the eroded surface layer was only 1.4 μm after the long term operation. Such thickness is substantially thinner than 50 μm-thick erosion depth observed on BSCF5582 membrane exposed to pure CO_2 at 875 °C for only 70 hours.[27] The oxygen permeation flux of the fiber remained stable at 0.78 mL min^{-1} cm^{-2} at 950 °C after exposure to pure CO_2 sweep gas for over 100 hours. In addition to the hollow fiber membranes, other configurations have also been developed. Gaudillere *et al.* fabricated a hierarchically-structured LSCF6428 membrane by freeze-casting with a maximum O_2 flux of 6.8 mL min^{-1} cm^{-2} at 1000 °C.[68] Upon introducing 50 vol. % CO_2 into Ar sweep gas, O_2 flux at 900 °C decreased quickly from 4.6 to 2.5 mL min^{-1} cm^{-2}. O_2 flux nonetheless remained stable at around 2.5 mL min^{-1} cm^{-2} during the 48 hour-test. The result indicated that the hierarchically-structured LSCF6428 membranes were robust and stable, at least identical in this aspect to the monolithic LSCF6428 membranes. An asymmetric LSCF6428 membrane consisting of a porous LSCF6428 support, a homogeneous dense thin LSCF6428 layer and a porous LSCF6428 activation layer was fabricated using tape casting method.[69] The oxygen permeation test was carried out under CO_2-containing sweep gas at 900 and 1000 °C. At 900 °C, the O_2 flux dropped 32 % from 2.98 to 1.94 mL min^{-1} cm^{-2} when Ar was completely replaced by CO_2; which was attributed to the competitive adsorption of CO_2 and O_2 species on the active sites of membrane surface. However, the test result at 1000 °C showed opposite

counterintuitive trend, displaying the increase of O_2 flux from 4.95 to 5.52 mL min^{-1} cm^{-2} when the CO_2 content was increased from 0 to 100 %. Two most plausible reasons were postulated, *i.e.*, (1) CO_2 adsorption rate at 1000 ^{o}C was lower compared with that at lower temperatures; and (2) Lowered oxygen partial pressure in the permeate side from using CO_2 sweep gas (relative to Ar sweep gas), or in another word, higher sweeping capacity of CO_2 (relative to Ar). Gaudillere *et al.* also fabricated a highly porous LSCF6428 freeze-cast asymmetric membrane with a 30 µm-thick LSCF6428 porous activation layer over the dense top layer.[70] The porous activation provided protective features against CO_2, as evidenced by the lower O_2 flux deterioration for the activated membrane with respect to the bare membrane. The obtained highest O_2 flux of 7.2 mL min^{-1} cm^{-2} was observed at 1000 ^{o}C using 100 % CO_2 as the sweep gas. This value was even higher than that obtained from using Ar as sweep gas (7.0 mL min^{-1} cm^{-2}), which was consistent with the results of Serra *et al.*.[69] The long-term test in CO_2-rich atmosphere (50 % CO_2 in Ar) over 92 hours led to a degradation rate of only 4.17 $\times$ 10^{-2} mL min^{-1} cm^{-2} per day (from 1.41 to 1.25 mL min^{-1} cm^{-2}).
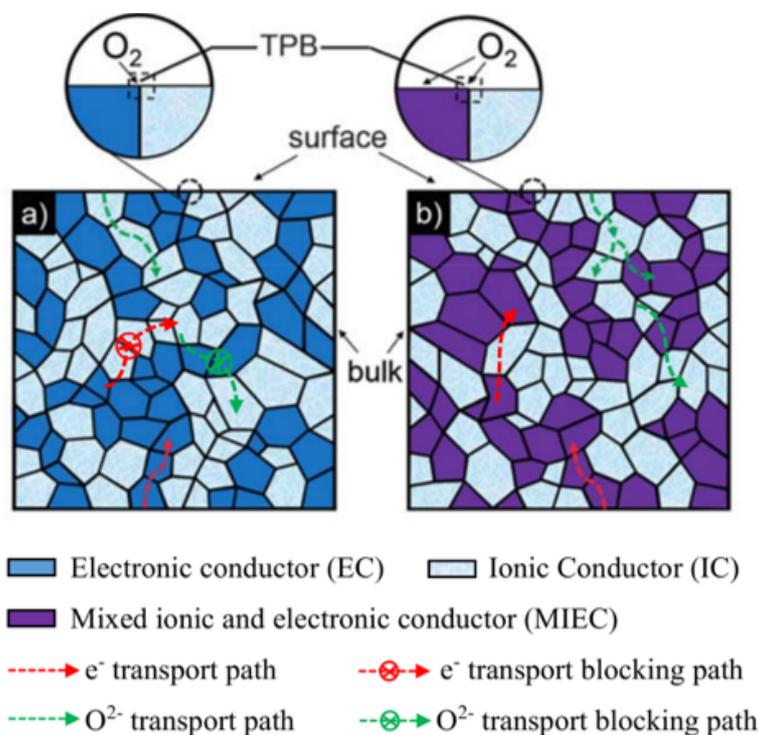
Figure 2.7 Dual-phase membranes concepts; (a) Ionic Conductor-Electronic Conductor (IC-EC) dual-phase membrane; (b) Ionic Conductor-Mixed Ionic-Electronic Conductor (MIEC) dual-phase membrane (Reproduced from ref. 61 with permission from Wiley).

2.2.2 Dual-phase materials

Dual-phase membrane comprises an ionic conducting phase and an electronic conducting phase. This concept is displayed in **Figure 2.7(a) and (b)** for two different composites, *i.e.,* ionic conductor-electronic conductor and ionic conductor-mixed ionic-electronic conductor, respectively. More details were discussed by Zhu and Yang on the critical factors required for appropriate selection of each phases.[131] Here, we have summarized the results from recent publications on dual-phase membranes in **Table 2.2** [61,73,132-159] and discussed current research status on this topic, but placing more efforts on the strategies to battle the influence of CO_2 erosion at high temperatures. The following definitions of terms are used throughout this section. Composite or dual phase membrane consisting of 45% A and 55% B by weight is expressed for short as A-B (45:55) and vice versa for other compositions, unless otherwise specially stated if the percentage is by volume.

2.2.2.1 Oxygen ionic conductor phase

In choosing the ionic conducting materials, three criteria should be fulfilled.[131] First, the materials have high ionic conductivity. Second, the materials remain stable under acidic gas or reducing atmosphere to ensure that no phase transition would occur. Third, the materials demonstrate chemical compatibility against the electronic conducting materials.

Oxide compounds with fluorite structure fulfill these criteria and are often used as an ionic conductor (IC, an electrolyte) in solid oxide fuel cells given its predominant ionic conductivity at a certain temperature range. **Figure 2.1(c) and (d)** illustrate the ideal fluorite structure and its packing arrangement. Fluorite compounds are defined as those having a general formula of AO_2; typified by calcium fluoride (CaF_2). Such structure is created by cubic-close packing of the A cations where the A cations occupy the face-centered cubic positions while the O anions occupy the tetrahedral interstices.[21] Zirconia (ZrO_2) exemplifies the classical example of oxides with fluorite structure which was once an important series of electrolyte in the old generation of solid oxide fuel cells. This compound requires temperature beyond 700 °C to provide substantial conductivity. Upon heating, ZrO_2 undergoes phase transitions from monoclinic to

tetragonal (at 1100-1200 °C) and tetragonal to cubic (2300 °C).[160] Partial substitution of zirconia with (approximately 10 mole % of) various lower valence metal cations, *e.g.*, Ca^{2+}, Mg^{2+}, and Ln^{3+} (Lanthanides) effectively stabilizes the cubic phase to room temperature. The tetragonal phase can also be stabilized using approximately 3 mole % of Y^{3+}. The ionic conductivity of the monoclinic ZrO_2 is quite negligible, only about 10^{-7}-10^{-6} S cm^{-1} which is improved on its tetragonal phase to 10^{-3}-10^{-2} S cm^{-1} and approaches 10 S cm^{-1} for cubic ZrO_2 beyond 2100 °C. Higher conductivity can actually be realized at lower temperature by partially substituting ZrO_2 with CaO or Y_2O_3; leading to a conductivity value close to 10^{-1} S cm^{-1} at 1300 °C. Still, given the very high temperature required to achieve substantial oxygen ionic conductivity, the use of zirconia is considered impractical.
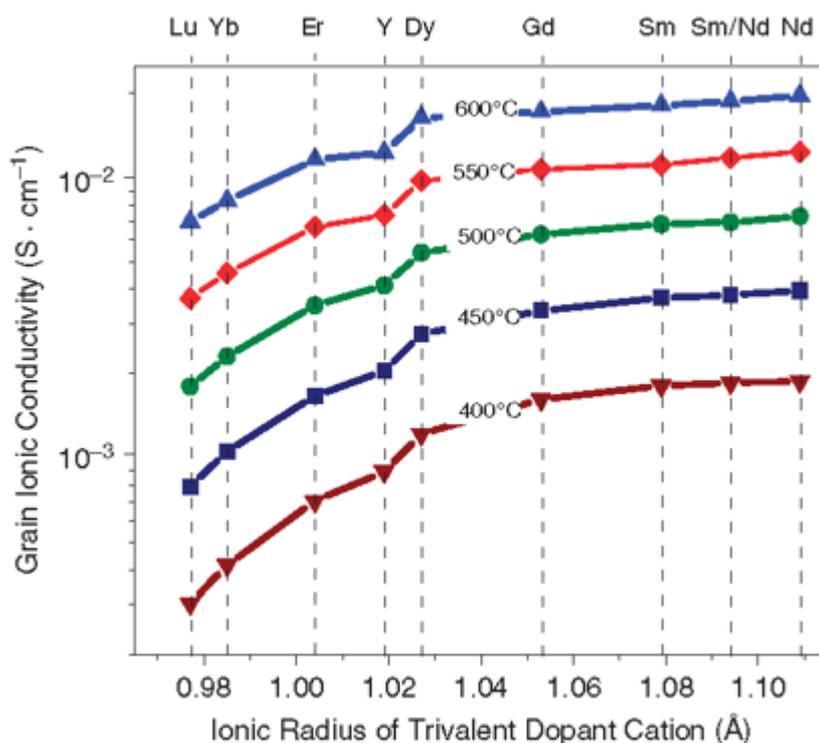
Figure 2.8 Correlation of the temperature-dependent grain ionic conductivity of doped ceria (in air) with the ionic radius of the dopant (All contain 10 mole % lanthanide dopant (except for Y) and synthesized using solid-state route – Reproduced from ref. 164 with permission from Wiley).

Ceria (CeO_2) represents another fluorite compound of interest. Strictly speaking, pure CeO_2 actually behaves more as a mixed conductor showing almost similar magnitude of ionic and electronic conductivities.[161] This is related with the change in

the oxidation state of cerium ion as a function of oxygen partial pressure, *i.e.*, Ce^{4+} may be reduced to Ce^{3+} under reducing atmosphere (and vice-versa).[162] This problem can be solved by partially substituting Ce with other metal cations having lower and fixed valence, *e.g.*, Ln^{3+} (lanthanides, to promote the formation of oxygen vacancies so that the ionic conductivity far outweighs the electronic conductivity). What makes ceria-based materials attractive is its high oxygen ionic conductivity which at 750 °C is analogous to that of yttria-doped zirconia at 1000 °C. Although Bi_2O_3 based materials have superior conductivity, their disadvantages lie in their instability and reducibility in reducing atmosphere. Ceria based materials on the other hand are quite stable. These materials have in fact replaced yttria-doped zirconia as an electrolyte for lower temperature operation (less than 800 °C).[161] Various dopants can be used to improve the ionic conductivity, *e.g.*, Ba, Ca, Dy, Gd, Ho, La, Mg, Nd, Sm, Sr, Y and Yb.[161,163] Doping with Ln elements generally provides the best conductivity with Gd, Nd, and Sm-doped ceria showing the highest conductivity values.[161,163,164] This is attributed to the high concentration of mobile oxygen vacancies in the cubic lattice. **Figure 2.8** suggests that the grain ionic conductivity of the lanthanide-doped ceria increase with increasing ionic radius of the dopant.[164] Two special aspects in this figure deserve further discussion. Firstly, within this lanthanide-doped ceria series (except for Y-doped ceria), the lowest ionic conductivity was shown by Lu-doped ceria despite the almost similar ionic radius of Lu^{3+} (0.977 Å) and Ce^{4+} (0.97 Å). This is due to the restrained oxygen vacancy diffusion, most likely due to the attractive electrostatic interaction between Lu^{3+} and oxygen vacancies. Secondly, Y-doped ceria shows ionic conductivity which deviates from the trend indicated by the plot. This can be understood by the fact that Y is not the lanthanide element and the electronegativity of the dopant may influence the ionic conductivity.[164] Although Nd-doped ceria demonstrate the highest conductivity among all lanthanide-doped ceria, Sm-doped ceria, *i.e.*, $Ce_{0.8}Sm_{0.2}O_{1.9}$ is the most attractive one to replace yttria-doped zirconia given its lowest reducibility among the doped ceria compounds.[163,164]

Another promising alternative is bismuth oxide (Bi_2O_3). This compound, upon heating, also exhibits phase transition from monoclinic (α-phase) to cubic (δ-phase) at 730 °C before its melting point at 825 °C.[165] Its cubic δ-phase has fluorite structure with ordered defects in the oxygen sub-lattice and shows 1-2 orders of magnitude higher conductivity than the yttria-doped zirconia, *i.e.*, 1 S cm^{-1} at 650 °C. The superior ionic

conductivity is characterized by the missing of one-fourth of oxygen anions in the lattice, the electronic configuration of Bi^{3+} consisting of $6s^2$ lone pair electrons which results in the high polarisability of the cation (and high oxide ion mobility) and Bi^{3+} capability to afford highly disordered surroundings.[165] Likewise, the cubic phase of Bi_2O_3 can be stabilized to room temperature by partial substitution of Bi with Dy, Er, Gd, Ho, Lu, Tb, Tm, Y, and Yb. Despite some dispute on the resultant structure, Dy, Er, Ho, and Tb-doped ones show the highest conductivity of 0.1-0.4 S cm^{-1} between 650-700 $^{\circ}$C.

$La_{1-x}Sr_xGa_{1-y}Mg_yO_{3-\delta}$ is another popular oxygen ionic conductor, frequently applied as an electrolyte layer in solid oxide fuel cells due to its high oxygen ionic conductivity. It is also suitable as the ionic conductor phase in dual-phase membranes for oxygen permeation. However, La and Sr in $La_{1-x}Sr_xGa_{1-y}Mg_yO_{3-\delta}$ have tendency to diffuse into the electronic conductor phase at high temperature; forming new perovskite oxide phase with inferior permeability. For example, in the case of $La_{0.8}Sr_{0.2}Ga_{0.8}Mg_{0.2}O_3$ (LSGM)-$La_{0.8}Sr_{0.2}Co_{0.2}Fe_{0.8}O_3$ (LSCF8228) dual-phase membrane, sintering at temperatures between 1320 and 1410 $^{\circ}$C induced fast cation interdiffusion between the two phases leading to the formation of single perovskite phase with local inhomogeneities. The ionic and electronic conductivities of the formed perovskite phase were lower than those of the original phases (LSGM and LSCF8228) unfavorable for oxygen permeation.[166]

2.2.2.2 Electronic conductor phase

Fluorite phase cannot be utilized as oxygen permeation membrane given its limited electronic conductivity. An electronic conductor (EC) phase having high electronic conductivity is required to form the continuous electronic conducting path within the membrane. EC phase should ideally have good stability, high thermal and chemical compatibility with respect to ionic conductor (IC) phase, and is relatively inert to the reaction with IC phase. EC phase mainly comes from three categories, *i.e.*, noble metals, electronic conducting oxides, and mixed conducting (MIEC) oxides.

Noble metals (*i.e.*, Au, Pt, Pd, Ag, etc) were the initial EC candidate for dual-phase membranes.[167-171] Both the individual EC and IC phases should be percolative throughout the membranes for the oxygen ions and electrons to be conducted from the

feed to the permeate side. Thus, the percolative threshold which refers to the minimum content of electronic phase is generally 40 vol. % or above using the conventional preparation protocols, *e.g.*, mixing, pressing, and sintering. For $Bi_{1.5}Y_{0.3}Sm_{0.2}O_3$ (BYS)-Ag membrane, for example, 40 vol. % of Ag was required to achieve percolative EC phase as indicated by 10^4-10^5 higher conductivity for BYS-40 vol. % Ag than that for BYS-30 vol. % Ag.[169] Conceptually, since there is practically no oxygen conductivity in noble metal phase, the oxygen conducting path in IC-noble metal composite is negatively blocked by EC phase (**Figure 2.7(a)**). IC phase also blocks the electronic conducting path given the very limited electronic conductivity in IC phase (such as $Ce_{0.8}Gd_{0.2}O_{1.9}$ (GDC)). This blocking effect thus limits the global conducting efficiency between these two phases. In addition to this so called "mutual blocking effect", high cost of noble metal renders this cermet dual-phase membrane approach less attractive.

Pure electronic conducting oxides or those with extremely low ionic conductivity and substantial oxygen reduction catalytic activity can be exploited as EC phase as represented by $Ce_{0.8}Gd_{0.2}O_{1.9}$ (GDC)-$La_{0.7}Sr_{0.3}MnO_3$ (LSM) membrane.[172] Given its high electronic conductivity, the electronic conducting oxide phase is generally perovskite-type material (such as $La_{1-x}Sr_xMn(Cr)O_3$)[131,173-176] or spinel oxides (such as $MnFe_2O_4$, $CoFe_2O_4$, $FeCo_2O_4$, $MnCo_2O_4$, $CuCo_2O_4$, $NiFe_2O_4$, *etc*).[133,134,140,150,151,159,177,178] Besides the blocking effect from EC phase (**Figure 2.7(a)**), interphase reaction becomes another important consideration in dual-phase membrane design. Although the mixing with LSM solved the limited electronic conducting issue, the long term test (up to 800 hours) revealed continuous oxygen flux decrease due to the formation of poorly ionic conducting layers at the boundary of GDC grains from the diffusion of lanthanum and strontium.[172] In some cases, new phases formed on the grain boundary can also promote ionic transport *via* modification of phase structure and compositions.[179] A recent work on dual-phase $Ce_{0.8}Gd_{0.2}O_{2-\delta}$ (GDC)-$CoFe_2O_4$ (CF) showed new crystalline phase containing Gd, Fe, Ce, and Co (denoted as GFCCO) formed along the grain boundaries during sintering.[180] On one hand, the perovskite GFCCO has high level of oxygen vacancies which promotes oxygen ionic conductivity. On the other hand, the formation of GFCCO phase mitigates the space charge effect near the GDC-GDC grain boundaries which can also improve the oxygen ion transport. Their work demonstrates a novel direction in EC phase selection, *i.e.*, the possibility to generate *in situ* beneficial phase reaction with IC that creates new phase with high ionic

conductivity.[180] Another example of this direction comes from dual-phase membranes of $Ce_{0.8}Sm_{0.2}O_{2-\delta}$ (SDC) + $SrCO_3$ + Co_3O_4, where highly conductive tetragonal perovskite phase $Sr_{0.95}Sm_{0.05}CoO_{3-\delta}$ formed along the SDC grain boundary. The permeation flux through a 0.5 mm-thick SDC + 20 wt. % $SrCO_3$ + 10.89 wt. % Co_3O_4 reached 1.19 mL min^{-1} cm^{-2} at 900 ^oC under air/helium gradient. This composite membrane furthermore displayed a stable oxygen permeation flux during 110 hour-test using pure CO_2 as the sweep gas.[181]

Mixed ionic-electronic conducting (MIEC) oxide such as $Ln_x(Ba,Sr,Ca)_{1-x}Co_yFe_{1-y}O_{3-\delta}$; Ln = La, Pr, Nd, Sm, and Gd) is the other EC phase option.[138,139,146,182-188] The oxygen permeability of IC-MIEC composite is typically higher than that of IC-EC composite due to the higher amount of oxygen ion conducting paths through the membranes and the enhanced surface exchange reaction rate (**Figure 2.7(b)**). The presence of MIEC phase within the dual-phase composite substantially enlarges the triple-phase boundaries (TPBs, reaction contact areas between oxygen ions, electrons, and oxygen gases) on the membrane surfaces as well as the contact areas between oxygen ions and electrons within the bulk membrane. Note that both oxygen ions and electrons can pass through MIEC phase. This is unlike the IC-EC composite case where the TPBs and the oxygen ions to electron contact areas are limited only to IC-EC interfaces (**Figure 2.7(a)**).[189] A representative example is $Ce_{0.9}Gd_{0.1}O_{2-\delta}$ (GDC)-$Ba_{0.5}Sr_{0.5}Co_{0.8}Fe_{0.2}O_{3-\delta}$ (BSCF5582) which consists of GDC IC phase and BSCF5582 MIEC phase. BSCF5582 has high oxygen ionic conductivity of about 1 S cm^{-1} (above 300 ^oC) and an even higher electronic conductivity.[190] BSCF5582 is a popular oxygen permeation membrane material that has good compatibility with GDC.[74,191] A quite high oxygen permeation flux of 2.1 mL min^{-1} cm^{-2} was obtained from 0.5 mm-thick 60 wt. % GDC-40 wt. % BSCF5582 membrane under air/He gradient at 975 ^oC.[192] This is much significantly higher than that from GDC (ionic conducting phase)-LSM (electronic conducting phase) composite membrane.[172] When the helium sweep gas was swapped to pure CO_2, a stable oxygen permeation flux of 0.67 mL min^{-1} cm^{-2} at 950 ^oC was retained for at least 250 hours.[132] Such long term stability to CO_2 is counterintuitive and was attributed to the protection of BSCF5582 by GDC.[28] Accordingly, $Ce_{0.8}Sm_{0.2}O_{2-\delta}$ (SDC)-$SrCo_{0.9}Nb_{0.1}O_{3-\delta}$ (SCN) (60:40) also showed excellent CO_2 stability for at least 120 hours under 50 vol. % CO_2 in N_2.[153] CO_2 resistance can further be improved by replacing alkaline earth metal containing perovskite with non-alkaline earth metal containing perovskite, such as $Ln_{1-x}Sr_xFeO_{3-\delta}$ (Ln = La, Pr, Nd, Sm, and

Gd).[141,146,149,193] For example, $La_{1-x}Sr_xFeO_{3-\delta}$ showed appreciable oxygen permeation flux under He, N_2, and even reducing CO, CO_2, and H_2 atmosphere;[194-196] indicating its good stability in harsh atmosphere. IC-MIEC dual-phase membrane can simultaneously provide high oxygen permeation flux and good chemical stability in the presence of acidic gas. Moreover, the thermal expansion coefficients mismatch and the interphase reaction between the two phases should also be accounted for the design of IC-MIEC dual phase membranes. Other electronic conducting oxides such as double perovskite oxides and transition metal oxides (such as Fe_2O_3) were employed in dual-phase oxygen permeation membranes.[151,182,184]

2.2.2.3 Preparation routes

Ceramic-based dual-phase membrane offers different preparation routes. For the single-phase membrane, the preparation methods mainly affect the grain size and defects of the membranes. The different preparation methods may also influence the distribution of the two phase compositions for the dual-phase membranes.[197] Powders of each individual phase can initially be synthesized using solid-state reaction or sol-gel method and then combined by manually mixing using mortar and pestle or by mechanical mixing using ball-milling. It is also possible to use an *in-situ* one-pot sol-gel synthesis to prepare the dual-phase directly from the precursors. One of the best examples comparing distinct morphology and oxygen permeability of dual-phase membranes arisen from the different preparation routes is given by Luo *et al.*.[134] For $NiFe_2O_4$ (NF)-$Ce_{0.9}Gd_{0.1}O_{2-\delta}$ (GDC) (40:60), they showed that powder mixing using hand in mortar and pestle led to the formation of largest grains (**Figure 2.9(a) and (b)**) followed by mixing using ball-milling (smaller grains – **Figure 2.9(c) and (d)**) and then one-pot route (smallest grains – **Figure 2.9(e) and (f)**). Their results showed close correlation between the grain size and the oxygen fluxes with the composites having the smaller grain size exhibited higher fluxes. As such, one-pot route is favored over these physical mixing.

According to the precursors and synthesis routes, one-pot method can be divided into several types, *i.e.*, one-pot solid state reaction (SSR), one-pot co-precipitation (CP), one-pot glycine-nitrate combustion (GN), and one-pot sol-gel (SG). For example, Luo *et al.* applied one-pot glycine-nitrate combustion techniques to

prepare $Mn_{1.5}Co_{1.5}O_{4-\delta}$-$Ce_{0.9}Pr_{0.1}O_{2-\delta}$ (40:60) dual-phase membrane.[150] Glycine-nitrate
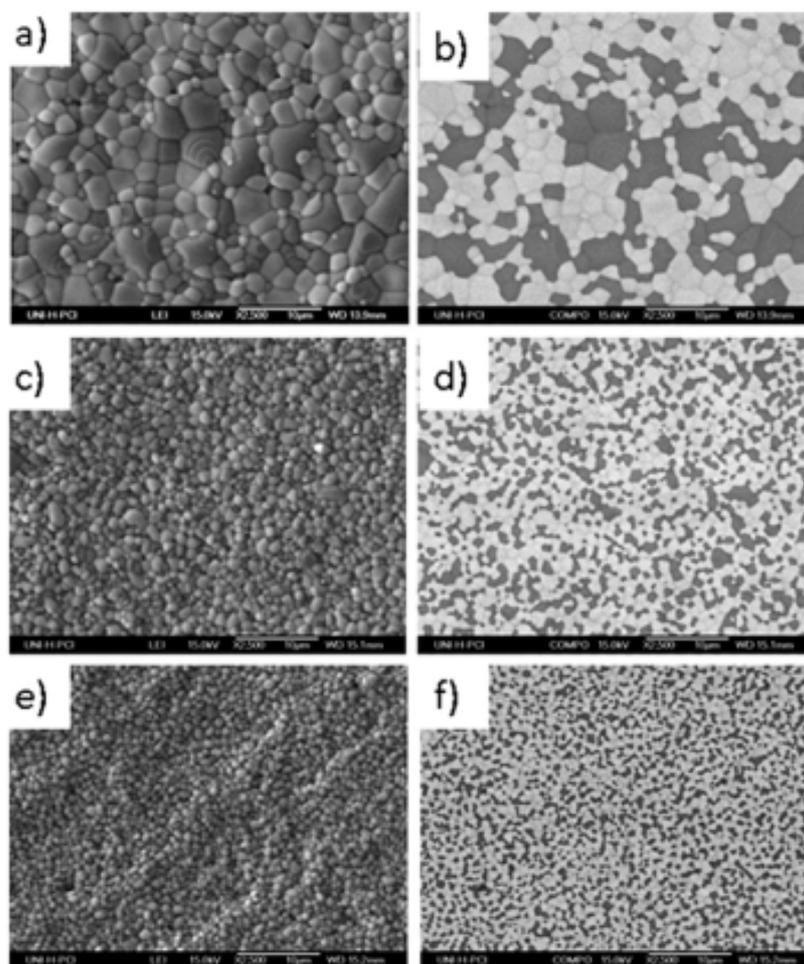
Figure 2.9 Scanning electron microscopy images (left column) and backscattered electron microscopy images (right column) of the grain morphology of $Ce_{0.9}Gd_{0.1}O_{2-\delta}$ (GDC)-$NiFe_2O_4$ (NFO) (40:60) prepared by the powder mixing using (a and b) mortar and pestle and (c and d) ball-milling; and (e and f) by an *in-situ* one-pot sol-gel route (Reproduced from ref. 134 with permission from Wiley).

combustion is a common method to synthesize ceramic oxide powders with an atomic scale uniform composition and fine grain size, *i.e.*, to obtain improved sintering effect.[150,198] The powders obtained from rapid glycine-nitrate combustion were pressed into disk membranes followed by sintering at 1300 ^{o}C for 10 hours. Sintered disk membrane consisted of well-distributed grains of $Mn_{1.5}Co_{1.5}O_{4-\delta}$ and $Ce_{0.9}Pr_{0.1}O_{2-\delta}$ with the average grain size areas of 0.265 μm^2 and 0.329 μm^2, respectively. Zhu *et al.* studied the effect of preparation methods on dual-phase membranes. They synthesized $Ce_{0.85}Sm_{0.15}O_{1.925}$ (SDC)-$Sm_{0.6}Sr_{0.4}Al_{0.3}Fe_{0.7}O_3$ (SSAF) (75:25) dual-phase membranes using three different methods, *i.e.*, EDTA-citrate (EC) sol-gel process, SSR method and

CP method.[158] The two phases were most homogeneously mixed using EC method. SSR method gave the most inhomogeneous phases mixture. Nonetheless, composite obtained from EC method displayed the lowest total electrical conductivity and oxygen permeation flux whereas that obtained from SSR method showed the highest total conductivity and oxygen flux. Such discrepancy was attributed to the volume fraction of perovskite phase that was lower than the percolation threshold (30 wt. %) which becomes more important for homogenously mixed phases (EC case). For an inhomogeneous composite system (SSR case), on the other hand, continuous conduction network was likely to form over random sections within the membrane.

2.2.2.4 Internal and external short circuit concepts

Dual-phase or composite membrane is a manifestation of internal short-circuit concept given the separate pathways for the ionic and the electronic conductions within such membrane. Such approach combines the advantages of individual phases to attain high oxygen permeability and high chemical stability to acidic gas (CO_2). One of its drawbacks lies in the relatively high amount of the individual phases required; for instance, at least 40 vol. % of each phase is necessary to form its continuous network across the membrane, particularly prepared by conventional preparation route with steps of mixing, pressing, and sintering. Moreover, numerous isolated areas may form within the membrane (marked by red circles in **Figure 2.10(a)**) which leads to ionic and electronic species blocked by each other and eventually low oxygen permeation flux. This isolation issue can be circumvented by increasing the amount of IC phase to its maximum (which is equivalent to decreasing the amount of EC phase to its minimum) while ensuring that both phases are still continuous. To this end, **Figure 2.10(b)** illustrates one of the possible design concepts as realized in Chen *et al.*'s work.[199] They dispersed fiber-shaped $PrBaCo_2O_{5+\delta}$ (PBC) into SDC matrix. Only 20 vol. % of PBC phase was required in the dual-phase membrane to attain a relatively high oxygen permeability (for dual-phase membrane) of 0.56 mL min^{-1} cm^{-2} at 940 ^{o}C. Twenty percent by volume can be regarded as the lowest volume fraction of EC reported so far. What they illustrated essentially leads to the internal short-circuited membrane design with the lowest amount of electronic conducting pathway (and phase). Zhang *et al.* showed another good example of this minimum EC phase approach using SDC

membrane.[200] A channel through the disk SDC membrane was first made by an ultra-high speed drill, after which a thin Ag wire was implanted into the channel and sealed with silver paste. Single internal short circuit can provide the oxygen flux as high as those attained by putting a larger number of short-circuit wires through the membranes. Still along this approach, Joo's group developed novel 'internal short circuit' concept, *i.e.*, a modification of the traditional dual-phase membrane concept, which they defined as segmented structure.[154,155] Instead of mixing the two ceramic powders together, they fabricated fluorite membrane (YSZ or GDC) with segmented electron conducting oxides (LSM) in the membrane, which manifested into the identical structure shown in **Figure 2.10(b)**. Such segmented structure did not display the phase-to-phase reaction issue regularly observed in dual phase membranes such as GDC-LSM and YSZ-LSM enabled by the presence of numerous interfacial areas between the two phases that promotes such reaction.[172,201] In membrane with segmented structure, there is a limited interfacial contact area between the two phases. Long-term constant performance of this segment membrane highlights its stability.

Another concept was recently devised to address the limited electronic conductivity of IC membrane via the external short circuit.[202-205] **Figure 2.10(c)** represents the external short circuit approach. The electronic conductor layer (such as noble metal, EC, and/or MIEC) and metal sealant over the membrane surface are employed as an electron pathway from the high oxygen potential side to the low oxygen potential side. Relatively high oxygen permeation fluxes through the Ag decorated SDC membrane can be obtained at relatively low temperatures even at 600 $^{\circ}$C by employing such approach using Ag.[202] EC decoration on the surface has two functions. The first function is to provide external electron pathway so the electrons released from the surface oxygen exchange reactions at the permeate side can be shuttled to the other membrane surface to consume the coming electrons and complete the oxygen reduction from molecular state to the lattice oxygen. The second function specifically can be best achieved using MIEC materials that display high surface oxygen exchange reaction rates such as BSCF5582 and $La_{0.8}Sr_{0.2}CoO_{3-\delta}$.[203,205] The utilization of MIEC for external short circuit approach is attractive to replace noble metal and to increase the oxygen permeability. Most perovskite-based MIEC materials nevertheless are not stable to acidic gas (CO_2).[205] However, in real applications, the feed side is in relatively mild gas atmosphere (pressurized air); thus these MIEC materials can be applied as the catalyst in the membrane surface in the feed side leaving the other membrane surface

side to use some CO_2 tolerant materials. A recent work demonstrates the use of dual-phase decoration over GDC membrane to generalize the extendibility of composite concept to external short-circuit approach.[206] **Figure 2.10(d)** displays the structure of such dual-phase decoration that provides electronic conducting pathway and additionally, higher amount of triple-phase boundaries on the surfaces of the membrane (relative to regular EC decoration in **Figure 2.10(c)**). Besides the higher oxygen permeability, this approach provides advantages in terms of the lower amount of Ag required (relative to Ag decoration) and higher stability against CO_2 (relative to MIEC decoration).
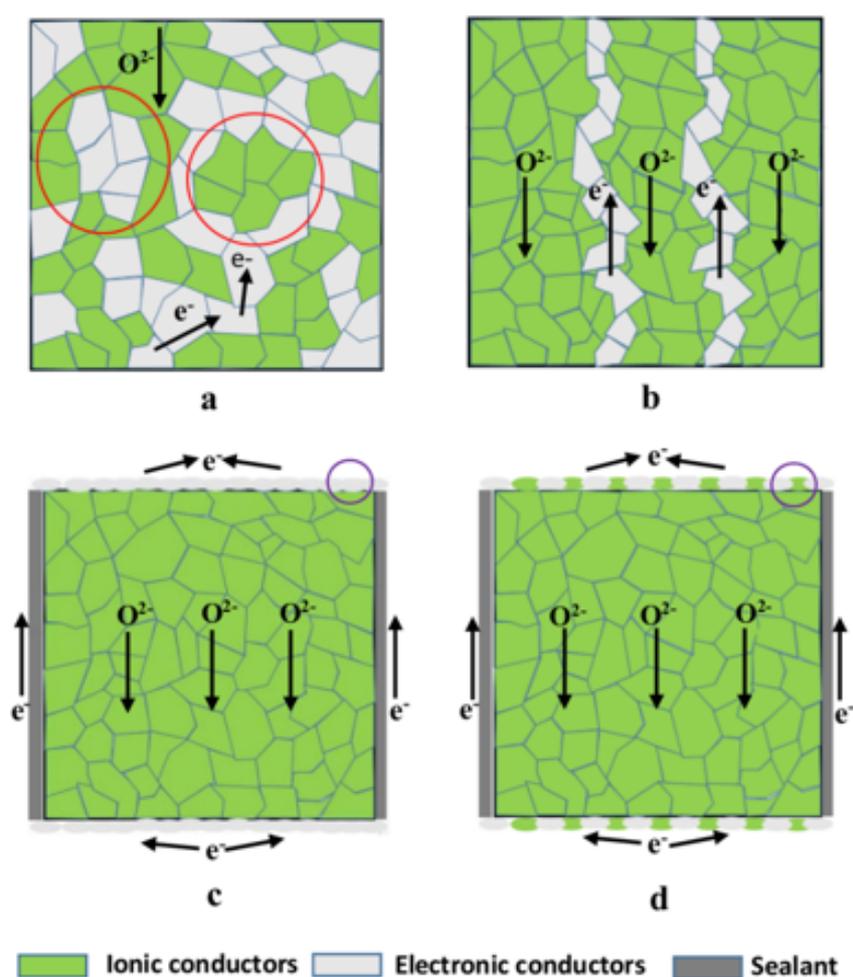
Figure 2.10 Cross-section schematic diagram for (a) dual-phase membrane; (b) dual-phase membrane with minimum electronic conducting phase (internal short-circuit); (c) membrane with external short-circuit decoration; and (d) membrane with dual-phase external short-circuit decoration (Reproduced from ref. 206 with permission from Royal Society of Chemistry).

Despite the very low oxygen permeation fluxes demonstrated by the best performing membrane utilizing internal and external short circuit approaches, they have very high chemical stability that allows their application in membrane reactors such as syngas production from methane. Under such reaction conditions, the oxygen concentration gradient through the membranes is substantially larger than that employed in our permeation experiments (for pure oxygen production), *i.e.*, 0.21 atm (air)/10^{-8} to 10^{-16} atm (reaction) as opposed to 0.21 atm (air)/10^{-3} atm (sweep) (permeation); thus allowing substantially higher oxygen fluxes to be attained.

2.2.2.5 Recent status and advances

$Ce_{0.9}Pr_{0.1}O_{2-\delta}$ (CP)-$Pr_{0.6}Sr_{0.4}Fe_{0.5}Co_{0.5}O_{3-\delta}$ (PSFC) (60:40) membrane was prepared *via* a one-pot sol-gel synthesis method and tested for its CO_2 resistance.[137] *In-situ* powder x-ray diffraction (XRD) between 30 and 1000 ^oC in CO_2-containing atmosphere (CO_2-air = 50:50 vol.%) showed no carbonate formation on this composite and that CP phase retained cubic structure while PSFC phase underwent two phase transitions, *e.g.*, from orthorhombic to rhombohedral at ca. 600 ^oC and from rhombohedral to cubic at ca. 800 ^oC. In an earlier work, a cobalt-free $Ce_{0.9}Pr_{0.1}O_{2-\delta}$ (CP)-$Pr_{0.6}Sr_{0.4}FeO_{3-\delta}$ (PSF) (60:40) was synthesized and tested under the harsh partial oxidation of methane (POM) reaction condition and in a CO_2 atmosphere.[146] Unlike CP-PSFC, CP-PSF showed no phase transitions during *in-situ* powder XRD test in air. No carbonate formation was observed during *in-situ* XRD test in CO_2-containing atmosphere (CO_2-N_2 = 50:50 vol. %). Using CO_2 as the sweep gas at 950 ^oC, the O_2 flux of a 0.6-mm thick membrane reached up to 0.22 mL min^{-1} cm^{-2} and then slightly decreased and stabilized at around 0.18 mL min^{-1} cm^{-2} for more than 100 hours. At POM reaction condition, the O_2 flux of the membrane approached 4.4 mL min^{-1} cm^{-2} at 950 ^oC for 100 hours. The powder XRD pattern for the 100 hour-POM tested membrane indicated the retaining of the original two phases in the composite; highlighting the membrane stability in reducing atmosphere. Fang *et al.* developed $Ce_{0.85}Gd_{0.1}Cu_{0.05}O_{2-\delta}$ (CGC)-$La_{0.6}Ca_{0.4}FeO_{3-\delta}$ (LCF) (75:25) membrane.[61] Five percent (mole) of Ce in $Ce_{0.9}Gd_{0.1}O_{2-\delta}$ was substituted by Cu, forming CGC with the aim to increase the ionic conductivity and to induce the p-type electronic conductivity as well as to improve the sintering behavior and densification of ceria. Since Cu-doped $Ce_{0.9}Gd_{0.1}O_{2-\delta}$ showed larger grain size than $Ce_{0.9}Gd_{0.1}O_{2-\delta}$,

44

Cu can be considered to act as a sintering aid. Based on the electron energy loss spectroscopy, it can be found that the grain boundary in between CGC grains contains La, Ca and Fe with negligible amount of Cu; thus ruling out significant segregation of Cu in grain boundary. The membranes were prepared using one-pot method and powder mixing. In terms of surface morphology, the former membranes were much more homogeneous than the latter ones which consequently led to higher oxygen permeation fluxes for the former membranes. Cu doping can also be performed in the electronic conducting perovskite phase (instead of the ionic conducting phase), for example, to partially substitute Fe.[145] Partial substitution of B-site cation with Cu was reported to enhance the oxygen permeation flux.[207-209] In this context, dual-phase $Sm_{0.5}Sr_{0.5}Cu_{0.2}Fe_{0.8}O_{3-\delta}$ (SmSrCF5528)-$Ce_{0.8}Sm_{0.2}O_{2-\delta}$ (SDC) (40:60) and $Sm_{0.3}Sr_{0.7}Cu_{0.2}Fe_{0.8}O_{3-\delta}$ (SmSrCF3728)-$Ce_{0.8}Sm_{0.2}O_{2-\delta}$ (SDC) (40:60) membranes were prepared *via* EDTA-citric acid complexing sol-gel process. Powder X-ray diffraction, scanning electron microscopy, and energy dispersive X-ray analysis results revealed the formation of CuO phase on the surface of SmSrCF5528-SDC membrane. CuO phase disappeared with increasing Sr content (SmSrCF3728-SDC) and parallel increase in the unit cell of SmSrCF3728; suggesting that Cu was incorporated into the perovskite structure at larger Sr content. Relatively high oxygen fluxes of 1.12 and 1.15 mL min^{-1} cm^{-2} were obtained at 1000 $^{\circ}$C from SmSrCF5528-SDC and SmSrCF3728-SDC membranes, respectively. At 1000 $^{\circ}$C, both membranes demonstrated good stability against CO_2. Based on the Ellingham diagram,[41] the stability of $SrCO_3$ conceptually increases with decreasing temperature at constant CO_2 partial pressure. Accordingly, at lower temperatures (*i.e.*, 950 and 900 $^{\circ}$C), a stabilization stage occurred before the oxygen fluxes can reach their stable values. This is likely related to the tendency for Sr to react with CO_2 to form $SrCO_3$ on the sweep side. A CuO layer appeared on the surface of the feed side of SmSrCF3728-SDC membrane which was caused by cationic counter-diffusion of Cu to the oxygen-rich side during permeation process. Regardless of the presence of CuO layer and Cu-depleted layer, a steady-state oxygen permeation flux was observed; the reasons of which requires further investigation.

Balaguer *et al.* reported the $Ce_{0.8}Tb_{0.2}O_{2-\delta}$ (CT)-$NiFe_2O_4$ (NF) (40:60 vol. %) membranes prepared by one pot method.[140] Powder X-ray diffraction, energy dispersive X-ray spectroscopy and Raman spectroscopy demonstrated that CT-NF was stable in CO_2 environment without reactions occurred between the two phases and CO_2. Furthermore, relative to $Ce_{0.8}Gd_{0.2}O_{2-\delta}$ (GDC)-$NiFe_2O_4$ (NF) (40:60 vol. %) membrane,

CT-NF exhibited larger oxygen permeation flux due to the higher p-type electronic conductivity of CT enabling the mixed ionic-electronic conducting behavior to occur. A similar work on $Ce_{0.8}Tb_{0.2}O_{2-\delta}$ (CT)-$NiFe_2O_4$ (NF) (50:50 vol. %) displayed an O_2 flux of 0.13 mL min^{-1} cm^{-2} for a 0.59 mm-thick membrane under air/CO_2 gradient.[156] Prolonged stability test under 100 % CO_2 showed that the O_2 flux progressively increased from 0.13 to 0.14 mL min^{-1} cm^{-2} during 40 hour-test. Similar improvement of O_2 flux during long-term test under CO_2 was reported by other studies.[133,136,140,155] Yun *et al.* suggested that the possible reason is the 'electrode activation' effect which is widely observed in SOFC field.[155] The exact reason behind the O_2 flux enhancement has not yet been clarified. For GDC-NF dual-phase membranes, Luo *et al.* developed $Ce_{0.9}Gd_{0.1}O_{2-\delta}$ (GDC)-$NiFe_2O_4$ (NF) (40:60) *via* one-pot and powder-mixing methods.[133,134] No carbonate was formed during *in-situ* powder X-ray diffraction between 30 ^oC and 1000 ^oC in an atmosphere containing 50 vol. % CO_2 and 50 vol. % N_2 (as well as 50 vol. % CO_2 and 50 vol. % air). Another spinel structured $MnCo_2O_{4-\delta}$ possessing excellent electronic conductivity and structural stability, exhibited a thermal expansion coefficient (11.7 $\times$ 10^{-6} K^{-1}) close to that of Pr-doped ceria $Ce_{0.9}Pr_{0.1}O_{2-\delta}$ (10-11 $\times$ 10^{-6} K^{-1}).[210,211] Luo *et al.* synthesized dual-phase $Mn_{1.5}Co_{1.5}O_{4-\delta}$ (MC)-$Ce_{0.9}Pr_{0.1}O_{2-\delta}$ (CP) (40:60) membrane.[150] Powder X-ray diffraction results showed that $Mn_{1.5}Co_{1.5}O_{4-\delta}$ was comprised of 57.9 wt. % cubic $MnCo_2O_{4-\delta}$ and 42.1 wt. % tetragonal $Mn_2CoO_{4-\delta}$. The highest O_2 flux of 0.48 mL min^{-1} cm^{-2} was obtained through a 0.3 mm-thick membrane at 1000 ^oC under air/CO_2 gradient. The membrane could operate for at least 60 hours under pure CO_2 at 1000 ^oC without degradation; maintaining an O_2 flux of 0.2 mL min^{-1} cm^{-2} within this period. Zhu *et al.* made $Ce_{0.8}Sm_{0.2}O_{1.9}$ (SDC)-$SmMn_{0.5}Co_{0.5}O_3$ (SMC) (75:25) and $Ce_{0.8}Sm_{0.2}O_{1.9}$ (SDC)-$Sm_{0.8}Ca_{0.2}Mn_{0.5}Co_{0.5}O_3$ (SCMC) (75:25) and studied their stability under CO_2.[138] They found that SDC-SCMC showed a higher O_2 flux at 940 °C yet a lower O_2 flux at 850 °C (relative to SDC-SMC). The decreased O_2 flux at lower temperature was due to the stronger CO_2 adsorption on the membrane surface. Ca^{2+} doped $SmCoO_{3-\delta}$ is envisioned to have higher CO_2 stability but lower flux (relative to $SmCoO_{3-\delta}$). A dual phase membrane comprises of 75 wt. % SDC and 25 wt. % $Sm_{1-x}Ca_xCoO_{3-\delta}$ was developed to investigate Ca^{2+} doping effect.[152] Two compositions, *i.e.*, $Ce_{0.8}Sm_{0.2}O_{2-\delta}$ (SDC)-$Sm_{0.8}Ca_{0.2}CoO_3$ (SCC82) (75:25) and $Ce_{0.8}Sm_{0.2}O_{2-\delta}$ (SDC)-$Sm_{0.6}Ca_{0.4}CoO_3$ (SCC64) (75:25) were studied. At lower temperatures (*i.e.*, 800-875 ^oC), for both membranes, the O_2 fluxes were lower when pure CO_2 was used as sweep gas, compared to pure He as sweep gas case. However,

the O_2 flux increased under pure CO_2 at higher temperatures (875-950 $^{\circ}$C). This trend can be explained by the weaker CO_2 adsorption at higher temperature. Both SDC-SCC82 and SDC-SCC64 membranes showed stable O_2 fluxes under pure CO_2 for at least 100 hours. SDC-SCC64 and SDC-SCC82 membranes exhibited O_2 flux of 0.16 and 0.19 mL min^{-1} cm^{-2}, respectively. Li *et al.* further compared the oxygen permeation behaviors of $Ce_{0.8}Sm_{0.2}O_{2-\delta}$-$Sm_{0.6}Ca_{0.4}CoO_{3-\delta}$ (SDC-SCC) and $Ce_{0.8}Sm_{0.2}O_{2-\delta}$-$Sm_{0.6}Ca_{0.4}FeO_{3-\delta}$ (SDC-SCF).[73] Two different composites were made for each composite type, resulting in 4 composites, *i.e.*, SDC-SCC (75:25), SDC-SCC (67:33), SDC-SCF (75:25), and SDC-SCF (67:33). Co containing membranes displayed significantly higher O_2 flux than Fe containing membranes. Upon comparing SDC-SCC (75:25) to SDC-SCC (67:33), the O_2 flux of the latter was almost 4 times that of the former. This is due to the fact that 25 wt. % SCC did not provide the sufficient electronic conductivity and catalytic activity as 33 wt. % SCC did. Still, SDC-SCF (75:25) showed higher O_2 permeability than SDC-SCF (67:33) due to the lower O_2 permeability of SCF (compared to SDC). Despite the discrepancy in the oxygen fluxes observed for these four membranes, all of them showed excellent stability during 100 hour-operation using CO_2 as the sweep gas. Jiang *et al.* doped the electronic conducting phase $PrBaCo_{2-x}Fe_xO_{3-\delta}$ ($PBC_{2-x}F_x$)into GDC to fabricate a dual-phase membrane $GDC-PBC_{2-x}F_x$ (60:40).[135] Earlier, it was found that the fluorite structure SDC can enhance both the oxygen permeability and structural stability of $PrBaCo_2O_{5+\delta}$ (PBC) membrane.[183] In the case of $GDC-PBC_{2-x}F_x$, the introduction of Fe (x = 1.5) can improve the oxygen flux by ~1.7 times than GDC-PBC. For example, the $GDC-PBC_{0.5}F_{1.5}$ showed the oxygen flux of 0.36 mL min^{-1} cm^{-2} at 925 °C with pure CO_2 as the sweep gas. A ZnO doped $Gd_{0.1}Ce_{0.9}O_{1.95-\delta}$ membrane was reported recently.[136] The $Al_{0.02}Ga_{0.02}Zn_{0.96}O_{1.02}$ (AGZ)-$Gd_{0.1}Ce_{0.9}O_{1.95-\delta}$ (GDC) (50:50 vol. %) dual-phase membrane showed chemical stability against CO_2. By doping a slight amount of Al and Ga, ZnO exhibits excellent electronic conductivity in the membrane without sacrificing the ionic conductivity of GDC. Moreover, ZnO is chemically stable in CO_2 at high temperatures due to the decomposition of $ZnCO_3$ at above 200 $^{\circ}$C in air. At 860 and 940 °C, a stable O_2 flux was proven for over 500 hours with pure CO_2 as the sweep gas. To further enhance the oxygen ion conductivity of $Ce_{0.8}Gd_{0.2}O_{2-\delta}$, Pr can be used to substitute half of the original Gd to form $Pr_{0.1}Gd_{0.1}Ce_{0.8}O_{2-\delta}$.[212] $Pr_{0.1}Gd_{0.1}Ce_{0.8}O_{2-\delta}$ (PGC)-$CoFe_2O_4$ (CF) (50:50) membrane was fabricated to evaluate its oxygen permeation behavior in CO_2 atmosphere.[159] The O_2 flux was found to gradually increase within the first 100 hours

before reaching its steady value of 0.36 mL min^{-1} cm^{-2} for the next 100 hours. Compared with Gd and Sm, Nd-doped ceria is reported to exhibit the highest ionic conductivity.[164] Recognizing this fact, Luo *et al.* developed a $Ce_{0.9}Nd_{0.1}O_{2-\delta}$ (CN)-$Nd_{0.6}Sr_{0.4}FeO_{3-\delta}$ (NSF) (60:40) dual-phase membrane which showed excellent chemical stability under CO_2.[141] A stable oxygen flux of 0.48 mL min^{-1} cm^{-2} under CO_2 atmosphere was obtained with a porous $La_{0.6}Sr_{0.4}CoO_{3-\delta}$ coating on the 0.6 mm membrane. *In-situ* powder X-ray diffraction between 30 and 1000 ^{o}C of the dual-phase membrane in a CO_2 containing atmosphere dismissed the existence of carbonate and phase transition; suggesting that the dual-phase membrane is thermally and chemically stable in CO_2. Further on, the incorporation of Al dopant at B-site was reported to increase the thermochemical stability under reducing atmosphere.[213,214] The oxygen permeability can also be enhanced by such Al incorporation at B-site. $Nd_{0.6}Sr_{0.4}Al_{0.2}Fe_{0.8}O_{3-\delta}$ (NSAF6428)-$Ce_{0.9}Nd_{0.1}O_{2-\delta}$ (CN91) (40:60) and $Nd_{0.5}Sr_{0.5}Al_{0.2}Fe_{0.8}O_{3-\delta}$ (NSAF5528)-$Ce_{0.8}Nd_{0.2}O_{2-\delta}$ (CN82) (40:60) were developed and their oxygen permeation properties were studied under He and CO_2 atmosphere.[157] Higher Sr content composition (NSAF5528-CN82) exhibited higher O_2 flux than the lower Sr content composition (NSAF6428-CN91) irrespective of whether He or CO_2 was used as the sweep gas. The O_2 flux of NSAF5528-CN82 however decreased from 0.24 to 0.19 mL min^{-1} cm^{-2} at 900 ^{o}C during 130 hour-test under CO_2. In NSAF6428-CN91 case, stable O_2 flux of 0.15 mL min^{-1} cm^{-2} at 900 ^{o}C was maintained for at least 100 hours. These results denote the negative effect of Sr towards the stability under CO_2 atmosphere. A novel cobalt-free dual-phase membrane with a composition of $Ce_{0.8}Sm_{0.2}O_{2-\delta}$ (SDC)-$Ba_{0.95}La_{0.05}Fe_{1-x}Zr_xO_{3-\delta}$ (BLF$_{1-x}$Z$_x$) (60:40) were developed as oxygen permeable membranes for oxy-fuel combustion.[142] The substitution of Fe by Zr reduced the basicity of BLF$_{1-x}$Z$_x$ as is evident from X-ray photoelectron spectra; thus enhancing the stability of the dual-phase membrane under CO_2. For a 1.0 mm thick membrane with 15 % Zr doping (SDC-$BLF_{0.85}Z_{0.15}$), when pure CO_2 was applied as the sweep gas at 925 ^{o}C, a stable oxygen flux of 0.24 mL min^{-1} cm^{-2} was obtained for more than 80 hours. The oxygen permeation behaviors under CO_2 for a similar dual-phase material series $Ce_{0.8}Gd_{0.2}O_{2-\delta}$ (GDC)-$Ba_{0.95}La_{0.05}Fe_{1-x}Nb_xO_{3-\delta}$ (BLF$_{1-x}$N$_x$) (60:40) were studied by Cheng *et al.*.[144] Oxygen flux of approximately 0.19 mL min^{-1} cm^{-2} was displayed by GDC-$BLF_{0.9}N_{0.1}$ for 95 hours at the same condition (under pure CO_2 sweep gas). It is quite counterintuitive that the oxygen permeation flux of GDC-BLF$_{1-x}$N$_x$ membrane could not be fully recovered after the sweep gas was changed from CO_2 to He, unlike the full

recovery observed for SDC-BLF$_{1-x}$Z$_x$ membrane, despite the absence of carbonate formation in both cases. For example, the oxygen flux of GDC-BLF$_{0.85}$N$_{0.15}$ was 0.23 mL min^{-1} cm^{-2} in pure He during the first 10 h, but after 30 h under CO$_2$-containing sweep gas, the oxygen flux became 0.18 mL min^{-1} cm^{-2} when the sweep gas was changed from CO$_2$ to He. There was no explicit explanation given for this phenomenon, particularly for the oxygen flux decrease with increasing CO$_2$ concentration (from 15% to 100%). Very recently, a highly stable dual-phase Y$_{0.8}$Ca$_{0.2}$Cr$_{0.8}$Co$_{0.2}$O$_3$ (YCCC)-Sm$_{0.2}$Ce$_{0.8}$O$_{1.9}$ (SDC) (50:50) membrane was developed for oxygen separation in harsh operation conditions.[143] The membrane was composed of Ca- and Co-doped yttrium chromite (YCCC) and samarium doped ceria (SDC). Generally, chromite-based ceramic is difficult to be densified by sintering due to the formation of thin Cr$_2$O$_3$ layers at the inter-particle neck at the beginning of sintering. In their work, low melting point cobalt dopant was used to lower the sintering temperature by forming liquid phase during sintering. The relative density of the sintered YCCC-SDC was over 97 % (gas-tight) after being sintered at 1400 $^{\circ}$C, in contrast to the highly porous structure of YCC-SDC without Co-doping that featured poor sintering characteristics. The oxygen permeation flux was as high as 6.7 mL min^{-1} cm^{-2} at 950 $^{\circ}$C for a 1.3 mm-thick membrane when the forming gas (*i.e.*, 3 vol. % H$_2$ and 97 vol. % N$_2$) was used as the sweep gas. When 50 vol. % CO$_2$ was introduced into the forming gas, the oxygen flux decreased to 3.08 mL min^{-1} cm^{-2} with the degradation rate of less than 2 % during the 350-hour test. Moreover, after the 350-hour test with the co-existence of H$_2$ and CO$_2$, the membrane showed no phase decomposition and carbonate formation as evidenced by powder XRD patterns. It should be noted that the very high oxygen flux (of 6.7 mL min^{-1} cm^{-2} at 950 $^{\circ}$C) was ascribed to the 3 % H$_2$ in the sweep gas. Moreover, under reducing condition, the electronic conductivity of SDC can be more dominant than its ionic conductivity which also contributes to such high oxygen flux.[215,216] The work of Yoon and Marina showed that without H$_2$ in the sweep gas, the oxygen flux was very low, only 0.34 mL min^{-1} cm^{-2}.

Kharton *et al.* reported that the oxygen permeation flux through GDC/LSM composites was 10 times lower than that expected due to the inter-diffusion of the constituents.[172] However, another work on Ce$_{0.9}$Gd$_{0.1}$O$_{2-\delta}$ (GDC)-La$_{0.7}$Sm$_{0.3}$MnO$_{3\pm\delta}$ (LSM) (80:20 vol. %) dual-phase membrane demonstrated that O$_2$ flux can be increased substantially by applying surface decoration and lowering the LSM content to 20 vol. %.[147] Without surface decoration, the bare GDC-LSM (80:20 vol. %) displayed

identical O_2 flux relative to GDC membrane. The presence of $La_{0.6}Sr_{0.4}CoO_{3-\delta}$ (LSC) as the surface decoration on feed side led to marginal increase in the O_2 flux. However, the increase was improved by an order of magnitude when LSC decoration was present on permeate side. The more significant oxygen flux enhancement by permeate side decoration indicates that the oxygen surface reaction in the permeate side was the rate limiting step. Furthermore, coating LSC porous layer on both sides further increased the O_2 flux of GDC-LSM membrane, *i.e.*, by 3 orders of magnitude at 800 ^{o}C compared with the values of bare membrane, which can be attributed to the formation of electrical short circuit via LSC layer and LSM.[147] However, LSC-decorated dual-phase membrane showed low stability under CO_2 atmosphere due to the decomposition of LSC to a Ruddlesden-Popper phase (*i.e.*, $(LaSr)_2CoO_4$) and the reaction of CO_2 with the segregated SrO.[147] The oxygen permeation flux of the dual-phase membrane made of GDC and LSM phases can be further enhanced by applying hierarchically porous structure.[148] A bilayer dual-phase membrane with a dense $Ce_{0.9}Gd_{0.1}O_{1.95}$ (GDC)-$(La_{0.8}Sr_{0.2})_{0.95}MnO_{3-\delta}$ (LSM) (60:40 vol. %) layer and hierarchically porous GDC-LSM support was fabricated by a combined freeze-drying tape-casting and screen-printing method. The dense film layer was about 30 μm-thick to minimize the bulk diffusion resistance. A 870 μm-thick porous top layer with a porosity of 41.6 % was present on top of the dense layer to enhance to the oxygen exchange rate on feed side. The O_2 flux of this bilayer membrane was improved by 81 % relative to the 900 μm-thick dense GDC-LSM membrane. Such increment implied that the oxygen transport process was limited by the surface exchange reaction. By depositing a porous SDC-LSCF6428 layer on the permeate side, the oxygen permeation flux was enhanced by 600 % relative to the GDC-LSM membrane without surface deposition, *i.e.*, from 0.105 to 0.780 mL min^{-1} cm^{-2}. After switching the sweep gas from He to CO_2, an O_2 permeation flux of 0.659 mL min^{-1} cm^{-2} could still be achieved.[148] Park and Choi reported similar observation that, using $LaCrO_3$ porous layer, oxygen flux of yttria-stabilized zirconia (YSZ) was enhanced by ~4 times with permeate-side surface modification and by ~1.4 times with feed-side surface modification.[217] A site-deficient $Sr_{0.97}Ti_{0.5}Fe_{0.5}O_{3-\delta}$, which has been reported to be highly stable against CO_2,[105] was decorated on the membrane surface. The oxygen flux was decreased by only 12.5 % from 0.32 to 0.28 mL min^{-1} cm^{-2} over 93 hour-operation under pure CO_2. The stability against CO_2 was significantly enhanced although at the expense of oxygen flux. The chemical stability could be

further improved using SFT-GDC (50:50 vol. %) as the decoration material for which the O_2 flux stabilized to 0.44 mL min^{-1} cm^{-2} after 93 h operation in CO_2 atmosphere. This work provides an effective method to improve the O_2 permeation flux and chemical stability of membranes under CO_2 atmosphere. Another related work is $Ce_{0.8}Sm_{0.2}O_{2-\delta}$ (SDC)-$PrBaCo_2O_{5+\delta}$ (PBC) (60:40 vol. %) dual-phase membrane,[184] based on which it was found that SDC-PBC (50:50 vol. %) surface decoration can contribute towards 26 % improvement of O_2 flux. $Ce_{0.8}Sm_{0.2}O_{2-\delta}$ (SDC)-$La_{0.9}Sr_{0.1}FeO_{3-\delta}$ (LSF) (70:30 vol. %) dual-phase membrane was also developed by Wang et al..[149] They mentioned that cobalt-containing perovskites have structural instability while chromium within chromium-containing perovskites can easily evaporate at high temperature. By utilizing LSF, the membrane showed excellent stability without any performance degradation at 900 ^{o}C with CO_2 as sweep gas for 150 hours. The ionic inter-diffusion between SDC and LSF was probed using inductively coupled plasma atomic emission spectrometry (ICP-AES). The results showed that Sm, La, and Fe were co-doped into CeO_2 in the dual-phase membrane. The tested CeO_2 phase had chemical composition of $Ce_{0.774}(Sm_{0.132}La_{0.087}Fe_{0.007})O_{2-\delta}$. Such co-doped CeO_2 was conceived to have enhanced conductivity which contributed positively towards the oxygen permeability of the dual-phase membrane.

Transition metal oxide such as Fe_2O_3 can also be used as electronic conductor phase in dual-phase membranes. A O_2 flux of 0.18 mL min^{-1} cm^{-2} could be achieved through 0.5 mm-thick Fe_2O_3 (FO)-$Ce_{0.9}Gd_{0.1}O_{2-\delta}$ (GDC) (40:60) membrane under an air/He gradient at 1000 ^{o}C.[151] After depositing a porous LSC layer on the surface of the feed side, a steady O_2 flux of 0.2 mL min^{-1} cm^{-2} was detected for more than 150 h using pure CO_2 as the sweep gas, indicating that the coated FO-GDC membrane was CO_2 stable.

2.2.3 Other materials

Another type of materials which belongs to the K_2NiF_4 family also shows potential in terms of stability to CO_2. $La_2NiO_{4+\delta}$ is one of the main examples. The substantial interest on $La_2NiO_{4+\delta}$ originates from its relatively low thermal expansion coefficients (11.9-13.8 x 10^{-6} K^{-1}) compared to perovskite oxides and its distinct crystal structure which consists of alternating perovskite-like and rock-salt-like layers along the c-axis

(**Figure 2.11**).[40] At elevated temperatures, the oxygen transport through this compound mainly takes place *via* a 2-dimensional interstitial oxygen diffusion in the rock-salt layers. $La_2NiO_{4+\delta}$, however, exhibits a much lower oxygen flux relative to the benchmark perovskite oxide material such as $Ba_{0.5}Sr_{0.5}Co_{0.8}Fe_{0.2}O_{3-\delta}$. Klande *et al.* also found that the partial substitution of 10 mole % Ni in $La_2NiO_{4+\delta}$ by various cations, *i.e.*, Al, Co, Cu, Fe, Mg and Zr diminish the original oxygen flux (of non-doped material).[40] U-shaped K_2NiF_4 hollow fiber membranes based on $(Pr_{0.9}La_{0.1})_2(Ni_{0.74}Cu_{0.21}Ga_{0.05})O_{4+\delta}$ material was synthesized by a phase-inversion spinning/sintering process.[42,218] Ni, Cu, and Ga were incorporated to this composition to increase the CO_2 resistance in accord with the facts that $NiCO_3$ is less stable than $La_2(CO_3)_3$, $La_2O_2CO_3$, and $Pr_2(CO_3)_3$ (as deduced from Ellingham diagram), $CuCO_3$ is not stable above ambient temperature and $Ga_2(CO_3)_3$ is rarely known to form (at least under the reported conditions). The fiber retained its original structure during *in-situ* powder x-ray diffraction under CO_2 atmosphere from room temperature to 1000 ^oC. Compared with disk $(Pr_{0.9}La_{0.1})_2(Ni_{0.74}Cu_{0.21}Ga_{0.05})O_{4+\delta}$ disk membrane, the O_2 flux of this U-shape hollow fibre was significantly higher (0.32 versus 0.9 mL min^{-1} cm^{-2} under pure CO_2).[219] By substituting Pr with Nd, O_2 flux was further enhanced under the same test conditions.[220] Xue *et al.* found that the A-site deficient $(Pr_{0.9}La_{0.1})_{1.9}(Ni_{0.74}Cu_{0.21}Ga_{0.05})O_{4+\delta}$ exhibited O_2 flux of more than two times higher than that of $(Pr_{0.9}La_{0.1})_2(Ni_{0.74}Cu_{0.21}Ga_{0.05})O_{4+\delta}$ without any evidence of reduced CO_2 resistance.[221] Since Nd and Al are considered to be cheaper than Pr and Ga, $(Nd_{0.9}La_{0.1})_2(Ni_{0.74}Cu_{0.21}Al_{0.05})O_{4+\delta}$ was then developed which was also stable to pure CO_2 up to 975 ^oC.[222] Similarly, a sandwich structured $(Pr_{0.9}La_{0.1})_2(Ni_{0.74}Cu_{0.21}Nb_{0.05})O_{4+\delta}$ was also tested as CO_2 resistant oxygen permeation membrane.[223] The performance details of the above materials are also listed in **Table 2.3**.[40,42,219-222]
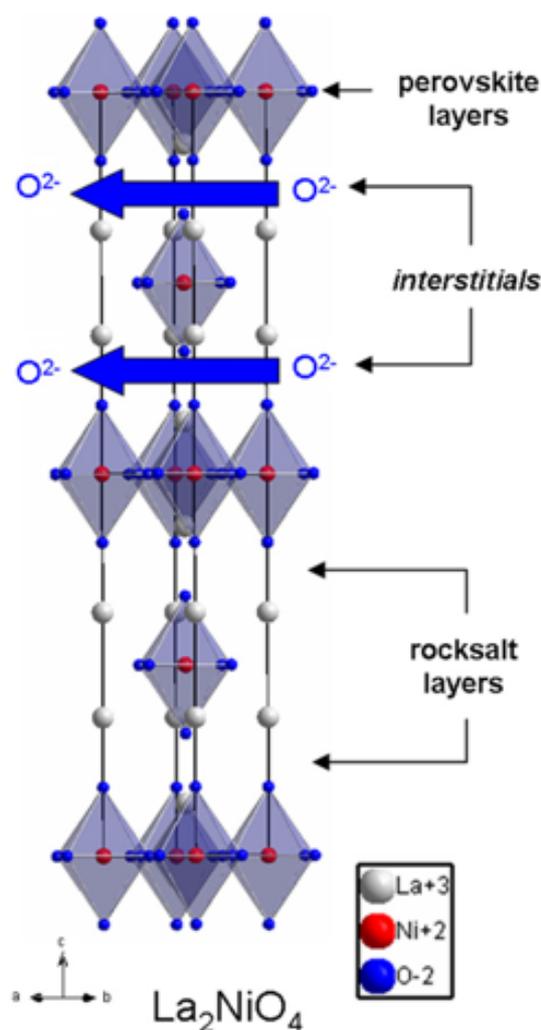
Figure 2.11 Crystal structure of a typical K_2NiF_4 material, $La_2NiO_{4+\delta}$; consisting of alternating perovskite layers and rock-salt layers along the c-axis. The arrows indicate interstitial oxygen diffusion through the rock-salt layers (Reproduced from ref. 40 with permission from Elsevier).

2.3 CO$_2$-resistant oxygen-selective mixed ionic-electronic conducting membranes: engineering approaches

Besides the chemical and structural modification approach to enhance CO_2 resistance, engineering approach such as surface decoration can also be applied. Surface decoration has been frequently used in solid oxide fuel cell (SOFC) field to enhance the cathode performance or stability in harsh atmosphere.[224-228] Within the context of increasing the oxygen permeation flux by enhancing the surface exchange reaction rate, for example, $La_{1-x}Sr_xCoO_{3-\delta}$ were often deposited as porous layer on dense membrane surface.[133,136,141,147,154,229] A previous study demonstrated that the oxygen permeation flux of a 120 μm-thick BSCF5582 membrane with a 6.5 μm-thick porous layer was 3.6

times that of the BSCF5582 membrane without such layer.[230] Weight relaxation curves established higher surface exchange rate (k_{chem}) in the presence of porous layer coating; indicating that the larger reaction area of the porous coating promoted faster surface exchange. Other coating materials such as silver (Ag), platinum (Pt), $Sm_{0.5}Sr_{0.5}CoO_{3-\delta}$, SDC, $LaNiO_{4+\delta}$, LSCF6428, $SrCo_{0.8}Fe_{0.2}O_{3-\delta}$, $SrCo_{0.9}Nb_{0.1}O_{3-\delta}$, $La_{0.5}Sr_{0.5}FeO_{3-\delta}$, and $La_{1-x}Sr_xFe_{1-y}Ga_yO_{3-\delta}$ have also been applied as surface decoration on oxygen permeation membranes.[128,130,203,204,231-238] The studies involving these aforementioned surface decorations were nonetheless focused into oxygen permeation properties in normal air to inert sweep gas gradient, *i.e.*, in the absence of CO_2. Still, surface decoration can be applied to design CO_2-resistant membrane *via* proper choice of decoration materials that are stable to CO_2.

Development of CO_2-protective layers on the surfaces of membranes is an effective route to obtain CO_2-resistant membranes. CO_2-resistant layer can simply be coated onto the membrane surfaces. Zhang *et al.*'s work provides such example.[239] They made a bi-layer structure $Ba_{0.5}Sr_{0.5}Co_{0.8}Fe_{0.2}O_{3-\delta}$-$Pr_{0.5}Ce_{0.5}O_{2-\delta}$ (BSCF5582-PrCe) membranes by wet spraying PrCe ink (*i.e.*, a pre-milled mixture of isopropyl alcohol, ethylene glycol, glycerol, and PrCe) onto BSCF5582 membrane followed by calcination. PrCe layer was CO_2-resistant as confirmed by Fourier-Transform Infra-Red and CO_2-temperature programmed desorption results. The oxygen permeation test under CO_2-containing atmosphere (10 vol. % CO_2 in He) showed a flux of around 1.35 mL min^{-1} cm^{-2} at 850 °C. At the same temperature, the flux was 1.6 mL min^{-1} cm^{-2} under pure helium. The retainment of relatively large portion of oxygen flux even after CO_2 was introduced to the sweep gas was most likely due to the weak adsorption of CO_2 onto the PrCe surface. Another example is the coating $SrFe_{0.8}Nb_{0.2}O_{3-\delta}$ (SFN) nano-sized layer onto BSCF5582 membrane.[240] SFN has been proven as a perovskite that has high chemical stability against CO_2.[62] The resultant membrane maintained stable oxygen flux in CO_2-containing atmosphere at 850 °C. Spray pyrolysis method can also be used to make dense CO_2-resistant layer.[241] Spray pyrolysis is considered as a scalable and low-cost process. Furthermore, the morphology and chemical composition can be controlled *via* appropriate selection of solvents, precursor concentrations, droplet sizes, and deposition temperatures.[241,242] The 250 nm-thick GDC protective layer on the permeate side prevented the formation of strontium carbonate on LSCF6428 membrane; thus the O_2 flux of the protected LSCF6428 showed no decrease when CO_2 was introduced in the sweep gas. He *et al.* fabricated a sandwich structure LSCF6428

membrane containing a dense LSCF6428 layer in the center and two porous LSCF6428 layer on the opposite surfaces.[243] GDC particles were coated onto the porous LSCF6428 layers by impregnating the membrane with gadolinium nitrate ($Gd(NO_3)_3$) and cerium nitrate ($Ce(NO_3)_3$) solution mixture. After being heated at 900 ^{o}C for 1 hour to remove the nitrate ions and organics and form fluorite phase. Their powder X-ray diffraction patterns confirmed the formation of GDC on the LSCF6428 surface. GDC particle modification simultaneously improved the surface exchange kinetics and enhanced the chemical resistance of LSCF6428 membrane as evidenced by long-term stability under CO_2-containing atmosphere for 100 hours. Using the same method, a sandwich structured $(Pr_{0.9}La_{0.1})_2(Ni_{0.74}Cu_{0.21}Nb_{0.05})O_{4+\delta}$ (PLNCN) was modified by GDC particles on the porous layer.[223] By doing such GDC modification, the O_2 flux of the ultrathin (5-6 μm) PLNCN membrane reached up to 4.22 mL min^{-1} cm^{-2} at 950 ^{o}C with 100 mL min^{-1} He sweep gas flow. During the subsequent 200 hour-test under pure CO_2 at 900 ^{o}C, this membrane demonstrated stable oxygen permeation fluxes of 3.22 mL min^{-1} cm^{-2}. Unlike the dense GDC layer reported in the work of García-Torregrosa *et al.*,[241] the GDC particles on the porous layers contributed to the higher surface exchange rate and the resultant higher oxygen permeation flux. Likewise, Zhang *et al.* also demonstrated this concept by coated a 100 nm-thick SDC dense layer onto BSCF5582 surface.[244] With such CO_2-resistant SDC dense layer, the membrane displayed a stable oxygen flux for at least 60 hours when 10 vol. % CO_2 + 90 vol. % He was used as the sweep gas, in contrast to BSCF5582 membrane without coating that showed continuous decrease in CO_2-containing sweep gas. In addition, the protective layer can also be made of the same material as the dense layer. A research work on $SrFe_{0.95}W_{0.05}O_{3-\delta}$ membrane, for example, was carried out to study the effect of surface decoration on the stability of membrane in CO_2 atmosphere.[245] The test results indicated enhancement of CO_2 stability for the doped $SrFe_{0.95}W_{0.05}O_{3-\delta}$ by decoration of protective layer. Moreover, by decorating porous layer and silver particles on the permeate side, the oxygen flux under helium was increased due to the enhanced oxygen desorption process. Furthermore, the protective porous layer obstructed the circulation of CO_2 in pores; preventing the complete blockage of the surface by the strontium carbonate. This factor contributed to minimize the degradation rate of oxygen fluxes.

2.4 Performance overview

Single-phase perovskite-based membranes especially barium and cobalt containing perovskites generally have higher O_2 permeation flux than dual phase membranes. In **Table 2.1**, most of Ba and Co-containing perovskite compositions display fluxes higher than 1.0 mL min^{-1} cm^{-2} in inert gas-containing sweep gas atmosphere. The highest O_2 flux was exhibited by $BaBi_{0.05}Co_{0.8}Ta_{0.15}O_{3-\delta}$ membrane.[67] Its O_2 flux could reach up to 3.57 mL min^{-1} cm^{-2} for a 0.8 mm-thick $BaBi_{0.05}Co_{0.8}Ta_{0.15}O_{3-\delta}$ membrane at 950 ^{o}C under an air/He oxygen gradient. $BaCo_xFe_yNb(Zr)O_{3-\delta}$ perovskites also displayed high O_2 flux of around 1 mL min^{-1} cm^{-2} for its 1 mm-thick disk membrane at 900 ^{o}C using He as the sweep gas.[30,39,65] O_2 flux decreased to as low as 0.12 mL min^{-1} cm^{-2} at 900 ^{o}C for 0.85-mm thick $BaFe_{0.65}Nb_{0.35}O_{3-\delta}$ membrane at 900 ^{o}C using He as the sweep gas, which highlights the fact that the high redox activity of Co promotes high O_2 permeability.[30] However, when pure CO_2 was used as the sweep gas, O_2 flux degraded to zero due to the formation of $BaCO_3$ that fully covered the membrane surface, especially at lower temperatures.[30,246] Complete replacement of Ba by Sr or La in addition to reduction of Co content effectively enhanced CO_2 resistance. For example, $SrFe_{0.8}Nb_{0.2}O_{3-\delta}$ membrane could maintain 0.31 mL min^{-1} cm^{-2} O_2 flux at 900 ^{o}C for at least 210 hours using pure CO_2 as sweep gas[62] whereas for $BaCo_{0.6}Fe_{0.2}Nb_{0.2}O_{3-\delta}$ membrane at the same conditions, O_2 flux was reduced to almost negligible value.[30] Likewise, LSCF6428 and $Pr_{0.6}Sr_{0.4}Co_{0.2}Fe_{0.8}O_{3-\delta}$ membrane could maintain stable O_2 flux for more than 90 hours while for BSCF6428 membrane, the O_2 flux started to degrade immediately after CO_2 was introduced.[27,70,72]

Although appropriate selection of A and B-site cations components can improve CO_2 resistance, performance deterioration is inevitable in pure CO_2 atmosphere.[53,69,123] An attractive alternative to perovskite that has been widely studied is K_2NiF_4-based materials. Examples of these materials are $La_2NiO_{4+\delta}$ and doped $La_2NiO_{4+\delta}$ such as $(Pr_{0.9}La_{0.1})_2(Ni_{0.74}Cu_{0.21}Ga_{0.05})O_{4+\delta}$ and $(Nd_{0.9}La_{0.1})_2(Ni_{0.74}Cu_{0.21}Al_{0.05})O_{4+\delta}$ membranes. They have been proven to be completely CO_2-resistant during long-term operation in CO_2 atmosphere.[40,42,219-222] K_2NiF_4-based materials have better stability but lower O_2 permeability than perovskite materials. For example, O_2 flux of a 0.66 mm-thick $(Pr_{0.9}La_{0.1})_{1.9}(Ni_{0.74}Cu_{0.21}Ga_{0.05})O_{4+\delta}$ membrane was only 0.66 mL min^{-1} cm^{-2} at 900 ^{o}C under an air/CO_2 oxygen gradient.[221]

Dual-phase membranes generally have better stability than perovskite membranes. **Table 2.2** summarized the performances of CO_2-resistant dual-phase membranes. After CO_2 exposure, these membranes did not show evidence of phase change and carbonate formation. These dual-phase membranes normally displayed less than 1 mL min^{-1} cm^{-2} at 950 ^oC when CO_2 was used as sweep gas. The main reason for the low O_2 flux is the large amount of fluorite phase such as $Ce_{0.8}Tb_{0.2}O_{2-\delta}$, $Ce_{0.9}Pr_{0.1}O_{2-\delta}$, $Ce_{0.8}Sm_{0.2}O_{2-\delta}$, $Ce_{0.9}Gd_{0.1}O_{2-\delta}$, $Y_{0.08}Zr_{0.92}O_{2-\delta}$, and $Ce_{0.8}Nd_{0.2}O_{2-\delta}$; all of which have very low O_2 permeability due to the limited electronic conductivity. It is worth repeating that when the electronic conducting phase with low or negligible ionic conductivity is used, the oxygen ionic conducting path is blocked. This leads to lower oxygen flux relative to the case using the mixed ionic-electronic conducting phase. To take $NiFeO_4$ (NF)-$Ce_{0.8}Tb_{0.2}O_{2-\delta}$ (CT) (60:40 vol. %) as an example on which NF electronic conductor was used, its O_2 flux at 900 ^oC swept by CO_2, was only 0.14 mL min^{-1} cm^{-2}.[140] In $Ce_{0.9}Pr_{0.1}O_{2-\delta}$ (CP)-$Pr_{0.6}Sr_{0.4}Fe_{0.5}Co_{0.5}O_{3-\delta}$ (PSFC) (60:40 wt. %) case which includes MIEC PSFC phase, on the other hand, its O_2 flux was 0.7 mL min^{-1} cm^{-2} at 950 ^oC.[137] Such value is among the highest fluxes observed for dual-phase membranes.

2.5 Degradation behavior and mechanism probing

The simultaneous use of several spectroscopy techniques to probe the degradation processes during membrane exposure to CO_2 is a powerful method as demonstrated by Yi *et al.*.[30] In their work on $BaCo_{0.4}Fe_{0.4}Nb_{0.2}O_{3-\delta}$ (BCFN), powder X-ray diffraction (XRD), scanning electron microscopy (SEM, including back scattered electron (BSE) imaging), energy dispersive X-ray (EDX) analysis (including elemental mapping) and scanning transmission electron microscopy (STEM, including electron energy loss spectroscopy (EELS), high-angle annular dark field (HAADF) imaging, and selected area electron diffraction (SAED) pattern) were combined. Powder XRD for BCFN annealed at 900 ^oC in CO_2 showed the formation of $BaCO_3$ and CoO. SEM and STEM (**Figure 2.12(a)**) revealed the formation of a top carbonate layer mainly consisting of $BaCO_3$ followed with a porous layer containing BSCF5582 layer which was depleted of Co and enriched in Fe and Nb as well as CoO on top of the unaffected bulk perovskite layer. SAED (**Figure 2.12(a)**) showed major reflections from the main cubic phase of Co-depleted BCFN phase together with minor reflections from $BaCO_3$ (indicated as b)
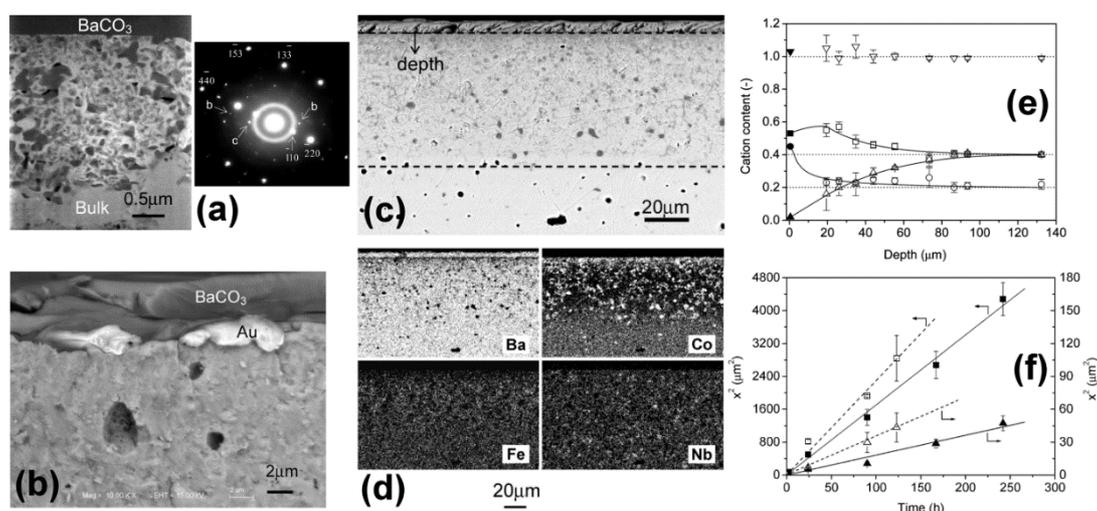
Figure 2.12 Characterization of $BaCo_{0.4}Fe_{0.4}Nb_{0.2}O_{3-\delta}$ membranes exposed to CO_2 at 900 °C; (a) Scanning transmission electron microscopy high-angle annular dark field micrograph of porous layer (left) and electron diffraction pattern (right) along [334] zone axis of the perovskite phase (b and c represent $BaCO_3$ and CoO phase, respectively) – after 2 hours; (b) back-scattered electron microscopy (BSEM) image of the cross-section of the membrane initially deposited with gold particles on its top surface – after 90 hours; (c) BSEM image and (d) elemental mapping of the cross-section of the membrane – after 240 hours; (e) Cation composition as a function of sample depth from scanning electron microscopy-energy dispersive x-ray analysis – after 240 hours; and (f) The plot of the square of the thickness of the decomposed layer versus the exposure time (linear plot indicates the adequacy of the parabolic rate law to describe the decomposition process) (Reproduced from ref. 30 with permission from American Chemical Society).

and CoO (indicated as c). The gold particles which were deposited on the surface of BCFN prior to the CO_2 exposure became embedded between the carbonate layer and the porous layer which indicates the outward growth of $BaCO_3$ at the surface (**Figure 2.12(b)**). BSE image and elemental mapping of BCFN annealed at 900 °C in CO_2 for 10 days (**Figure 2.12(c) and (d)**) confirmed the retaining of previous morphology (with larger thickness for each layer) at longer exposure time. The variation of the cation composition with the depth of the membrane (from the boundary of the carbonate layer and porous layer to the bulk) was obtained using SEM-EDX (**Figure 2.12(e)**). Despite the variation in Co, Fe and Nb, the ratio between A and B cations remained constant. The authors also found that the thickness of both layers, *i.e.*, carbonate and porous increased with CO_2 annealing time following a simple parabolic rate law (**Figure**

2.12(f)) which suggests that the process is a diffusion-controlled one. They proposed that during the decomposition, initially $BaCO_3$ formed on the surface (and grew outward) while the layer below became depleted in Ba due to diffusion of Ba^{2+} from the bulk layer to the surface. This resulted in the precipitation of CoO to form Co-depleted porous layer. At the outer surface, Ba^{2+} reacted with CO_2 and O_2 in the presence of electron to form $BaCO_3$ (instead of reacting within the porous layer which requires O_2 and CO_2 to diffuse into the layer; as summarized in **Eq. (2.14)**).

$$aCO_2 + bO_2 + BaCo_{0.4}Fe_{0.4}Nb_{0.2}O_{3-\delta} \longrightarrow aBaCO_3 + cCoO + (1-a)BaCo_{(0.4-y)}Fe_{(0.4+z)}Nb_{(0.2+y-z)}O_{3-\delta'} \qquad \text{(Eq. 2.14)}$$
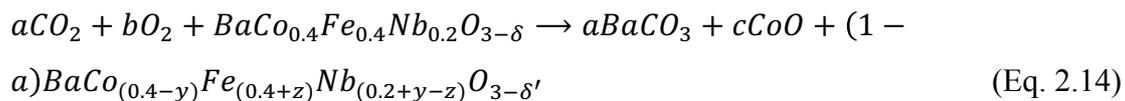
In this work, Yi *et al.* also studied the effect of increasing the content of Fe or Nb on $BaCo_{1-x-y}Fe_xNb_yO_{3-\delta}$ (x = 0.2-0.8, y = 0.2-0.5). Increasing Fe or Nb resulted in higher CO_2 resistance and reduced oxygen permeation flux, *i.e.*, the trade-off problem we mentioned earlier. Notably, incorporating cations with high oxidation state affects the oxygen non-stoichiometry, *i.e.*, decreasing the oxygen non-stoichiometry according to charge neutrality criterion and strengthening the metal-oxygen bonding; both of which inhibit the formation of oxygen vacancies and therefore, high oxygen ionic conductivity. Zhou *et al.* also investigated the degradation and recovery mechanisms of BCFN perovskite.[246] They observed the same phase and microstructure change of the BCFN membranes after annealed under pure CO_2 at 850 $^{\circ}$C for 10 hours. They further tested the recovery of BCFN membranes under permeation conditions by using pure CO_2 as the sweep gas, followed by switching the sweep gas to 5 vol. % CO_2 in He. After applying 5 vol. % CO_2 in He for 60 hours, the fully covered $BaCO_3$ top layer broke; generating pores and cracks on the surface. The O_2 flux could be partially recovered at the end of the 60 hour-permeation test. The main contributor to the carbonate layer decomposition and the partial O_2 flux recovery is the fast exchange of oxygen ions between BCFN and carbonate, which possibly leads to a dynamical equilibrium of carbonate decomposition and formation. The presence of O_2 in the sweep gas restrained the carbonate formation through competitive adsorption of O_2 and CO_2 on the BCFN surface and stabilized the cubic perovskite structure.

Another example of excellent work using STEM in combination with EDX mapping and EELS is the work of Ravkina *et al.*.[44] **Figure 2.13(a)-(d)** shows the

59
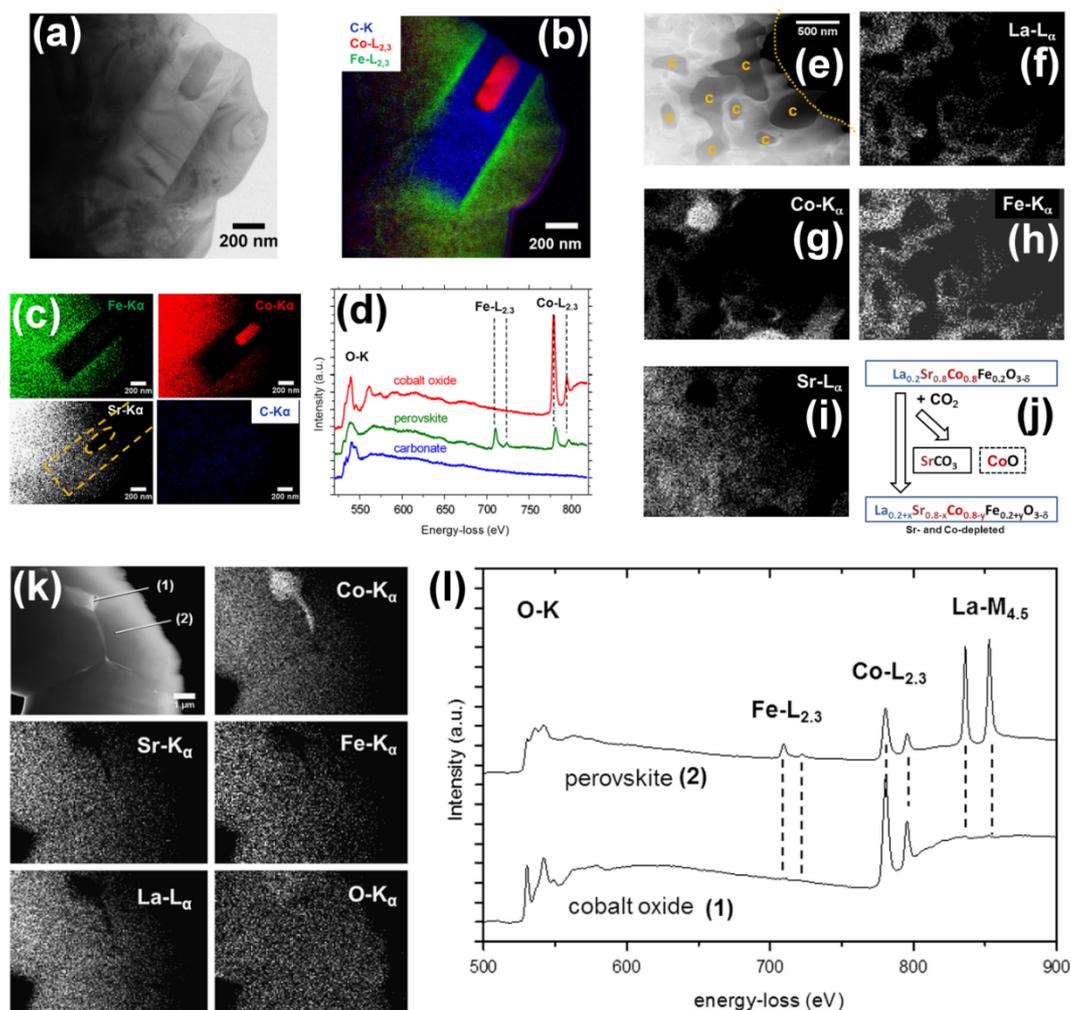
Figure 2.13 Characterization of the sweep side of $SrCo_{0.8}Fe_{0.2}O_{3-\delta}$ membrane after exposure to CO_2 at 900 ^{o}C for 30 hours; (a) Scanning transmission electron microscopy (STEM) image; (b) Energy-filtered transmission electron microscopy (EFTEM) image; (c) Energy-dispersive x-ray spectroscopy (EDXS) maps (Orange dashed line represents border of $SrCO_3$); (d) Electron energy loss spectra (EELS) for perovskite phase, cobalt oxide and strontium carbonate; Characterization of the sweep side of LSCF6482 membrane after exposure to CO_2 at 900 ^{o}C for 200 hours; (e) High-angle annular dark field STEM image; (f), (g), (h) and (i) EDXS maps; (j) Decomposition scheme; Characterization of the sweep side of LSCF6482 membrane after exposure to CO_2 at 900 ^{o}C for 200 hours; (k) High-angle annular dark field STEM image and EDXS maps; and (l) EELS for perovskite phase and cobalt oxide (Reproduced from ref. 44 with permission from Elsevier).

characterization results on the $SrCo_{0.8}Fe_{0.2}O_{3-\delta}$ membrane side subjected to CO_2 exposure at 900 ^{o}C for 30 hours. HAADF imaging (**Figure 2.13(a)**) displays regions with different phase composition. Energy-filtered transmission electron microscopy (EFTEM) image and EDX mapping (**Figure 2.13(b) and (c)**) clearly reveal different

60

phases; regions dominated by CoO (red region), $SrCO_3$ (blue region) and perovskite phase (green region). EELS onto these different phases (**Figure 2.13(d)**) verify the presence of peaks characteristic of Fe-$L_{2,3}$ (710 and 723 eV) for perovskite phase, Co-$L_{2,3}$ (782 and 796 eV) for CoO phase which are absence for carbonate phase. Similar results on $La_{0.2}Sr_{0.8}Co_{0.8}Fe_{0.2}O_{3-\delta}$ membrane side subjected to CO_2 exposure at 900 ^{o}C for 200 hours which feature HAADF imaging, EDX mapping, and the resultant decomposition scheme are included as **Figure 2.13(e)-(j)**. Areas with different contrast appear in these figures, particularly the carbonate phase ("c" in **Figure 2.13(e)** – which shows lack of signals from La, Sr, Co and Fe – **Figure 2.13(f)-(i)**) and CoO rich phase (**Figure 2.13(g)** – which also shows lack of signals from La, Sr and Fe – **Figure 2.13(f), (h) and (i)**). Another set of results for LSCF6482 membrane side (also subjected to CO_2 exposure at 900 ^{o}C for 200 hours – **Figure 2.13(k) and (l)**) show the formation of CoO rich phase ("1" in **Figure 2.13(k)**) and perovskite phase ("2" in **Figure 2.13(k)**) without any indication of carbonate phase. These microscopy imaging and analysis results are consistent with the oxygen permeation testing results; both of which substantiate the fact that LSCF6482 is stable to CO_2 at 900 ^{o}C while $SrCo_{0.8}Fe_{0.2}O_{3-\delta}$ and LSCF2882 are not.

Benson *et al.* studied degradation mechanism of LSCF6428 in an aggressive atmosphere containing carbon dioxide and water ($H_2O/CO_2/O_2$ in the ratio of 2:1:1).[248] They characterized the degradation evolution using powder XRD, Raman spectroscopy, isotope exchange depth profiling, and secondary ion mass spectrometry (**Figure 2.14**). The powder X-ray diffraction (XRD) pattern of sample aged for 1 week at 1 atm pressure showed no discernible differences relative to the untreated sample (**Figure 2.14(a)**). Pattern for sample aged for 1 week at 5 atm pressure nonetheless revealed the presence of secondary phases of $SrCO_3$ and mixed transition metal oxides. $La_2O_2CO_3$ phase and A-site deficient LSCF6428 emerged when the aging time was extended to 6 weeks (**Figure 2.14(a)**). To this end, another study showed that B-site cations may precipitate into oxides when A-site deficiency reached a certain level; resulting in the presence of substantial amount of transition metal oxides detected in powder XRD pattern.[249] Raman spectra further confirmed the decomposition of the LSCF6428 surface (**Figure 2.14(b)**). Increase in the aging annealing time and $H_2O/CO_2/O_2$ pressure led to the generation of the distinct peaks at 474, 620, and 695 cm^{-1} in addition to the main LSCF6428 peak at 570 cm^{-1}. The peaks at 474 and 620 cm^{-1} were assigned to Fe_2O_3 and that at 695 was assigned to $(Co, Fe)_3O_4$ phase.[250,251] In addition, the main
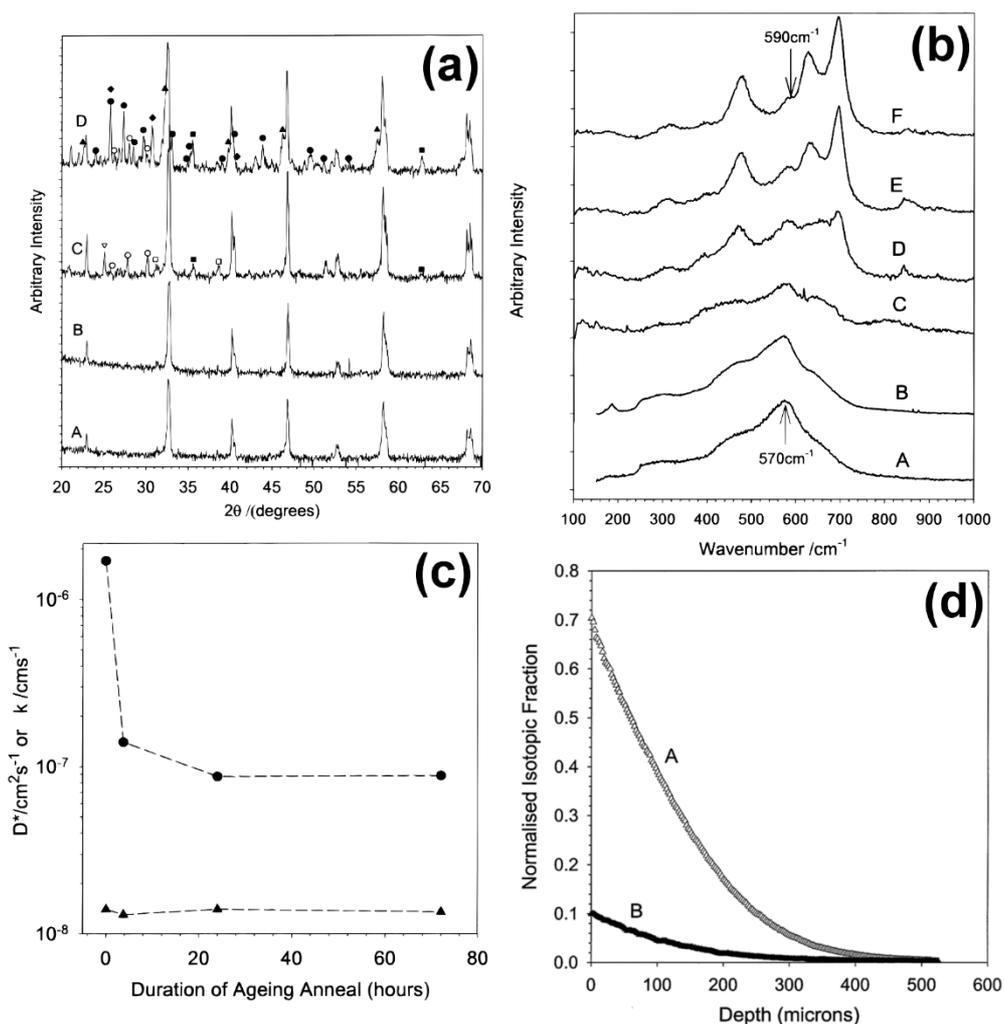
Figure 2.14 (a) Powder X-ray diffraction patterns of aged samples: (A) untreated standard LSCF6428, (B) aged 1 week at 1 atm total pressure, (C) aged 1 week at 5 atm, (D) aged 6 weeks at 5 atm; (b) Raman spectra of the bulk material of the aged samples: (A) standard untreated LSCF, (B) aged 1 day at 1 atm total pressure, (C) aged 3 day at 1 atm total pressure, (D) aged 1 week at 1 atm total pressure, (E) aged 1 week at 5 atm total pressure, (F) aged 6 weeks at 5 atm total pressure; (c) The effect of the duration of the ageing annealing on the ^{18}O tracer diffusivity D^* (▲) and surface exchange coefficient k (●); and (d) ^{18}O diffusion profiles obtained for unaged LSCF (A) and LSCF exposed to ageing atmosphere for 3 days (B) (Reproduced from ref. 248 with permission from The Electrochemical Society).

LSCF6428 peak which was originally located at 570 cm^{-1} for the untreated material shifted to 590 cm^{-1} for the sample aged for 6 weeks. Benson *et al.* attributed this to the gradual transformation of cation-stoichiometric LSCF6428 to modified perovskite composition. Powder XRD and Raman spectra consistently showed the surface

composition changes upon exposure to $H_2O/CO_2/O_2$ atmosphere. Isotope exchange depth profiling and secondary ion mass spectrometry were used to determine the oxygen transport properties of oxide ion conducting ceramics. Two main parameters from the two characterization methods were the tracer diffusion coefficient $D*$ and the surface exchange coefficient k. $D*$ represents the bulk diffusion rate of oxygen ions through the oxide and k represents the exchange rate between oxygen in the gas atmosphere and that in the oxide. The related theory details can be found elsewhere.[248] $D*$ continued almost constant for the materials exposed to $H_2O/CO_2/O_2$ atmosphere ranging from 3.75 hours to 3 days at 750 ^{o}C before isotope exchange; while k decreased dramatically after 4 hour-treatment in $H_2O/CO_2/O_2$ atmosphere (**Figure 2.14(c)**). The oxygen exchange furthermore appears to be inhibited by surface corrosion by $H_2O/CO_2/O_2$ atmosphere (**Figure 2.14(d)**). The exposure to H_2O and CO_2 led to significant erosion of surface layers during aging. The erosion essentially modified the surface by generating A-site deficient perovskite and Co or Fe oxides which inhibited the surface oxygen exchange.

2.6 Future directions

In retrospect, there is an obvious trade-off between CO_2 resistance and O_2 permeation flux which makes it difficult to achieve simultaneously high CO_2 resistance and high O_2 permeation flux within a single-phase material. To this end, it is more realistic to enhance the O_2 permeation flux of CO_2-resistant materials with low flux (rather than the other way around, *i.e.*, enhancing the CO_2 resistance of unstable materials with high flux) *via* the application of internal and/or external short-circuit concepts and/or engineering approaches, resulting in what we called "hybrid material-engineering optimized membranes". Another equally important factor that cannot be overlooked is that such optimized membranes should have low materials and production cost to realize their commercialization. Despite the major improvements demonstrated by numerous works within the last decade, there are still many avenues and opportunities to be pursued. Two most promising major directions can be delineated as follows:

(1) New membrane materials and configurations with high CO_2 resistance and high O_2 permeation flux

This direction covers the development of new perovskite and K_2NiF_4-type compositions as well as new dual-phase combinations. For perovskite materials, the incorporation of Ba in A-site and Co in B-site almost always provide high oxygen permeability such as in the case of $BaBi_{0.05}Co_{0.8}Ta_{0.15}O_{3-\delta}$ and $BaCo_xFe_yNb(Zr)O_{3-\delta}$.[30,39,65,67] The longest stability in CO_2 nonetheless has thus far been obtained using perovskites that do not contain Ba and Co as represented by $SrFe_{0.8}Nb_{0.2}O_{3-\delta}$ hollow fiber which was stable for 600 hours in CO_2 atmosphere.[63]

Caro's group has published extensively on new CO_2-resistant dual-phase combinations.[61,133,134,137,141,145,146,150,157] Survey into the existing literature highlighted three most promising phase combinations, *i.e.*, fluorite-perovskite, fluorite-spinel, and fluorite-metal oxide. Despite their lower fluxes relative to perovskite membranes, rapid advances in the oxygen permeability of dual-phase membranes over the past half-decade means that attaining an economic flux of above 1 mL min^{-1} cm^{-2} *via* such composite technology in the near future is almost a certainty.[247] Modification of membrane structure and configuration can also be performed to further improve the oxygen permeability. This is exemplified by thin dual-phase membrane with porous coating and bilayer dual-phase membrane with hierarchically porous structure.[147,148]

The amount of studies addressing membrane configuration is relatively sparse in comparison to those focusing on developing new perovskite compositions. There are still many opportunities ahead as well as large improvement margin associated with the former aspect.

(2) Beneficial phase reactions and conductive phase generation along grain boundaries in dual-phase membranes

An innovative direction emerged recently that exploits beneficial "*in situ*" phase reactions on certain dual-phase combinations to create conductive new phases along the grain boundaries that enhance the oxygen permeability of the resultant membrane (relative to the mechanically mixed dual-phase mixture). Traditionally, chemical compatibility between the ionic conducting phase and the electronic conducting phase was the main consideration to ensure that these two phases did not react to form new phases that have low ionic and/or electronic conductivities. Such non-desirable reactions, for example, occurred in the case of GDC-LSM composite which displayed decreasing oxygen permeation flux with time.[172] Therefore, phases with low kinetic stability, *i.e.*, high cation diffusion tendency

generally are the last choice for composite component. The phase reactions nonetheless can also create new phases that have higher ionic and electronic conductivities (relative to the original individual phases). Lin *et al.*, for example, detected such new phase formation in $Ce_{0.8}Gd_{0.2}O_{2-\delta}$-$CoFe_2O_4$ dual-phase membrane using scanning transmission electron microscopy-high angle annular dark-field (STEM-HAADF), STEM-energy dispersive X-ray spectroscopy (STEM-EDX), STEM-electron energy loss spectroscopy (STEM-EELS), and selected area electron diffraction (SAED).[180] Gd- and Fe-rich phase containing Gd, Fe, Ce, Co and O (denoted as GFCCO phase) formed initially at the GDC-GDC boundaries. This GFCCO phase had a perovskite structure and high concentration of oxygen vacancies that promotes the oxygen ionic conductivity. The *in situ* production of GFCCO phase also decreased Gd accumulation at GDC-GDC boundaries which facilitates the oxygen transport within these boundaries. The work of Zhang *et al.* represents another example of this direction.[181] SDC, $SrCO_3$, and Co_3O_4 were used as the precursors to prepare dual-phase membranes. A new tetragonal perovskite phase, *i.e.*, $Sm_xSr_{1-x}CoO_{3-\delta}$ formed during sintering. This phase contributed towards higher permeability for the sintered membrane. Despite the apparent potential this direction provided, there are no clear guidelines on the design of the new phase. This is associated with the difficulties to predict what reactions will occur as well as the formed phase properties. Additional potential offered by this direction is the modification of the mechanical strength. Future studies that evaluate systematically the mechanical strength before and after beneficial phase reactions as well as the origins behinds the change are warranted given their current absence. Breakthrough in the performance of dual-phase membrane is likely to come from pursuing this direction which also may provide insights into ionic and electronic transport processes around grain boundaries.

2.7 Conclusions

Our literature survey into vast bodies of works on the development of CO_2-resistant oxygen-selective mixed ionic-electronic conducting (MIEC) membranes revealed that only two materials candidates display the highest potential, *i.e.*, perovskite and fluorite-based materials.

Perovskite-based MIEC materials generally offer high O_2 permeability and low CO_2 resistance especially those that contain alkaline earth metals such Ba and Sr. *From thermodynamics perspective,* stability diagram that correlates different phases as a function of the activity ratio of different metal oxides pairs can be used to quantify CO_2 resistance of perovskite oxides. A more popular alternative is Ellingham diagram which expresses the relative tendency for a certain carbonate formation at different temperatures and CO_2 partial pressures. In **Thermodynamics perspective** section, we have provided the essential steps required to construct Ellingham diagram. *From Lewis acid-base perspective,* metal (or perovskite) oxide is viewed as a base whereas CO_2 is viewed as an acid. Accordingly, lower basicity represents higher CO_2 resistance. Sanderson's electronegativity and the oxidation state of the cations can be utilized to assess the relative basicity of the metal oxides. An indispensable resource we included in **Chemistry perspective** section is **Figure 2.5** that displays the relative basicity for 101 metal oxides. In the absence of ready to-be-used data, the basicity of metal (or perovskite) oxide can also be experimentally determined from the O1s binding energy (BE) value of X-ray photoelectron spectra. Within this context, higher O1s binding energy reflects lower electron density (or higher oxidation state) and therefore, lower basicity. Another parameter that indicates the basicity of the metal (or perovskite) oxide is the average metal-oxygen bond energy (ABE).

We can generalize *three major directions* that have been undertaken to enhance CO_2 resistance of perovskite materials, *i.e.*, **(1)** Adopting rare earth metal cation as A-site cation; **(2)** Reduction in the Co content in B-site; and **(3)** Partial substitution of the original transition metals components in B-site with more acidic (less basic) or more stable transition metal components. Nevertheless, since the ABE reflects the basicity of perovskite oxide while the oxygen sorption from the lattice is also determined by how strong the oxygen is bonded to the metal and thus, the ABE (*i.e.*, lower ABE provides high sorption tendency and high oxygen permeability), it becomes apparent that a compromise between oxygen permeability and CO resistance exists where the increase in CO_2 resistance leads to the decrease in O_2 permeability. Such trade-off effect is not encountered in fluorite material that is practically CO_2-resistant but has low O_2 permeability. The electronic conductivity limitation origin of such low permeability can be addressed using internal and/or external electronic short-circuit concepts. These concepts represent different ways of adding the second electronic conducting (EC) or MIEC phase. The literature trend showed that incorporating MIEC second phase

generally leads to higher O_2 permeability than that obtained from incorporating EC second phase.

For industrial applications that prioritizes consistent performance for hundreds or even thousands of hours, dual-phase materials appear to be the more promising candidate than perovskite materials. We envision major performance breakthrough for dual-phase membrane technology given the rapid advances over the past 5 years in addition to the emergence of new direction that exploits *in situ* phase reaction to create conductive new phase within the composite along the boundary area. Despite the long way ahead towards the commercialization of CO_2-resistant oxide-based membrane technology, this field would certainly benefit from having the guidelines we provided here.

2.8 Key research questions and challenges

In the above literature review, we summarized the current research status and relative concepts of CO_2-resistant MIEC membranes. The comprehensive review of this area provides us the whole picture of the key questions and challenges to be solved in this thesis. Within our research interests, the first challenge is to modify the fluorite-oxide membrane to increase its oxygen permeability by enhance its electronic conductivity. To solve this challenge, several methods have been studies such as dual-phase membrane. There have been plenty of researches working on dual-phase membranes as summarized by this review above. Therefore, in this thesis, we will focus on the external short-circuit method, aiming to find an effective approach to form the external short-circuit. Besides, adding transition metal sintering aid in fluorite-oxide membrane is an alternative approach that is worth studying in this thesis. Perovskite oxide membrane generally possesses high O_2 permeation flux but inferior CO_2-resistance. Improve the CO_2-resistance of perovskite membranes remains another main challenge in this field. In this thesis, we designed and performed different methods to address these challenges, which will be displayed in the following Chapters 3-6. We hope to provide useful information in developing CO_2-resistant membrane with high O_2 permeation flux, which will be promising in enabling clean energy delivery through membrane technology.

Table 2.1 CO_2-resistance and performance of perovskite membranes

Materials	Instantaneous performance		Long term CO_2 test					Ref.
	T (°C)	$J(O_2)$ (mL min^{-1} cm^{-2})	T (°C)	$J(O_2)$ (mL min^{-1} cm^{-2})	Feed side	Permeate side	Time (h)	
$BaCo_xFe_yZr_zO_{3-\delta}$			800	2.3-0.7	150 mL min^{-1} air	50 mL min^{-1} He (3% CO_2)	0-0.5	39
(x+y+z = 1)			850	2.6-1.7			0-0.5	
			800	2.26-0.125		50 mL min^{-1} He (10% CO_2)	0-0.5	
			850	2.61-0.2			0-0.5	
			900	3.05-0.375			0-0.5	
$BaCo_{0.6}Fe_{0.2}Nb_{0.2}O_{3-\delta}$	900	1.09 (He)						30
		0 (CO_2)						
$BaCo_{0.4}Fe_{0.4}Nb_{0.2}O_{3-\delta}$	900	0.7 (He)	800	0.46	air	Ar	0	30
		0.07 (CO_2)		0-0.05		CO_2	0-1.25	
			900	0.7		Ar	0	
				0.05-0.08		CO_2	0-1.24	
			1000	0.92		Ar	0	
				0.92-0.26		CO_2	0-1.275	
$BaCo_{0.2}Fe_{0.6}Nb_{0.2}O_{3-\delta}$	900	0.51 (He)						30
		0.097 (CO_2)						

Table 2.1 CO_2-resistance and performance of perovskite membranes (continued)

Materials	Instantaneous performance		Long term CO_2 test					Ref.
	T (°C)	$J(O_2)$ (mL min^{-1} cm^{-2})	T (°C)	$J(O_2)$ (mL min^{-1} cm^{-2})	Feed side	Permeate side	Time (h)	
$BaFe_{0.8}Nb_{0.2}O_{3-\delta}$	900	0.4 (He)						30
		0.26 (CO_2)						
$BaFe_{0.65}Nb_{0.35}O_{3-\delta}$	900	0.12 (He)						30
		0.106 (CO_2)						
$La_{0.6}Ca_{0.4}Co_{0.8}Fe_{0.2}O_{3-\delta}$			850	0.09	150 mL min^{-1} air	29 mL min^{-1} CO_2	110-185	41
			900	0.27		29 mL min^{-1} He	0-10	
				0.155		29 mL min^{-1} CO_2	10-110	
$La_{0.6}Ca_{0.4}FeO_{3-\delta}$	800-950	0.08-0.41 (He)						61
		0.04-0.24 (CO_2)						
$SrCo_{0.8}Fe_{0.2}O_{3-\delta}$			900	1.35-1.5	100 mL min^{-1} air	50 mL min^{-1} He	4-26	46
				1.06		50 mL min^{-1} CO_2	28-47	
				0.59		50 mL min^{-1} CO_2	64	
				0.18		50 mL min^{-1} CO_2	73	
				0		50 mL min^{-1} CO_2	83	

Table 2.1 CO_2-resistance and performance of perovskite membranes (continued)

| Materials | Instantaneous performance | | Long term CO_2 test | | | | Ref. |
	T (^{o}C)	$J(O_2)$ (mL min^{-1} cm^{-2})	T (^{o}C)	$J(O_2)$ (mL min^{-1} cm^{-2})	Feed side	Permeate side	Time (h)	
$SrCo_{0.8}Fe_{0.2}O_{3-\delta}$			950	1.86	100 mL min^{-1} air	50 mL min^{-1} CO_2	0-5	45
				1.72			19-23	
				0.88			51	
				0.44			71	
$SrCo_{0.8}Fe_{0.2}O_{3-\delta}$			950	1.78	100 mL min^{-1} air	50 mL min^{-1} CO_2	0	47
				0.84			3	
				0.25			10	
				0.07			15	
				0.04			25	
$SrCo_{0.8}Fe_{0.2}O_{3-\delta}$			950	1.94	100 mL min^{-1} air	50 mL min^{-1} CO_2 (5% O_2)	0	47
				1.28			8	
				1.64			50	
				1.76			90	
$Sr(Co_{0.8}Fe_{0.2})_{0.9}Ta_{0.1}O_{3-\delta}$			900	0.98-1.34	100 mL min^{-1} air	50 mL min^{-1} He	5-56	46
				1.25-1.22		50 mL min^{-1} CO_2	57-61	
				1.16		50 mL min^{-1} CO_2	72-103	

Table 2.1 CO_2-resistance and performance of perovskite membranes (continued)

Materials	Instantaneous performance		Long term CO_2 test					Ref.
	T (°C)	$J(O_2)$ (mL min^{-1} cm^{-2})	T (°C)	$J(O_2)$ (mL min^{-1} cm^{-2})	Feed side	Permeate side	Time (h)	
$Sr(Co_{0.8}Fe_{0.2})_{0.95}Ti_{0.05}O_{3-\delta}$			950	1.61	100 mL min^{-1} air	50 mL min^{-1} CO_2	0-6	45
				1.17			20-21	
				0.92			30	
				0.73			51	
				0.63			69	
$Sr(Co_{0.8}Fe_{0.2})_{0.9}Ti_{0.1}O_{3-\delta}$			950	1.47	100 mL min^{-1} air	50 mL min^{-1} CO_2	0-4	45
				1.59			13-88	
$Sr(Co_{0.8}Fe_{0.2})_{0.8}Ti_{0.2}O_{3-\delta}$			950	1.34	100 mL min^{-1} air	50 mL min^{-1} CO_2	0-83	45
$Sr(Co_{0.8}Fe_{0.2})_{0.9}Ti_{0.1}O_{3-\delta}$	900	0.44 (CO_2) 0.84 (CO_2)						45
$SrFe_{0.8}Nb_{0.2}O_{3-\delta}$			900	0.31	150 mL min^{-1} air	50 mL min^{-1} CO_2	0-210	62
$SrFe_{0.8}Nb_{0.2}O_{3-\delta}$	800-900	0.52-1.24 (He) 0.38-1.12 (CO_2)	900	1.24	120 mL min^{-1} air	80 mL min^{-1} He	0-75	63
				1.12		80 mL min^{-1} CO_2	75-390	
				1.06	120 mL min^{-1} air (20% CO_2)	80 mL min^{-1} CO_2	400-600	

Table 2.1 CO_2-resistance and performance of perovskite membranes (continued)

Materials	Instantaneous performance		Long term CO_2 test					Ref.
	T (°C)	$\textbf{\textit{J}}(O_2)$ (mL min^{-1} cm^{-2})	T (°C)	$\textbf{\textit{J}}(O_2)$ (mL min^{-1} cm^{-2})	Feed side	Permeate side	Time (h)	
$SrFe_{0.8}Zr_{0.2}O_{3-\delta}$	750-900	0.135-0.525 (He)	850	0.35	ambient air	100 mL min^{-1} He	0-3.3	64
				0.3-0.27		100 mL min^{-1} CO_2	3.3-13.3	
				0.3		100 mL min^{-1} He	13.3-16.7	
$SrFe_{0.8}Mo_{0.2}O_{3-\delta}$	750-900	0.148-0.27 (He)	850	0.21	ambient air	100 mL min^{-1} He	0-3.3	64
				0.15		100 mL min^{-1} CO_2	3.3-13.3	
				0.16		100 mL min^{-1} He	13.3-16.7	
$SrFe_{0.8}W_{0.2}O_{3-\delta}$	750-900	0.149-0.25 (He)	850	0.22	ambient air	100 mL min^{-1} He	0-3.3	64
				0.17		100 mL min^{-1} CO_2	3.3-13.3	
				0.19		100 mL min^{-1} He	13.3-16.7	
$BaCo_{0.7}Fe_{0.26}Zr_{0.04}O_{3-\delta}$	750-925	1.32-2.65 (He)	925	2.65	300 mL min^{-1} air	100 mL min^{-1} He	0-10	65
				1.8-0.5		85 mL min^{-1} He + 15 mL min^{-1} CO_2	10-20	
				0.13-0.03		50 mL min^{-1} He + 50 mL min^{-1} CO_2	20-30	
				2.65		100 mL min^{-1} He	30-40	

Table 2.1 CO_2-resistance and performance of perovskite membranes (continued)

Materials	Instantaneous performance		Long term CO_2 test					Ref.
	T (°C)	$J(O_2)$ (mL min^{-1} cm^{-2})	T (°C)	$J(O_2)$ (mL min^{-1} cm^{-2})	Feed side	Permeate side	Time (h)	
$BaCo_{0.7}Fe_{0..24}Zr_{0.06}O_{3-\delta}$	750-925	1.36-2.7 (He)	925	2.7	300 mL min^{-1} air	100 mL min^{-1} He	0-10	65
				2.12-0.85		85 mL min^{-1} He + 15 mL min^{-1} CO_2	10-20	
				0.25-0.08		50 mL min^{-1} He + 50 mL min^{-1} CO_2	20-30	
				2.7		100 mL min^{-1} He	30-40	
$BaCo_{0.7}Fe_{0.22}Zr_{0.08}O_{3-\delta}$	750-925	1.3-2.53 (He)	925	2.53	300 mL min^{-1} air	100 mL min^{-1} He	0-10	65
				1.88-1.0		85 mL min^{-1} He + 15 mL min^{-1} CO_2	10-20	
				0.31-0.14		50 mL min^{-1} He + 50 mL min^{-1} CO_2	20-30	
				2.53		100 mL min^{-1} He	30-40	
$BaCo_{0.7}Fe_{0.2}Zr_{0.1}O_{3-\delta}$	750-925	1.26-2.43 (He)	925	2.43	300 mL min^{-1} air	100 mL min^{-1} He	0-10	65
				1.95-1.15		85 mL min^{-1} He + 15 mL min^{-1} CO_2	10-20	
				0.37-0.19		50 mL min^{-1} He + 50 mL min^{-1} CO_2	20-30	
				2.43		100 mL min^{-1} He	30-40	

Table 2.1 CO_2-resistance and performance of perovskite membranes (continued)

| Materials | Instantaneous performance | | | | Long term CO_2 test | | | Ref. |
	T (°C)	$J(O_2)$ (mL min^{-1} cm^{-2})	T (°C)	$J(O_2)$ (mL min^{-1} cm^{-2})	Feed side	Permeate side	Time (h)	
$BaCo_{0.7}Fe_{0.18}Zr_{0.12}O_{3-\delta}$	750-925	1.16-2.2 (He)	925	2.2	300 mL min^{-1} air	100 mL min^{-1} He	0-10	65
				1.63-0.87		85 mL min^{-1} He + 15 mL min^{-1} CO_2	10-20	
				0.24-0.125		50 mL min^{-1} He + 50 mL min^{-1} CO_2	20-30	
				2.2		100 mL min^{-1} He	30-40	
$Ba_{0.5}Sr_{0.5}Co_{0.78}Fe_{0.2}W_{0.02}O_{3-\delta}$	750-950	1.0-2.5 (He)	800	1.375	200 mL min^{-1} air	50 mL min^{-1} He	0-0.25	66
				0.75		40 mL min^{-1} He + 10 mL min^{-1} CO_2	0.25-1.75	
				0.18		50 mL min^{-1} CO_2	1.75-2.0	
$BaBi_{0.05}Co_{0.8}Ta_{0.15}O_{3-\delta}$	775-900	1.5-2.86 (He)	950	3.57	180 mL min^{-1} air	100 mL min^{-1} He	0-1.3	67
				3.4-3.3		90 mL min^{-1} He + 10 mL min^{-1} CO_2	1.3-2.75	
				3.1-2		80 mL min^{-1} He + 20 mL min^{-1} CO_2	2.75-6.7	
				1.5-0.9		60 mL min^{-1} He + 40 mL min^{-1} CO_2	6.7-7.75	
				0.5-0.2		20 mL min^{-1} He + 80 mL min^{-1} CO_2	7.75-9.4	

Table 2.1 CO_2-resistance and performance of perovskite membranes (continued)

| Materials | Instantaneous performance | | | | Long term CO_2 test | | | Ref. |
	T (°C)	$J(O_2)$ (mL min^{-1} cm^{-2})	T (°C)	$J(O_2)$ (mL min^{-1} cm^{-2})	Feed side	Permeate side	Time (h)	
$La_{0.6}Sr_{0.4}Co_{0.2}Fe_{0.8}O_{3-\delta}$	600-1000	0.07-6.8 (Ar)	900	2.5	300 mL min^{-1} air	150 mL min^{-1} Ar + 150 mL min^{-1} CO_2	0-41.7	68
$La_{0.6}Sr_{0.4}Co_{0.2}Fe_{0.8}O_{3-\delta}$	750-1000	0.45-4.32 (Ar)						69
	900	2.02 (CO_2)						
		2 (Ar+CO_2)						
		2.1 (Ar+CO_2)						
		2.25 (Ar+CO_2)						
		2.95 (Ar)						
	1000	5.52 (CO_2)						
		5.2 (Ar+CO_2)						
		5 (Ar+CO_2)						
		4.9 (Ar+CO_2)						
		4.95 (Ar)						

Table 2.1 CO_2-resistance and performance of perovskite membranes (continued)

Materials	Instantaneous performance		Long term CO_2 test					Ref.
	T (^{o}C)	$J(O_2)$ (mL min^{-1} cm^{-2})	T (^{o}C)	$J(O_2)$ (mL min^{-1} cm^{-2})	Feed side	Permeate side	Time (h)	
$La_{0.6}Sr_{0.4}Co_{0.2}Fe_{0.8}O_{3-\delta}$	800-1000	1.9-7.0 (Ar)	1000	1.41-1.25	300 mL min^{-1} air	150 mL min^{-1} Ar + 150 mL min^{-1} CO_2	0-90	70
		0.15-7.2 (CO_2)						
$SrFe_{0.9}Ta_{0.1}O_{3-\delta}$	750-950	0.17-0.63 (He)	900	0.3	120 mL min^{-1} air	60 mL min^{-1} CO_2	0-130	71
		0.12-0.38 (CO_2)						
		0.41-1.51 (CO_2)						
$SrFe_{0.8}Sb_{0.2}O_{3-\delta}$	750-950	0.12-0.47 (He)		0.22	120 mL min^{-1} air	60 mL min^{-1} CO_2	0-130	71
		0.09-0.32 (CO_2)						
		0.3-1.3 (CO_2)						
$Pr_{0.6}Sr_{0.4}Co_{0.2}Fe_{0.8}O_{3-\delta}$	750-1000	0.1-1.3 (He)	1000	1.3	150 mL min^{-1} air	50 mL min^{-1} He	0-125	72
		0.08-1.24 (CO_2)	1000	1.24		50 mL min^{-1} CO_2	125-175	
			850	0.42			175-215	
			1000	1.24			215-340	
			850	0.42			340-450	

Table 2.1 CO_2-resistance and performance of perovskite membranes (continued)

Materials	Instantaneous performance		Long term CO_2 test					Ref.
	T (^oC)	$J(O_2)$ (mL min^{-1} cm^{-2})	T (^oC)	$J(O_2)$ (mL min^{-1} cm^{-2})	Feed side	Permeate side	Time (h)	
$La_{0.6}Sr_{0.4}Co_{0.2}Fe_{0.8}O_{3-\delta}$	800-1000	0.1-3.15 (He)	950	2.6	200 mL min^{-1} air	151 mL min^{-1} He	0-7.8	53
		0.01-1.2 (CO_2)		0.79		151 mL min^{-1} CO_2	7.8-31	
				2.44			31-40	
				0.78			40-59	
			900	0.2			59-79	
				0.78			79-100	
$Sm_{0.6}Ca_{0.4}CoO_{3-\delta}$			950	0.02	100 mL min^{-1} air	30 mL min^{-1} He	0-100	73
				0.01		30 mL min^{-1} CO_2	100-200	
$Sm_{0.6}Ca_{0.4}FeO_{3-\delta}$			950	0.0	100 mL min^{-1} air	30 mL min^{-1} He	0-100	73
				0.017		30 mL min^{-1} CO_2	100-200	

Table 2.2 CO_2-resistance and performance of dual-phase membranes

Materials	Instantaneous performance		Long term CO_2 test					Ref.
	T (°C)	$J(O_2)$ (mL min^{-1} cm^{-2})	T (°C)	$J(O_2)$ (mL min^{-1} cm^{-2})	Feed side	Permeate side	Time (h)	
$Ce_{0.85}Gd_{0.1}Cu_{0.05}O_{2-\delta}$-$La_{0.6}Ca_{0.4}FeO_{3-\delta}$ (75:25 wt.%)	800-950	0.25-0.87 (He)	800	0.15	100 mL min^{-1} air	30 mL min^{-1} CO_2	0-50	61
		0.15-0.7 (CO_2)	900	0.47			50-100	
		0.11-0.52 (He)						
		0.06-0.46 (CO_2)						
$Ce_{0.9}Gd_{0.1}O_{2-\delta}$-$Ba_{0.5}Sr_{0.5}Co_{0.8}Fe_{0.2}O_{3-\delta}$ (60:40 wt.%)	825-975	0.20-0.85 (CO_2)	950	0.59	150 mL min^{-1} air	40 mL min^{-1} CO_2	0-72	132
				0.67			150-250	
$Ce_{0.8}Gd_{0.2}O_{2-\delta}$-$NiFe_2O_4$ (40:60 vol.%)	900-1000	0.11-0.31 (He)	1000	0.27	150 mL min^{-1} air	29 mL min^{-1} CO_2 + 1 mL min^{-1} Ne	0-40	133
		0.09-0.27 (CO_2)		0.3			40-100	
		0.08-0.2 (He)						
		0.06-0.17 (CO_2)						
$Ce_{0.8}Gd_{0.2}O_{2-\delta}$-$NiFe_2O_4$ (40:60 vol.%)	900-1000		1000	0.29-0.31	150 mL min^{-1} air	29 mL min^{-1} He + 1 mL min^{-1} Ne	0-36.667	134
				0.27-0.31		29 mL min^{-1} CO_2 + 1 mL min^{-1} Ne	0-101.667	

Table 2.2 CO_2-resistance and performance of dual-phase membranes (continued)

Materials	Instantaneous performance		Long term CO_2 test					Ref.
	T (^{o}C)	$J(O_2)$ (mL min^{-1} cm^{-2})	T (^{o}C)	$J(O_2)$ (mL min^{-1} cm^{-2})	Feed side	Permeate side	Time (h)	
$Ce_{0.8}Gd_{0.2}O_{2-\delta}$-$PrBaCo_{0.5}Fe_{1.5}O_{5+\delta}$ (60:40 wt.%)	925	0.3 (CO_2)	925	0.40-0.38	300 mL min^{-1} air	50% CO_2 + 50% He	0-1	135
		0.33 (CO_2)		0.39			1-12	
		0.35 (CO_2)		0.38-0.37		100% CO_2	12.5-14	
		0.36 (CO_2)		0.36			14-25	
		0.38 (CO_2)						
		0.33 (CO_2)						
		0.35 (CO_2)						
		0.37 (CO_2)						
		0.38 (CO_2)						
		0.4 (CO_2)						

Table 2.2 CO_2-resistance and performance of dual-phase membranes (continued)

Materials	Instantaneous performance		Long term CO_2 test					Ref.
	T (°C)	$J(O_2)$ (mL min⁻¹ cm⁻²)	T (°C)	$J(O_2)$ (mL min⁻¹ cm⁻²)	Feed side	Permeate side	Time (h)	
$Ce_{0.9}Gd_{0.1}O_{1.95-\delta}$-$Zn_{0.96}Al_{0.02}Ga_{0.02}O_{1.02}$ (50:50 vol.%)	700-940	0.06-0.39 (N_2)	860	0.22	100 mL min⁻¹ air	150 mL min⁻¹ N_2	0-30	136
		0.057-0.34 (CO_2)		0.19		150 mL min⁻¹ CO_2	30-100	
				0.18		150 mL min⁻¹ CO_2	100-130	
				0.22		150 mL min⁻¹ N_2	130-275	
				0.18-0.16		150 mL min⁻¹ CO_2	275-480	
			940	0.27		150 mL min⁻¹ CO_2	480-580	
$Ce_{0.9}Pr_{0.1}O_{2-\delta}$-$Pr_{0.6}Sr_{0.4}Fe_{0.5}Co_{0.5}O_{3-\delta}$ (60:40 wt.%)	800-1000	0.24-1.08 (He)	950	0.7-0.84	150 mL min⁻¹ air	50 mL min⁻¹ He	0-40	137
		0.11-1.01 (CO_2)	950	0.7		50 mL min⁻¹ CO_2	60-350	
			1000	1.04		50 mL min⁻¹ CO_2	350-450	
			950	0.7		50 mL min⁻¹ CO_2	450-510	
			800	0.19-0.13		50 mL min⁻¹ CO_2	0-300	

Table 2.2 CO_2-resistance and performance of dual-phase membranes (continued)

Materials	Instantaneous performance		Long term CO_2 test					Ref.
	T (°C)	$J(O_2)$ (mL min^{-1} cm^{-2})	T (°C)	$J(O_2)$ (mL min^{-1} cm^{-2})	Feed side	Permeate side	Time (h)	
$Ce_{0.8}Sm_{0.2}O_{1.9}$-$Sm_{0.8}Ca_{0.2}Mn_{0.5}Co_{0.5}O_3$ (75:25 vol.%)	800-940	0.13-0.61 (He)	940	0.39-0.46	100 mL min^{-1} air	30 mL min^{-1} He	0-10	138
		0.1-0.51 (CO_2)		0.46			10-155	
				0.41		30 mL min^{-1} CO_2	155-220	
			850	0.2			220-475	
$Ce_{0.8}Sm_{0.2}O_{1.9}$-$SmMn_{0.5}Co_{0.5}O_3$ (75:25 vol.%)	800-940	0.15-0.52 (He)	940	0.36-0.42	100 mL min^{-1} air	30 mL min^{-1} He	0-45	139
		0.13-0.48 (CO_2)		0.42			45-155	
				0.37-0.39		30 mL min^{-1} CO_2	155-165	
				0.39			165-220	
			850	0.21			220-475	
$Ce_{0.8}Tb_{0.2}O_{2-\delta}$-$NiFe_2O_4$ (40:60 vol.%)	700-1000	0.015-0.17 (He)	900	0.13	synthetic air	CO_2 (No flow rate)	0-50	140
		0.01-0.2 (CO_2)		0.14			50-76	
	900-1000	0.028-0.115 (CO_2)						

Table 2.2 CO_2-resistance and performance of dual-phase membranes (continued)

Materials	Instantaneous performance		Long term CO_2 test					Ref.
	T (°C)	$J(O_2)$ (mL min^{-1} cm^{-2})	T (°C)	$J(O_2)$ (mL min^{-1} cm^{-2})	Feed side	Permeate side	Time (h)	
$Ce_{0.9}Nd_{0.1}O_{2-\delta}$-$Nd_{0.6}Sr_{0.4}FeO_{3-\delta}$ (60:40 wt.%)	850-950	0.21-0.48 (CO_2)	950	0.48	150 mL min^{-1} air	49 mL min^{-1} CO_2 + 1 mL min^{-1} Ne	0-150	141
$Ce_{0.8}Sm_{0.2}O_{2-\delta}$-$Ba_{0.95}La_{0.05}Fe_{0.85}Zr_{0.15}O_{3-\delta}$ (60:40 wt.%)	750-925	0.1-0.3 (He)	925	0.3	300 mL min^{-1} air	100 mL min^{-1} He	0-12	142
				0.275		85 mL min^{-1} He + 15 mL min^{-1} CO_2	12-26	
				0.255		50 mL min^{-1} He + 50 mL min^{-1} CO_2	26-39	
				0.24		50 mL min^{-1} He + 50 mL min^{-1} CO_2	39-52	
				0.3		100 mL min^{-1} He	52-65	
			925	0.3	300 mL min^{-1} air	100 mL min^{-1} He	0-18	
				0.24		100 mL min^{-1} CO_2	18-105	

Table 2.2 CO_2-resistance and performance of dual-phase membranes (continued)

Materials	Instantaneous performance				Long term CO_2 test			Ref.
	T (°C)	$J(O_2)$ (mL min^{-1} cm^{-2})	T (°C)	$J(O_2)$ (mL min^{-1} cm^{-2})	Feed side	Permeate side	Time (h)	
$Y_{0.8}Ca_{0.2}Cr_{0.8}Co_{0.2}O_3$-$Sm_{0.2}Ce_{0.8}O_{1.9}$ (50:50 wt.%)	700-950	0.58-6.7 (H_2+N_2)	950	3.08	30 mL min^{-1} air	30 mL min^{-1} (1.5% H_2 + 48.5% N_2 + 50% CO_2)	0-350	143
		0.37-3.08 (H_2+N_2+CO_2)						
		0.05-0.34 (N_2)						
$Ce_{0.8}Gd_{0.2}O_{2-\delta}$-$Ba_{0.95}La_{0.05}Fe_{0.9}Nb_{0.1}O_{3-\delta}$ (60:40 wt.%)	925	0.275 (He)	925	0.20-0.19	300 mL min^{-1} air	100 mL min^{-1} CO_2	0-5	144
		0.23 (He+CO_2)		0.19			5-95	
		0.21 (He+CO_2)						
		0.195 (CO_2)						
		0.27 (He)						

Table 2.2 CO_2-resistance and performance of dual-phase membranes (continued)

Materials	Instantaneous performance				Long term CO_2 test			Ref.
	T (°C)	$J(O_2)$ (mL min^{-1} cm^{-2})	T (°C)	$J(O_2)$ (mL min^{-1} cm^{-2})	Feed side	Permeate side	Time (h)	
$Sm_{0.5}Sr_{0.5}Cu_{0.2}Fe_{0.8}O_{3-\delta}$-$Ce_{0.8}Sm_{0.2}O_{2-\delta}$ (40:60 wt.%)	800-1000	0.29-1.27 (He)	1000	1.27	150 mL min^{-1} air	49 mL min^{-1} He + 1 mL min^{-1} Ne	0-25	145
		0.08-1.12 (CO_2)	1000	1.15-1.11		49 mL min^{-1} CO_2 + 1 mL min^{-1} Ne	25-75	
			950	0.70-0.67		49 mL min^{-1} CO_2 + 1 mL min^{-1} Ne	75-200	
			900	0.29-0.25		49 mL min^{-1} CO_2 + 1 mL min^{-1} Ne	200-290	
$Sm_{0.3}Sr_{0.7}Cu_{0.2}Fe_{0.8}O_{3-\delta}$-$Ce_{0.8}Sm_{0.2}O_{2-\delta}$ (40:60 wt.%)	800-1000	0.34-1.35 (He)	1000	1.35	150 mL min^{-1} air	49 mL min^{-1} He + 1 mL min^{-1} Ne	0-40	145
		0.11-1.15 (CO_2)	1000	1.17		49 mL min^{-1} CO_2 + 1 mL min^{-1} Ne	40-115	
			950	0.77-0.70		49 mL min^{-1} CO_2 + 1 mL min^{-1} Ne	115-155	
			900	0.46-0.38		49 mL min^{-1} CO_2 + 1 mL min^{-1} Ne	155-230	

Table 2.2 CO_2-resistance and performance of dual-phase membranes (continued)

| Materials | Instantaneous performance | | | Long term CO_2 test | | | | Ref. |
	T (°C)	$J(O_2)$ (mL min^{-1} cm^{-2})	T (°C)	$J(O_2)$ (mL min^{-1} cm^{-2})	Feed side	Permeate side	Time (h)	
$Ce_{0.9}Pr_{0.1}O_{2-\delta}$-$Pr_{0.6}Sr_{0.4}FeO_{3-\delta}$ (60:40 wt.%)	850-950	0.1-0.26 (He)	950	0.18	150 mL min^{-1} air	29 mL min^{-1} CO_2 + 1 mL min^{-1} Ne	0-137.5	146
		0.06-0.17 (CO_2)	1000	0.28			140-163	
		2.2-4.4 (CH_4)	950	4.4		7.32 mL min^{-1} CH_4 + 1 mL min^{-1} Ne	0-100	
$Ce_{0.9}Gd_{0.1}O_{2-\delta}$-$La_{0.7}Sr_{0.3}MnO_{3\pm\delta}$ (80:20 vol.%)	700-850	0.4-1.7 (He)	800	1.7	synthetic air	400 mL min^{-1} He	0-4	147
				1.21-0.5		200 mL min^{-1} He + 200 mL min^{-1} CO_2	4-88	
				0.43-0.3		400 mL min^{-1} CO_2	88-150	
			800	0.65	synthetic air	400 mL min^{-1} He	0-7	
				0.32-0.28		400 mL min^{-1} CO_2	7-100	
			800	0.48	synthetic air	400 mL min^{-1} He	0-7	
				0.44		400 mL min^{-1} CO_2	7-100	

Table 2.2 CO_2-resistance and performance of dual-phase membranes (continued)

Materials	Instantaneous performance			Long term CO_2 test				Ref.
	T (°C)	$J(O_2)$ (mL min^{-1} cm^{-2})	T (°C)	$J(O_2)$ (mL min^{-1} cm^{-2})	Feed side	Permeate side	Time (h)	
$Ce_{0.9}Gd_{0.1}O_{1.95}$-$(La_{0.8}Sr_{0.2})_{0.95}MnO_{3-\delta}$ (60:40 vol.%)	875-950	0.025-0.104 (He)						148
		0.024-0.104 (CO_2)						
	875-950	0.323-0.780 (He)						
		0.251-0.659 (CO_2)						
$Ce_{0.8}Sm_{0.2}O_{2-\delta}$-$La_{0.9}Sr_{0.1}FeO_{3-\delta}$ (70:30 vol.%)	800-1000	0.045-0.329 (He)	900	0.15	ambient air	40 mL min^{-1} He	0-150	149
				0.15		40 mL min^{-1} CO_2	150-300	
$Mn_{1.5}Co_{1.5}O_{4-\delta}$-$Ce_{0.9}Pr_{0.1}O_{2-\delta}$ (40:60 wt.%)	900-1000	0.26-0.48 (CO_2)	1000	0.22	200 mL min^{-1} air	29 mL min^{-1} He + 1 mL min^{-1} Ne	0-1.25	150
				0.2		29 mL min^{-1} CO_2 + 1 mL min^{-1} Ne	1.25-3.0	
				0.2		29 mL min^{-1} He + 1 mL min^{-1} Ne	3.0-4.6	
				0.2		29 mL min^{-1} CO_2 + 1 mL min^{-1} Ne	4.6-6.0	
				0.2	200 mL min^{-1} air	29 mL min^{-1} CO_2 + 1 mL min^{-1} Ne	0-60	

Table 2.2 CO_2-resistance and performance of dual-phase membranes (continued)

Materials	Instantaneous performance			Long term CO_2 test				Ref.
	T (°C)	$J(O_2)$ (mL min^{-1} cm^{-2})	T (°C)	$J(O_2)$ (mL min^{-1} cm^{-2})	Feed side	Permeate side	Time (h)	
Fe_2O_3-$Ce_{0.9}Gd_{0.1}O_{2-\delta}$ (40:60 wt.%)	900-1000	0.06-0.18 (He)	1000	0.2	150 mL min^{-1} air	29 mL min^{-1} CO_2 + 1 mL min^{-1} Ne	0-150	151
$Ce_{0.8}Sm_{0.2}O_{2-\delta}$-$Sm_{0.8}Ca_{0.2}CoO_3$ (75:25 wt.%)	800-950	0.0675-0.167 (He)	950	0.23-0.16	100 mL min^{-1} air	He	0-100	152
		0.055-0.168 (CO_2)		0.16		CO_2	100-200	
$Ce_{0.8}Sm_{0.2}O_{2-\delta}$-$Sm_{0.6}Ca_{0.4}CoO_3$ (75:25 wt.%)	800-950	0.0825-0.18 (He)	950	0.13-0.18	100 mL min^{-1} air	He	0-100	152
		0.075-0.188 (CO_2)		0.19		CO_2	100-200	
$Ce_{0.8}Sm_{0.2}O_{2-\delta}$-$SrCo_{0.9}Nb_{0.1}O_{3-\delta}$ (60:40 wt.%)	800-950	0.51-1.54 (He)	950	0.49-0.53	120 mL min^{-1} air	60 mL min^{-1} CO_2	0-120	153
$Ce_{0.9}Gd_{0.1}O_{2-\delta}$-$La_{0.7}Sr_{0.3}MnO_3$			700	0.55	400 mL min^{-1} air	He	0-7	154
				0.42		50% He + 50% CO_2	7-17	
				0.55		He	17-21	

Table 2.2 CO_2-resistance and performance of dual-phase membranes (continued)

Materials	Instantaneous performance				Long term CO_2 test			Ref.
	T (°C)	$J(O_2)$ (mL min^{-1} cm^{-2})	T (°C)	$J(O_2)$ (mL min^{-1} cm^{-2})	Feed side	Permeate side	Time (h)	
$Y_{0.08}Zr_{0.92}O_{2-\delta}$-$La_{0.7}Sr_{0.3}MnO_3$	800-950	0.15-0.5 (He)	900	0.28	100 mL min^{-1} air	100 mL min^{-1} He	0-50	155
				0.27		50 mL min^{-1} He + 50 mL min^{-1} CO_2	50-200	
$NiFe_2O_4$-$Ce_{0.8}Tb_{0.2}O_{2-\delta}$ (50:50 vol.%)	750-1000	0.034-0.34 (Ar)	850	0.11	100 mL min^{-1} air	150 mL min^{-1} Ar	0-4	156
		0.02-0.21 (CO_2)		0.13-0.14		150 mL min^{-1} CO_2	4-44	
				0.11		150 mL min^{-1} Ar	44-50	
$Nd_{0.6}Sr_{0.4}Al_{0.2}Fe_{0.8}O_{3-\delta}$-$Ce_{0.9}Nd_{0.1}O_{2-\delta}$ (40:60 wt.%)	800-1000	0.08-0.6 (He)	1000	0.61	150 mL min^{-1} air	49 mL min^{-1} He + 1 mL min^{-1} Ne	0-60	157
		0.02-0.52 (CO_2)	1000	0.52		49 mL min^{-1} CO_2 + 1 mL min^{-1} Ne	60-85	
			950	0.31			85-125	
			900	0.15			125-225	

Materials	Instantaneous performance		Long term CO_2 test					Ref.
	T (°C)	$\mathbf{\mathit{J}}(O_2)$ (mL min^{-1} cm^{-2})	T (°C)	$\mathbf{\mathit{J}}(O_2)$ (mL min^{-1} cm^{-2})	Feed side	Permeate side	Time (h)	
$Nd_{0.5}Sr_{0.5}Al_{0.2}Fe_{0.8}O_{3-\delta}$-$Ce_{0.8}Nd_{0.2}O_{2-\delta}$ (40:60 wt.%)	800-1000	0.15-1.0 (He)	1000	1	150 mL min^{-1} air	49 mL min^{-1} He + 1 mL min^{-1} Ne	0-50	157
		0.03-0.81 (CO_2)	1000	0.81		49 mL min^{-1} CO_2 + 1 mL min^{-1} Ne	50-75	
			950	0.5			75-170	
			900	0.24-0.19			170-300	
$Ce_{0.8}Sm_{0.2}O_{1.9}$-$Sm_{0.6}Ca_{0.4}CoO_{3-\delta}$ (75:25 wt.%)			950	0.1-0.14	100 mL min^{-1} air	30 mL min^{-1} He	0-100	73
				0.14-0.16		30 mL min^{-1} CO_2	100-200	
$Ce_{0.8}Sm_{0.2}O_{1.9}$-$Sm_{0.6}Ca_{0.4}CoO_{3-\delta}$ (67:33 wt.%)			950	0.45-0.55	100 mL min^{-1} air	30 mL min^{-1} He	0-100	73
				0.4		30 mL min^{-1} CO_2	100-200	
$Ce_{0.8}Sm_{0.2}O_{1.9}$-$Sm_{0.6}Ca_{0.4}FeO_{3-\delta}$ (75:25 wt.%)			950	0.36-0.45	100 mL min^{-1} air	30 mL min^{-1} He	0-100	73
				0.37		30 mL min^{-1} CO_2	100-200	

Table 2.2 CO_2-resistance and performance of dual-phase membranes (continued)

Materials	Instantaneous performance		Long term CO_2 test					Ref.
	T (°C)	$J(O_2)$ (mL min^{-1} cm^{-2})	T (°C)	$J(O_2)$ (mL min^{-1} cm^{-2})	Feed side	Permeate side	Time (h)	
$Ce_{0.8}Sm_{0.2}O_{1.9}$-$Sm_{0.6}Ca_{0.4}FeO_{3-\delta}$ (67:33 wt.%)			950	0.22-0.41	100 mL min^{-1} air	30 mL min^{-1} He	0-100	73
				0.34		30 mL min^{-1} CO_2	100-200	
$Ce_{0.85}Sm_{0.15}O_{1.925}$-$Sm_{0.6}Sr_{0.4}Al_{0.3}Fe_{0.7}O_3$ (75:25 wt.%)	800-950	0.34-0.7 (He)	950	0.7	100 mL min^{-1} air	30 mL min^{-1} He	0-140	158
				0.63		30 mL min^{-1} CO_2	140-280	
		0.21-0.43 (He)		0.4		30 mL min^{-1} He	0-140	
		0.2-0.34 (He)		0.35	100 mL min^{-1} air	30 mL min^{-1} He	0-140	
$Pr_{0.1}Gd_{0.1}Ce_{0.8}O_{2-\delta}$-$CoFe_2O_4$ (50:50 wt.%)	900-1000	0.15-0.54 (He)	950	0.36	100 mL min^{-1} air	150 mL min^{-1} CO_2	0-200	159
		0.26-0.84 (He)						

Table 2.3 CO_2-resistance and performance of other membranes

Materials	Instantaneous performance		Long term CO_2 test					Ref.
	T (°C)	$J(O_2)$ (mL min^{-1} cm^{-2})	T (°C)	$J(O_2)$ (mL min^{-1} cm^{-2})	Feed side	Permeate side	Time (h)	
$La_2NiO_{4+\delta}$			900	0.39	150 mL min^{-1} air	29 mL min^{-1} He	0-6.667	40
				0.22		29 mL min^{-1} CO_2	6.667-100	
$(Nd_{0.9}La_{0.1})_2(Ni_{0.74}Cu_{0.21}Al_{0.05})O_{4+\delta}$	975	0.5 (He)	975	0.5	150 mL min^{-1} air	30 mL min^{-1} He	0-100	222
		0.39 (CO_2)		0.4		30 mL min^{-1} CO_2	100-200	
				0.5		30 mL min^{-1} He	200-300	
				0.3		30 mL min^{-1} CO_2	0-260	
$(Pr_{0.9}La_{0.1})_2(Ni_{0.74}Cu_{0.21}Ga_{0.05})O_{4+\delta}$	850-975	0.17-0.34 (He) 0.15-0.32 (CO_2)	975	0.32	150 mL min^{-1} air	30 mL min^{-1} CO_2	0-230	219
$(Pr_{0.9}La_{0.1})_2(Ni_{0.74}Cu_{0.21}Ga_{0.05})O_{4+\delta}$			975	0.96	180 mL min^{-1} air	60 mL min^{-1} He	0-0.5	42
				0.9		60 mL min^{-1} CO_2	0.5-3.417	
				0.94		60 mL min^{-1} He	3.417-4.583	

Table 2.3 CO_2-resistance and performance of other membranes (continued)

Materials	Instantaneous performance		Long term CO_2 test				Time (h)	Ref.
	T (°C)	$J(O_2)$ (mL min^{-1} cm^{-2})	T (°C)	$J(O_2)$ (mL min^{-1} cm^{-2})	Feed side	Permeate side		
$(Pr_{0.9}La_{0.1})_{1.9}(Ni_{0.74}Cu_{0.21}Ga_{0.05})O_{4+\delta}$	800-975	0.36-0.89 (He)	975	0.89 (He)	150 mL min^{-1} air	30 mL min^{-1} He	0-1	221
		0.32-0.88 (CO_2)		0.88 (CO_2)		30 mL min^{-1} CO_2	1-3	
				0.89 (He)		30 mL min^{-1} He	3-4	
				0.88 (CO_2)		30 mL min^{-1} CO_2	4-6	
				0.89 (He)		30 mL min^{-1} He	6-7	
			900	0.69 (He)	150 mL min^{-1} air	30 mL min^{-1} He	0-1	
				0.66 (CO_2)		30 mL min^{-1} CO_2	1-3	
				0.69 (He)		30 mL min^{-1} He	3-4	
				0.66 (CO_2)		30 mL min^{-1} CO_2	4-6	
				0.69 (He)		30 mL min^{-1} He	6-7	

Table 2.3 CO_2-resistance and performance of other membranes (continued)

Materials	Instantaneous performance		Long term CO_2 test				Time (h)	Ref.
	T (°C)	$J(O_2)$ (mL min^{-1} cm^{-2})	T (°C)	$J(O_2)$ (mL min^{-1} cm^{-2})	Feed side	Permeate side		
$(Nd_{0.9}La_{0.1})_2(Ni_{0.74}Cu_{0.21}Ga_{0.05})O_{4+\delta}$			975	0.53 (He)	150 mL min^{-1} air	30 mL min^{-1} He	0-1	220
				0.48 (CO_2)		30 mL min^{-1} CO_2	1-2.5	
				0.53 (He)		30 mL min^{-1} He	2.5-4	
				0.48 (CO_2)		30 mL min^{-1} CO_2	4-5.5	
				0.53 (He)		30 mL min^{-1} He	5.5-6.5	
				0.48-0.53 (CO_2)	150 mL min^{-1} air	30 mL min^{-1} CO_2	0-420	

2.9 References

1. J. D. Figueroa, T. Fout, S. Plasynski, H. McIlvried and R. D. Srivastava, Int. J. Greenhouse Gas Control, 2008, 2, 9-20.

2. M. A. Habib, H. M. Badr, S. F. Ahmed, R. Ben-Mansour, K. Mezghani, S. Imashuku, G. J. la O', Y. Shao-Horn, N. D. Mancini, A. Mitsos, P. Kirchen and A. F. Ghoneim, Int. J. Energy Res., 2011, 35, 741-764.

3. R. Kneer, D. Toporov, M. Förster, D. Christ, C. Broeckmann, E. Pfaff, M. Zwick, S. Engels and M. Modigell, Energy Environ. Sci., 2010, 3, 198-207.

4. P. A. Armstrong, D. L. Bennett, E.P. (Ted) Foster and V. E. Stein, ITM oxygen for gasification, Air Products and Chemicals, Inc., Washington, D.C., 2004.

5. S. Engels, F. Beggel, M. Modigell and H. Stadler, J. Membr. Sci., 2010, 359, 93-101.

6. Y. Wei, W. Yang, J. Caro and H. Wang, Chem. Eng. J., 2013, 220, 185-203.

7. X. Dong, W. Jin, N. Xu and K. Li, Chem. Commun., 2011, 47, 10886-10902.

8. A. Thursfield and I. S. Metcalfe, J. Mater. Chem., 2004, 14, 2475-2485.

9. Y. Liu, X. Tan and K. Li, Catal. Rev. Sci. Eng., 2006, 48, 145-198.

10. W. Yang, H. Wang, X. Zhu and L. Lin, Top. Catal., 2005, 35, 155-167.

11. I. Riess, J. Power Sources, 2008, 175, 325-337.

12. M. Yano, A. Tomita, M. Sano and T. Hibino, Solid State Ionics, 2007, 177, 3351-3359.

13. T. Hibino, A. Hashimoto, T. Inoue, J.-i. Tokuno, S.-i. Yoshida and M. Sano, Science, 2000, 288, 2031-2033.

14. Y. Hao, Z. Shao, J. Mederos, W. Lai, D. Goodwin and S. Haile, Solid State Ionics, 2006, 177, 2013-2021.

15. J. Sunarso, S. Baumann, J. M. Serra, W. A. Meulenberg, S. Liu, Y. Lin and J. C. Diniz da Costa, J. Membr. Sci., 2008, 320, 13-41.

16. K. Zhang, J. Sunarso, Z. Shao, W. Zhou, C. Sun, S. Wang and S. Liu, RSC Adv., 2011, 1, 1661-1676.

17. A. Leo, S. Liu and J. C. Diniz da Costa, Int. J. Greenhouse Gas Control, 2009, 3, 357-367.

18. S. Smart, C. X. C. Lin, L. Ding, K. Thambimuthu and J. C. Diniz da Costa, Energy Environ. Sci., 2010, 3, 268-278.

19. D. D. Athayde, D. F. Souza, A. M. A. Silva, D. Vasconcelos, E. H. M. Nunes, J. C.

Diniz da Costa and W. L. Vasconcelos, Ceram. Int., 2016, 42, 6555-6571.

20. A. S. Bhalla, R. Guo and R. Roy, Mater. Res. Innovations, 2000, 4, 3-26.

21. H. D. Megaw, Acta Crystallogr., Sect. A: Found. Adv., 1974, A30, 605-606.

22. V. M. Goldschmidt, Naturwissenschaften, 1926, 14, 477-485.

23. R. D. Shannon, Acta Crystallogr., Sect. A: Found. Adv., 1976, A32, 751-767.

24. A. Feldhoff, J. Martynczuk, M. Arnold, M. Myndyk, I. Bergmann, V. Šepelák, W. Gruner, U. Vogt, A. Hähnel and J. Woltersdorf, J. Solid State Chem., 2009, 182, 2961-2971.

25. M. Arnold, Q. Xu, F. D. Tichelaar and A. Feldhoff, Chem. Mater., 2009, 21, 635-640.

26. T. Ishihara, H. Matsuda and Y. Takita, J. Am. Chem. Soc., 1994, 116, 3801-3803.

27. M. Arnold, H. Wang and A. Feldhoff, J. Membr. Sci., 2007, 293, 44-52.

28. M. Schulz, R. Kriegel and A. Kämpfer, J. Membr. Sci., 2011, 378, 10-17.

29. J. Yi and M. Schroeder, J. Membr. Sci., 2011, 378, 163-170.

30. J. Yi, M. Schroeder, T. Weirich and J. Mayer, Chem. Mater., 2010, 22, 6246-6253.

31. A. Brandão, J. F. Monteiro, A. V. Kovalevsky, D. P. Fagg, V. V. Kharton and J. R. Frade, Solid State Ionics, 2011, 192, 16-20.

32. H. Yokokawa, T. Kawada and M. Dokiya, J. Am. Ceram. Soc., 1989, 72, 2104-2110.

33. H. Yokokawa, N. Sakai, T. Kawada and M. Dokiya, J. Solid State Chem., 1991, 94, 106-120.

34. H. Yokokawa, N. Sakai, T. Kawada and M. Dokiya, Solid State Ionics, 1992, 52, 43-56.

35. H. Yokokawa, T. Kawada and M. Dokiya, J. Am. Ceram. Soc., 1989, 72, 152-153.

36. H. Yokokawa, N. Sakai, T. Kawada and M. Dokiya, J. Am. Ceram. Soc., 1990, 73, 649-658.

37. J. Martynczuk, K. Efimov, L. Robben and A. Feldhoff, J. Membr. Sci., 2009, 344, 62-70.

38. T. Klande, O. Ravkina and A. Feldhoff, J. Membr. Sci., 2013, 437, 122-130.

39. O. Czuprat, M. Arnold, S. Schirrmeister, T. Schiestel and J. Caro, J. Membr. Sci., 2010, 364, 132-137.

40. T. Klande, K. Efimov, S. Cusenza, K.-D. Becker and A. Feldhoff, J. Solid State Chem., 2011, 184, 3310-3318.

41. K. Efimov, T. Klande, N. Juditzki and A. Feldhoff, J. Membr. Sci., 2012, 389, 205-

215.

42. Y. Wei, O. Ravkina, T. Klande, H. Wang and A. Feldhoff, J. Membr. Sci., 2013, 429, 147-154.

43. I. Barin, Thermochemical data of pure substances, Wiley-VCH Verlag GmbH, Weinheim, Germany, 1995.

44. O. Ravkina, T. Klande and A. Feldhoff, J. Membr. Sci., 2015, 480, 31-38.

45. Q. Zeng, Y. Zuo, C. Fan and C. Chen, J. Membr. Sci., 2009, 335, 140-144.

46. W. Chen, C. Chen and L. Winnubst, Solid State Ionics, 2011, 196, 30-33.

47. W. Chen, C. Chen, H. J. M. Bouwmeester, A. Nijmeijer and L. Winnubst, J. Membr. Sci., 2014, 463, 166-172.

48. N. C. Jeong, J. S. Lee, E. L. Tae, Y. J. Lee and K. B. Yoon, Angew. Chem. Int. Ed., 2008, 47, 10128-10132.

49. H. Noller, J. A. Lercher and H. Vinek, Mater. Chem. Phys., 1988, 18, 577-593.

50. Y. Zhu, J. Sunarso, W. Zhou and Z. Shao, Appl. Catal., B, 2015, 172-173, 52-57.

51. R. L. Cook and A. F. Sammells, Solid State Ionics, 1991, 45, 311-321.

52. E. Y. Konysheva, X. Xu and J. T. Irvine, Adv. Mater., 2012, 24, 528-532.

53. X. Tan, N. Liu, B. Meng, J. Sunarso, K. Zhang and S. Liu, J. Membr. Sci., 2012, 389, 216-222.

54. G. Z. Cao, J. Appl. Electrochem., 1994, 24, 1222-1227.

55. Y.-S. Lin, W. Wang and J. Han, AIChE J., 1994, 40, 786-798.

56. Z. Homonnay , K. Nomura , G. Juhász , M. Gál , K. Sólymos, S. Hamakawa, T. Hayakawa and A. Vértes, Chem. Mater., 2002, 14, 1127-1135.

57. K. Nornura, Y. Ujihira, T. Hayakawa and K. Takehira, Appl. Catal., A, 1996, 137, 25-36.

58. A. Yan, B. Liu, Y. Dong, Z. Tian, D. Wang and M. Cheng, Appl. Catal., B, 2008, 80, 24-31.

59. W. Fang, F. Steinbach, C. Chen and A. Feldhoff, Chem. Mater., 2015, 27, 7820-7826.

60. J. Yi, S. Feng, Y. Zuo, W. Liu and C. Chen, Chem. Mater., 2005, 17, 5856-5861.

61. W. Fang, F. Liang, Z. Cao, F. Steinbach and A. Feldhoff, Angew. Chem. Int. Ed., 2015, 54, 4847-4850.

62. J. Yi, M. Schroeder and M. Martin, Chem. Mater., 2013, 25, 815-817.

6. J. Zhu, S. Guo, Z. Zhang, X. Jiang, Z. Liu and W. Jin, J. Membr. Sci., 2015, 485, 79-86.

64. Z. Zhang, D. Chen, F. Dong and Z. Shao, J. Membr. Sci., 2015, 495, 187-197.

65. W. Yao, H. Cheng, H. Zhao, X. Lu, X. Zou, S. Li and C. Li, J. Membr. Sci., 2016, 504, 251-262.

66. M. P. Popov, I. A. Starkov, S. F. Bychkov and A. P. Nemudry, J. Membr. Sci., 2014, 469, 88-94.

67. Q. Liao, Y. Wang, Y. Chen, Y. Wei and H. Wang, J. Membr. Sci., 2014, 468, 184-191.

68. C. Gaudillere, J. Garcia-Fayos and J. M. Serra, J. Mater. Chem. A, 2014, 2, 3828-3833.

69. J. M. Serra, J. Garcia-Fayos, S. Baumann, F. Schulze-Küppers and W. A. Meulenberg, J. Membr. Sci., 2013, 447, 297-305.

70. C. Gaudillere, J. Garcia-Fayos and J. M. Serra, ChemPlusChem, 2014, 79, 1720-1725.

71. J. Zhu, S. Guo, Z. Chu and W. Jin, J. Mater. Chem. A, 2015, 3, 22564-22573.

72. K. Partovi, B. Geppert, F. Liang, C. H. Rüscher and J. Caro, Chem. Mater., 2015, 27, 2911-2919.

73. H. Li, X. Zhu, Y. Liu, W. Wang and W. Yang, J. Membr. Sci., 2014, 462, 170-177.

74. Z. Shao, W. Yang, Y. Cong, H. Dong, J. Tong and G. Xiong, J. Membr. Sci., 2000, 172, 177-188.

75. H. Wang, Y. Cong and W. Yang, J. Membr. Sci., 2002, 210, 259-271.

76. S. Liu and G. R. Gavalas, J. Membr. Sci., 2005, 246, 103-108.

77. T. Klande, O. Ravkina and A. Feldhoff, J. Eur. Ceram. Soc., 2013, 33, 1129-1136.

78. M. A. Alaee, M. M. Movahednia and T. Mohammadi, J. Chem. Eng. Data, 2009, 54, 3082-3091.

79. S. Liu, X. Tan, Z. Shao and J. C. Diniz da Costa, AIChE J., 2006, 52, 3452-3461.

80. S. Baumann, J. M. Serra, M. P. Lobera, S. Escolástico, F. Schulze-Küppers and W. A. Meulenberg, J. Membr. Sci., 2011, 377, 198-205.

81. A. V. Kovalevsky, A. A. Yaremchenko, V. A. Kolotygin, F. M. M. Snijkers, V. V. Kharton, A. Buekenhoudt and J. J. Luyten, Solid State Ionics, 2011, 192, 677-681.

82. D. Han, X. Tan, Z. Yan, Q. Li and S. Liu, Ceram. Int., 2013, 39, 431-437.

83. X. Li, T. Kerstiens and T. Markus, J. Membr. Sci., 2013, 438, 83-89.

84. S. Baumann, F. Schulze-Küppers, S. Roitsch, M. Betz, M. Zwick, E. M. Pfaff, W. A. Meulenberg, J. Mayer and D. Stöver, J. Membr. Sci., 2010, 359, 102-109.

85. C. Buysse, A. Kovalevsky, F. Snijkers, A. Buekenhoudt, S. Mullens, J. Luyten, J.

Kretzschmar and S. Lenaerts, J. Membr. Sci., 2011, 372, 239-248.

86. A. V. Kovalevsky, A. A. Yaremchenko, V. A. Kolotygin, A. L. Shaula, V. V. Kharton, F. M. M. Snijkers, A. Buekenhoudt, J. R. Frade and E. N. Naumovich, J. Membr. Sci., 2011, 380, 68-80.

87. W. K. Hong and G. M. Choi, J. Membr. Sci., 2010, 346, 353-360.

88. F. Schulze-Küppers, S. Baumann, W. A. Meulenberg, D. Stöver and H. P. Buchkremer, J. Membr. Sci., 2013, 433, 121-125.

89. J. H. Park, J. P. Kim and S. H. Son, Energy Procedia, 2009, 1, 369-374.

90. A. Yan, M. Cheng, Y. Dong, W. Yang, V. Maragou, S. Song and P. Tsiakaras, Appl. Catal., B, 2006, 66, 64-71.

91. E. Bucher, A. Egger, G. B. Caraman and W. Sitte, J. Electrochem. Soc., 2008, 155, B1218-B1224.

92. Z. Yáng, A. S. Harvey and L. J. Gauckler, Scripta Mater., 2009, 61, 1083-1086.

93. A. Yan, M. Yang, Z. Hou, Y. Dong and M. Cheng, J. Power Sources, 2008, 185, 76-84.

94. A. Feldhoff, M. Arnold, J. Martynczuk, T. M. Gesing and H. Wang, Solid State Sci., 2008, 10, 689-701.

95. A. Feldhoff, J. Martynczuk and H. Wang, Prog. Solid State Chem., 2007, 35, 339-353.

96. A. M. Kalinkin, Russ. J. Phys. Chem. A, 2008, 82, 263-268.

97. K. Partovi, F. Liang, O. Ravkina and J. Caro, ACS Appl. Mater. Interfaces, 2014, 6, 10274-10282.

98. A. Waindich, A. Möbius and M. Müller, J. Membr. Sci., 2009, 337, 182-187.

99. P. Zeng, R. Ran, Z. Chen, H. Gu, Z. Shao, J. Dacosta and S. Liu, J. Membr. Sci., 2007, 302, 171-179.

100. D. Han, J. Wu, Z. Yan, K. Zhang, J. Liu and S. Liu, RSC Adv., 2014, 4, 19999-20004.

101. D. Schlehuber, E. Wessel, L. Singheiser and T. Markus, J. Membr. Sci., 2010, 351, 16-20.

102. M. F. Carolan, P. N. Dyer, S. A. Motika and P. B. Alba, United States Pat., 1998.

103. M. J. Shin and J. H. Yu, J. Membr. Sci., 2012, 401-402, 40-47.

104. S. K. Kim, M. J. Shin, J. Rufner, K. van Benthem, J. H. Yu and S. Kim, J. Membr. Sci., 2014, 462, 153-159.

105. V. Kharton, A. Kovalevsky, E. Tsipis, A. Viskup, E. Naumovich, J. Jurado and J.

Frade, J. Solid State Electrochem., 2002, 7, 30-36.

106. Y. He, X. Zhu and W. Yang, AIChE J., 2011, 57, 87-95.

107. Z. Shao, G. Xiong, H. Dong, W. Yang and L. Lin, Sep. Purif. Technol., 2001, 25, 97-116.

108. L. Ge, W. Zhou, R. Ran, S. Liu, Z. Shao, W. Jin and N. Xu, J. Membr. Sci., 2007, 306, 318-328.

109. Y. Zhu, Z. G. Chen, W. Zhou, S. Jiang, J. Zou and Z. Shao, ChemSusChem, 2013, 6, 2249-2254.

110. A. Yaremchenko, V. Kharton, A. Valente, F. Snijkers, J. Cooymans, J. Luyten and F. Marques, J. Membr. Sci., 2008, 319, 141-148.

111. J. Liu, H. Cheng, B. Jiang, X. Lu and W. Ding, Int. J. Hydrogen Energy, 2013, 38, 11090-11096.

112. Y. Cheng, H. Zhao, D. Teng, F. Li, X. Lu and W. Ding, J. Membr. Sci., 2008, 322, 484-490.

113. H. Luo, Y. Wei, H. Jiang, W. Yuan, Y. Lv, J. Caro and H. Wang, J. Membr. Sci., 2010, 350, 154-160.

114. J. Tong, W. Yang, R. Cai, B. Zhu and L. Lin, Catal. Lett., 2002, 78, 129-137.

115. M. Harada, K. Domen, M. Hara and T. Tatsumi, Chem. Lett., 2006, 35, 1326-1327.

116. Q. Li, X. Zhu, Y. He and W. Yang, Catal. Today, 2010, 149, 185-190.

117. H. Luo, B. Tian, Y. Wei, H. Wang, H. Jiang and J. Caro, AIChE J., 2010, 56, 604-610.

118. T. Nagai, W. Ito and T. Sakon, Solid State Ionics, 2007, 177, 3433-3444.

119. Z. Zhang, Y. Chen, M. O. Tade, Y. Hao, S. Liu and Z. Shao, J. Mater. Chem. A, 2014, 2, 9666-9674.

120. F. Yang, H. Zhao, J. Yang, M. Fang, Y. Lu, Z. Du, K. Świerczek and K. Zheng, J. Membr. Sci., 2015, 492, 559-567.

121. J. Tong, W. Yang, R. Cai, B. Zhu and L. Lin, Mater. Lett., 2002, 56, 958-962.

122. Z. Shao, G. Xiong, Y. Cong and W. Yang, J. Membr. Sci., 2000, 164, 167-176.

123. C. Zhang, H. Tian, D. Yang, J. Sunarso, J. Liu and S. Liu, ChemSusChem, 2016, 9, 505-512.

124. Z. Zhang, D. Chen, F. Dong, X. Xu, Y. Hao and Z. Shao, J. Membr. Sci., 2016, 519, 11-21.

125. X. Tan, Y. Liu and K. Li, AIChE J., 2005, 51, 1991-2000.

126. X. Tan, Z. Pang and K. Li, J. Membr. Sci., 2008, 310, 550-556.

127. Z. Wang, N. Yang, B. Meng and X. Tan, Ind. Eng. Chem. Res., 2009, 48, 510-516.

128. X. Tan, Z. Wang, H. Liu and S. Liu, J. Membr. Sci., 2008, 324, 128-135.

129. X. Tan, N. Liu, B. Meng and S. Liu, J. Membr. Sci., 2011, 378, 308-318.

130. H. Pan, L. Li, X. Deng, B. Meng, X. Tan and K. Li, J. Membr. Sci., 2013, 428, 198-204.

131. X. Zhu and W. Yang, in Membrane Science and Technology, ed. S. T. Oyama and S. M. Stagg-Williams, Elsevier, 2011, ch. 12, pp. 275-293.

132. J. Xue, Q. Liao, Y. Wei, Z. Li and H. Wang, J. Membr. Sci., 2013, 443, 124-130.

133. H. Luo, K. Efimov, H. Jiang, A. Feldhoff, H. Wang and J. Caro, Angew. Chem. Int. Ed., 2011, 50, 759-763.

134. H. Luo, H. Jiang, K. Efimov, J. Caro and H. Wang, AIChE J., 2011, 57, 2738-2745.

135. B. Jiang, H. Cheng, L. Luo, X. Lu and Z. Zhou, J. Mater. Sci. Technol., 2014, 30, 1174-1180.

136. S. Cheng, M. Søgaard, L. Han, W. Zhang, M. Chen, A. Kaiser and P. V. Hendriksen, Chem. Commun., 2015, 51, 7140-7143.

137. F. Liang, H. Luo, K. Partovi, O. Ravkina, Z. Cao, Y. Liu and J. Caro, Chem. Commun., 2014, 50, 2451-2454.

138. X. Zhu, H. Liu, Y. Cong and W. Yang, Chem. Commun., 2012, 48, 251-253.

139. X. Zhu, Q. Li, Y. He, Y. Cong and W. Yang, J. Membr. Sci., 2010, 360, 454-460.

140. M. Balaguer, J. García-Fayos, C. Solís and J. M. Serra, Chem. Mater., 2013, 25, 4986-4993.

141. H. Luo, T. Klande, Z. Cao, F. Liang, H. Wang and J. Caro, J. Mater. Chem. A, 2014, 2, 7780-7787.

142. H. Cheng, L. Luo, W. Yao, X. Lu, X. Zou and Z. Zhou, J. Membr. Sci., 2015, 492, 220-229.

143. K. J. Yoon and O. A. Marina, J. Membr. Sci., 2016, 499, 301-306.

144. H. Cheng, N. Zhang, X. Xiong, X. Lu, H. Zhao, S. Li and Z. Zhou, ACS Sustainable Chem. Eng., 2015, 3, 1982-1992.

145. K. Partovi, C. H. Rüscher, F. Steinbach and J. Caro, J. Membr. Sci., 2016, 503, 158-165.

146. H. Luo, H. Jiang, T. Klande, Z. Cao, F. Liang, H. Wang and J. Caro, Chem. Mater., 2012, 24, 2148-2154.

147. J. H. Joo, K. S. Yun, J. H. Kim, Y. Lee, C. Y. Yoo and J. H. Yu, ACS Appl. Mater.

Interfaces, 2015, 7, 14699-14707.

148. T. Liu, Y. Chen, S. Fang, L. Lei, Y. Wang, C. Ren and F. Chen, J. Membr. Sci., 2016, 520, 354-363.

149. Z. Wang, W. Sun, Z. Zhu, T. Liu and W. Liu, ACS Appl. Mater. Interfaces, 2013, 5, 11038-11043.

150. H. Luo, H. Jiang, T. Klande, F. Liang, Z. Cao, H. Wang and J. Caro, J. Membr. Sci., 2012, 423-424, 450-458.

151. H. Luo, H. Jiang, K. Efimov, F. Liang, H. Wang and J. Caro, Ind. Eng. Chem. Res., 2011, 50, 13508-13517.

152. H. Li, Y. Liu, X. Zhu, Y. Cong, S. Xu, W. Xu and W. Yang, Sep. Purif. Technol., 2013, 114, 31-37.

153. S. Guo, Z. Liu, J. Zhu, X. Jiang, Z. Song and W. Jin, Fuel Process. Technol., 2016, 154, 19-26.

154. J. H. Joo, K. S. Yun, C.-Y. Yoo and J. H. Yu, J. Mater. Chem. A, 2014, 2, 8174-8178.

155. K. S. Yun, C.-Y. Yoo, S.-G. Yoon, J. H. Yu and J. H. Joo, J. Membr. Sci., 2015, 486, 222-228.

156. J. Garcia-Fayos, M. Balaguer and J. M. Serra, ChemSusChem, 2015, 8, 4242-4249.

157. K. Partovi, M. Bittner and J. Caro, J. Mater. Chem. A, 2015, 3, 24008-24015.

158. X. Zhu, Y. Liu, Y. Cong and W. Yang, Solid State Ionics, 2013, 253, 57-63.

159. X. Bi, X. Meng, P. Liu, N. Yang, Z. Zhu, R. Ran and S. Liu, J. Membr. Sci., 2017, 522, 91-99.

160. P. Aldebert and J.-P. Traverse, J. Am. Ceram. Soc., 1985, 68, 34-40.

161. H. Inaba and H. Tagawa, Solid State Ionics, 1996, 83, 1-16.

162. S. Kuharuangrong, J. Power Sources, 2007, 171, 506-510.

163. K. Eguchi, T. Setoguchi, T. Inoue and H. Arai, Solid State Ionics, 1992, 52, 165-172.

164. S. Omar, E. D. Wachsman, J. L. Jones and J. C. Nino, J. Am. Ceram. Soc., 2009, 92, 2674-2681.

165. N. M. Sammes, G. A. Tompsett, H. Näfe and F. Aldinger, J. Eur. Ceram. Soc., 1999, 19, 1801-1826.

166. A. L. Shaula, V. V. Kharton and F. M. B. Marques, J. Eur. Ceram. Soc., 2004, 24, 2631-2639.

167. C. S. Chen, B. A. Boukamp, H. J. M. Bouwmeester, G. Z. Cao, H. Kruidhof, A. J.

A. Winnubst and A. J. Burggraaf, Solid State Ionics, 1995, 76, 23-28.

168. C. S. Chen, H. Kruidhof, H. J. M. Bouwmeester, H. Verweij and A. J. Burggraaf, Solid State Ionics, 1997, 99, 215-219.

169. J. Kim and Y. S. Lin, J. Membr. Sci., 2000, 167, 123-133.

170. J. Kim and Y. S. Lin, AIChE J., 2000, 46, 1521-1529.

171. K. Wu, S. Xie, G. S. Jiang, W. Liu and C. S. Chen, J. Membr. Sci., 2001, 188, 189-193.

172. V. V. Kharton, A. V. Kovalevsky, A. P. Viskup, F. M. Figueiredo, A. A. Yaremchenko, E. N. Naumovich and F. M. B. Marques, J. Electrochem. Soc., 2000, 147, 2814-2821.

173. B. Wang, J. Yi, L. Winnubst and C. Chen, J. Membr. Sci., 2006, 286, 22-25.

174. J. Yi, Y. Zuo, W. Liu, L. Winnubst and C. Chen, J. Membr. Sci., 2006, 280, 849-855.

175. C. Yang, Q. Xu, C. Liu, J. Liu, C. Chen and W. Liu, Mater. Lett., 2011, 65, 3365-3367.

176. W. Li, J. J. Liu and C. S. Chen, J. Membr. Sci., 2009, 340, 266-271.

177. H. Takamura, H. Sugai, M. Watanabe, T. Kasahara, A. Kamegawa and M. Okada, J. Electroceram., 2006, 17, 741-748.

178. M. Ramasamy, S. Baumann, J. Palisaitis, F. Schulze-Küppers, M. Balaguer, D. Kim, W. A. Meulenberg, J. Mayer, R. Bhave, O. Guillon, M. Bram and J. Stevenson, J. Am. Ceram. Soc., 2016, 99, 349-355.

179. A. L. Shaula, V. V. Kharton, F. M. B. Marques, A. V. Kovalevsky, A. P. Viskup and E. N. Naumovich, J. Solid State Electrochem., 2006, 10, 28-40.

180. Y. Lin, S. Fang, D. Su, K. S. Brinkman and F. Chen, Nat. Commun., 2015, 6, 6824.

181. Z. Zhang, W. Zhou, Y. Chen, D. Chen, J. Chen, S. Liu, W. Jin and Z. Shao, ACS Appl. Mater. Interfaces, 2015, 7, 22918-22926.

182. T. Chen, H. Zhao, N. Xu, Y. Li, X. Lu, W. Ding and F. Li, J. Membr. Sci., 2011, 370, 158-165.

183. T. Chen, H. Zhao, Z. Xie, L. Feng, X. Lu, W. Ding and F. Li, Int. J. Hydrogen Energy, 2012, 37, 5277-5285.

184. T. Chen, H. Zhao, Z. Xie, Y. Lu and N. Xu, Int. J. Hydrogen Energy, 2012, 37, 19133-19137.

185. M. B. Choi, S. Y. Jeon, H. J. Hwang, J. Y. Park and S. J. Song, Solid State Ionics, 2010, 181, 1680-1684.

186. Q. Li, X. Zhu, Y. He, Y. Cong and W. Yang, J. Membr. Sci., 2011, 367, 134-140.

187. X. Zhu, M. Li, H. Liu, T. Zhang, Y. Cong and W. Yang, J. Membr. Sci., 2012, 394-395, 120-130.

188. X. Zhu, H. Liu, Q. Li, Y. Cong and W. Yang, Solid State Ionics, 2011, 185, 27-31.

189. S. B. Adler, Chem. Rev., 2004, 104, 4791-4844.

190. P. Zeng, Z. Chen, W. Zhou, H. Gu, Z. Shao and S. Liu, J. Membr. Sci., 2007, 291, 148-156.

191. Z. Duan, M. Yang, A. Yan, Z. Hou, Y. Dong, Y. Chong, M. Cheng and W. Yang, J. Power Sources, 2006, 160, 57-64.

192. J. Xue, Q. Zheng, Y. Wei, K. Yuan, Z. Li and H. Wang, Ind. Eng. Chem. Res., 2012, 51, 4703-4709.

193. S. Cheng, H. Huang, S. Ovtar, S. B. Simonsen, M. Chen, W. Zhang, M. Søgaard, A. Kaiser, P. V. Hendriksen and C. Chen, ACS Appl. Mater. Interfaces, 2016, 8, 4548-4560.

194. J. E. ten Elshof, H. J. M. Bouwmeester and H. Verweij, Solid State Ionics, 1995, 81, 97-109.

195. J. E. ten Elshof, H. J. M. Bouwmeester and H. Verweij, Solid State Ionics, 1996, 89, 81-92.

196. M. Søgaard, P. Vang Hendriksen and M. Mogensen, J. Solid State Chem., 2007, 180, 1489-1503.

197. X. Zhu, H. Wang and W. Yang, J. Membr. Sci., 2008, 309, 120-127.

198. G. Zhu, X. Fang, C. Xia and X. Liu, Ceram. Int., 2005, 31, 115-119.

199. T. Chen, H. Zhao, Z. Xie, J. Wang, Y. Lu and N. Xu, J. Power Sources, 2013, 223, 289-292.

200. K. Zhang, L. H. Liu, Z. P. Shao, R. Xu, J. C. D. da Costa, S. B. Wang and S. M. Liu, J. Mater. Chem. A, 2013, 1, 9150-9156.

201. Y. Ji, J. A. Kilner and M. F. Carolan, Solid State Ionics, 2005, 176, 937-943.

202. K. Zhang, Z. Shao, C. Li and S. Liu, Energy Environ. Sci., 2012, 5, 5257-5264.

203. S. Imashuku, L. Wang, K. Mezghani, M. A. Habib and Y. Shao-Horn, J. Electrochem. Soc., 2013, 160, E148-E153.

204. L. Wang, S. Imashuku, A. Grimaud, D. Lee, K. Mezghani, M. A. Habib and Y. Shao-Horn, ECS Electrochem. Lett., 2013, 2, F77-F81.

205. C. Zhang, R. Ran, G. H. Pham, K. Zhang, J. Liu and S. Liu, RSC Adv., 2015, 5,

5379-5386.

206. C. Zhang, X. Meng, J. Sunarso, L. Liu, R. Xu, Z. Shao and S. Liu, J. Mater. Chem. A, 2015, 3, 19033-19041.

207. Y. Teraoka, T. Nobunaga and N. Yamazoe, Chem. Lett., 1988, 17, 503-506.

208. V. V. Kharton, V. N. Tikhonovich, L. Shuangbao, E. N. Naumovich, A. V. Kovalevsky, A. P. Viskup, I. A. Bashmakov and A. A. Yaremchenko, J. Electrochem. Soc., 1998, 145, 1363-1373.

209. Y. Teraoka, T. Nobunaga, K. Okamoto, N. Miura and N. Yamazoe, Solid State Ionics, 1991, 48, 207-212.

210. Z. Yang, G. Xia, X. Li and J. Stevenson, Int. J. Hydrogen Energy, 2007, 32, 3648-3654.

211. Ch. Ftikos, M. Nauer and B. C. H. Steele, J. Eur. Ceram. Soc., 1993, 12, 267-270.

212. K. Ahn, D. S. Yoo, D. H. Prasad, H.-W. Lee, Y.-C. Chung and J.-H. Lee, Chem. Mater., 2012, 24, 4261-4267.

213. Z. Wu, W. Jin and N. Xu, J. Membr. Sci., 2006, 279, 320-327.

214. J. Martynczuk, F. Liang, M. Arnold, V. Šepelák and A. Feldhoff, Chem. Mater., 2009, 21, 1586-1594.

215. H. L. Tuller and A. S. Nowick, J. Phys. Chem. Solids, 1977, 38, 859-867.

216. W. Lai and S. M. Haile, J. Am. Ceram. Soc., 2005, 88, 2979-2997.

217. H. J. Park and G. M. Choi, J. Electroceram., 2006, 17, 781-786.

218. Y. Wei, J. Tang, L. Zhou, J. Xue, Z. Li and H. Wang, AIChE J., 2012, 58, 2856-2864.

219. J. Tang, Y. Wei, L. Zhou, Z. Li and H. Wang, AIChE J., 2012, 58, 2473-2478.

220. Q. Zheng, J. Xue, Q. Liao, Y. Wei, Z. Li and H. Wang, Chem. Eng. Sci., 2013, 101, 240-247.

221. J. Xue, Q. Liao, W. Chen, H. J. M. Bouwmeester, H. Wang and A. Feldhoff, J. Mater. Chem. A, 2015, 3, 19107-19114.

222. Y. Chen, Q. Liao, Y. Wei, Z. Li and H. Wang, Ind. Eng. Chem. Res., 2013, 52, 8571-8578.

223. B. He, G. Li, L. Gui, Y. Ling and L. Zhao, J. Mater. Chem. A, 2016, 4, 4003-4008.

224. D. Ding, X. Li, S. Y. Lai, K. Gerdes and M. Liu, Energy Environ. Sci., 2014, 7, 552-575.

225. Y. Gong, D. Palacio, X. Song, R. L. Patel, X. Liang, X. Zhao, J. B. Goodenough and K. Huang, Nano Lett., 2013, 13, 4340-4345.

226. M. Risch, K. A. Stoerzinger, S. Maruyama, W. T. Hong, I. Takeuchi and Y. Shao-Horn, J. Am. Chem. Soc., 2014, 136, 5229-5232.

227. E. O. Oh, C. M. Whang, Y. R. Lee, S. Y. Park, D. H. Prasad, K. J. Yoon, J. W. Son, J. H. Lee and H. W. Lee, Adv. Mater., 2012, 24, 3373-3377.

228. W. Zhou, F. Liang, Z. Shao and Z. Zhu, Sci. Rep., 2012, 2, 327.

229. J. H. Joo, K. S. Yun, Y. Lee, J. Jung, C.-Y. Yoo and J. H. Yu, Chem. Mater., 2014, 26, 4387-4394.

230. Y. Hayamizu, M. Kato and H. Takamura, J. Membr. Sci., 2014, 462, 147-152.

231. A. Leo, S. Liu and J. C. Diniz da Costa, J. Membr. Sci., 2009, 340, 148-153.

232. S. Murphy, D. Slade, K. Nordheden and S. Staggwilliams, J. Membr. Sci., 2006, 277, 94-98.

233. Y. Liu, X. Zhu, M. Li, H. Liu, Y. Cong and W. Yang, Angew. Chem. Int. Ed., 2013, 52, 3232-3236.

234. T. Hong, L. Zhang, F. Chen and C. Xia, J. Power Sources, 2012, 218, 254-260.

235. Y. Teraoka, Y. Honbe, J. Ishii, H. Furukawa and I. Moriguchi, Solid State Ionics, 2002, 152-153, 681-687.

236. W. Ito, T. Nagai and T. Sakon, Solid State Ionics, 2007, 178, 809-816.

237. A. V. Kovalevsky, V. V. Kharton, F. Maxim, A. L. Shaula and J. R. Frade, J. Membr. Sci., 2006, 278, 162-172.

238. A. Vivet, P. M. Geffroy, E. Thune, C. Bonhomme, F. Rossignol, N. Richet and T. Chartier, J. Membr. Sci., 2014, 454, 97-108.

239. Z. Zhang, D. Chen, Y. Chen, Y. Hao, M. O. Tade and Z. Shao, J. Membr. Sci., 2014, 472, 10-18.

240. Z. Zhang, D. Chen, Y. Gao, G. Yang, F. Dong, C. Chen, F. Ciucci and Z. Shao, RSC Adv., 2014, 4, 25924-25932.

241. I. García-Torregrosa, M. P. Lobera, C. Solís, P. Atienzar and J. M. Serra, Adv. Energy Mater., 2011, 1, 618-625.

242. G. L. Messing, S.-C. Zhang and G. V. Jayanthi, J. Am. Ceram. Soc., 1993, 76, 2707-2726.

243. B. He, K. Zhang, Y. Ling, J. Xu and L. Zhao, J. Membr. Sci., 2014, 464, 55-60.

244. K. Zhang, C. Zhang, L. Zhao, B. Meng, J. Liu and S. Liu, Energy Fuels, 2016, 30, 1829-1834.

245. O. A. Savinskaya and A. P. Nemudry, J. Membr. Sci., 2014, 459, 45-51.

246. J. Zhou, X. Tang, C. Wu, H. Wang, Y. Zhang, W. Ding, Y. Jin and C. Sun, J. Phys.

Chem. C, 2015, 119, 24229-24237.

247. B. C. H. Steele, Mater. Sci. Eng., B, 1992, 13, 79-87.

248. S. J. Benson, D. Waller and J. A. Kilner, J. Electrochem. Soc., 1999, 146, 1305-1309.

249. D. Waller, J. A. Lane, J. A. Kilner and B. C. H. Steele, Mater. Lett., 1996, 27, 225-228.

250. J. S. Ledford, Y.-M. Kim, M. Houalla, A. Proctor and D. M. Hercules, Analyst, 1992, 117, 323-327.

251. D. Renusch, B. Veal, K. Natesan and M. Grimsditch, Oxid. Met., 1996, 46, 365-381.

Chapter 3: $Ce_{0.9}Gd_{0.1}O_{2-\delta}$ membranes coated with porous $Ba_{0.5}Sr_{0.5}Co_{0.8}Fe_{0.2}O_{3-\delta}$ for oxygen separation

Abstract

Robust oxygen ion-conducting membranes based on doped-ceria oxides can be used as oxygen permeation membranes via the short circuit to provide the required electronic conduction. Previous studies used expensive noble metals to be coated on both surface sides of the ion conducting electrolyte membrane as the electronic conducting phase to fulfil the functions for electron shuttling between the two membrane surfaces required for the oxygen reduction and oxidation. During the membrane operation, the atmosphere surrounding the two membrane sides is different with feed side exposing to air and the permeate side possibly confronting CO_2 or reducing gases like CH_4 or H_2. At high operating temperature, such different gas atmosphere poses different requirements on the material choice to prepare the membranes thus leaving space for further optimization to reduce the material cost. In this work, a novel $Ce_{0.9}Gd_{0.1}O_{2-\delta}$ (GDC) with cost-effective mixed conductive $Ba_{0.5}Sr_{0.5}Co_{0.8}Fe_{0.2}O_{3-\delta}$ (BSCF) layer to replace the preciously employed noble metal layer on the membrane surface facing the air atmosphere was developed to deliver a highly stable oxygen flux for possible applications in clean energy or membrane reactors for chemical synthesis. Further on, we noted that the membranes coated with BSCF improved the oxygen fluxes compared to the membranes coated with pure silver. A triple-phase boundary (TPB) theory has been put forward to deeply explain the observed improvement on oxygen flux values.

3.1 Introduction

The annual global oxygen production is predicted to reach hundreds of millions of tons from air separation and contributes the largest section in the industrial gases market with sales worthy of more than \$5 billion in 2014.[1] Oxygen has wide applications touching almost every sector of the global economy from a variety of industries like

metal manufacturing, chemicals, pharmaceuticals, petroleum, glass, cement, ceramics, pulp/paper manufacturing, waste treatment, rocket fuel, medical/health care and other life support systems. Currently in oxygen market, the power generation industry is only sharing 4%.[2] However, in the near future, this market will be massively expanded by the required deployment of clean energy technologies like IGCC and Oxyfuel projects to decrease the CO_2 emission; these clean energy projects require the oxygen as the feed gas. It is estimated that, in 2040, the energy industry sector will occupy the oxygen market by 60% requiring approximately two million tons per day.[2]

Currently, the industrial tonnage oxygen is produced at a lower purity (<93%) with intermediate scale by pressure swing adsorption or a high purity (>93%) and large scale (i.e. >1000 tons per day) by cryogenic distillation. Both methods are highly capital-expensive and energy-intensive; in particular, the cryogenic distillation, a very mature technique, has been used for more than one century without space for improvement. These conventional high-cost oxygen production technologies largely prohibit the clean energy technology application. To battle the extreme climate change via carbon capture and storage (CCS), our contemporary society urgently needs to upgrade the oxygen production technology to be more cost-effective to enable these clean energy schemes.

Among the emerging new technologies, ceramic membrane technology offers the greatest potential due to its energy efficiency and less capital investment. Starting from 1997, Air Products and US DoE have initiated the longest and biggest investment worthy of $148 million to advance this novel technique often referred as revolutionary ion transporting membrane (ITM) technology.[3] The associated research was actually started in 1980s when the appreciable oxygen permeation flux through dense perovskite membrane in a general formula of $La_{1-x}Sr_xCo_{1-y}Fe_yO_{3-\delta}$ was reported by Teraoka and co-workers.[4] Since then, a variety of perovskite ceramics with oxygen permeation properties have been explored and reported with a general formula $ABO_{3-\delta}$ where A and B sites can be individually or jointly occupied by La, Sr, Ba, Ca, or Zr and Mg, Al, Ti, Cr, Mn, Fe, Co, Ni, Cu, Ga, Zr, Ta, W, Sc or Zn, respectively.[5-20] Due to the structural flexibility of the perovskite structure, 90% of the metals listed in the element periodic table have been attempted to accommodate inside perovskite structure.[21] One common feature of these membranes is that they are able to simultaneously conduct both oxygen ions and electrons at elevated temperatures and thereby classified as mixed ionic and electronic conducting (MIEC) ceramic membranes with working principle

schematically shown in **Figure 3.1(a)**. When exposed to oxygen partial pressure gradient, oxygen can permeate through these perovskite membranes through surface reactions and bulk diffusion without the necessity for external electric loadings thus simplifying the membrane design compared to pure ionic conductors (**Figure 3.1(b)**).[22] To sustain a high oxygen flux, the membranes must possess not only sufficient ionic and electronic conductivities but also good surface reaction kinetics for oxygen exchange between its gaseous molecular state and solid lattice oxygen.

An apparent progress has been evidenced in the past two decades during material optimisation and scale up for engineering applications. For instance, oxygen flux up to 14.5 ml min^{-1} cm^{-2} at 950°C was achieved on thin $Ba_{0.5}Sr_{0.5}Co_{0.8}Fe_{0.2}O_{3-\delta}$ (BSCF) membrane supported on hollow fibre geometry under the oxygen pressure gradient created by non-pressurized air and sweep gas.[23] Long term operational stability over thousands of hours has been achieved on BSCF and $La_{0.6}Sr_{0.4}Co_{0.2}Fe_{0.8}O_{3-\delta}$ (LSCF) membranes for oxygen production under vacuum operation or non-reacting sweep gas models.[5,24,25] Encouraging news also come from Air Products that their ITM project has been advanced to Phase-5 testing the oxygen producing capability of 2000 tons per day.[26] Inspired by the success of membrane technology for pure oxygen production, the research communities have initiated another ambitious project to develop ITM syngas to combine the oxygen separation and gas oxidation in a single unit with working principles displayed in **Figure 3.1(c)**. Once successful, this novel technology will greatly advance our current petrochemical industries and clean energy deployment as it can save 20 to 30% capital cost for the overall synthesis gas and H_2 production.[3] In particular, it will help to improve the viability of the Oxyfuel project by retrofitting the existing power plants rather than setting up the new boiler system.[26]

These ambitious targets pose stricter requirement on the membrane material stability. As shown in **Figure 3.1(c)**, the permeate side of the membrane would face the reducing gases like CH_4 or acid gases like CO_2 for high temperature reactions. However, all these developed membranes cannot survive in such harsh reducing or acid gas atmosphere at high temperatures for the long term due to fact that these perovskite oxides are easily damaged by the reaction with these gases.[27,28] Fortunately, robust membranes with sufficient stability to endure these gases can be found from fluorite-type ion conducting ceramics such as yttria-stabilized zirconia (YSZ), gadolinium (or samaria)-doped ceria (GDC/SDC), which is evidenced by the wide applications in solid oxide fuel cells as the high temperature electrolyte for oxygen ion transport.[29-31] Despite

of their proven robustness, their application as oxygen production membrane is quite limited owning to their insufficient electronic conductivity and the associated more complex membrane design via oxygen pump with external electric loadings (**Figure 3.1(b)**). To simplify the membrane design, researchers have attempted to mix the noble metal powders like Pt, Au, Pd and Ag with YSZ, SDC or GDC to prepare a dual phase membrane in which metal and ion conductor phases can individually transfer oxygen ions and electrons simultaneously. However, it is difficult to guarantee the continuous conducting path for each phase, often leading to super low oxygen fluxes due to the mismatch problem between the two phases.[22]

Recently, based on the configuration of solid oxide fuel cell, a novel ion conducting ceramic membrane design with short circuit has been reported.[32] Noble metals, instead of mixing with ceramics, were decorated as a thin coating layer on the ceramic surface. Together with electronic conducting sealant (i.e. Ag paste) as the short circuit, the porous metal layer functions as the continuous electric conducting phase for electrons shuttling between the two membrane surfaces during the oxygen exchange reactions. In the previous research, noble Ag or Pt was decorated on both membrane surfaces as the electronic conducting phase to verify this concept as schematically shown in **Figure 3.1(d)**,[32,33] but the high cost of these precious metals is a drawback for the future large-scale applications. As aforementioned, some MIEC perovskites are good electronic conductors with sufficient oxygen exchange kinetics and high stability in air atmosphere, thus they can be used as the coating material to reduce the material cost by replacing the Ag or Pt layer in the air (feed) side of the GDC, YSZ or SDC membranes during air separation.

In this chapter, we tested this membrane design using the porous MIEC perovskite to coat the membrane surface facing the air side but leaving the permeate side still with precious metal (Ag) coating to confront the sweep gas containing CO_2. To test this hypothesis, $Ba_{0.5}Sr_{0.5}Co_{0.8}Fe_{0.2}O_{3-\delta}$ (BSCF) was used as the perovskite phase and ion conducting membrane was selected from gadolinium-doped ceria (GDC). In order to fully understand the effects of different electronic conducing phases from ceramics or precious metals on the overall oxygen transport, some membrane samples were coated on both sides with BSCF and performances were compared with that from Ag coated membranes.
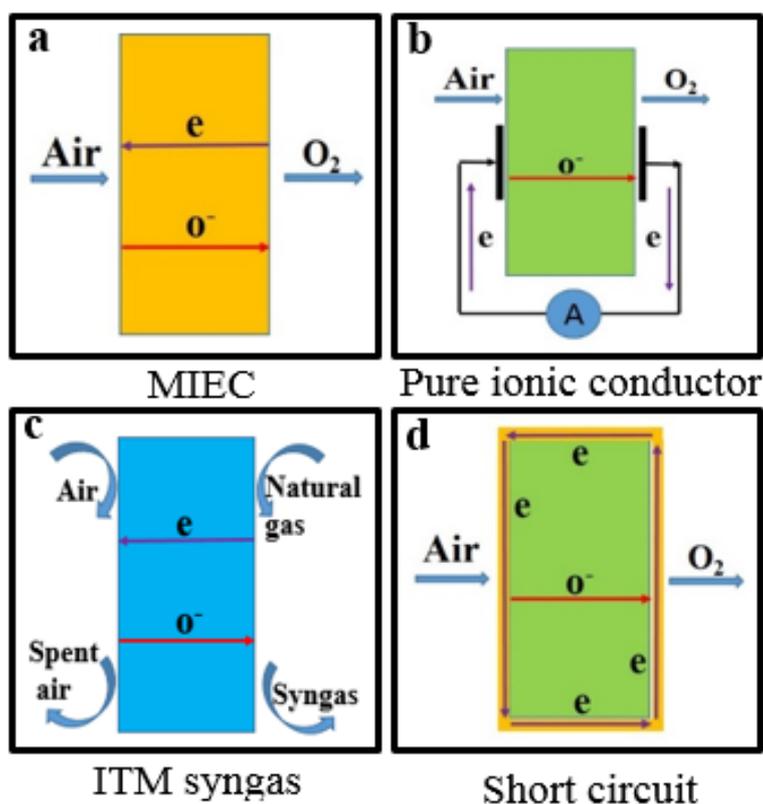
Figure 3.1 Schematic diagram of different oxygen permeation membrane design models. (a) Mixed ionic-electronic conducting oxide membranes; (b) Pure oxygen ionic conducting membranes with external power; (c) Ion transport membrane (ITM) reactors for syngas production; (d) Pure oxygen ionic conducting membranes with short-circuit coating.

3.2 Experimental

$Ce_{0.9}Gd_{0.1}O_{2-\delta}$ (GDC) and $Ba_{0.5}Sr_{0.5}Co_{0.8}Fe_{0.2}O_{3-\delta}$ (BSCF) ceramic oxides were synthesized by a combined EDTA-citrate complexing sol-gel process. The metal element precursors are from their nitrate salts of $Ce(NO_3)_2 \cdot xH_2O$, $Gd(NO_3)_2 \cdot xH_2O$, $Ba(NO_3)_2$, $Sr(NO_3)_2$, $Co(NO_3)_2 \cdot 6H_2O$ and $Fe(NO_3)_3 \cdot 9H_2O$, which were purchased from Aldrich and used as received. The stoichiometric quantities of metal nitrates in aqueous solution were dissolved in distilled water. Then EDTA and citric acid were added as the complexing agents. $NH_3 \cdot H_2O$ was added into the above solution to control the pH value at around 6 ~ 8. The molar ratios of total metal ions, EDTA, citric acid were controlled at 1:1:2. The solution was heated at 90 °C to evaporate the water and obtain a transparent gel. The gel was pre-fired at 250 °C and heated at 700 or 950°C for GDC or BSCF, respectively, in air for 5 h to get the ceramic powder with desired structure.

111

To fabricate the membrane, 0.4 grams of the ceramic powder was pressed into a disk-shaped membrane in a stainless steel mould (15.0 mm in diameter) under a hydraulic pressure of approximately 1.5×10^8 Pa. These green membranes (~0.8 mm in thickness) were further sintered at 1350 °C for 10 h at a ramping/cooling rate of 2°C/min. BSCF was dispersed in an ink vehicle mixed solution and then was coated to the surfaces of some GDC membranes by brush painting followed by calcination at 1000 °C in air for 2 h. Silver slurry was applied to the surface of other GDC membranes by a similar brush painting and subsequently calcined at 600 °C for 2 h.

To investigate the phase composition of membranes, the XRD analysis was carried out by a Bruker D8 Advance X-ray diffractometer using Cu Ka radiation generated at 40 kV and 30 mA. Scanning Electron Microscopy (SEM) images were obtained using a Zeiss EVO 40XVP at an accelerating voltage of 15 kV.

A Shimadzu 2014A gas chromatography (GC) equipped with a 5 Å capillary molecule column and thermal conductivity detector for quantitative oxygen concentration analysis was used during the high temperature oxygen permeation test. To set up the permeation cell, a silver paste was applied as the sealant to fix the disk membrane onto a dense quartz tube. The effective membrane area was about 0.45 cm^2. The partial pressure of oxygen in the feed stream was 0.21 atm. Helium was applied as the sweep gas to bring the permeated oxygen to the GC for concentration analysis. Assuming that leakage of nitrogen and oxygen through pores or cracks is in accordance with Knudsen diffusion, the fluxes of leaked N$_2$ and O$_2$ are related by

$$J^{Leak}_{N_2} : J^{Leak}_{O_2} = \sqrt{32/28} \times 0.79 : 0.21 = 4.02. \qquad \text{(Eq. 3.1)}$$

The O$_2$ permeation flux was then calculated by subtracting the leaked oxygen using the equation below:

$$J_{O_2}(\text{ml min}^{-1} \text{ cm}^{-2}) = \left[C_{O_2} - C_{N_2}/4.02 \right] \times \frac{F}{S} \qquad \text{(Eq. 3.2)}$$

where C_{O_2} and C_{N_2} are the measured concentrations of oxygen and nitrogen in the gas on the permeate side, respectively, F is the flow rate of the exit gas on the permeate side (ml min^{-1}), and S is the membrane geometric surface area of the sweep side (cm^2).

3.3 Results and discussion

To test the phase components of GDC membranes and the coating decorations, XRD analysis was carried out. **Figure 3.2** shows the typical XRD patterns of the membranes used for oxygen permeation test. As shown in **Figure 3.2(a)**, the characteristic peaks of GDC are located at the respective 2θ angles of 28° (111), 33° (200), 47° (220), 52° (311), 58° (222), 76° (331) and 79° (420), which agrees with the previously reported.[34,35] **Figure 3.2(b)** displays the XRD patterns of the GDC with BSCF coating on the surface. All the peaks can be clearly assigned to GDC and BSCF, respectively. No other undesired phases can be observed, which rules out the reaction between these two phases and proves the stable coexistence of GDC and BSCF. **Figure 3.2(c)** shows that the existence of Ag coating; however, compared to the strong diffraction signal from Ag, GDC peaks are relatively weak thus its observation in **Figure 3.2(c)** is not as distinguishable as that in **Figure 3.2(a) or (b)**.
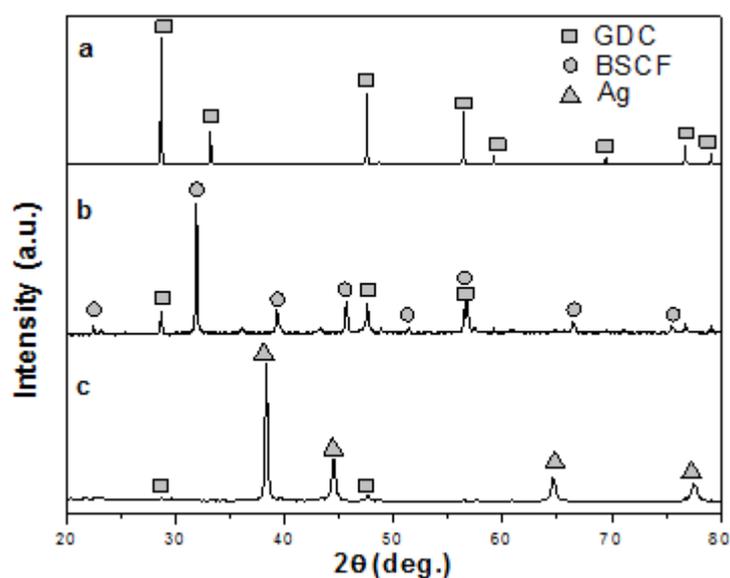
Figure 3.2 XRD patterns of (a) GDC, (b) GDC coated with BSCF and (c) GDC coated with Ag.

Figure 3.3(a) and (b) show the SEM images of the surface and cross section views of the pure GDC membrane with the GDC grain size of 0.5-1.0 μm (the inset of **Figure 3.3(a)**). The dense structure of sintered GDC membrane is observed not only from the surface but also from the cross-section view (**Figure 3.3(b)**) as no apparent

porosity can be detected in the SEM image. The BSCF was initially dispersed inside the ink vehicle solution and then coated on the GDC membrane followed by sintering at high temperature to increase the interface adhesion. The SEM of the obtained porous coating structure is displayed in **Figure 3.3(c)**. As seen, the pore size is in the range of 2-3 μm and the porous BSCF coating layer has the thickness around 5.0 μm as marked by the horizontal line in **Figure 3.3(d)**; in contrast, the thick supporting bulk layer is the densified GDC structure (as shown in the inset of **Figure 3.3(d)**). The GDC membrane coated with Ag paste presents a porous structure as well (**Figure 3.3(e)**). The porous structure, no matter BSCF or Ag, would be used to promote the oxygen permeation fluxes.[9,32,36]
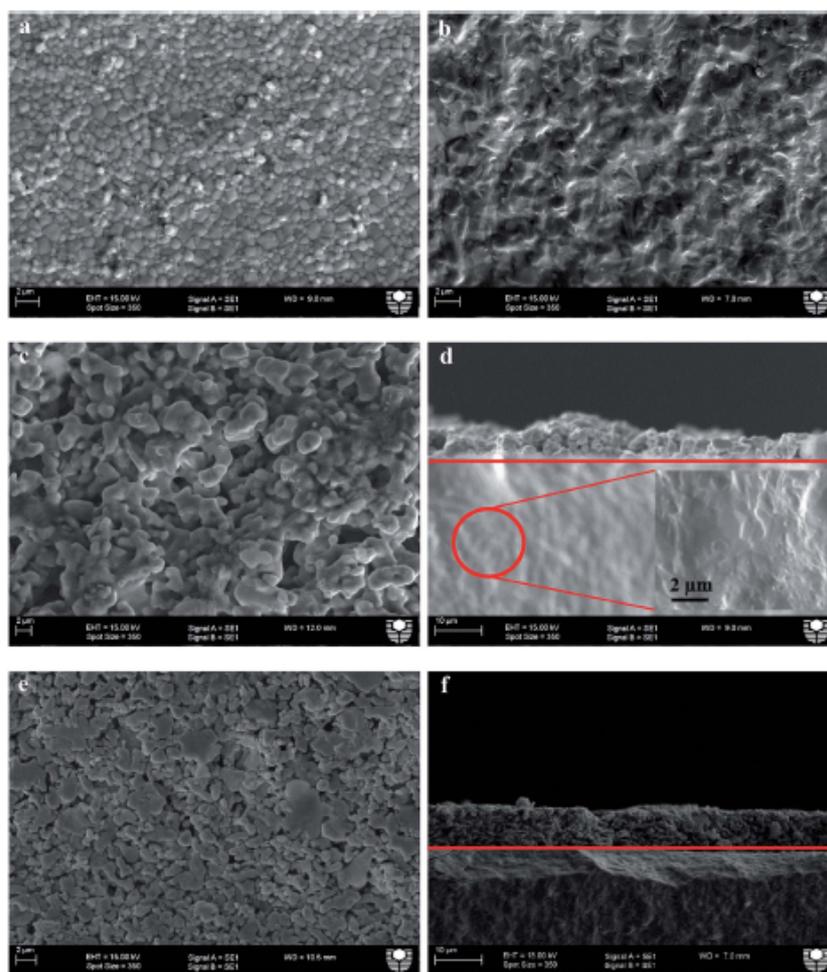
Figure 3.3 SEM images of: (a) surface of GDC; (b) cross-section of GDC; (c) surface of GDC membrane decorated with BSCF coating; (d) cross-section of GDC membrane decorated with BSCF coating; (e) surface of GDC membrane decorated with Ag coating; and (f) cross-section of GDC membrane decorated with Ag coating.

In order to test the feasibility of the BSCF coating to promote the oxygen transport through the GDC membrane, three typical membranes (Samples a, b and c) with varied coating layers were purposely chosen to display the flux difference based on the similar 0.8 mm thickness of the bulk diffusion GDC layer. Sample-a has Ag coatings on both membrane sides; Sample-b has Ag coating on one side but the other side with BSCF coating; Sample-c has both sides with BSCF coatings. As shown in **Figure 3.4**, the coating of BSCF layer (Sample-b or c) on the membrane significantly improved the oxygen fluxes at relatively similar operating temperatures and sweep gas rate. For example, at 650 °C, the oxygen flux of Sample-a with Ag coating on both membrane sides was 0.017 ml min^{-1} cm^{-2} (**Figure 3.4(a)**) while the flux of BSCF coating in the permeate side with Ag coating still in feed side (Sample-b) was improved by 16%
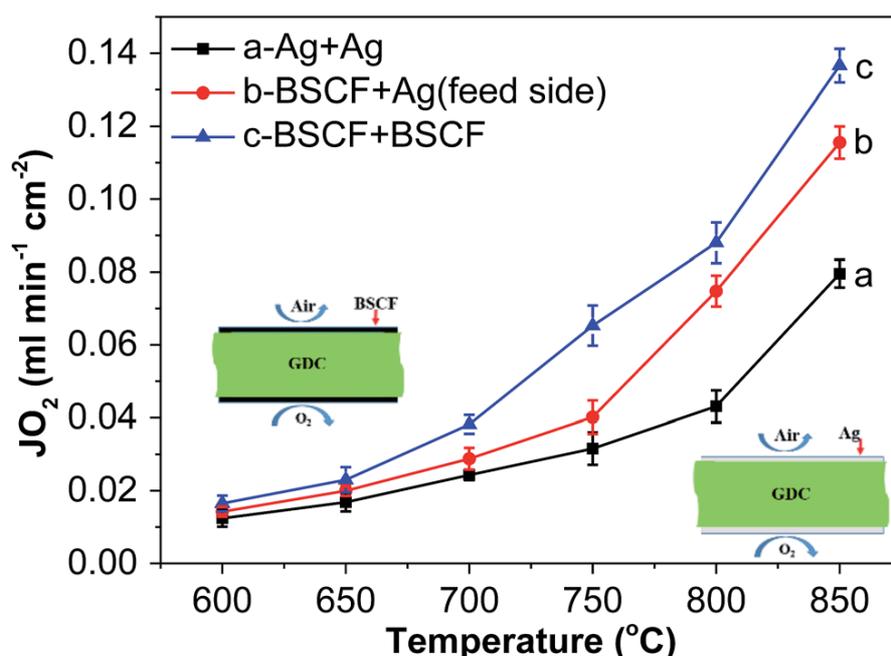
Figure 3.4 Oxygen permeation of GDC membrane coated with (a) Ag on both the feed side and the permeate side, (b) Ag on the feed side and BSCF on the permeate side and (c) BSCF on both the feed side and the permeate side. The sweep gas flow-rate was 100 ml min^{-1}.

to 0.02 ml min^{-1} cm^{-2} (**Figure 3.4(b)**). When both membrane sides were coated by the BSCF layer (Sample-c), the flux was further raised by 27% to 0.023 ml min^{-1} cm^{-2} compared to Sample-a at the operation temperature of 650 °C. When the temperature was continuously rising, the oxygen fluxes of all the three samples had been lifted up
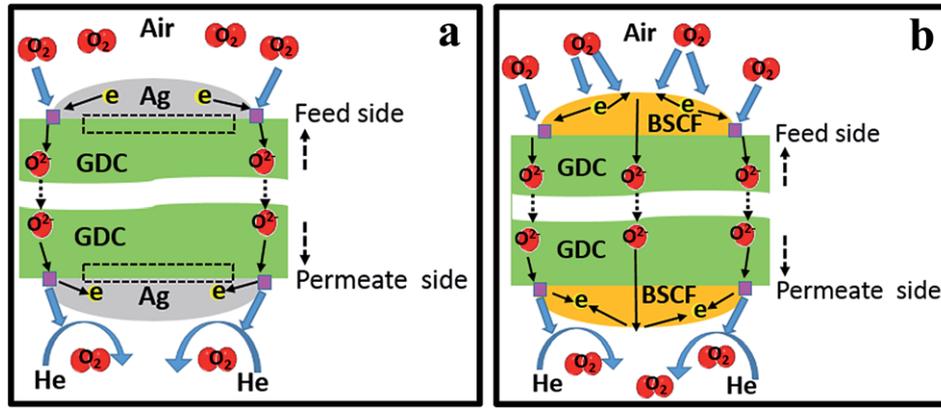
Figure 3.5 Schematic diagram showing the effects of different coatings on the oxygen permeation process: (a) pure electronic conductor of Ag; and (b) mixed conductor of BSCF.

compared to that operated on lower temperatures; such promoting effect of temperature on the flux value can be easily interpreted by the temperature activation on the oxygen exchange surface reactions and oxygen ion bulk diffusion. However, a careful inspection of the flux enlargement by the BSCF coating at different temperatures illustrates that at higher temperatures such flux improvement is more distinguishable than that at lower temperatures. For instance, at 800 °C, compared to the flux of 0.043 ml min^{-1} cm^{-2} from Sample-a, the respective fluxes of Samples-b and c were 0.075 and 0.088 ml min^{-1} cm^{-2} with improvement percentage by 42% and 51%, respectively. The relative larger flux improvement with BSCF coating at higher temperatures indicating the percentage of surface reaction resistance in the overall resistance (surface reaction plus bulk diffusion) to determine the limiting step for oxygen transport gradually increases with the rise of the operating temperature. However, to explain theoretically the larger improvement in oxygen permeation obtained by coating with a mixed conductor such as BSCF rather than a pure electronic conductor like Ag, we need to consider the two membrane surface reactions:

$\frac{1}{2}O_2 + V_O^{..} + 2e \rightarrow O_O^x$ (air side of the membrane surface) $\qquad$ (1);

$O_o^x \rightarrow \frac{1}{2}O_2 + V_O^{..} + 2e^{.}$ (permeate side of the membrane surface) $\qquad$ (2).
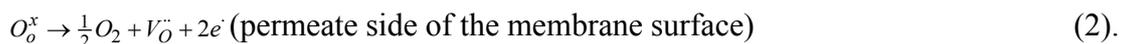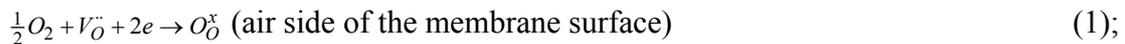
where $O_o^\times$ stands for lattice oxygen, $V_O^{..}$ for an oxygen vacancy and e for an electron. At the membrane surface facing the air, molecular oxygen is reduced to lattice (or ionized) oxygen with the acceptance of electrons. On the other membrane surface facing the sweep gas, molecular oxygen and electrons are released via the oxidation of lattice oxygen. Thus, each surface reaction only takes place in the respective triple-phase

boundary (TPB) areas. This is shown schematically in **Figure 3.5(a)**: when the membrane is coated with Ag, the TPB areas marked by pink squares are the points where Ag, GDC and oxygen (or the sweep gas He) can meet to make the surface reactions possible. This requires the Ag coating layer to be continuous, uniform and porous, with a strong adherence to the GDC surface. However, the Ag coating produced via brush-painting and a high temperature treatment is agglomerated; in this instance the GDC areas covered by the Ag agglomerates (marked in **Figure 3.5(a)** by the dotted rectangle) are sacrificed and do not contribute to the surface reactions. In another word, the large Ag particles from the coating layer block the ionic bulk diffusion as a result of the very limited TPB area. However, this restriction is removed if the coating layer is replaced by a mixed conductor such as BSCF (**Figure 3.5(b)**). Here, the TPB area is expanded from the area marked by the pink squares to the entire particle surface of BSCF, thus improving the kinetics of the oxygen surface reaction. Of course, the BSCF particles should adhere strongly to the GDC surface to decrease the interfacial resistance to ionic or electron transport. This is why a mixed conductor-BSCF coating on GDC improves the oxygen permeation flux compared with an Ag coating. A similar observation was made by Wang et al.[37] and Imashuku et al.,[38] who used a pulse laser method to deposit $La_{0.8}Sr_{0.2}CoO_{3-\delta}$ oxide on an SDC membrane.

In addition to temperature activation, **Figure 3.6** shows that the oxygen flux can also be increased by increasing the sweep gas flow-rate, which lowers the oxygen partial pressure on the permeate side, thus increasing the partial pressure gradient of oxygen. For example, the oxygen flux through the membrane of sample c increased from 1.02 to 1.21 ml min^{-1} cm^{-2} as the sweep gas flow-rate was increased from80 to 120 ml min^{-1} at 850 °C. In this work, which used ambient air and He as the feed and sweep gases, respectively, the largest oxygen partial pressure gradient only reached 0.21/0.001. However, under the reaction conditions in industrial applications, the air used as the feed gas is pressurized to 50 atm and the permeated oxygen is consumed in the reaction so that the oxygen partial pressure gradient can be as large as $10/10^{-16}$ atm. Under such circumstances, the oxygen flux is very fast. Therefore the factor that restricts the performance of the reaction is not the oxygen flux, but the stability of the membrane materials in real-life applications.

If the oxygen flux is completely controlled by bulk diffusion as the membrane surface coating improves the oxygen exchange surface reaction kinetics to a minimum

resistance, we can estimate the maximum theoretical oxygen flux based on the Wagner equation:

$$J_{O_2} = \frac{RT}{16F^2L} \sigma_i \ln \frac{P'_{O_2}}{P''_{O_2}} \qquad \text{(Eq. 3.3)}$$

where T is the absolute temperature, R is the ideal gas constant, F is the Faraday constant, L is the thickness of the membrane, σ_i is the oxygen ion conductivity of GDC, and P'_{O_2} and P''_{O_2} are the oxygen partial pressures at the feed and permeate sides of the membrane.
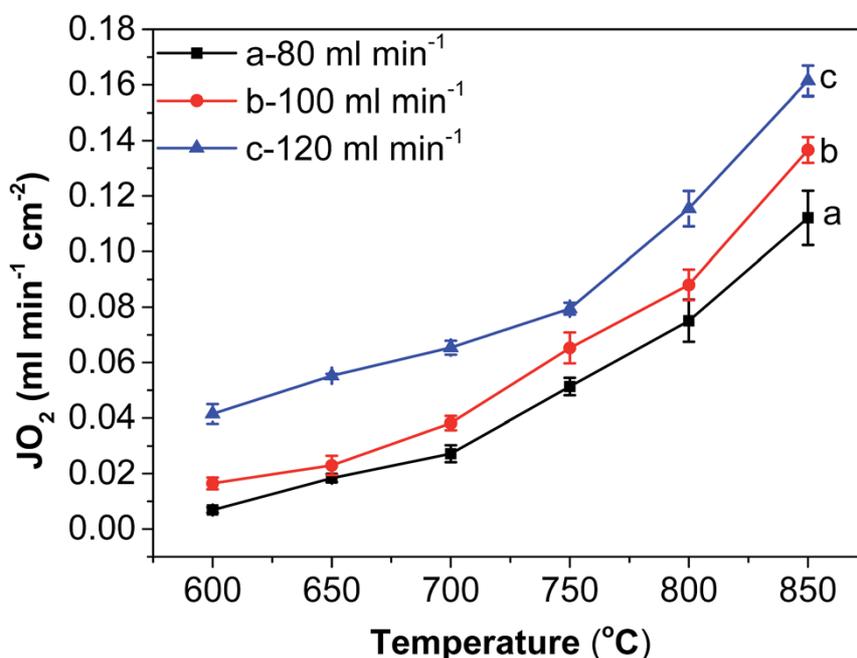
Figure 3.6 Effect of sweep gas flow-rate on oxygen permeation fluxes.

Table 3.1 Oxygen ion conductivity and theoretical oxygen permeation flux of GDC membrane coated with BSCF on both sides.

Temp °C	σ_i (S cm^{-1}) [39]	Theoretical J_{O_2} (ml min^{-1}cm^{-2})	Measured J_{O_2} (ml min^{-1}cm^{-2})
600	4.05·10-3	0.018	0.016
650	8.44·10-3	0.039	0.023
700	1.29·10-2	0.063	0.038
750	2.03·10-2	0.104	0.065

A number of studies have been carried out to measure the oxygen ion conductivity of the GDC membrane.[39–43] There may be minor differences in the conductivity values when using different synthesis methods for GDC. **Table 3.1** shows

the oxygen ion conductivity at different temperatures from previously published data.[39] The maximum theoretical oxygen flux was then calculated using the results in Table 3.1. Compared with the theoretical oxygen flux, the measured fluxes in this work were 10–40% smaller, indicating that the surface reaction kinetics contributed a certain resistance in limiting the overall oxygen transport.

Two types of coated GDC membranes (samples c and d) were tested for long-term use by adding CO_2 to the sweep gas on the permeate side. Sample c has BSCF coatings on both sides of the membrane, but sample d consisted of GDC coated by Ag on one side of the membrane and BSCF on the other. **Figure 3.7** shows the stability performance tests of two typical membranes. During the test, the BSCF coating side of the membrane in sample d faced the feed air and the side with the Ag coating faced the sweep gas containing CO_2. As expected, the oxygen flux of sample c coated on both sides with BSCF showed a continuous decrease when the sweep gas was switched from pure He to a mixture with 10% CO_2 (**Figure 3.7(a)**). At 800 °C and after 600 minutes, the flux for sample c decreased by more than 50%. After the sweep gas had been changed back to pure helium, the oxygen flux could not be recovered to its original value as a result of the formation of carbonate from the reactions between the alkaline earth metals (such as Ba/Sr) and CO_2.[27,44] In sharp contrast, sample d worked very well under these conditions. The GDC membrane with coatings of BSCF and Ag showed very stable oxygen fluxes in either pure He or mixtures containing CO_2. **Figure 3.7(b)** shows that, after introducing CO_2 into the He sweep gas, the flux value was slightly lowered, but could be maintained at a stable value of 0.044 mL min^{-1} cm^{-2}. The temporary decrease in flux with the introduction of CO_2 is a result of the stronger adsorption of CO_2 to the membrane surface relative to helium, not due to the reaction between CO_2 and GDC. The wide application of GDC as a solid electrolyte in solid oxide fuel cells verifies that it is sufficiently stable to withstand gases such as CO_2 and CH_4.[45] Therefore when the sweep gas was switched back to pure He, the oxygen flux was quickly recovered to the original value.

119
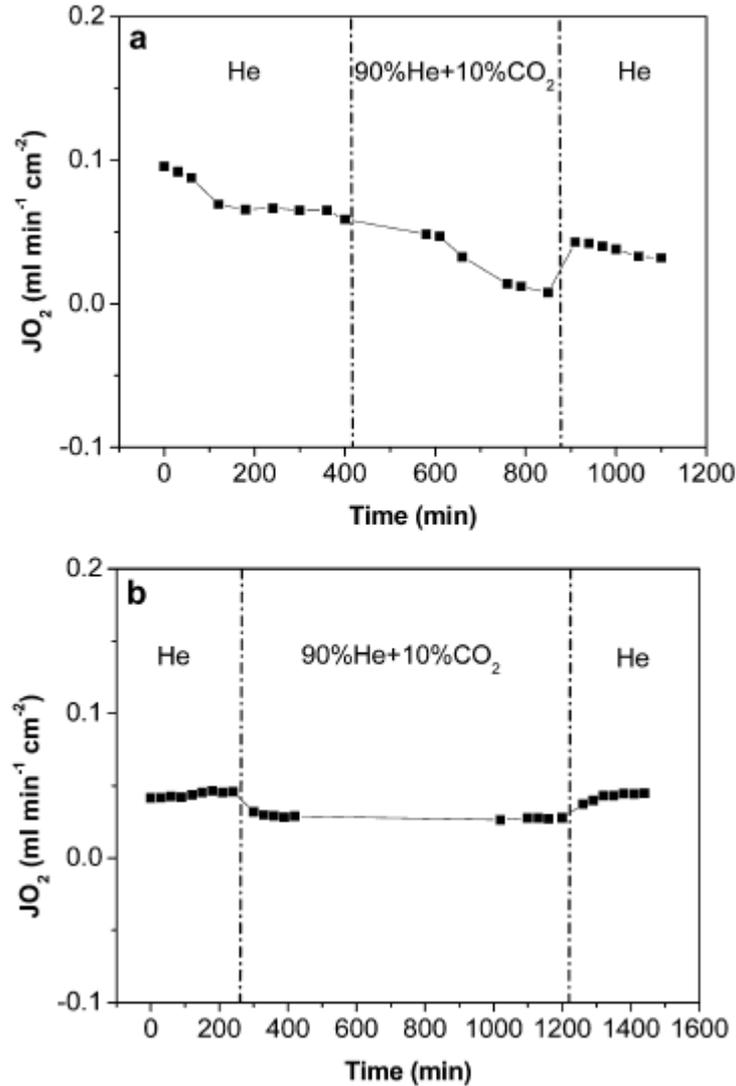
Figure 3.7 Long-term oxygen permeation tests through GDC membranes coated with (a) BSCF on both sides and (b) BSCF on feed side and Ag on the sweep side. The sweep gas flow-rate is 100 ml min^{-1}.

3.4 Conclusions

Based on the working principles of solid oxide fuel cells, a short circuit robust ion conducting ceramic membrane configuration has been proposed to overcome the weak stability of ceramic membranes in atmospheres of CO_2 or reducing gases at high temperatures.[32] However, this reported design had a high cost because it used expensive noble metals on both sides of the membrane. This study demonstrated the feasibility of using a cheaper mixed conducting ceramic coating for electronic conduction on robust ion conducting ceramic membranes for oxygen separation. To illustrate the concept,

120

GDC membranes coated with BSCF or Ag paste were used as ion conducting membranes with a mixed or pure electronic conductor, respectively. The experimental results show that the replacement of the Ag coating on the GDC membrane by BSCF significantly improved the oxygen flux as a result of the increased TPB area, with improved oxygen-exchange surface reaction kinetics. The maximum oxygen flux was 0.13 ml min^{-1} cm^{-2} at 850 °C with a dense GDC thickness of 0.8 mm and with both sides of the membrane coated by BSCF. The GDC membrane with a BSCF coating facing the air and an Ag coating exposed to a CO_2 mixture was very stable during a long-term permeation test, making it suitable for clean energy applications such as the Oxyfuel project and in membrane reactors for the production of syngas.

3.5 References

1.   PRWeb, http://www.prweb.com/releases/2013/11/prweb11347927, (accessed November 2013).

2.   World nuclear association, http://www.world-nuclear.org/info/Energy and-Environment/-Clean-Coal-Technologies/, (accessed May 2014).

3. T. Foster, Air products, Air Separation Technology-Ion Transport Membrane (ITM), Allentown, 2008.

4. Y. Teraoka, H. M. Zhang, S. Furukawa and N. Yamazoe, Chem. Lett., 1985, 14, 1743-1746.

5. Z. P. Shao, W. S. Yang, Y. Cong, H. Dong, J. H. Tong and G. X. Xiong, J. Membr. Sci., 2000, 172, 177-188.

6. Z. B. Zhang, D. J. Chen, Y. Gao, G. M. Yang, F. F. Dong, C. Chen, F. Ciucci and Z. P. Shao, RSC Adv., 2014, 4, 25924-25032.

7. D. Z. Han, J. H. Wu, Z. F. Yan, K. Zhang, J. Liu and S. M. Liu, RSC Adv., 2014, 4, 19999-20004.

8. H. H. Wang, R. Wang, D. T. Liang and W. S. Yang, J. Membr. Sci., 2004, 243, 405-415.

9. S. Baumann, J. M. Serra, M. P. Lobera, S. Escolástico, F. Schulze Küppers and W. A. Meulenberg, J. Membr. Sci., 2011, 377, 198-205.

10. X. Y. Lin, T. Kerstiens and T. Markus, J. Membr. Sci., 2013, 438, 83-89.

11. F. Schulze-Küppers, S. Baumann, W. A. Meulenberg, D. Stöver and H.-P. Buchkremer, J. Membr. Sci., 2013, 433, 121-125.

12. M. Katsuki, S. R. Wang, M. Dokiya and T. Hashimoto, Solid State Ionics, 2003, 156, 453-461.

13. J. Luyten, A. Buekenhoudt, W. Adriansens, J. Cooymans, H. Weyten, F. Servaes and R. Leysen, Solid State Ionics, 2000, 135, 637-642.

14. T. Ramos and A. Atkinson, Solid State Ionics, 2004, 170, 275-286.

15. Y. Zou, W. Zhou, S. M. Liu and Z. P. Shao, J. Eur. Ceram. Soc., 2011, 31, 2931-2938.

16. B. Meng, Z. G. Wang, Y. Y. Liu, X. Y. Tan, J. C. D. da Costa and S. M. Liu, Sep. Purif. Technol., 2011, 78, 175-180.

17. X. Z. Chen, L. Huang, Y. Y. Wei and H. H. Wang, J. Membr. Sci., 2011, 368, 159-164.

18. M. Shang, J. H. Tong and R. O'Hayre, RSC Adv., 2013, 3, 15769-15775.

19. V. V. Kharton, S. B. Li, A. V. Kovalevsky and E. N. Naumovich, Solid State Ionics, 1997, 96, 141-151.

20. J. X. Yi, S. J. Feng, Y. B. Zuo, W. Liu and C. S. Chen, Chem. Mater., 2005, 17, 5856-5861.

21. K. Zhang, J. Sunarso, Z. Shao, W. Zhou, C. Sun, S. Wang and S. Liu, RSC Adv., 2011, 1, 1661-1676.

22. J. Sunarso, W. A. Meulenberg, S. Baumann, J. M. Serra, S. Liu, J. C. D. da Costa and Y. S. Lin, J. Membr. Sci., 2008, 320, 13-41.

23. A. Leo, S. Smart, S. Liu and J. C. D. da Costa, J. Membr. Sci., 2011, 368, 64-68.

24. D. Schlehuber, E. Wessel, L. Singheiser and T. Markus, J. Membr. Sci., 2010, 351, 16-20.

25. X. Tan, Z. Wang, B. Meng, X. Meng and K. Li, J. Membr. Sci., 2010, 352, 189-196.

26. J. Repasky, D. McCarthy, P. Armstrong and M. Carolan, Workshop on Technology Pathways Forward for Carbon Capture & Storage on Natural Gas Power Systems, Washington DC, 2014.

27. A. Waindich, A. Mobius and M. Müller, J. Membr. Sci., 2009, 337, 182-187.

28. J. Yi and M. Schroeder, J. Membr. Sci., 2011, 378, 163-170.

29. J. Kim and Y. S. Lin, J. Membr. Sci., 2000, 167, 123-133.

30. C. S. Chen, B. A. Boukamp, H. J. M. Bouwmeester, G. Z. Cao, H. Kruidhof, A. J. A. Winnubst and A. J. Burggraaf, Solid State Ionics, 1995, 76, 23-28.

31. T. J. Mazanec, T. L. Cable and J. G. Frye Jr, Solid State Ionics, 1992, 53, 111-118.

32. K. Zhang, Z. Shao, C. Li and S. Liu, Energy Environ. Sci., 2012, 5, 5257-5264.

33. K. Zhang, L. Liu, Z. Shao, R. Xu, J. C. D. da Costa, S. Wang and S. Liu, J. Mater. Chem. A, 2013, 1, 9150-9156.

34. J. Xue, Q. Liao, Y. Y. Wei, Z. Li and H. H. Wang, J. Membr. Sci., 2013, 443, 124-130.

35. J. Xue, Q. Zheng, Y. Y. Wei, K. J. Yuan, Z. Li and H. H. Wang, Ind. Eng. Chem. Res., 2012, 51, 4703-4709.

36. Z. G. Wang, H. Liu, X. Y. Tan, Y. G. Jin and S. M. Liu, J. Membr. Sci., 2009, 345, 65-73.

37. L. Wang, S. Imashuku, A. Grimaud, D. Lee, K. Mezghani, M. A. Habib and Y. Shao-Horn, ECS Electrochem. Lett., 2013, 2, F77-F81.

38. S. Imashuku, L. Wang, K. Mezghani, M. A. Habib and Y. Shao-Horn, J. Electrochem. Soc., 2013, 160, E148-E153.

39. S. Lübke and H.-D. Wiemhöfer, Ber. Bunsenges. Phys. Chem., 1998, 102, 642-649.

40. B. C. H. Steele, Curr. Opin. Solid State Mater. Sci., 1996, 1, 684-691.

41. R. V. Mangalaraja, S. Ananthakumar, M. Paulraj, K. Uma, M. L´opez, C. P. Camurri and R. E. Avila, Process. Appl. Ceram., 2009, 3, 137-143.

42. H. Yahiro, Y. Eguchi, K. Eguchi and H. Arai, J. Appl. Electrochem., 1988, 18, 527-531.

43. J. Liu and W. Weppner, Ionics, 1999, 5, 115-121.

44. M. Arnold, H. H. Wang, J. Martynczuk and A. Feldhoff, J. Am. Ceram. Soc., 2007, 90, 3651-3655.

45. W. Wang, C. Su, Y. Z. Wu, R. Ran and Z. P. Shao, Chem. Rev., 2013, 113, 8104-8151.

Chapter 4: Oxygen permeation behavior through $Ce_{0.9}Gd_{0.1}O_{2-\delta}$ membranes electronically short circuited by dual-phase $Ce_{0.9}Gd_{0.1}O_{2-\delta}$–Ag decoration

Abstract

Electronically short-circuited ion conducting fluorite membranes for air separation are a relatively novel category of ceramic membranes overcoming the long-standing stability problem of the state-of-the-art perovskite membranes under reducing and acidic conditions. Such robust membranes have particular potential to further improve the economics of clean energy projects and syngas production. In this work, we adopted the conventional dual-phase membrane idea to decorate the fluorite membrane surface. Previously, a pure noble metal layer was employed as an electronic decoration layer which displayed several limitations. In this work, instead, a dual-phase mixture of $Ce_{0.9}Gd_{0.1}O_{2-\delta}$ (50 wt%)–Ag (50 wt%) was applied as the decoration layer of the $Ce_{0.9}Gd_{0.1}O_{2-\delta}$ bulk membrane. Such a strategy not only reduces the material cost and enhances the interface adherence but also significantly improves the O_2 flux rates as more triple-phase boundary area is created for surface O_2 exchange reactions. We further confirm the stability of the resultant short-circuited $Ce_{0.9}Gd_{0.1}O_{2-\delta}$ membrane during the 130-hour permeation test at high temperatures under a CO_2 containing atmosphere.

4.1 Introduction

Mixed ionic-electronic conducting (MIEC) ceramic membranes are a highly active research topic given their potential to replace the conventional high cost oxygen production method with savings around 35% by a novel cost-effective membrane separation technology.[1–3] MIEC ceramic membranes have been majorly classified into single phase perovskite oxides and dual phase membranes. These perovskite membranes are successfully developed from the viewpoint of pure oxygen production.

This is due to the relatively mild operating conditions for air separation as the membranes are only exposed to atmospheres of pressurized air and pure oxygen. Such success is evidenced by the progress of the ion-transport-membrane (ITM) project from Air Products (US) as it is currently in phase-5, using wafer-like planar ceramic membrane modules with an oxygen production capability of 2000 tons per day.[3] Such an achievement is very encouraging as this is the first example of ceramic membrane application in gas separation on a large scale. This cost-effective method will undoubtedly advance many sectors of the global economy from a variety of industries like metal manufacturing, chemicals, pharmaceuticals, petroleum, glass, cement, ceramics, and pulp/paper manufacturing as all of them need a large quantity of pure oxygen as the oxidant. However, the stability of these perovskite membranes is low and cannot be applied in atmospheres containing reducing or acidic gases like CH_4, H_2, CO and CO_2 due to the reactions of perovskites and these gases; otherwise, they can be more economically applied in recently emerging markets, and clean energy technologies (IGCC and Oxyfuel projects).[4–8] It has been estimated that these clean energy projects will expand the oxygen market from the current 4% to 60% in 2040 with an O_2 requirement of approximately two million tons per day.[9] Nonetheless, the robust dual phase membrane with strong chemical stability has the potential to fill this gap despite quite low O_2 permeation flux, which can be improved by engineering approaches e.g. by developing a very thin dense layer on top of a thick porous substrate.[10–15] Once there is a breakthrough, this novel ceramic membrane reactor technology will greatly advance our current petrochemical industries and clean energy technology deployment as it can save 20 to 30% of the capital cost for the overall synthesis gas and H_2 production.[3,16] In particular, it will help to improve the viability of the Oxyfuel project by providing artificial "air" – 30% of O_2 in CO_2 for clean combustion; in this case, the existing power plants can be easily retrofitted for CO_2 capture and storage rather than setting up a new boiler system.[17]

Different from single perovskite membranes where the required mixed (oxygen ionic and electronic) conduction is completed in one phase, dual phase membranes comprise an ionic conducting phase and an electronic conducting phase, to fulfill these two functions separately.[18–23] These essentially pure ionic conductors which are currently attracting intense interest are fluorite-type ceramics such as samarium-doped ceria (SDC), gadolinium-doped ceria (GDC) and yttria-stabilized zirconia (YSZ). The accompanying electronic conductor is one of the noble metals such as Au, Ag, or Pd.

In order to save the material cost, other cheaper electronic conducting perovskites or spinels are also attempted in this dual phase membrane design, but their chemical stability is still a concern. **Figure 4.1(a)** briefly displays the working principles of ionic transport through such membranes. Due to the requirement of continuous material pathways for individual ion and electron transport, 40% by volume fraction is frequently required from each phase using the conventional preparation protocols, e.g. mixing, pressing and sintering.[24] However, this preparation method often results in many isolated areas (referred to as an "island") from each of the two phases i.e. marked by red rings in **Figure 4.1(a)**; these islands would not contribute as a part of the dual phase membrane. This unfavorable mutual blocking effect greatly reduces the O_2 flux rates, in some cases, several orders of magnitude lower than that of the perovskite membranes.[24] Novel methods to achieve the uniform mixing of the two phases at a molecular level would of course help to improve the membrane performance, but the particle aggregation during the subsequent sintering would put a similar limit on the enhancement. On the other hand, the electronic conductivity of these noble metals is much higher than the ionic conductivity of the fluorite oxide phase; thereby ionic conduction is normally the limiting factor determining the bulk diffusion resistance. This provides another guideline for synthesis of the dual phase membrane; the ionic conducting phase should be formulated as much as possible and the electronic conducting phase should be reduced to a minimum amount as long as its continuous material phase is maintained as schematically shown in **Figure 4.1(b)**. Chen et al. showed this effective strategy by using a coating method to prepare such a dual phase membrane where the SDC content was up to 80 vol.% balanced by the fibre-shaped electronic conducting phase.[25] They observed that the SDC increment improved the O_2 flux by 90% when operated at 950 °C, compared to the dual phase membrane with 60 vol.% SDC.

Recently, a novel membrane design has attracted much research interest using short circuit decoration on the two membrane surfaces, SDC or GDC, (**Figure 4.1(c)**) based on the solid oxide fuel cell configurations.[13,26–28] In such a way, the entire SDC or GDC bulk membrane, without mixing with other phases, can be solely used for ion transport where the electron transport occurs via the external short-circuit from the surface coatings and the sealant. More recently, Caro's group published an interesting paper using the Nafion® membrane via a similar short-circuit design without applying an electrical voltage for hydrogen separation at room temperature.[29]

126
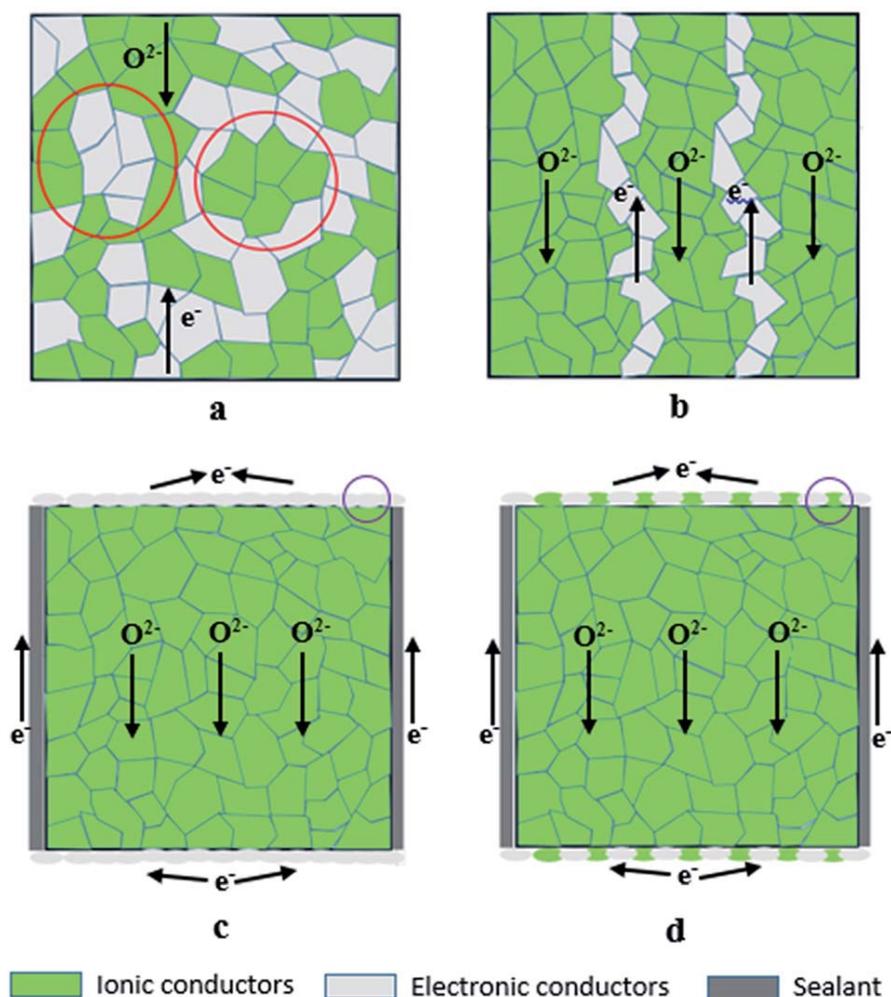
Figure 4.1 Cross-section schematic diagram of: (a) dual-phase membrane, (b) dual-phase membrane with a minimum electronic conducting phase, (c) membrane with external short-circuit decoration and (d) membrane with dual-phase external short-circuit decoration.

Different from molecular sieving membranes where the separation is a pure physical process, O_2 permeation through the ion conducting membrane also involves surface exchange reactions which usually take place in the triple-phase boundary (TPB) area. In our previous short circuit design, a pure noble metal of Ag or Pt was applied, which not only results in high material costs but also provides very limited TPB area for surface reactions thus leading to lower O_2 flux.

In this work, a novel dual-phase decoration by mixing $Ce_{0.9}Gd_{0.1}O_{2-\delta}$ and Ag was examined to short-circuit the $Ce_{0.9}Gd_{0.1}O_{2-\delta}$ bulk membrane surfaces for O_2 separation (**Figure 4.1(d)**). Compared to the previous decoration using a pure noble metal coating, this dual phase decoration strategy brings in at least three advantages in terms of reduced material cost, improved O_2 flux rates due to the expanded TPB area

and promoted interface adhesion by reduced thermal expansion mismatch. The current work is aimed to provide a new understanding towards the longstanding ambition to realize robust membranes or membrane reactors for a clean environment and greener chemical synthesis.

4.2 Experimental

4.2.1 Synthesis of fluorite oxide powder and disk membranes

$Ce_{0.9}Gd_{0.1}O_{2-\delta}$ (GDC) powder was synthesized using a combined EDTA-citrate complexing sol–gel process. The metal nitrate precursors are $Ce(NO_3)_3 \cdot 6H_2O$ (Sigma-Aldrich, 99.99% purity) and $Gd(NO_3)_3 \cdot 6H_2O$ (Sigma-Aldrich, 99.9% purity). Stoichiometric quantities of these metal nitrates were dissolved in distilled water resulting in an aqueous solution. EDTA (Sigma-Aldrich, 99.0% purity) was dissolved in $NH_3 \cdot H_2O$ (Sigma-Aldrich, 28.0–30.0% NH_3) and added into the aqueous solution followed by the addition of citric acid (Sigma-Aldrich, 99.5%). An extra amount of $NH_3 \cdot H_2O$ was added into the solution to adjust the pH value between 6 and 8. The molar ratio of the (total) metal ions, EDTA and citric acid was kept at 1 : 1 : 2. The solution was then heated at 100 °C to evaporate the water resulting in a transparent gel. This gel was later pre-fired at 250 °C for 3 h and calcined at 700 °C in air for 5 h; resulting in a fluorite oxide powder precursor.

For membrane preparation, ~0.5 g of the powder precursor was pressed into a disk in a stainless-steel mold (15.0 mm in diameter) under a hydraulic pressure of approximately 1.5×10^8 Pa. These disks (~1.0 mm in thickness) were then sintered at 1450 °C for 10 h using a ramping and cooling rate of 2 °C min^{-1}. For comparison, the $Ba_{0.5}Sr_{0.5}Co_{0.8}Fe_{0.2}O_{3-\delta}$ (BSCF) membrane was also fabricated through the above EDTA–citrate method with the final sintering temperature at 1100 °C for 5 h. A GDC–Ag slurry mixture was used as the coating material. Ag paste (~85 wt%) was used as the metal decoration. Several different GDC–Ag slurries with a weight ratio of (GDC to Ag) 8 : 2, 6 : 4, 5 : 5, 4 : 6 and 2 : 8 were prepared by stirring for 1 h. A terpineol based solution (Ink vehicle, Fuel Cell Materials), which is often used to create ceramic paste, was added as a solvent to adjust the slurry viscosity. The best viscosity was attained when the weight ratio of GDC to the ink vehicle was kept at ~1 : 2. The slurry was applied onto the surface of the disk by painting with a brush. As reference data, Ag

paste and GDC powder mixed with an ink vehicle were also prepared as a coating onto the disk. The weight of the disk was measured before and after coating to obtain a consistent weight of coating. After coating, all disks were heated in air at 900 °C for 5 h. **Table 4.1** lists several different decoration configurations for this work.

Table 4.1 GDC membranes with different configuration of decoration

Decoration No	Decoration materials
0	No decoration
I	GDC-Ag (8:2) mixture on both feed and permeate sides
II	GDC-Ag (6:4) mixture on both feed and permeate sides
III	GDC-Ag (5:5) mixture on both feed and permeate sides
IV	GDC-Ag (4:6) mixture on both feed and permeate sides
V	GDC-Ag (2:8) mixture on both feed and permeate sides
VI	Ag on both feed and permeate sides
VII-1	GDC-Ag (6:4) mixture on feed side and Ag on permeate side
VII-2	GDC-Ag (6:4) mixture on permeate side and Ag on feed side
VIII-1	GDC-Ag (5:5) mixture on feed side and Ag on permeate side
VIII-2	GDC-Ag (5:5) mixture on permeate side and Ag on feed side
IX-1	GDC-Ag (4:6) mixture on feed side and Ag on permeate side
IX-2	GDC-Ag (4:6) mixture on permeate side and Ag on feed side

4.2.2 Characterization and analysis

The phase and structure of the disks were determined by powder X-ray diffraction (XRD) analysis on a Bruker D8 Advance X-ray diffractometer with Cu-Ka radiation (40 kV and 30 mA). The disk morphology was probed using a Zeiss Neon 40EsB FIBSEM scanning electron microscope (SEM) equipped with an energy dispersive X-ray (EDX) analyzer (15 kV accelerating voltage).

The gas composition of the permeate stream was analyzed using a Shimadzu 2014A gas chromatograph (GC) equipped with a 5 °A capillary molecule column and thermal conductivity detector. The disk was fixed onto the quartz tube and sealed using silver paste. The effective disk membrane area was 0.45 cm^2 calculated using the inner diameter of the quartz tube. The disk was exposed to ambient air with an oxygen partial pressure of 0.21 atm. Ultra-high purity helium (BOC, 99.999%) was applied as the sweep gas to carry the permeated oxygen to the GC. Assuming that the leakage of nitrogen and oxygen through pores or cracks follows Knudsen diffusion, the O_2 leakage can be obtained from N_2 leakage from the relationship of

$J_{N_2}^{Leak} : J_{O_2}^{Leak} = \sqrt{32/28} \times 0.79 : 0.21 = 4.02$. The O$_2$ permeation flux can be obtained

after subtracting the O$_2$ leakage using the equation below:

$$J_{O_2}(\text{mL min}^{-1} \text{ cm}^{-2}) = \left[C_{O_2} - C_{N_2}/4.02 \right] \times \frac{F}{S} \qquad \text{(Eq. 4.1)}$$

where C_{O_2} and C_{N_2} are the concentration of oxygen and nitrogen in the permeate stream, respectively, F is the flow rate of the permeate stream (mL min^{-1}) and S is the effective disk membrane area (cm^2).

The electrochemical impedance spectra of the decorated GDC were tested at 650–800 °C using a GAMRY electrochemical workstation with a frequency of 0.1–10^5 Hz, and the signal amplitude was 10 mV. Helium of 100 mL min^{-1} was applied to the permeate side during the test. The GDC–Ag mixture was decorated onto a 1 mm thick GDC membrane with an effective area of ~0.3 cm^2, and was connected with Ag wire.

4.3 Results and discussion

Figure 4.2 depicts the powder X-ray diffraction patterns of a typical Ce$_{0.9}$Gd$_{0.1}$O$_{2-\delta}$ (GDC) disk membrane decorated with a GDC–Ag dual-phase mixture on the feed side; represented by GDC–Ag (5 : 5). The GDC phase co-existed with the Ag phase since the peaks can be resolved into two sets of characteristic peaks; one from CeO$_2$ (PDF no. 43-1002) and another from Ag (PDF no. 65-2871).[30] No other additional peaks were observed, indicating the absence of the reaction between GDC and Ag and the inertness of both phases, at least up to 900 °C.

We utilized a simple brush-painting method to decorate the disk membrane as reported previously.[31,32] The surface morphology of the GDC membrane decorated with GDC-Ag mixture of different weight ratios is shown in **Figure 4.3(a-e)**. For the 80 wt.% GDC (balanced by 20 wt.% Ag) containing decoration, **Figure 4.3(a)** indicates the formation of a porous decoration layer with increased surface area (relative to the dense disk surface) which is expected to improve the surface kinetics. Upon adding the Ag content to 40 wt.% (**Figure 4.3(b)**), several distinct particle spots start appearing on the surface (one of which is confined within the red circle). These brighter spots are Ag grains, which become uniformly distributed all over the surface at 50 wt.% Ag (**Figure 4.3(c)**) and dominate at even higher contents of 60 and 80 wt.% Ag (**Figure 4.3(d)** and **Figure 4.3(e)**). This observation is reminiscent of the previously for yttria-stabilized

zirconia-Pd and $Bi_{1.5}Y_{0.3}Sm_{0.2}O_3$-Ag composite membranes.[19,22] **Figure 4.3(f)** in turn shows the interface between the dense GDC disk membrane and GDC-Ag (5:5) decoration. The decoration adheres well to the disk surface.
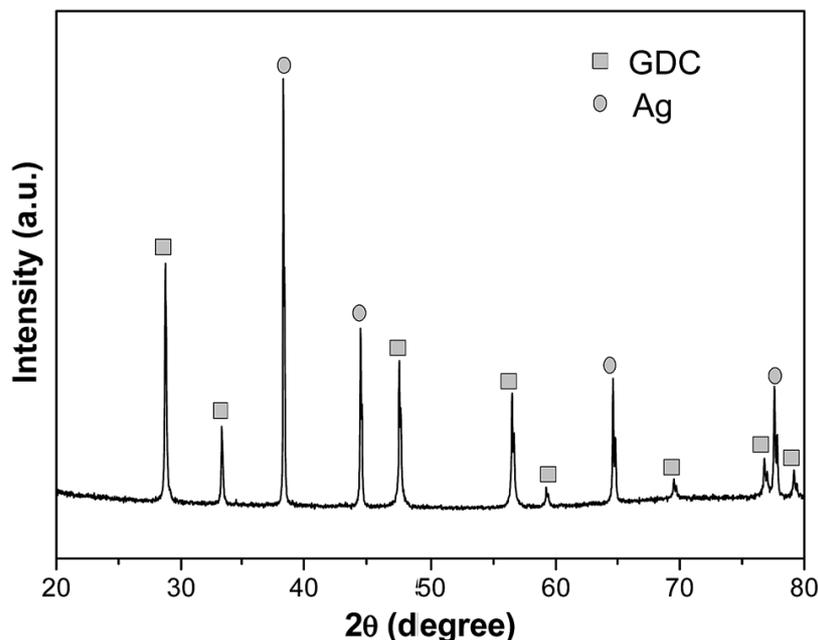
Figure 4.2 Typical powder x-ray diffraction pattern of GDC membrane decorated with GDC-Ag mixture (Represented by GDC-Ag (5:5)).

To check the characteristics of the electronic conducting phase, Ag distribution was probed using energy dispersive x-ray (EDX) mapping; the results of which are displayed as **Figure 4.4**. White spots represent Ag locations; the amount of which is increasing with higher Ag content. For 20 and 40 wt. % Ag-containing decorations, Ag phase are surrounded by GDC phase (**Figure 4.4(a) and (b)**). Here, Ag grains are lumped and therefore, are quite isolated from each other. At higher than 40 wt.% Ag, Ag grains can be spotted almost everywhere (**Figure 4.4(c) and (d)**); which indicates that the Ag phase become continuous. This assessment brought forward the hypothesis that the improved electronic conductivity arisen from continuous electronic conductor network is attained only for a higher than 40 wt.% Ag composition.

Figure 4.5 depicts the temperature-dependent oxygen permeation fluxes of GDC disk membranes using different compositions of Ag-GDC decorations in feed and permeate sides. With the exception of sample 0 and VI, all other samples (samples I-V) were decorated with identical dual-phase compositions on feed and permeate sides. The results reflect the average of three repeated measurements with an error margin within
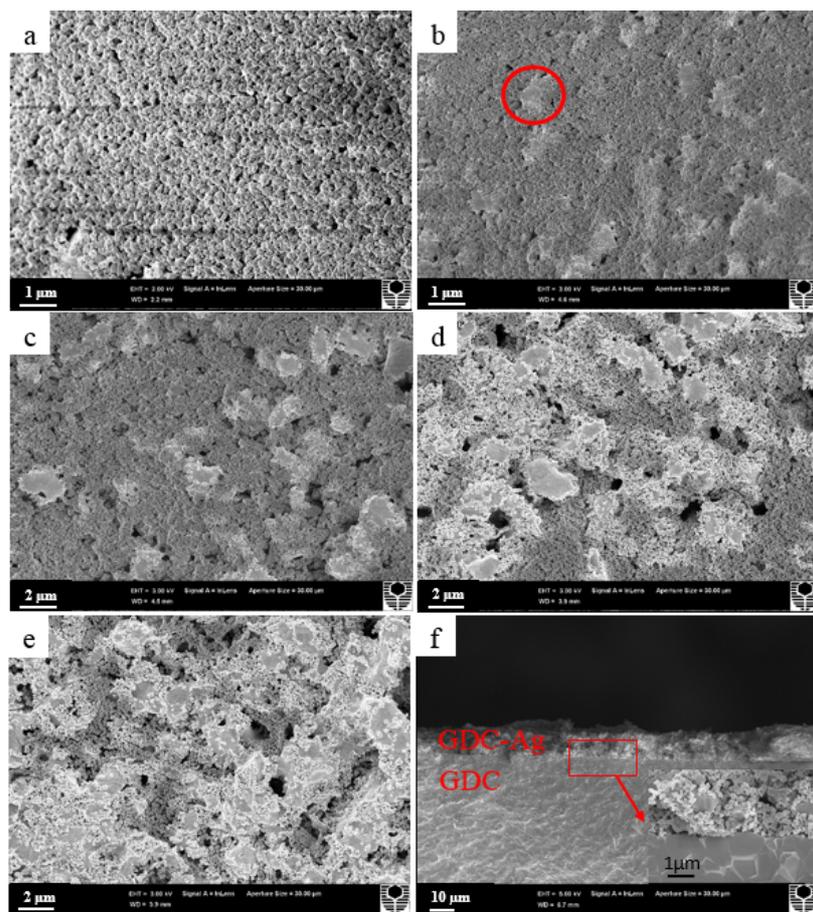
Figure 4.3 Scanning electron microscope images on the surface of GDC membranes decorated with GDC-Ag mixture: (a) GDC-Ag (8: 2) (c I), (b) GDC-Ag (6: 4) (sample II), (c) GDC-Ag (5: 5) (sample III), (d) GDC-Ag (4: 6) (sample IV), (e) GDC-Ag (2: 8) (sample V) and (f) on the cross-section image of GDC membranes coated with GDC: Ag mixture: GDC-Ag (5: 5) (sample III), inset is the magnification image of interface area.

10%. Sample 0 with no decoration showed the lowest oxygen flux due to the lack of electronic conductivity. Similar as sample 0, sample I with 20 wt.% Ag decoration started to permeate oxygen at above 750 °C. It showed the lowest fluxes among all decorated membranes with the largest flux of 0.022 mL min^{-1} cm^{-2} at 850 °C. This value is quite similar to the reported oxygen flux for samarium-doped ceria membrane, $Sm_{0.2}Ce_{0.8}O_{1.9}$ in the absence of surface decoration.[13,26] For sample II utilizing 40 wt.% Ag decoration, increased oxygen fluxes are noted at all tested temperatures due to formation of more TPBs (will be discussed in more detail below). The flux reaches 0.034 mL min^{-1} cm^{-2} at 850 °C. Relative to sample II, the oxygen fluxes of sample III with 50 wt.% Ag decoration markedly increase by up to an order of magnitude. The
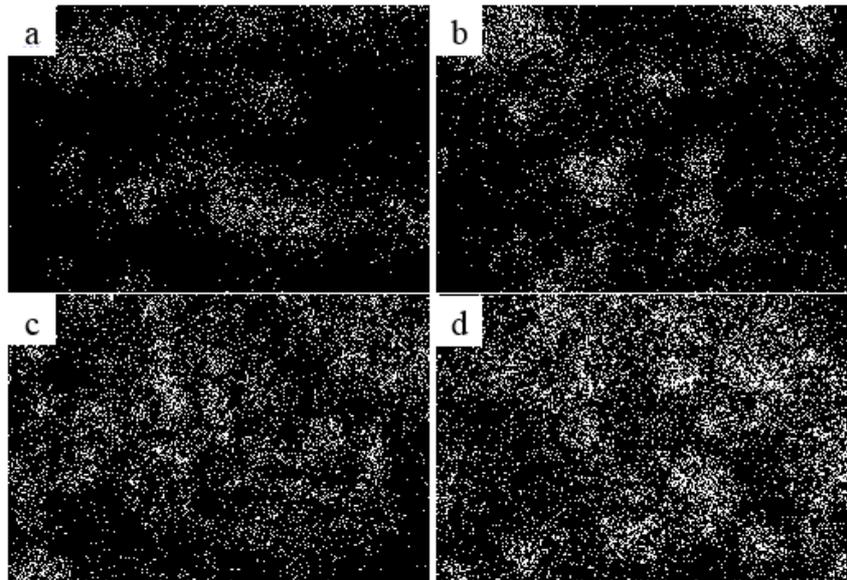
Figure 4.4 Energy dispersive mapping of Ag on GDC-Ag decoration: (a) GDC-Ag (8: 2) (sample I), (b) GDC-Ag (6: 4) (sample II), (c) GDC-Ag (5: 5) (sample III), (d) GDC-Ag (2: 8) (sample V).
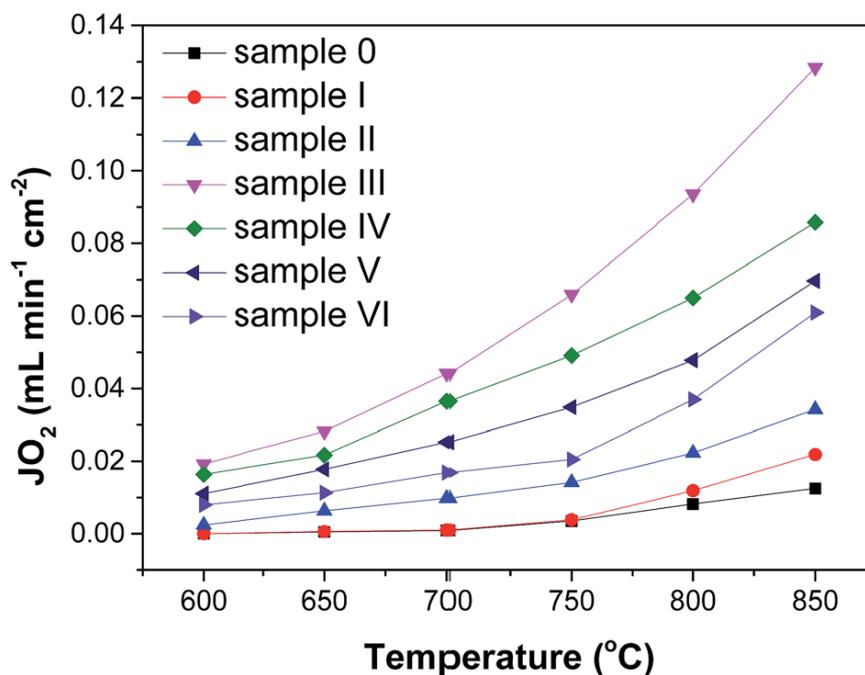
Figure 4.5 Oxygen permeation fluxes of GDC disk membranes decorated with a GDC–Ag mixture or Ag (refer to **Table 4.1** for the configuration).

largest flux was 0.128 mL min^{-1} cm^{-2} at 850 °C. This phenomenon supports our hypothesis above. Since the Ag phase became continuous at this composition, the percolation threshold of GDC-Ag is therefore 50 wt.%. Above this threshold, the

oxygen transport is no longer limited by the electronic conductivity. The oxygen ionic conductivity alternately, can be argued as a more dominant factor onward. The progressive decrease of fluxes encountered on going from sample III to sample IV and finally to sample V seems to correlate with the amount of fluorite phase in these samples' decorations. As a reference, the performance of sample VI with Ag decoration on feed and permeate sides is included; displaying a maximum flux of 0.061 mL min^{-1} cm^{-2} at 850 °C. Notably, the performance of sample VI was lower than the performances of samples III-V, yet higher than those for samples I and II. The observed trend in **Figure 4.5** can be explained in terms of the contributions from electronic conductivity and the triple-phase boundaries (TPBs); where the latter is defined as the contact area between ionic conductor (oxygen ions), electronic conductor (electrons) and gas phase (oxygen gas).[33-36] Despite the formation of more TPBs attained from adding the isolated Ag (metal) phase to continuous GDC (fluorite) phase, the enhanced surface activity (for samples I and II) could not overtake the performance of Ag decoration (of sample VI) given their limited electronic conductivity. Once the Ag phase percolated, the electronic conductivity limitation was surpassed (for samples III, IV and V) and the performance could be rationalized based on the amount of TPBs (which was reduced upon decreasing the amount of the fluorite phase, assuming Ag phase is the dominant phase). According to our previous calculation,[31] the obtained oxygen fluxes here are lower than the theoretical value. This indicates that the surface resistance contributes to limit the overall oxygen permeation although we applied effective surface decoration.

The calculated activation energy values reflect the beneficial effect of using optimized dual-phase compositions where the fluxes for sample III provided substantially lower activation energy (63.76 kJ mol^{-1}) with respect to the fluxes for sample I (166.77 kJ mol^{-1}) and sample VI (104.16 kJ mol^{-1}) at temperature range of 700-850 °C. Since lower activation energy implies less dependence of performance with temperature change, it is of interest particularly when high performance at lower temperatures is sought after.

We re-confirmed the effect of the TPBs by implementing Ag decoration on the permeate side or feed side (instead of dual-phase decoration) for 3 samples (compare samples VII-1-IX-2 to the originals, samples II-IV – Refer to Table 1). **Figure 4.6** reveals that the oxygen fluxes of the resultant samples, denoted as samples VII-1, were inferior to the fluxes of the original configurations (samples II- IV) (See also **Figure 4.5**), but better than samples VII-2, VIII-2 and IX-2, giving evidence that the presence

of TPBs in the feed side was essential to enhance the surface reaction here *e.g.* oxygen gases dissociation into oxygen ions.
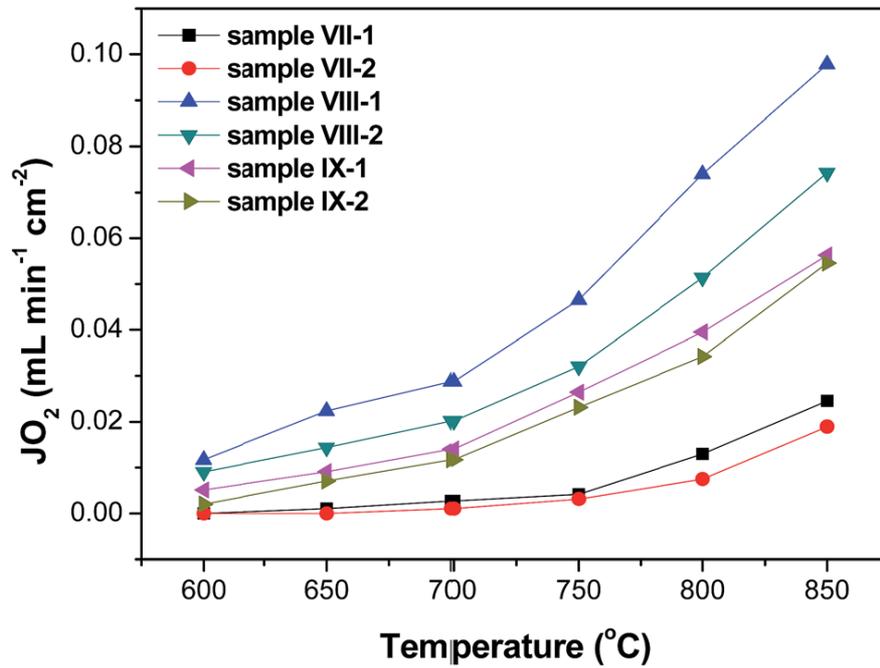
Figure 4.6 Oxygen permeation fluxes of GDC disk membranes with asymmetric decoration (Refer to **Table 4.1** for the configuration).

Our discussion on the percolation concept and TPBs is illustrated in **Figure 4.7**. The green and grey colored substrate corresponds to oxygen ionic and electronic conductor phase, respectively. **Figure 4.7(a)** shows the oxygen permeation process with single Ag decoration, while **Figure 4.7(b)** shows that with dual-phase GDC-Ag decoration. For both kinds of decoration, the surface exchange reactions on the feed and permeate side are:

$$\frac{1}{2}O_2 + V_O^{\cdot\cdot} + 2e \rightarrow O_O^{\times} \text{ (feed side)} \tag{1}$$

$$O_o^{\times} \rightarrow \frac{1}{2}O_2 + V_O^{\cdot\cdot} + 2e^{\cdot} \text{ (permeate side)} \tag{2}$$
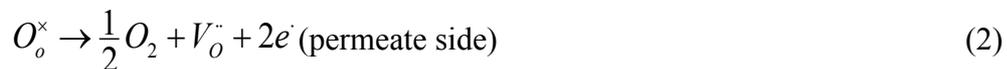
These reactions occur on the TPBs (purple square section on **Figure 4.7(a) and (b)**). Here the TPBs are the connection points of GDC, Ag and gas (oxygen or He). For single Ag decoration, the Ag will be agglomerated during the high temperature treatment, leading to the coverage of GDC areas by large Ag particles, therefore decreasing the TPB areas (**Figure 4.7(a)**). In this case, the very limited TPB areas result in the less reaction sites for oxygen deposition and diffusion on GDC membrane. By decorating

dual phase GDC-Ag, the Ag agglomeration is restricted due to the existence of GDC particles around Ag particles. In addition, the TPB areas can form at every interface between GDC and Ag particles (more purple squares section in **Figure 4.7(b)**). The increased amount of the reaction sites leads to increased surface reaction activity; more oxygen is decomposed on the surface and then transfers to the dense GDC membrane. Of course, a strong adhesion between the decoration layer and GDC membrane is essential to guarantee the oxygen ion transfer, which can be confirmed by **Figure 4.3(f).** Upon increasing the amount of Ag beyond 50 wt.%, the amount of TPBs is expected to decrease due to the less amount of GDC phase (in contact with the Ag phase) as well as the agglomeration of Ag. However, decreasing the amount of Ag below 50 wt.% results in the decrease of continuous electronic conducting paths, leading to the low oxygen flux.
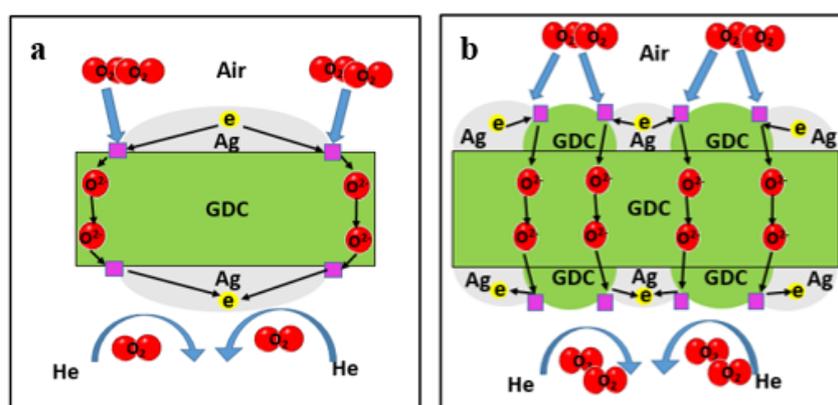
Figure 4.7 Schematic diagram showing the effects of different coatings on the oxygen permeation process: (a) pure electronic conductor of Ag; and (b) dual-phase GDC-Ag.

We further studied the effect of decoration from the view of electrochemistry. **Figure 4.8** shows the electrochemical impedance spectra (EIS) of GDC membranes coated with different decorations (sample I to sample VI) at open circuit voltage at different temperatures. Based on previous research of EIS of oxygen separation membranes[37-40] and the data from this study, the results were evaluated based on an equivalent circuit with a configuration of $LR_{ohm}(RCPE)_1(RCPE)_2$ (**Figure 4.8(g)**), where L is ascribed to the inductance of Ag leads and current collectors; R_{ohm} includes the ohmic resistance from the electrolyte (bulk membrane), the electrode (decoration) and the Ag lead and current collector; R_1 and R_2 are surface polarization resistance (R_p) including electron transfer, oxygen surface adsorption/ dissociation and surface

diffusion; R_{ohm} and R_p present the total ohmic resistance of the decorated membrane, denoted as R_t (Refer to Figure 8a 800 °C as an example).[37,40] From **Figure 4.8(a-f)**, it is observed that the ohmic resistance of sample I is larger than sample II, and both are larger than the rest samples, which have a similar ohmic resistance. For example, at 800 °C, the ohmic resistance of sample I is 4.24 Ω cm^{-2}, compared with 3.09 Ω cm^{-2} of sample II and about 1.20 Ω cm^{-2} of the other four samples. This is quite consistent with our analysis that the electronic conductivity was not sufficient when Ag content was lower than 40 wt.%. Furthermore, 50 wt.% Ag is a threshold value, above which the Ag particles are continuous and provide highest electronic conductivity for the oxygen permeation process. High oxygen surface reactivity is reflected by low R_p. Taken the test at 800 °C as an example, the R_p of sample III was 0.33 Ω cm^{-2}, which is lower than 0.39, 0.87, 1.38,1.70 and 2.85 Ω cm^{-2} of samples IV, V, VI, II and I, respectively, mirroring that the 50 wt.% Ag provides sufficient electronic conductivities and the maximum TPBs. For sample III, the largest amount of TPBs can promote the oxygen surface reactions to a maximum state thus providing the best flux values. On the other hand, the total resistances for all samples are still high, suggesting that the oxygen permeability of membranes is determined by both bulk diffusion and surface exchange reactions. Therefore, oxygen permeation flux can be increased through decreasing bulk diffusion resistance apart from the surface decoration.

Figure 4.9 shows evidence that the oxygen permeation process through GDC disk membranes decorated by GDC-Ag (5:5) is partly limited by the bulk-diffusion step. When the bulk-diffusion step dominates, the oxygen flux has a reciprocal relationship to the membrane thickness. At 850 °C, reducing the thickness from 1.5 mm to 1 mm gives ~60% higher fluxes (from 0.079 to 0.128 mL min^{-1} cm^{-2}). Less enhancement is noted upon reducing the thickness further from 1 mm to 0.6 mm *e.g.* ~30% from 0.128 to 0.167 mL min^{-1} cm^{-2}). This is in accordance with the more prevalent role the surface reaction step plays at a lower thickness. It can be noted that the enhancement of oxygen fluxes are more evident at higher temperatures in view of the thermally activated nature of both bulk-diffusion and surface reaction steps.[19,41,42]

Another process variable which affects the oxygen fluxes through GDC disk membrane decorated by GDC-Ag (5:5), to a much less extent than temperature, is the oxygen partial pressure on the permeate side (**Figure 4.10**). Decreasing the effective oxygen partial pressure can be achieved by increasing the sweep gas flow rate. The relationship between oxygen fluxes and the oxygen partial pressure follows the Wagner

equation:

$$J_{O_2} = \frac{RT}{16F^2L} \sigma_i \ln \frac{P'_{O_2}}{P''_{O_2}}$$
(Eq. 4.2)

Where R is the ideal gas constant, T is the absolute temperature, F is the Faraday constant, L is the thickness of membranes, σ_i is the oxygen ion conductivity, and P'_{O_2} and P''_{O_2} are the oxygen partial pressure at the feed and sweep side.
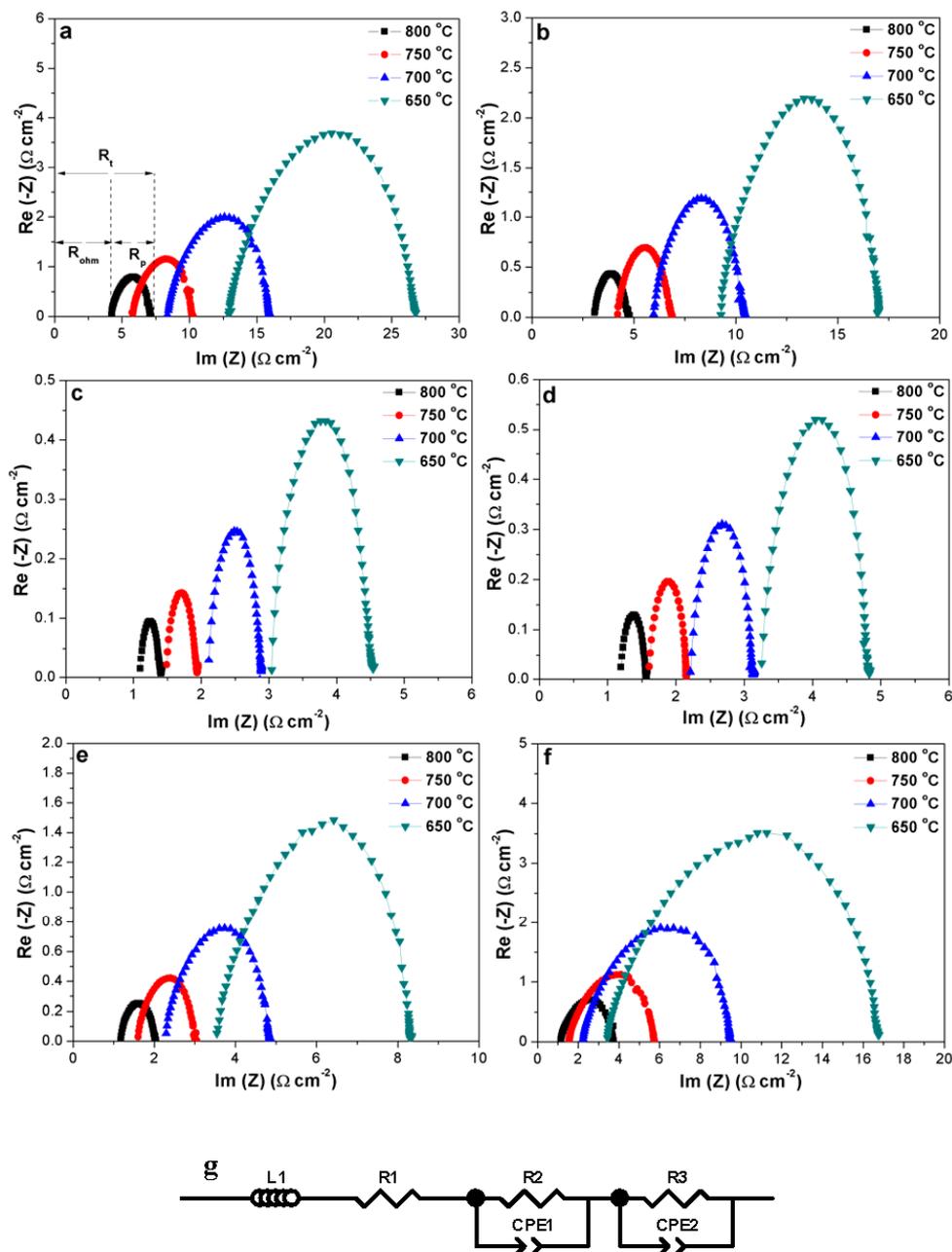
Figure 4.8 Impedance spectra of decorated GDC at different temperatures, (a)–(f) correspond to sample I–sample VI, and (g) is the equivalent circuit.
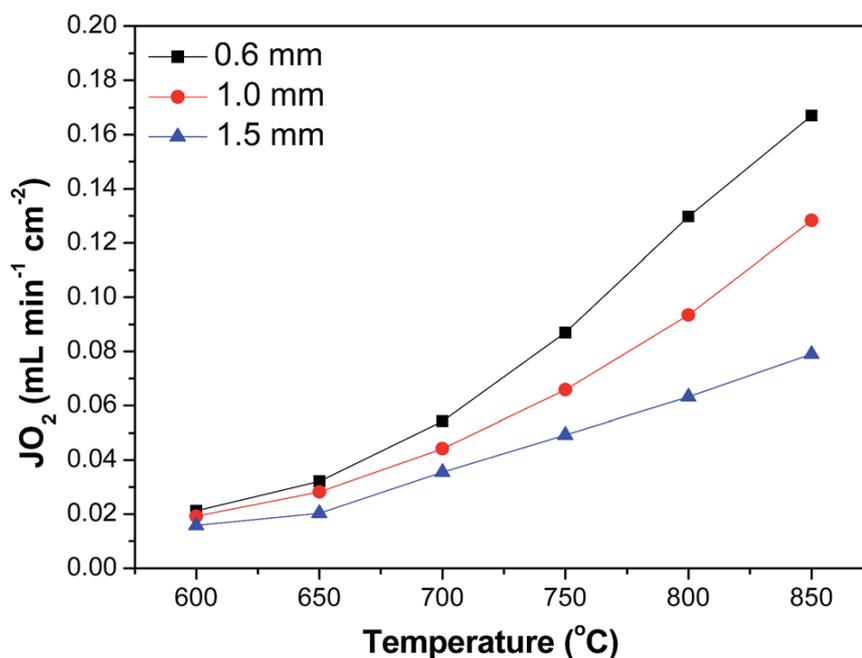
Figure 4.9 The thickness dependence of oxygen permeation fluxes of GDC disk membranes decorated with the GDC–Ag (5 : 5) mixture (sample III).
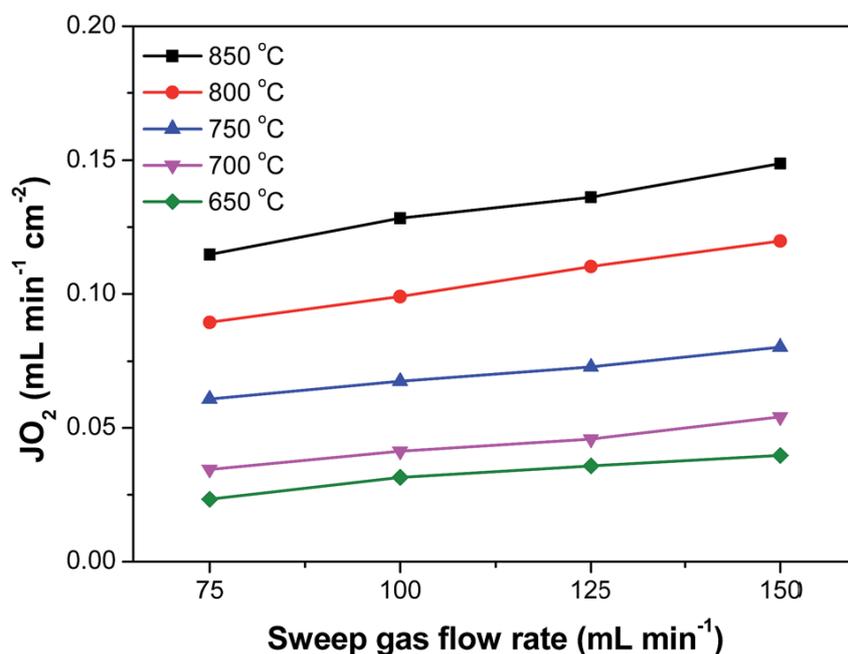
Figure 4.10 The effect of sweep gas flow rate on oxygen permeation fluxes of GDC disk membranes decorated with the GDC–Ag (5 : 5) mixture (sample III).

For practical operations, long-term performance and stability of the membrane is important. Stability to CO_2 in particular, is of interest for Oxyfuel applications.[15,43,44] We carried out stability test by operating the GDC disk membrane decorated by GDC-

Ag (5:5) at 800 $^{\circ}$C and exposed the membrane to a pure helium stream and a mixture of He and CO_2 sweep gas (**Figure 4.11(a)**). The membrane maintained fluxes of ~0.091 mL min^{-1} cm^{-2} during the initial 20 hours. Introduction of 10 vol.% CO_2 induced minor reduction, ~24 % drop from the initial fluxes, which is related to the CO_2 adsorption on the membrane surface impeding some reaction sites.[41,45,46] During the next 130 hours testing using 10 vol.% CO_2, no flux decay was observed; most likely due to the excellent resistance of GDC towards CO_2.[47,48] More importantly, the initial fluxes values could be recovered when the sweep gas was switched back to He. This full recovery rules out the presence of reactions between the membranes and CO_2. We also noticed that the decoration was still strongly attached to the membrane surface after the test. Compared to the pure Ag coating, the thermal expansion mismatch of the decoration from the dual phase (GDC+Ag) coating with the bulk membrane GDC has been reduced, thus resulting in a more stable membrane integration.

For comparison purposes, the oxygen flux values of BSCF membrane (1.5-mm-thickness) operated at similar conditions were also presented in **Figure 4.11**. As can be seen, compared with single phase perovskite membranes, the initial flux through the short-circuited GDC membrane is 10 times lower. Thus the GDC membrane is not intended for pure oxygen production but mainly for membrane reactors such as syngas production from methane. Under these reaction conditions, the oxygen in the permeate side will be consumed by the reaction, creating a much larger oxygen concentration gradient through the membrane than that employed in this operating condition by inert sweep gas, i.e., 0.21 atm (air)/10^{-8} to 10^{-16} atm as opposed to 0.21 atm (air)/10^{-3} atm (sweep), which will no doubt drive the oxygen flux to a much higher value. Also noteworthy is that the oxygen flux rate through BSCF membrane (**Figure 4.11(b)**) dropped sharply and could not be recovered after introducing 10 vol.% CO_2 inside the sweep gas despite only 28 hours operation due to the surface reactions with CO_2 causing permanent membrane damage. In comparison with our previous short-circuited SDC membranes, the observed oxygen fluxes in this work are lower. We attribute this mainly to the lower ionic conductivities of gadolinium-doped ceria (GDC) relative to samarium doped ceria (SDC) which were used in our previous works.[49-52] In theory, the maximum oxygen fluxes can be calculated assuming that the surface reactions do not pose any resistance to overall oxygen transport rate which is completely controlled by the ionic bulk diffusion. According to the theoretical calculation of such maximum oxygen flux achieved for a short-circuited GDC, i.e., ~0.25 mL min^{-1} cm^{-2} at 800 $^{\circ}$C,[53] our observed

flux (~0.09 mL min^{-1} cm^{-2} at 800 ^{o}C) for sample III is quite reasonable given that in reality the resistance of the surface reactions also limits the overall oxygen transport.
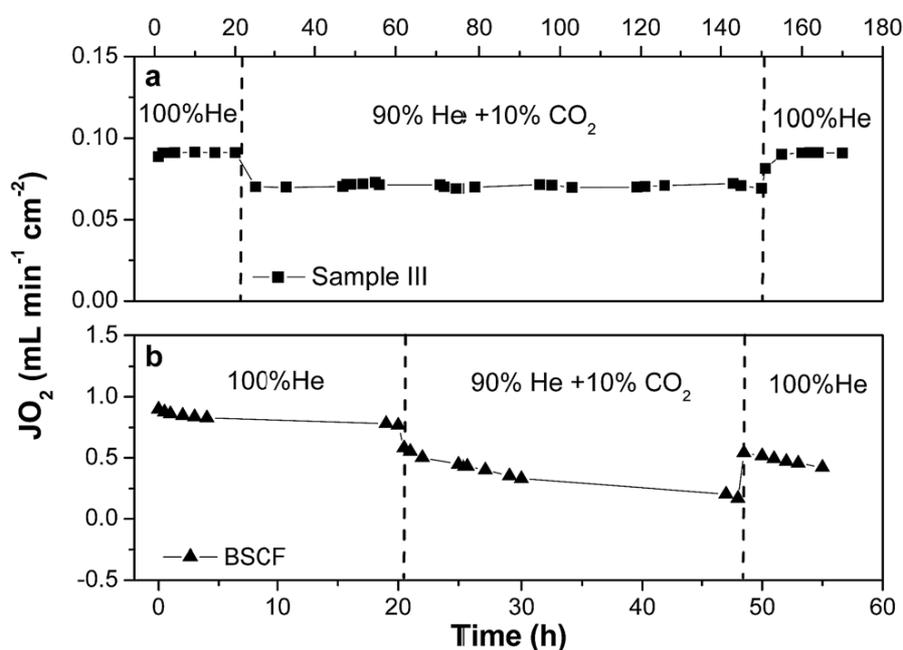
Figure 4.11 Long term oxygen permeation performance of (a) GDC disk membranes decorated with GDC-Ag (5:5) mixture (sample III) and (b) BSCF at 800 ^{o}C under He and a He + CO$_2$ mixture sweep gas. The sweep gas flow rate was 100 mL min^{-1}.

In comparison with the literature, we also noted that in some cases, the oxygen flux through the dual-phase decorated GDC membranes is comparable with these GDC dual-phase bulk membranes where the electronic phase is chosen from ceramic spinel (NiFe$_2$O$_4$), iron oxide or perovskite (La$_{0.7}$Sr$_{0.3}$MnO$_{3-\delta}$).[54-56] However, the long term stability of these membranes is still a concern as the reactions between the two phases or the reactions between electronic ceramics and CO$_2$ gases at high operating temperatures cannot be precluded. Higher oxygen fluxes were also reported on zinc oxide doped GDC dual phase membranes by designing a more robust ionic conducting phase.[53] More research activities are in progressing to optimize the ionic conducting phase or the electronic phase to further improve the flux, stability and to reduce the negative impacts from grain boundary area yielded by the high temperature membrane synthesis. However, we can predict that the reported strategy in this work using a short-circuit via dual phase decoration to improve the membrane performance is applicable to all these cases even in the future more robust ionic phase or the electronic phase is

identified and applied. Given these advantages, the robust fluorite ion conducting membranes decorated with appropriate dual-phase coatings would become a good choice to fabricate oxygen permeation membranes.

4.4 Conclusion

The present study demonstrates the feasibility of extending the dual-phase bulk membrane idea into a thin dual phase coating layer to decorate the pure bulk fluorite ion conducting membrane with short-circuited electronic phase for oxygen permeation. The effects of different GDC/Ag ratio in the decoration layer on the polarization resistance, triple-phase boundary area and the resultant oxygen permeation flux at various operating conditions have been discussed. We found that, for $Ce_{0.9}Gd_{0.1}O_{2-\delta}$ (GDC)-Ag dual-phase decoration, a continuous Ag network can be achieved by mixing 50 wt.% of Ag and GDC. EIS results demonstrated that GDC-Ag (5:5) has the lowest surface polarization resistance and provides the best oxygen fluxes. GDC disk membrane in 1-cm-thickness decorated with GDC-Ag (5:5) mixture showed a maximum flux of 0.128 mL min^{-1} cm^{-2} under an air/helium gradient at 850 °C. The short-circuited GDC membrane also demonstrated strong stability, retaining the original performance during the 130-hour-testing whilst exposing the membrane to an atmosphere containing CO_2. This dual-phase decoration strategy brings in at least three advantages: more triple-phase boundary area for membrane surface reaction, cheaper material cost by the reduced usage of precious metals and the increased membrane stability.

4.5 References

1. A. Leo, S. Liu and J. C. Diniz da Costa, Int. J. Greenhouse Gas Control, 2009, 3, 357-367.
2. M. Czyperek, P. Zapp, H. J. M. Bouwmeester, M. Modigell, K. Ebert, I. Voigt, W. A. Meulenberg, L. Singheiser and D. Stöver, J. Membr. Sci., 2010, 359, 149-159.
3. J. Repasky, D. McCarthy, P. Armstrong and M. Carolan, Air Products and Chemicals, Inc., ITM technology for carbon capture on natural gas and hybrid power systems, Washington DC, 2014.

4. S. Pei, M.S. Kleefisch, T.P. Kobylinski, J. Faber, C.A. Udovich, V. Zhang McCoy, B. Dabrowski, U. Balachandran, R. L. Mieville and R. B. Poeppel, Catal. Lett., 1994, 30, 201-212.

5. V.V. Kharton, A.A. Yaremchenko, A.V. Kovalevsky, A.P. Viskup, E.N. Naumovich and P. F. Kerko, J. Membr. Sci., 1999, 163, 307-317.

6. W. Jin, S. Li, P. Huang, N. Xu, J. Shi and Y. S. Lin, J. Membr. Sci., 2000, 166, 13-22.

7. H.J.M. Bouwmeester, Catal. Today, 2003, 82, 141-150.

8. A. Waindich, A. Möbius and M. Müller, J. Membr. Sci., 2009, 337, 182-187.

9. World nuclear association, http://www.world-nuclear.org/info/Energy and-Environment/-Clean-Coal-Technologies/, (accessed May 2014).

10. X. Tan, N. Liu, B. Meng and S. Liu, J. Membr. Sci., 2011, 378, 308-318.

11. J. H. Joo, K. S. Yun, C.-Y. Yoo and J. H. Yu, J. Mater. Chem A, 2014, 2, 8174-8178.

12. Q. Li, X. Zhu and W. Yang, J. Membr. Sci., 2008, 325, 11-15.

13. K. Zhang, Z. Shao, C. Li and S. Liu, Energy Environ. Sci., 2012, 5, 5257-5264.

14. J. Yi, Y. Zuo, W. Liu, L. Winnubst and C. Chen, J. Membr. Sci., 2006, 280, 849-855.

15. J. Xue, Q. Liao, Y. Wei, Z. Li and H. Wang, J. Membr. Sci., 2013, 443, 124-130.

16. C. M. Chen, Air Products and Chemicals, Inc., US DoE of energy hydrogen program annual review, 2004.

17. B. J. P. Buhre, L. K. Elliott, C. D. Sheng, R. P. Gupta and T. F. Wall, Prog. Energy Combust. Sci., 2005, 31, 283-307.

18. J. Sunarso, S. Baumann, J. M. Serra, W. A. Meulenberg, S. Liu, Y. S. Lin and J. C. Diniz da Costa, J. Membr. Sci., 2008, 320, 13-41.

19. J. Kim and Y. S. Lin, J. Membr. Sci., 2000, 167, 123-133.

20. B. Wang, J. Yi, L. Winnubst and C. Chen, J. Membr. Sci., 2006, 286, 22-25.

21. K. Zhang, J. Sunarso, Z. Shao, W. Zhou, C. Sun, S. Wang and S. Liu, RSC Adv., 2011, 1, 1661-1676.

22. C.S. Chen, B.A. Boukamp, H.J.M. Bouwmeester, G.Z. Cao, H. Kruidhof, A.J.A. Winnubst and A. J. Burggraaf, Solid State Ionics, 1995, 76, 23-28.

23. T. J. Mazanec, T. L. Cable and J. J.G. Frye, Solid State Ionics, 1992, 53-56, 111-118.

24. X. Zhu and W. Yang, in Inorganic, Polymeric and Composite Membranes, ed. S. T. Oyama and S. M. Stagg-Williams, Elsevier, Amsterdam, 1st edn., 2011, vol. 14, ch. 12, pp. 275-293.

25. T. Chen, H. Zhao, Z. Xie, J. Wang, Y. Lu and N. Xu, J. Power Sources, 2013, 223, 289-292.

26. K. Zhang, L. Liu, Z. Shao, R. Xu, J. C. Diniz da Costa, S. Wang and S. Liu, J. Mater. Chem. A, 2013, 1, 9150-9156.

27. S. Imashuku, L. Wang, K. Mezghani, M. A. Habib and Y. Shao-Horn, J. Electrochem. Soc., 2013, 160, E148-E153.

28. L. Wang, S. Imashuku, A. Grimaud, D. Lee, K. Mezghani, M. A. Habib and Y. Shao-Horn, ECS Electrochemistry Letters, 2013, 2, F77-F81.

29. S. Friebe, B. Geppert, and J. Caro, Angew. Chem. Int. Ed. 2015, 54, 7790-7794.

30. ICDD PDF-2 Release 2014, Joint Committee on Powder Diffraction Standards (JCPDS)-International Centre for Diffraction Data (ICDD), Pennsylvania, 2014, Powder Diffraction File (PDF) database.

31. C. Zhang, R. Ran, G. H. Pham, K. Zhang, J. Liu and S. Liu, RSC Adv., 2015, 5, 5379-5386.

32. J. H. Joo, K. S. Yun, Y. Lee, J. Jung, C.-Y. Yoo and J. H. Yu, Chem. Mater., 2014, 26, 4387-4394.

33. V. Dusastre and J. A. Kilner, Solid State Ionics, 1999, 126, 163-174.

34. S. B. Adler, Chem. Rev., 2004, 104, 4791-4843.

35. Y. Zhang, Y. Wang, Y. Wang, F. Chen and C. Xia, J. Power Sources, 2011, 196, 1983-1991.

36. V. M. Janardhanan, V. Heuveline and O. Deutschmann, J. Power Sources, 2008, 178, 368-372.

37. C. Huang, D. Chen, Y. Lin, R. Ran and Z. Shao, J. Power Sources, 2010, 195, 5176-5184.

38. K. Zhang, B. Meng, X. Tan, L. Liu, S. Wang, S. Liu and M. Menon, J. Am. Ceram. Soc., 2014, 97, 120-126.

39. Z. Chen, R. Ran, W. Zhou, Z. Shao and S. Liu, Electrochim. Acta, 2007, 52, 7343-7351.

40. Y. Chen, B. Qian, S. Li, Y. Jiao, M. O. Tade and Z. Shao, J. Membr. Sci., 2014, 449, 86-96.

41. P. F. Haworth, S. Smart, J. M. Serra and J. C. Diniz da Costa, Phys. Chem. Chem. Phys., 2012, 14, 9104-9111.

42. Z. Shao, G. Xiong, Y. Cong and W. Yang, J. Membr. Sci., 2000, 164, 167-176.

43. S. Engels, T. Markus, M. Modigell and L. Singheiser, J. Membr. Sci., 2011, 370, 58-69.

44. X. Zhu, H. Liu, Y. Cong and W. Yang, Chem. Commun., 2012, 48, 251-253.

45. X. Tan, N. Liu, B. Meng, J. Sunarso, K. Zhang and S. Liu, J. Membr. Sci., 2012, 389, 216-222.

46. J. Yi, M. Schroeder and M. Martin, Chem. Mater., 2013, 25, 815-817.

47. W. Wang, C. Su, Y. Wu, R. Ran and Z. Shao, Chem. Rev., 2013, 113, 8104-8151.

48. V. V. Kharton, F. M. Figueiredo, L. Navarro, E. N. Naumovich, A. V. Kovalevsky, A. A. Yaremchenko, A. P. Viskup, A. Carneiro, F. M. B. Marques and J. R. Frade, J. Mater. Sci., 2001, 36, 1105-1117.

49. S. Kuharuangrong, J. Power Sources, 2007, 171, 506-510.

50. H. Yahiro, Y. Eguchi, K. Eguchi and H. Arai, J. Appl. Electrochem., 1988, 18, 527-531.

51. T. Kudo and H. Obayashi, J. Electrochem. Soc., 1975, 122, 142-147.

52. R.T. Dirstine, R.N. Blumenthal and T.F. Kuech, J. Electrochem. Soc., 1979, 126, 264-269.

53. S. Cheng, M. Søgaard, L. Han, W. Zhang, M. Chen, A. Kaiser and P.V. Hendriksen, Chem. Commun., 2015, 51, 7140-7143.

54. H. Luo, H. Jiang, K. Efimov, F. Liang, H. Wang and J. Caro, Ind. Eng. Chem. Res. 2011, 50, 13508-13517.

55. H. Luo, K. Efimov, H. Jiang, A. Feldhoff, H. Wang and J. Caro, Angew. Chem. Int. Ed., 2011, 50, 759-763.

56. V.V. Kharton, A.V. Kovalevsky, A.P. Viskup, F.M. Figueiredo, A.A. Yaremchenko, E.N. Naumovich and F.M.B. Marques, J. Eur. Ceram. Soc., 2001, 21, 1763-1767.

Chapter 5: Enhanced oxygen permeability and electronic conductivity of $Ce_{0.8}Gd_{0.2}O_{2-\delta}$ membrane *via* the addition of transition metal oxide sintering aids

Abstract

Fluorite oxide is an excellent material candidate for oxygen production from air, oxyfuel combustion, and membrane reactor given its CO_2 resistance and high oxygen ionic conductivity. However, its limited electronic conductivity restricts its practical applications in these technologies. In this work, we probed the use of transition metals (Co, Fe, and Cu) oxides as the sintering aid and the electronic conductivity enhancement agent. The presence of CoO and CuO decreased the sintering temperature of GDC by 300 ^{o}C while that of FeO decreased the temperature by only 100 ^{o}C. Oxygen fluxes were also enhanced in their presence; reaching the highest of 0.112 mL min^{-1} cm^{-2} at 900 ^{o}C through a 0.8 mm-thick 2 mol.% Co containing GDC (2Co-GDC) membrane. Among the three sintering aids, CoO provided the maximum enhancement effect for oxygen fluxes. We showed that such enhancement primarily comes from the improved electronic conductivities and the modified element distribution across the grain boundaries. In overcoming the electronic conductivity limitation of a predominantly ionic conducting phase, the use of sintering aid offers an attractive non-precious metal-based alternative that enables competitive performance enhancement with respect to the external short-circuit decoration.

5.1 Introduction

Ceramic-based oxygen ionic transport membrane (ITM) has become one the most promising technologies that enables high purity oxygen production, oxy-fuel combustion, membrane reactor for chemical synthesis, and solid oxide fuel cells.[1-7]

146

Oxy-fuel combustion technology in particular offers an attractive route to mitigate CO_2 emission in coal-fired power plants.[2-4] In such technology, to obtain high concentration of CO_2 effluent gas for easy subsequent capture and sequestration purpose, the combustion is performed using pure O_2 which leads to an extremely high temperature. Since such temperature cannot be tolerated by the current combustion system, the use of CO_2 as a sweep gas in the permeate side of the membrane becomes necessary to dilute the heating effect. By letting only O_2 and CO_2 present in the combustion process, the production of nitrous oxide-related gases is additionally prevented. Applying ITM technology in oxy-fuel combustion provides significant cost and energy advantages over the conventional cryogenic distillation process.[2] To be integrated directly into the oxy-fuel combustion system, ITM materials however should be CO_2-resistant.

ITM is generally made from either pure oxygen ionic conducting (IC) or mixed ionic-electronic conducting (MIEC) materials.[1] In IC case, the presence of external circuit is required as an electron pathway to short circuit the two different membrane sides.[8] In MIEC case, on the other hand, such external circuit is not necessary since the electron can pass through the membrane.[8] In both cases, the oxygen transport is driven by the oxygen partial pressure gradient through the membrane.[1] Over the past decades, MIEC materials have been extensively developed, particularly those coming from perovskite oxide family with the structure formula of $ABO_{3-\delta}$. In such perovskite materials, A-site cation is typically alkaline earth metals, *i.e.*, Ca, Sr, and Ba or lanthanides, *i.e.*, La, Gd, and Pr; while B-site cation is normally transition metals, *i.e.*, Co, Fe, Cu, Ti, Zn, and Mn.[1, 9] Alkaline earth metals-containing perovskite oxides nonetheless have low resistance to acidic gases, *i.e.*, CO_2 and SO_2 which makes them impractical for oxyfuel combustion.[10-14] Fluorite oxides with the structure formula of AO_2 such as samarium-doped ceria (SDC), praseodymium-doped ceria (PDC), gadolinium-doped ceria (GDC), terbium-doped ceria (TDC), yttria-stabilized zirconia (YSZ), and yttria-stabilized bismuth oxide (YSB), on the other hand, feature high stability in an acidic atmosphere and high oxygen ionic conductivity but have electronic conductivity limitations.[8, 14-18] Their electronic conductivity limitations can be overcome by adding the second percolative electronic conducting phase inside the membrane; essentially forming the so-called "dual-phase membranes".[1, 19, 20] The second phase can come from either noble metals, electronic conducting oxides, or MIEC oxides.[21-26] One of the main drawbacks of these membranes comes from the chemical compatibility issue between the two constituent phases that can contribute to

significant performance degradation during long operation.[24]

An alternative to "dual-phase approach" that can be viewed as the internal electronic short-circuit approach is the external short-circuit approach. In such an approach, an electronic conductor decoration that is coated on the surface of the membrane, is connected to the metal or conductive ceramic sealant. The integrated decoration and sealant functions as the continuous external electron channel that allows fast electron transfer from one side to another side of the membrane. This concept has been applied onto SDC, GDC, YSZ, or $La_{0.8}Sr_{0.2}Ga_{0.8}Mg_{0.115}Co_{0.085}O_{3-\delta}$ membranes.[8, 27-30] The surface decoration additionally enhances the surface oxygen exchange reaction rate. Despite the relatively low oxygen permeation fluxes observed on the externally short-circuited fluorite membranes, these membranes generally display high stability that enables application in oxy-fuel combustion and membrane reactor.[27, 28, 31]

The electronic conductivity behavior of the fluorite oxide can also be tailored *via* the addition of transition metal oxides sintering aids, i.e., Co-, Fe-, Cu-, Ni- and Mn-oxide, generally in less than 5 mol.% amount. The sintering of ceria-based oxides which normally requires the use of temperature above 1300 ^{o}C to obtain fully dense body;[32] can be lowered down to 1000 ^{o}C in the case of GDC, TDC, and PDC containing the sintering aids.[33-36] More essential is the resultant improvement in the electronic conductivity of the fluorite oxides which, for example, enables PDC and TDC to exhibit oxygen fluxes that are comparable to the fluxes of perovskite membranes.[35-39] In this work, we systematically studied the effects of adding Co-, Fe-, and Cu-oxide as sintering aids into the sintering behavior and the oxygen permeation properties of GDC membrane. Further evaluation into the electronic conductivity behavior and microstructure was also performed. We demonstrated an enhancement in MIEC property *via* the use of sintering aids. The efficiency of this sintering aid strategy is demonstrated by the attainment of oxygen fluxes that is quite competitive to the externally short-circuited GDC membrane;[27, 28] thus highlighting its attractiveness as an alternative to external short-circuit approach in applications requiring CO_2 resistance.

5.2 Experimental

$Ce_{0.8}Gd_{0.2}O_{2-\delta}$ (GDC) powder was synthesized as reported elsewhere.[28] Into this powder, 1, 2 and 5 mol.% of sintering aids (cobalt oxide, iron oxide, and copper oxide) were

added in the form of ethanol solution of nitrates ($Co(NO_3)_2 \cdot 6H_2O$, $Fe(NO_3)_2 \cdot 9H_2O$, and $Cu(NO_3)_2 \cdot 3H_2O$, Sigma Aldrich, 99.9 % purity). To obtain homogeneous slurry, 1 g of GDC powder was soaked in a 1 mL of nitrate solution, as previously reported by Taub *et al.*[40] The mixture was then stirred thoroughly in an agate mortar for at least 30 min, followed by drying at 80 °C for 5 h. The dried powder was further ground for another 30 min, after which the powder was calcined in air for 5 h at 700 °C. The resultant powder was additionally ground for another 30 min to guarantee the homogeneous distribution of sintering aid, resulting in the sintering aid containing GDC powders. These samples are designated as 1Co-GDC, 2Co-GDC, and 5Co-GDC for GDC powders mixed with 1, 2, and 5 mol.% cobalt sintering aids. The samples containing Fe and Cu sintering aids are named following the same designation. To form dense disk membranes for oxygen permeation test, the as-synthesized powders were isostatically pressed into green disks in under a hydraulic pressure of 200 MPa in a stainless-steel mold. These green disks were sintered for 10 h at 1100-1400 °C to achieve high density. The thickness of the sintered disk membrane was adjusted to approximately 0.8 mm.

The phase composition of the sintered powder (crushed from the sintered disk) was determined by powder X-ray diffractometer (XRD, Bruker D8 Advance) with Cu-Kα radiation (30 mA and 40 kV). Microstructure of the membrane was characterized using a scanning electron microscope (SEM, Zeiss Neon 40EsB FIBSEM). High-resolution transmission electron microscopy (HRTEM) and selected area electron diffraction (SAED) images were obtained using a transmission electron microscope (FEI Titan G2 80-200). High angle annular dark field scanning transmission electron microscopy (HAADF-STEM) images and elemental mapping images were obtained with ChemiSTEM technology operating at 200 kV. Samples for TEM characterization were the powders crushed from the sintered disks.

The oxygen permeation fluxes of the GDC membranes were measured in high temperature permeation setup connected with gas chromatography (Shimadzu GC-2014) equipped with a 5A molecular sieve column and thermal conductivity detector. The disk membrane was fixed onto one side of a quartz tube using a silver paste as the sealant. The effective surface area of the disk at the permeate side was 0.45 cm^2. The required driving force, i.e., the oxygen partial pressure difference across the membrane was created by flowing helium or CO_2 as a sweep gas on the permeate side. The details on how to calculate the permeated oxygen flux (J_{O_2}) is reported elsewhere.[41]

Dense rectangular bars with dimensions of $2 \times 0.6 \times 0.1$ cm^3 were pressed and sintered for electrical conductivity measurements, which was performed through standard 4-point DC technique. The samples were connected to a source measuring unit (Keithley 2420) with silver wires and silver paste. The tests were carried out in a tube furnace under air between 350 and 900 °C. The electrochemical impedance spectra (EIS) of the disk membranes were tested using a Gamry electrochemical workstation with the signal amplitude of 10 mV and the frequency range of 0.1 Hz–1.0 MHz. The ionic transfer number was measured and calculated using modified electromotive force (EMF) method proposed by Liu and Hu.[42] This modified EMF method combines EIS and open-circuit voltage to achieve high accuracy. The disk membrane was covered with porous Ag paste with an effective area of ~0.3 cm^2 on both sides as current collector, which was also connected to Ag wire on both sides. The disk membrane was sealed onto a quartz tube with Ag paste. The EIS and open-circuit voltage measurements were performed on a cell with configuration of air, Ag | disk | Ag, p_{O_2}. The calculation details for ionic transfer number can be found elsewhere.[42]

5.3 Results and discussion

5.3.1 Structure characterization

Figure 5.1 depicts the room temperature powder X-ray diffraction (XRD) patterns of GDC, 2Co-GDC, 2Cu-GDC, and 2Fe-GDC powders calcined at 700 °C. All patterns can be indexed according to the single cubic (Fm-3m (225)) fluorite phase (PDF# 50-0201),[43] without the presence of any impurity phases containing Co, Cu, or Fe. The same phase formed for the other GDC powders containing 1, 3, and 5 mol.% sintering aids (**Figure 5.2**). Following the calcination at 700 °C for 5 h, GDC powders containing 2 mol.% transition metals, *i.e.*, 2Co-GDC, 2Cu-GDC and 2Fe-GDC, aggregated into clusters with particle size of approximately 100 nm. After a series of trial and error sintering at different temperatures, we found the lowest temperatures to obtain dense body for membranes containing sintering aids and the ones without them. Take for example the 2 mol.% sintering aids composition as a representative scenario. In the cases of 2Co-GDC and 2Cu-GDC, the membranes became dense with the minimum sintering temperature of 1100 °C (**Figure 5.3(b) and (c)**). In 2Fe-GDC case, on the

other hand, the surface was still porous after sintering at 1100 °C (**Figure 5.4(a)**). Modifying the sintering temperature to 1200 °C led to the formation of partially dense surface with the presence of some pores (**Figure 5.4(b)**). Only after the sintering temperature was increased to 1300 °C, a completely dense surface could be obtained (**Figure 5.3(d)**). This is only 100 °C lower than the minimum sintering temperature of 1400 °C required to obtain dense body for pure GDC membrane. Therefore, it becomes apparent that CoO and CuO are more effective sintering aids to densify GDC-based membranes. Our finding is in accord with the results of the previous studies that demonstrate that CoO and CuO can provide GDC densities over 98 % at lower sintering temperatures than FeO.[35, 44]
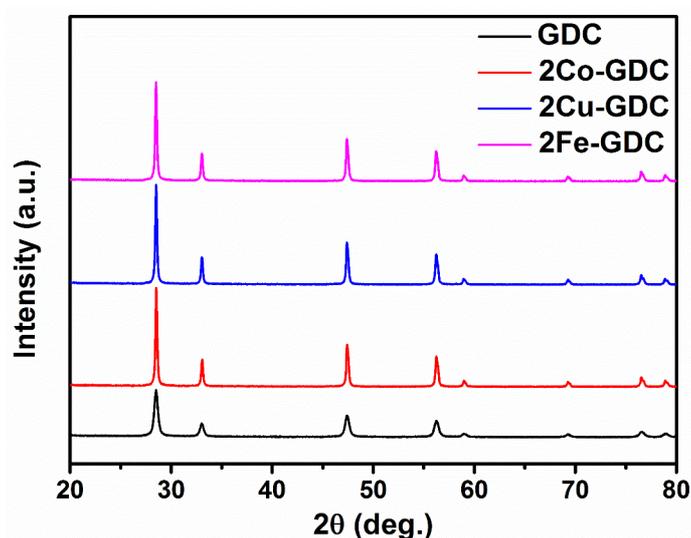
Figure 5.1 Powder X-ray diffraction patterns of GDC, 2Co-GDC, 2Cu-GDC, and 2Fe-GDC.
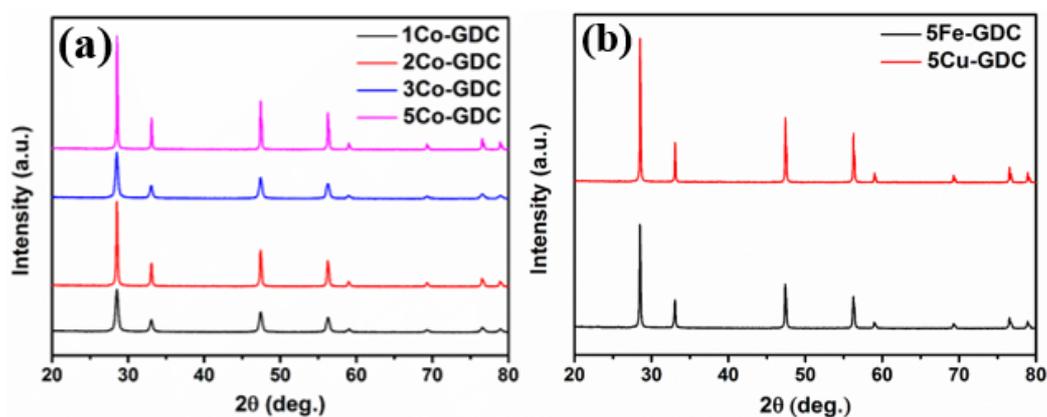
Figure 5.2 Powder X-ray diffraction patterns of (a) 1Co-GDC, 2Co-GDC, 3Co-GDC, and 5Co-GDC; and (b) 5Fe-GDC and 5Cu-GDC.
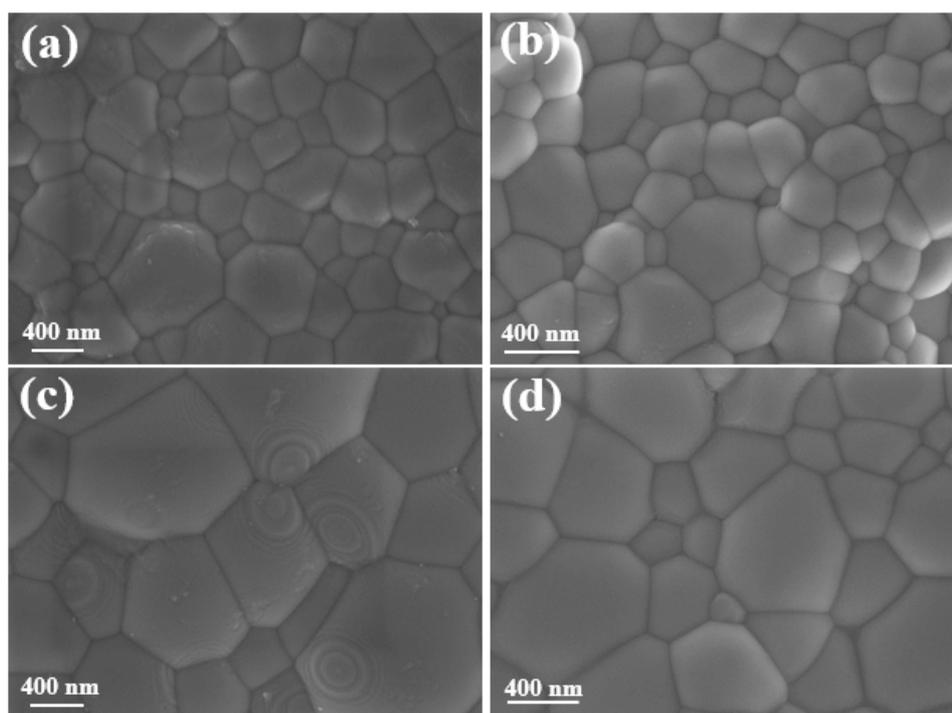
Figure 5.3 Scanning electron microscopy images of the surface of (a) GDC sintered at 1400 ^{o}C; (b) 2Co-GDC sintered at 1100 ^{o}C; (c) 2Cu-GDC sintered at 1100 ^{o}C; and (d) 2Fe-GDC sintered at 1300 ^{o}C.
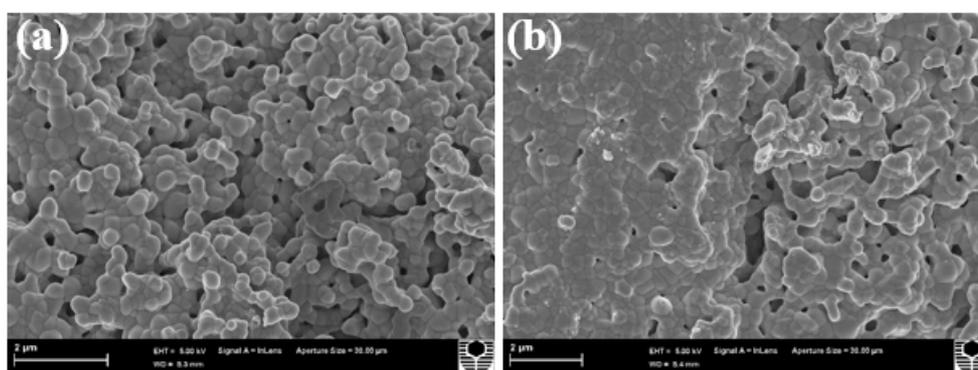
Figure 5.4 Scanning electron microscopy images of the surfaces of 2Fe-GDC sintered at (a) 1100 ^{o}C; and (b) 1200 ^{o}C.

5.3.2 Oxygen permeation performance

Figure 5.5(a) displays the temperature-dependent oxygen permeation fluxes through 0.8 mm-thick GDC disk membranes containing 2 mol.% of different sintering aids, *i.e.*, Co, Cu, or Fe (denoted as 2Co-GDC, 2Cu-GDC, or 2Fe-GDC) between 750 and 950 ^{o}C. Pure GDC exhibited the lowest oxygen fluxes with the maximum of 0.055 mL min^{-1} cm^{-2} at 900 ^{o}C. Temperature rise from 850 ^{o}C to 950 ^{o}C manifested into triple increase

152
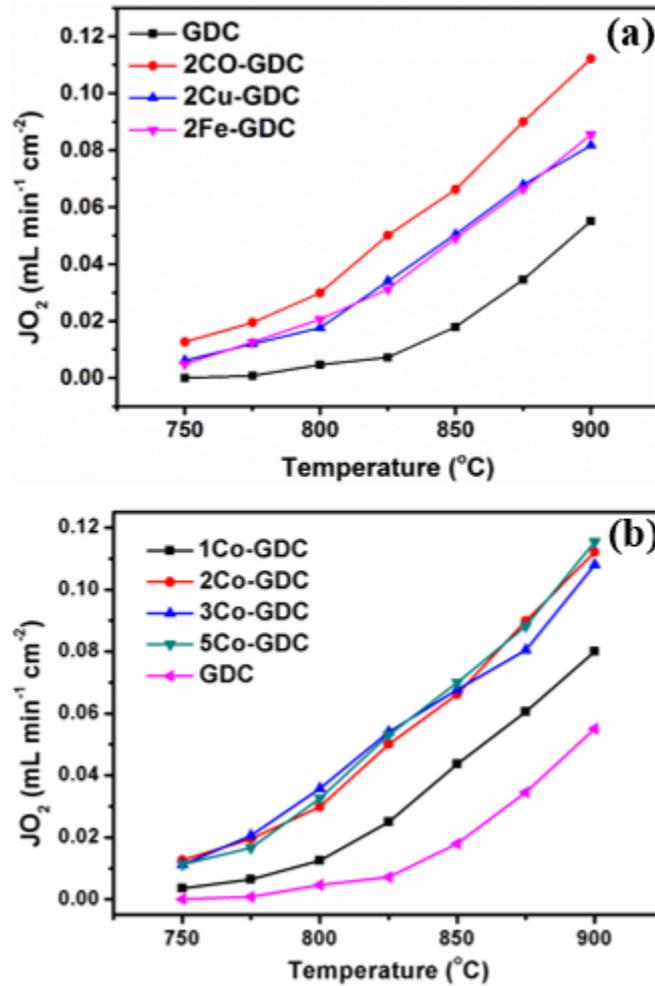
Figure 5.5 Temperature-dependent oxygen permeation fluxes of (a) GDC membranes containing 2 mol.% of Co, Cu and Fe sintering aids; and (b) GDC membranes containing different concentrations of Co sintering aid.

in oxygen flux. Below 825 $^{\circ}$C, GDC displayed negligible fluxes due to the very low electronic conductivity and accordingly, the limited surface oxygen exchange rate of fluorite-structured ceria materials at such temperatures.[36, 45, 46] The highest oxygen flux for pure GDC at 900 $^{\circ}$C was doubled to 0.112 mL min^{-1} cm^{-2} by the addition of 2 mol.% CoO. For 2Co-GDC membrane, the flux could reach 0.012 mL min^{-1} cm^{-2} at temperature as low as 750 $^{\circ}$C. Despite their lower oxygen fluxes relative to 2Co-GDC membrane, 2Cu-GDC and 2Fe-GDC membranes showed identical oxygen fluxes from 750 to 950 $^{\circ}$C. Their largest flux was approximately 0.08 mL min^{-1} cm^{-2} at 900 $^{\circ}$C. In terms of densification and oxygen permeation performances, CoO was clearly the best sintering aid. Therefore, next we evaluated the effect of Co content on the oxygen permeation fluxes.

Figure 5.5(b) shows the temperature-dependent oxygen permeation fluxes

153

through 0.8 mm-thick GDC disk membranes containing different amount of Cu, i.e., 1, 2, 3, and 5 mol.% (denoted as 1Co-GDC, 2Co-GDC, 3Co-GDC, and 5Co-GDC). Adding 1 mol.% CoO into pure GDC led to the significant oxygen flux enhancement. The enhancement is still observed for an extra 1 mol.% above this composition. However, above 2 mol.%, the oxygen permeation fluxes were no longer improved upon incorporating additional amount of CoO, up to 5 mol.%.
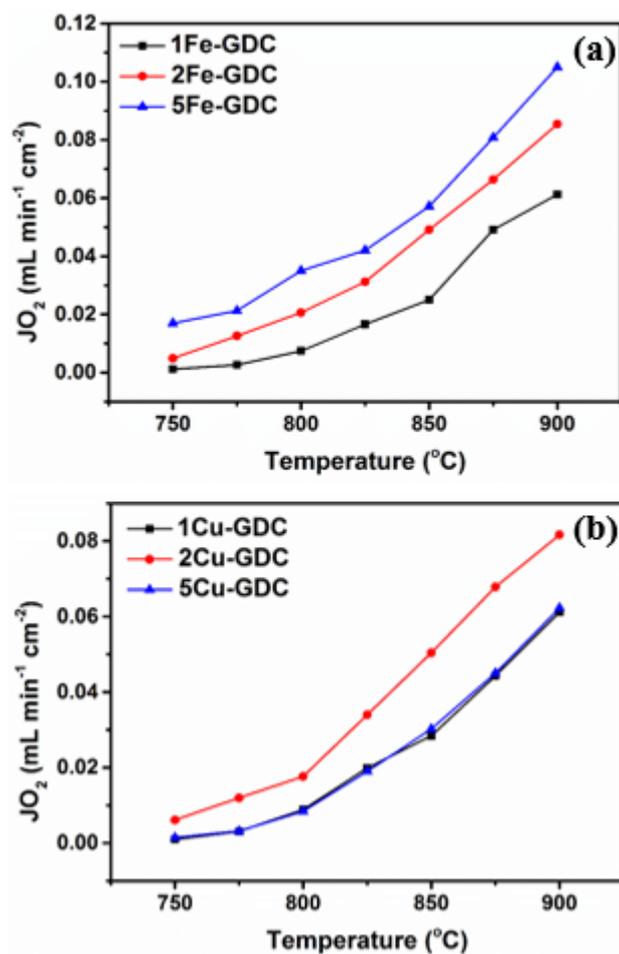
Figure 5.6 Temperature-dependent oxygen permeation fluxes of GDC membranes containing 1, 2, and 5 mol.% of (a) Fe sintering aid; and (b) Cu sintering aid.

The oxygen permeation behavior of Fe-GDC and Cu-GDC as a function of the sintering aid amount are displayed in **Figure 5.6(a) and (b)**. For example, the highest flux for 1Co-GDC membrane of 0.08 mL min^{-1} cm^{-2} at 900 ^{o}C is comparable to the highest fluxes for 2Fe-GDC and 2Cu-GDC membranes (Compare **Figure 5.5(b)** with **Figure 5.6(a) and (b)**). In Fe-GDC case, the oxygen permeation fluxes increased proportionally with the increase in Fe amount. For example, the highest oxygen fluxes

154

at 900 ^{o}C were 0.061, 0.085, and 0.105 mL min^{-1} cm^{-2} for 1Fe-GDC, 2Fe-GDC, and 5Fe-GDC, respectively. In Cu-GDC case, the oxygen fluxes exhibited optimum trend with increasing Cu amount; reaching their maximum at 2 mol.%. The oxygen fluxes for 1 mol.% Cu and 5 mol.% Cu containing GDC membranes were identical. The reason behind the distinct trend for Co-GDC, Fe-GDC, and Cu-GDC remains unclear. We postulate the existence of a maximum composition, over which the blocking effect caused by the accumulation of metal oxides along the grain boundaries of GDC, manifested. For Co-GDC, this composition is 2 mol.% while for Fe-GDC and Cu-GDC, these compositions are 5 mol.% and 2 mol.%, respectively. More detailed future experiments, outside the scope of this work, should be performed.

Although the highest flux for 2Co-GDC membrane that we obtained here of 0.065 mL min^{-1} cm^{-2} at 850 ^{o}C is still lower than the oxygen flux of 0.125 mL min^{-1} cm^{-2} at 850 ^{o}C displayed by the GDC membrane externally short-circuited with dual-phase Ag-GDC decoration, the use of non-precious metal sintering aids certainly offers an attractive alternative to achieve significant flux enhancement.[27]
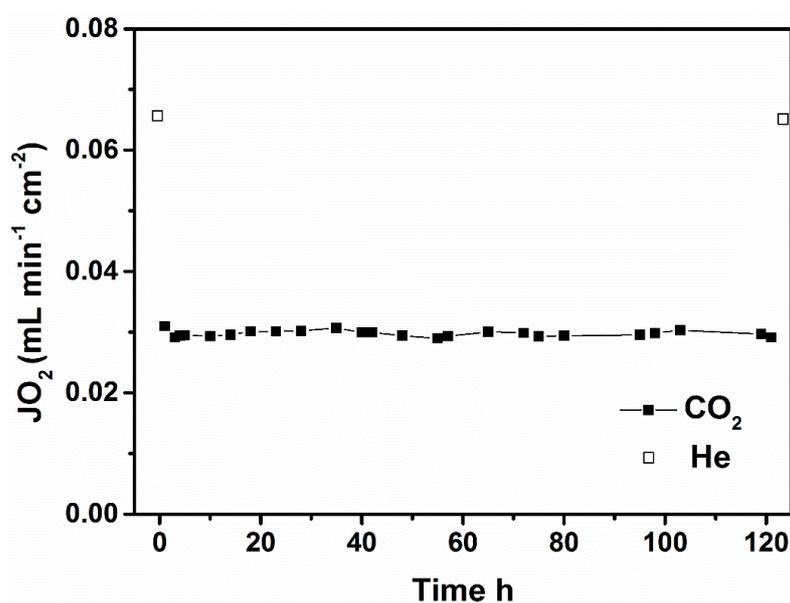
Figure 5.7 Long-term oxygen permeation flux performance of 2Co-GDC membrane under 100 vol.% CO_2 sweep gas at 850 ^{o}C (Note: The first and last open squares represent the fluxes under 100 vol.% helium).

For practical application in oxyfuel combustion and membrane reactor, CO_2 resistance becomes important. The oxygen permeation test results for 2Co-GDC membrane for 120 h reveals very stable fluxes of around 0.029 mL min^{-1} cm^{-2} under

pure CO_2 (**Figure 5.7**). The substantial decrease in oxygen fluxes when the sweep gas was changed from He to CO_2, *i.e.*, from around 0.06 to around 0.03 mL min^{-1} cm^{-2}, is due to the stronger adsorption of CO_2 on the membrane surface relative to He adsorption [47-49]. The original flux could nonetheless be recovered at the end of the test, when the CO_2 sweep gas was changed back to He. This highlights the excellent CO_2 resistance as has been widely known and reported elsewhere.[27, 28] What we perceived as the possible issue is the stability of CoO in CO_2 atmosphere. Klande *et al.* showed, using Ellingham diagram, that the cobalt carbonate ($CoCO_3$) decomposition starts at 300 °C under 1 atm CO_2.[50] Given that the membrane operation temperatures in this work are far beyond 300 °C, CoO is likely to be stable in CO_2 atmosphere. Furthermore, the relatively low oxygen fluxes for 2Co-GDC here, were achieved under normal permeation condition applicable for high purity oxygen production, which involves quite low oxygen partial pressure gradient across the membrane. The high stability for 2Co-GDC supports its application in membrane reactor, which involves the use of very large oxygen partial pressure gradients; thus potentially leads to significantly higher oxygen fluxes than what we could possibly obtain here.

Since the oxygen permeation process through ITM membrane constitutes bulk-diffusion step and surface exchange step, both steps can be affected in a unique way by the presence of sintering aid in the membrane.[1] Figuring out in details the possible effects of sintering aid into both steps requires more comprehensive study that is outside the scope of this work.

To discuss the origin of the oxygen fluxes enhancement obtained *via* the addition of sintering aids, we further performed microstructure and electrochemistry studies into GDC and 2Co-GDC membranes.

5.3.3 Electrochemical characterization

In MIEC materials, the electrical conductivity is the sum of the ionic and electronic conductivities. **Figure 5.8** presents the Arrhenius representation of the electrical conductivities of GDC and 2Co-GDC in air, obtained *via* a four-probe direct current (DC) method. Between 350 and 950 °C, the electrical conductivities of 2Co-GDC was slightly higher than those of pure GDC; in agreement with the works of Fagg *et al.*[35-37]
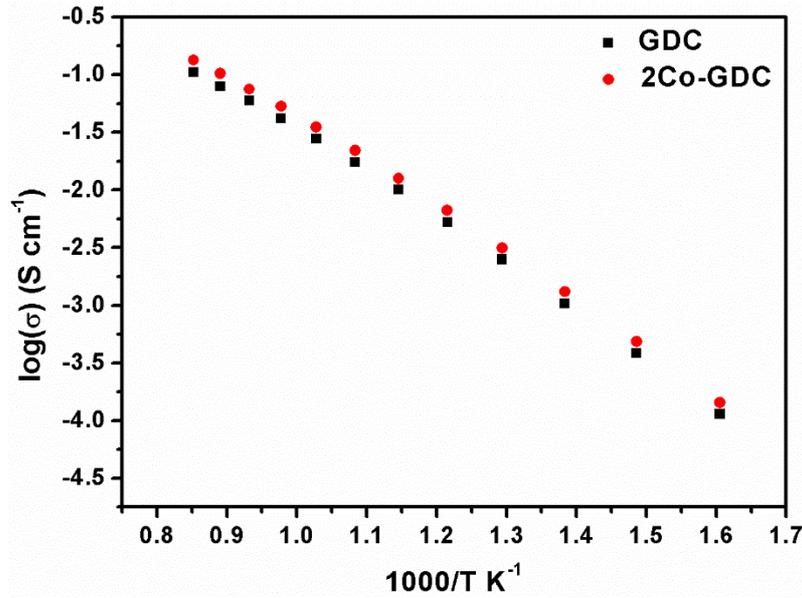
Figure 5.8 Arrhenius plot of the electrical conductivities of GDC and 2Co-GDC measured in air.

Figure 5.9(a)-(d) displays the results of more detailed conductivity study between 750 and 950 $^{\circ}$C. The electrical conductivities (denoted as σ_t), shown in **Figure 5.9(a)**, were obtained by electrochemical impedance spectroscopy (EIS) across a $p(O_2)$ gradient of 0.21 atm/0.09 atm. As a note, the electrical conductivities measured from the four-probe DC method (**Figure 5.8**) closely match the electrical conductivities obtained from EIS (**Figure 5.9(a)**). **Figure 5.9(b)** in turn shows the oxygen ionic transfer number (denoted as t_o), measured using the modified electromotive force (EMF) method developed by Liu and Hu.[42] Using this method, the contribution of the electrode polarization in cells can be determined and accounted for; thus allowing a more precise calculation of ionic transfer number relative to the conventional EMF method.[42, 51, 52] 2Co-GDC displayed lower ionic transfer numbers than GDC over the temperature range of 750 to 950 $^{\circ}$C. For example, the ionic transfer numbers of 2Co-GDC is 0.836, 0.872, 0.882, and 0.884 at 900, 850, 800, and 750 $^{\circ}$C, respectively while those for GDC is 0.951, 0.942, 0.926, and 0.913 at the respective temperatures. Analogous observation was also reported for PDC containing 2 mol.% Co sintering aid;[36, 37] the ionic transfer numbers of which were measured using Gorelov's modified EMF method.[53] The discrepancy between the ionic transfer number of 2Co-GDC and GDC furthermore increases with temperature rise. This is due to the negative and the positive thermal activation natures of the ionic transfer numbers for 2Co-GDC and GDC, respectively.
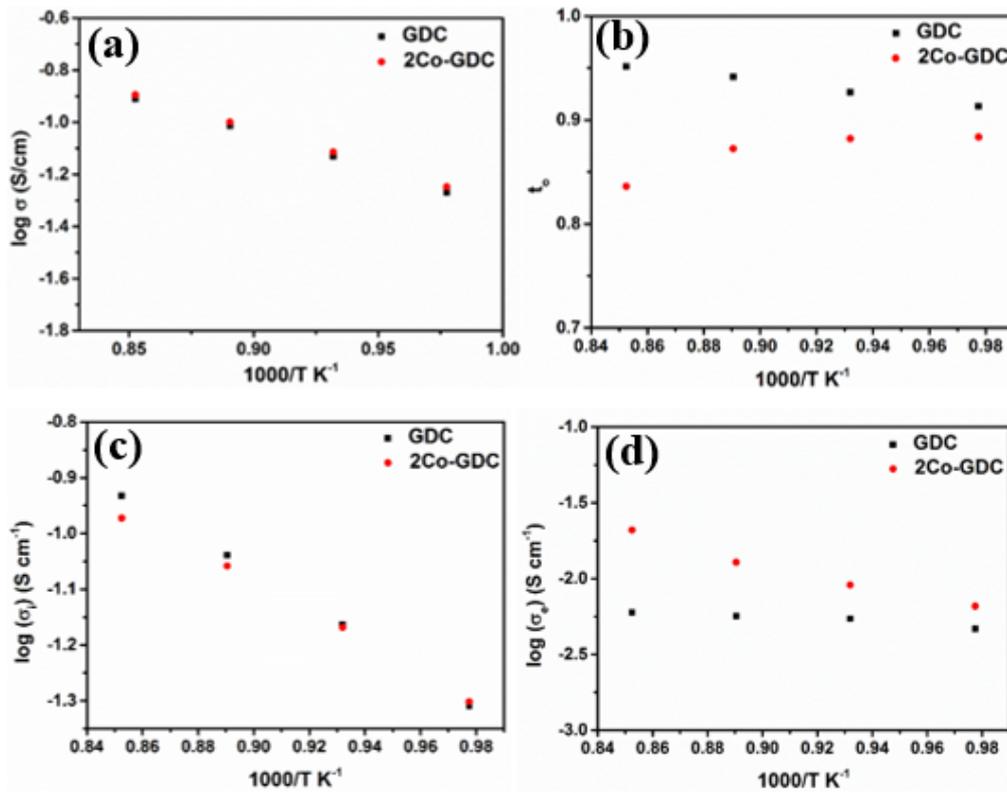
Figure 5.9 The influence of the addition of 2 mol.% Co into GDC on the temperature-dependent (a) total conductivity; (b) ionic transfer number; (c) ionic conductivity; and (d) electronic conductivity; obtained with the oxygen partial pressure gradient of 0.21 atm/0.09 atm.

The oxygen ionic conductivities (denoted as σ_o) can then be calculated from the electrical conductivities (σ_t) and the ionic transfer numbers (t_o) using the relationship of $\sigma_o = t_o\, \sigma_t$. The respective electronic conductivities (denoted as σ_e) can also be determined using the relationship of $\sigma_e = (1 - t_o)\, \sigma_t$. **Figure 5.9(c)** displays the ionic conductivities of 2Co-GDC and GDC; revealing analogous conductivities for both samples below 800 ^{o}C and lower conductivities for 2Co-GDC above 800 ^{o}C. Such trend manifested into the higher electronic conductivities for 2Co-GDC relative to GDC between 750 and 950 ^{o}C. The addition of 2 mol.% Co into GDC led to the increase in the electronic conductivities enhancement with increasing temperature, i.e., 1.4 times at 750 ^{o}C to 3.5 times at 900 ^{o}C relative to pure GDC. The enhancement effect we obtained here is not as large as that obtained by Fagg *et al.*, where up to 25 times enhancement was observed.[33, 35] This discrepancy is likely due to the higher sintering temperature (1100 °C) we used here relative to 900 °C sintering temperature they used in their works [33, 35]. It is likely that the higher sintering temperature promotes more dissolution of Co into the ceria lattice may eventually leads to the disappearance of Co-

rich layers along the grain boundaries.[54]

5.3.4 Transmission electron microscopy study

We performed transmission electron microscopy (TEM) studies on 2Co-GDC to assess Co distribution on grain boundaries after sintering at 1100 °C. **Figure 5.10** and **5.11** display the results on two different grains. **Figure 5.10(a)** presents high angle annular dark field-scanning transmission electron microscopy (HAADF-STEM) of two close-contact grains. The respective elemental maps (**Figure 5.10(c)-(f)**) reveal the uniform distribution of Ce, Gd, and Co: indicating that Co dissolves into GDC lattice. The grain boundary does not appear to be enriched in Co as indicated by the line scan profile result (**Figure 5.10(b)**). This is contradictory to the other works that reported the presence of Co-rich layer networks on the grain boundaries.[37, 54-56] In these cases nonetheless, their sintering aids-containing membranes were sintered below 1000 °C. Ramasamy *et al.* compared the microstructure evolution of CTO with Co sintering aid sintered at 900 and 1200 °C, respectively.[54] When the sample was sintered at 900 °C, the elemental maps revealed the occurrence of Co segregation along the grain boundaries. However, at higher sintering temperature of 1200 °C, Co-rich layers on the grain boundaries were significantly depleted. Instead, isolated Co-rich grains, with an average size of approximately 500 nm, were observed. Our additional TEM results suggest the existence of such isolated Co-rich grains, i.e., the presence of several Co-rich particles in GDC grains (**Figure 5.11**). The growth of CoO particles between GDC grains additionally manifested into the lower solubility of Co in GDC (**Figure 5.11(c)-(f)**). Zhang *et al.* also found that by sintering Co-containing GDC at 1050 °C, isolated Co oxide particles grew in triple junctions.[57] Ce concentration appears to decrease along the grain boundary (**Figure 5.10(b)**). Such depletion of Ce in grain boundary may induce an increase in the oxygen vacancies and consequently, an increase in the oxygen permeation fluxes. The depletion of oxygen vacancies at the grain boundaries was previously shown to deteriorate the ionic conductivity along the boundaries.[16] Our TEM results here evidently show that Co addition into GDC affects the elemental distribution in the grain boundaries. Such change in elemental distribution clearly contributes towards the observed change in the ionic and electronic conductivity behavior elaborated above.
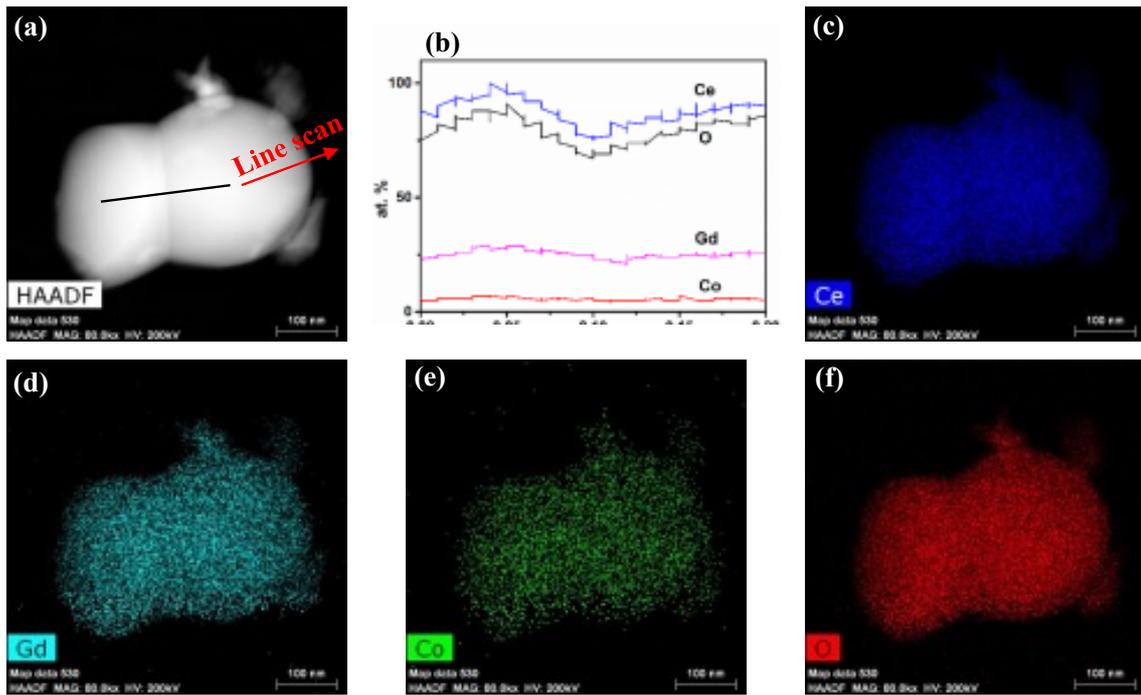
Figure 5.10 Transmission electron microscopy results on a typical grain boundary area of 2Co-GDC: (a) HAADF-STEM image; (b) Line scan profiles across the grain boundary; and (c)-(f) Elemental mapping image of Ce, Gd, Co, and O.
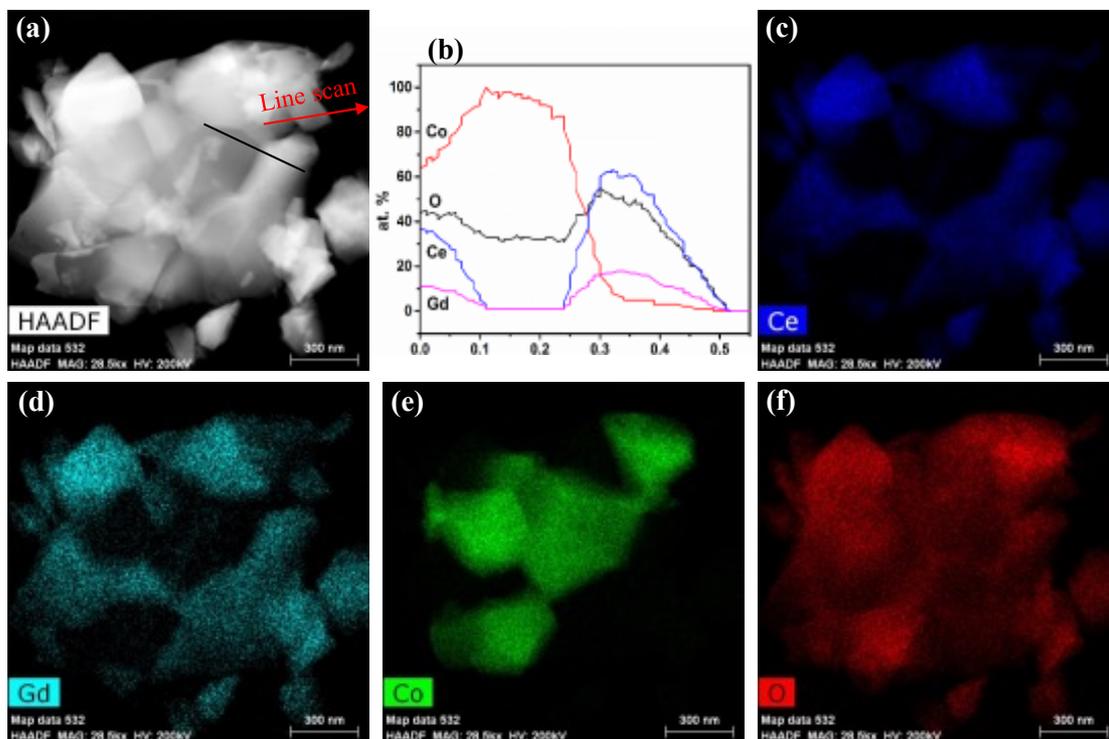
Figure 5.11 Transmission electron microscopy results on another typical grain boundary area

160

of 2Co-GDC: (a) HAADF-STEM image; (b) Line scan profiles across the grain boundary; and (c)-(f) Elemental mapping image of Ce, Gd, Co, and O.

5.4 Conclusion

The present study demonstrates the feasibility of adding sintering aid (cobalt oxide) to enhance the densification behavior and the electronic conductivity of GDC membranes. Oxygen permeation results demonstrate that 2 mol. % Co incorporated into GDC membrane (2Co-GDC) provided the highest oxygen permeation flux of 0.112 mL min^{-1} cm^{-2} at 900 °C. This oxygen flux was twice that of pure GDC membrane, indicating marked enhancement from the addition of Co sintering aid. Moreover, the sintering temperature of 2Co-GDC was reduced by 300 °C compared with pure GDC membrane. Ionic transfer numbers obtained from modified EMF method for 2Co-GDC were lower than those for GDC between 750 and 950 °C. The electronic conductivities of 2Co-GDC at this temperature range, on the other hand, were higher; indicating the electronic conductivity origin of the oxygen fluxes enhancement. Transmission electron microscopy results revealed that Co ions were homogeneously distributed along GDC grains with some of them precipitated in-between GDC grains. A 120 hour-length test of oxygen permeation using CO_2 as sweep gas additionally verified CO_2-resistance of 2Co-GDC. This work highlights the potential of applying CoO as a sintering aid to tailor the predominantly ionic conducting behavior of GDC towards mixed ionic-electronic conducting (MIEC) behavior.

5.5 References

1. J. Sunarso, S. Baumann, J. M. Serra, W. A. Meulenberg, S. Liu, Y. Lin and J. C. Diniz da Costa, J. Membr. Sci., 2008, 320, 13-41.

2. R. Kneer, D. Toporov, M. Förster, D. Christ, C. Broeckmann, E. Pfaff, M. Zwick, S. Engels and M. Modigell, Energy Environ. Sci., 2010, 3, 198-207.

3. M. A. Habib, M. Nemitallah and R. Ben-Mansour, Energy Fuels, 2013, 27, 2-19.

4. M. A. Habib, H. M. Badr, S. F. Ahmed, R. Ben-Mansour, K. Mezghani, S. Imashuku, G. J. la O', Y. Shao-Horn, N. D. Mancini, A. Mitsos, P. Kirchen and A. F. Ghoneim, Int. J. Energy Res., 2011, 35, 741-764.

5. Y. Wei, W. Yang, J. Caro and H. Wang, Chem. Eng. J., 2013, 220, 185-203.

6. Y. Liu, X. Tan and K. Li, Catal. Rev. Sci. Eng., 2006, 48, 145-198.

7. Y. Chen, W. Zhou, D. Ding, M. Liu, F. Ciucci, M. Tade and Z. Shao, Adv. Energy Mater., 2015, 5, 1500537 (1-34).

8. K. Zhang, Z. Shao, C. Li and S. Liu, Energy Environ. Sci., 2012, 5, 5257-5264.

9. K. Zhang, J. Sunarso, Z. Shao, W. Zhou, C. Sun, S. Wang and S. Liu, RSC Adv., 2011, 1, 1661-1676.

10. J. Martynczuk, K. Efimov, L. Robben and A. Feldhoff, J. Membr. Sci., 2009, 344, 62-70.

11. A. Waindich, A. Möbius and M. Müller, J. Membr. Sci., 2009, 337, 182-187.

12. O. Czuprat, M. Arnold, S. Schirrmeister, T. Schiestel and J. Caro, J. Membr. Sci., 2010, 364, 132-137.

13. Y. Wei, O. Ravkina, T. Klande, H. Wang and A. Feldhoff, J. Membr. Sci., 2013, 429, 147-154.

14. J. Garcia-Fayos, M. Balaguer and J. M. Serra, ChemSusChem, 2015, 8, 4242-4249.

15. H. Luo, H. Jiang, T. Klande, Z. Cao, F. Liang, H. Wang and J. Caro, Chem. Mater., 2012, 24, 2148-2154.

16. Y. Lin, S. Fang, D. Su, K. S. Brinkman and F. Chen, Nat. Commun., 2015, 6, 6824.

17. K. S. Yun, C.-Y. Yoo, S.-G. Yoon, J. H. Yu and J. H. Joo, J. Membr. Sci., 2015, 486, 222-228.

18. J. Han, Y. Zeng and Y. S. Lin, J. Membr. Sci., 1997, 132, 235-243.

19. X. Zhu, M. Li, H. Liu, T. Zhang, Y. Cong and W. Yang, J. Membr. Sci., 2012, 394-395, 120-130.

20. X. Zhu and W. Yang, in Membrane Science and Technology, eds. S. T. Oyama and S. M. Stagg-Williams, Elsevier, 2011, vol. 14, ch. 12, pp. 275-293.

21. C.S. Chen, B.A. Boukamp, H.J.M. Bouwmeester, G.Z. Cao, H. Kruidhof, A.J.A. Winnubst and A. J. Burggraaf, Solid State Ionics, 1995, 76, 23-28.

22. J. Kim and Y. S. Lin, J. Membr. Sci., 2000, 167, 123-133.

23. K. Wu, S. Xie, G. S. Jiang, W. Liu and C. S. Chen, J. Membr. Sci., 2001, 188, 189-193.

24. V. V. Kharton, A. V. Kovalevsky, A. P. Viskup, F. M. Figueiredo, A. A. Yaremchenko, E. N. Naumovich and F. M. B. Marques, J. Electrochem. Soc., 2000, 147, 2814-2821.

25. H. Luo, K. Efimov, H. Jiang, A. Feldhoff, H. Wang and J. Caro, Angew. Chem. Int. Ed., 2011, 50, 759-763.

26. W. Fang, F. Liang, Z. Cao, F. Steinbach and A. Feldhoff, Angew. Chem. Int. Ed., 2015, 54, 4847-4850.

27. C. Zhang, X. Meng, J. Sunarso, L. Liu, R. Xu, Z. Shao and S. Liu, J. Mater. Chem. A, 2015, 3, 19033-19041.

28. C. Zhang, R. Ran, G. H. Pham, K. Zhang, J. Liu and S. Liu, RSC Adv., 2015, 5, 5379-5386.

29. L. Wang, S. Imashuku, A. Grimaud, D. Lee, K. Mezghani, M. A. Habib and Y. Shao-Horn, ECS Electrochem. Lett., 2013, 2, F77-F81.

30. S. Imashuku, L. Wang, K. Mezghani, M. A. Habib and Y. Shao-Horn, J. Electrochem. Soc., 2013, 160, E148-E153.

31. B. He, G. Li, L. Gui, Y. Ling and L. Zhao, J. Mater. Chem. A, 2016, 4, 4003-4008.

32. K. Eguchi, T. Setoguchi, T. Inoue and H. Arai, Solid State Ionics, 1992, 52, 165-172.

33. D. P. Fagg, J. C. C. Abrantes, D. Pérez-Coll, P. Núñez, V. V. Kharton and J. R. Frade, Electrochim. Acta, 2003, 48, 1023-1029.

34. G.S. Lewis, A. Atkinson, B.C.H. Steele and J. Drennan, Solid State Ionics, 2002, 152-153, 567-573.

35. D. P. Fagg, V. V. Kharton and J. R. Frade, J. Electroceram., 2002, 9, 199-207.

36. D. P. Fagg, A. L. Shaula, V. V. Kharton and J. R. Frade, J. Membr. Sci., 2007, 299, 1-7.

37. D. P. Fagg, S. García-Martin, V. V. Kharton and J. R. Frade, Chem. Mater., 2009, 21, 381-391.

38. M. Balaguer, C. Solís and J. M. Serra, Chem. Mater., 2011, 23, 2333-2343.

39. S. Taub, K. Neuhaus, H.-D. Wiemhöfer, N. Ni, J. A. Kilner and A. Atkinson, Solid State Ionics, 2015, 282, 54-62.

40. S. Taub, R. E. A. Williams, X. Wang, D. W. McComb, J. A. Kilner and A. Atkinson, Acta Mater., 2014, 81, 128-140.

41. Z. Shao, W. Yang, Y. Cong, H. Dong, J. Tong and G. Xiong, J. Membr. Sci., 2000, 172, 177-188.

42. M. Liu and H. Hu, J. Electrochem. Soc., 1996, 143, L109-L112.

43. ICDD PDF-2 Release 2004, Joint Committee on Powder Diffraction Standards (JCPDS)-International Centre for Diffraction Data (ICDD), Pennsylvania, 2004, Powder Diffraction File (PDF) database.

44. C. Kleinlogel and L. J. Gauckler, Adv. Mater., 2001, 13, 1081-1085.

45. D. P. Fagg, I. P. Marozau, A. L. Shaula, V. V. Kharton and J. R. Frade, J. Solid State Chem., 2006, 179, 3347-3356.

46. P. Shuk and M. Greenblatt, Solid State Ionics, 1999, 116, 217-223.

47. P. F. Haworth, S. Smart, J. M. Serra and J. C. Diniz da Costa, Phys Chem Chem Phys, 2012, 14, 9104-9111.

48. X. Tan, N. Liu, B. Meng, J. Sunarso, K. Zhang and S. Liu, J. Membr. Sci., 2012, 389, 216-222.

49. J. Yi, M. Schroeder and M. Martin, Chem. Mater., 2013, 25, 815-817.

50. T. Klande, K. Efimov, S. Cusenza, K.-D. Becker and A. Feldhoff, J. Solid State Chem., 2011, 184, 3310-3318.

51. V.V. Kharton, A.P. Viskup, F.M. Figueiredo, E.N. Naumovich, A.A. Yaremchenko and F. M. B. Marques, Electrochim. Acta, 2001, 46, 2879-2889.

52. V.V. Kharton and F. M. B. Marques, Solid State Ionics, 2001, 140, 381-394.

53. V. P. Gorelov, Ehlektrokhimiya, 1988, 24, 1380-1381.

54. D. Ramasamy, A. L. Shaula, A. Gómez-Herrero, V. V. Kharton and D. P. Fagg, J. Membr. Sci., 2015, 475, 414-424.

55. M.-F. Han, S. Zhou, Z. Liu, Z. Lei and Z.-C. Kang, Solid State Ionics, 2011, 192, 181-184.

56. C. Kleinlogel and L. J. Gauckler, Solid State Ionics, 2000, 135, 567-573.

57. Z. Zhang, W. Sigle, M. Rühle, E. Jud and L. J. Gauckler, Acta Mater., 2007, 55, 2907-2917.

Chapter 6: Enhanced CO_2 resistance for robust oxygen separation through Ta-doped $SrFeO_{3-\delta}$ membranes

Abstract

Oxygen selective membranes with enhanced oxygen permeability and CO_2 resistance are highly required in sustainable clean energy generation technologies. Here, we present a novel cobalt-free, $SrFe_{1-x}Ta_xO_{3-\delta}$ (x = 0, 0.025, 0.05, 0.1, 0.2) perovskite membranes. Ta-doping induced the lattice structure progression from orthorhombic (x = 0) to cubic (x = 0.05). $SrFe_{0.95}Ta_{0.05}O_{3-\delta}$ showed the highest flux rates reaching 0.85 mL min^{-1} cm^{-2} at 950 ^{o}C on a 1.0-mm-thick membrane. Surface decoration can increase the permeation rate further. Ta inclusion within the perovskite lattice of SF enhanced the CO_2 resistance of the membranes significantly as evidenced by the absence of the carbonate functional groups on FT-IR spectrum when exposed to CO_2 atmosphere at 850 ^{o}C. The CO_2 resistance of Ta-doped SF compounds correlates with the lower basicity and the higher binding energy for the lattice oxygen. SFT0.05 demonstrated high operational stability during long term permeation test under CO_2 atmosphere.

6.1 Introduction

Oxy-fuel combustion is an attractive technique to deliver clean energy from the combustion of fossil fuels such as coal and gas using pure O_2 or O_2/CO_2 mixtures instead of air. This process enables cost-effective CO_2 separation and storage by generating a highly-concentrated CO_2 exhaust gas.[1-4] The O_2 supply for oxy-fuel process is normally provided through the conventional cryogenic distillation or pressure swing adsorption, both of which are expensive and energy-intensive. To reduce the cost, new oxygen production technologies are required to improve the viability of these clean energy technologies. With the cost saving advantage of approximately 35 %, oxygen transporting dense ceramic membranes, which can separate 100 % pure oxygen from air, are envisaged to replace the conventional oxygen production processes.[5-6] To retain

the usage of existing power generation plants however, "artificial air", i.e., oxygen within flue gas stream (30 % oxygen with the rest mostly CO_2) should be used since the combustion with pure oxygen results in the extremely high flame temperature which is outside the tolerable temperature range for the current boiler system. Concurrently, this combustion condition can be realized using a more practical sweep gas mode which recycles a minor portion of the flue gas (CO_2) back into the permeate side to carry the permeated oxygen into the combustion chamber with the feed side of the membrane exposed to the pressurized air. Compared to the normal sweep mode of using pure oxygen only, this recycling mode provides cost advantage although it requires the membrane material to have sufficient chemical stability under the presence of CO_2 at high operating temperatures. If these CO_2-tolerant membranes can also withstand the reducing gases like methane and hydrogen, they can also be applied as catalytic membrane reactors for greener chemical synthesis such as syngas production from methane.

In the past decades, MIEC perovskite oxide membranes have been widely investigated due their high oxygen permeability.[7] Ideal perovskite oxide has an ABO_3 crystal structure with a framework consisting of corner-shared BO_6 octahedra where a large A cation sits in the central void between the octahedral.[8] One of the factors determining the formation of the cubic perovskite structure is the size matching of A and B cations as there is a specific range of A cation size which can be accommodated in between the BO_6 octahedra; such size factor is also referred as the "Goldschmidt factor".[8] The A site cations can be chosen from the alkaline earth metal such as Ba, Ca or Sr or rare earth metals such as La or Pr and the B site cation is normally a transition metal such as Co or Fe. The ionic and electronic conductivity of perovskite originates from the oxygen non-stoichiometry (in $ABO_{3-\delta}$) and the redox activity of these transition metals, respectively.[7]

From both the thermodynamics and the Lewis acid-base theory perspectives, alkaline earth metal oxide reacts more readily with acid gases (i.e., CO_2) to form carbonates than the rare-earth metal oxides,[3,4,9-11] which confer these perovskite membranes poor chemical stability. This fact is also reflected by the more negative chemical potential for carbonate formation in the Ellingham diagram and the higher basicity for the former metal oxide. Replacing divalent alkaline earth metal cation completely with trivalent rare earth element would lower the ionic conductivity (and thus the oxygen permeability) due to the reduced oxygen non-stoichiometry. To

166

overcome this challenge, different approaches have been pursued including the partial substitution of Sr by La or Pr, the incorporation of Ca (with more positive chemical potential of carbonate formation) instead of Ba or Sr and the partial substitution of Co and Fe by Ta (to decrease the basicity).[9,10,12,13]

Doping strategy via substituting Co and/or Fe in (La, Ba, Sr)(Co, Fe)O_3-based perovskites by a minor amount of Ta has been attempted to improve the original lattice stability in reducing atmosphere and CO_2 resistance.[9,14-16] For example, $La_{0.2}Sr_{0.8}Fe_{0.8}Ta_{0.2}O_{3-\delta}$ exhibits higher onset temperature of decomposition in H_2 atmosphere (relative to $La_{0.2}Sr_{0.8}FeO_{3-\delta}$) indicating its enhanced kinetic stability.[14] Another example is $BaCo_{0.7}Fe_{0.2}Ta_{0.1}O_{3-\delta}$ perovskite membrane that can be operated in CH_4 and CO containing atmosphere at 900 ^{o}C for over 400 hours without any evidence of structure deterioration normally encountered by the non Ta-doped cobalt containing perovskite membranes.[15] Since the ionic radius of Ta in perovskite is less than the ionic radius of Co and Fe (in octahedra), Ta doping is less likely to impart direct and substantial negative effects on the Goldschmidt factor.[16] Rather, the improved lattice stability is arisen from the high valence of Ta which effectively increases the average valence of B-site cations and decreases the oxygen non-stoichiometry.[14,17] Likewise, in terms of CO_2 resistance, incorporation of Ta leads to the restrained reaction with CO_2 for $Sr(Co_{0.8}Fe_{0.2})_{0.9}Ta_{0.1}O_{3-\delta}$ as opposed to $SrCo_{0.8}Fe_{0.2}O_{3-\delta}$.[9] This correlates with the higher binding energy value of lattice oxygen for Ta-doped perovskite which implies its lower basicity.[9] Another supporting evidence towards stable structure is the stronger bonding energy of Ta with oxygen relative to cobalt and iron (i.e., Ta-O, Fe-O and Co-O bond strength is 799.1, 390.4 and 384.5 kJ mol^{-1}, respectively).[9,18]

In this work, our focus is Ta-doped $SrFeO_{3-\delta}$ (up to 20 mol.% Ta). Co has often been selected as the B-site metal cation due to its high redox activity which normally contributes to high oxygen permeation fluxes. Since Co is much more redox active than Fe, replacing Co by Fe would ensure structure stability upon heating and in reducing atmosphere despite some anticipated reduction in oxygen flux.[19] The latter drawback nonetheless can be overcome by engineering approach, i.e., thin film fabrication without compromising the materials lifetime which forms the more substantial factor towards evaluating its practical value. The effects of Ta doping on the phase, the oxygen permeability and CO_2 resistance (relative to the non-doped one) are systemically studied. Furthermore, different approaches, e.g., surface decoration, external short-

circuit and thin film are also explored to optimize the oxygen permeation flux of the Ta doped $SrFeO_{3-\delta}$ membranes.

6.2 Experimental Section

6.2.1 Powder synthesis and membrane fabrication

$SrFe_{1-x}Ta_xO_{3-\delta}$ (x = 0, 0.025, 0.05, 0.1, 0.2) were synthesized by planetary milling of the stoichiometric amount of $SrCO_3$, Fe_2O_3 and Ta_2O_5 powders, followed by calcination at 1000–1100 ^{o}C for 5 h. All precursors, i.e., $SrCO_3$, Fe_2O_3 and Ta_2O_5 were of analytical grade. In a typical synthesis for $SrFe_{0.95}Ta_{0.05}O_{3-\delta}$ (SFT0.05), for example, 0.05 mol of $SrCO_3$ and 0.02375 mol of Fe_2O_3 and 0.00125 mol of Ta_2O_5 were mixed with ethanol as a solvent media and milled for several hours. The final powder mixture obtained after evaporating ethanol was calcined at 1050 ^{o}C for 5 hours with a heating and cooling rate of 2 ^{o}C min^{-1}, resulting in the final composition of $SrFe_{0.95}Ta_{0.05}O_{3-\delta}$. Identical procedure was followed for other compositions, i.e., $SrFeO_{3-\delta}$ (SF), $SrFe_{0.0975}Ta_{0.025}O_{3-\delta}$ (SFT0.025), $SrFe_{0.9}Ta_{0.1}O_{3-\delta}$ (SFT0.1) and $SrFe_{0.8}Ta_{0.2}O_{3-\delta}$ (SFT0.2). To form dense disk membranes required for permeation testing, the powders were isostatically pressed into green disk bodies using a stainless-steel pellet die set (10.0 mm in diameter) under a hydraulic pressure of ~2.0 × 10^6 Pa. These green disks were sintered between 1200–1450 ^{o}C in air for 5–10 hours using a heating and cooling rate of 2 ^{o}C min^{-1}. The sintering temperatures for SF, SFT0.025, SFT0.05, SFT0.1 and SFT0.2 disks were 1200, 1230, 1250, 1300 and 1400 ^{o}C, respectively. The thickness of the sintered disk membranes varies between 0.5–1.5 mm. For some membranes, silver paste was uniformly coated onto the membrane using brush. A terpineol solution was mixed with the silver paste as a diluent.

6.2.2 Structure and microscopy characterization

Powder X-ray diffraction (XRD) analysis was performed on an X-ray diffractometer (XRD, Bruker D8 Advance) using Cu-Kα radiation at 40 kV and 30 mA. Membrane morphology was examined at 15 kV accelerating voltage using a scanning electron microscope (SEM, Zeiss Neon 40EsB FIBSEM). Selected area electron diffraction (SAED) was performed using a transmission electron microscope (TEM, FEI Titan G2

80-200). In addition, scanning transmission electron microscopy (STEM) images and energy-dispersive X-ray spectroscopy (EDX) mapping was also obtained under high-angle annular dark field (HAADF) mode. The SAED aperture size was 2 μm. Fourier-Transform Infra-Red spectra (FTIR, Bruker) were obtained with ATR correction mode to characterize the functional groups of the powders before and after treatment in pure CO_2 atmosphere for 10 h. Thermogravimetric analysis (TG-DTA) was carried out on the powders using a thermal analyzer (PerkinElmer Diamond TG/DTA) at a heating rate of 10 °C min^{-1} using air with a flow rate of 25 mL min^{-1}. X-ray photoelectron microscopy (XPS, Thermo Escalab 250) was obtained using an Al-Kα X-ray source to detect the O1s binding energy. The oxygen non-stoichiometry at room-temperature was measured by iodometry titration technique as detailed elsewhere.[20] The powders used for the above characterizations were obtained from grinding the respective sintered membranes.

6.2.3 Oxygen permeation tests

Oxygen permeation properties of the disk membranes were measured using a high temperature oxygen permeation setup as elaborated elsewhere.[21] Gas chromatography (GC, Shimadzu GC-2014) with a 5A molecular sieve column and TCD detector was used to analyze the composition of the permeate gas stream. GC Agilent 6780N with Hayesep® D packed column was used to test the stability under 100 % CO_2. The disk membrane was fixed onto one side of a quartz tube and a ceramic paste was applied as the sealant. The effective surface area of the disk at the sweep side was 0.45 cm^2. The calculation method of the oxygen flux can be found elsewhere.[22]

6.3 Results and Discussion

6.3.1 Structure and microscopy at room temperature

Room temperature powder X-ray diffraction (XRD) patterns of $SrFe_{1-x}Ta_xO_{3-\delta}$ (obtained by grinding the respective sintered dense membranes of x = 0, 0.025, 0.05, 0.1 and 0.2 into powders − denoted as SF, SFT0.025, SFT0.05, SFT0.1 and SFT0.2, respectively) are depicted in **Figure 6.1**. The patterns for both the non-doped and doped compounds display the presence of identical peaks characteristics of the perovskite

phase.[23] These peaks are slightly shifted to the lower angle at higher Ta content which indicates lattice expansion to accommodate more Ta cations. To identify the crystal structures, selected area electron diffraction (SAED) patterns for SF and SFT0.05 are displayed as **Figure 6.2(a)** and **(b)**. **Figure 6.2(a)** reveals the formation of polycrystalline rings which can be indexed according to the orthorhombic lattice from its (1 1 2), (4 0 2) and (4 2 2) reflections (marked by red lines in **Figure 6.2(a)**); indicating that SF crystallizes in orthorhombic perovskite lattice with ordered oxygen vacancies.[24,25] For SFT0.05, however, ($\bar{1}$ 0 1), ($\bar{1}$ 1 0) and ($\bar{2}$ 1 1) spots (**Figure 6.2(b)**) follow the cubic lattice indexation in [1 1 1] zone axis which implies cubic lattice formation. This is quite consistent with the trend reported in the previous work, i.e., the crystal structure of $SrFeO_{3-\delta}$ family evolves (i.e., from orthorhombic to tetragonal and then to cubic) with decreasing oxygen non-stoichiometry (i.e., from 0.27 to 0.14 and then to 0.03). Note the lowering of oxygen non-stoichiometry on SF upon Ta doping (**Table 6.1**) and the fact that in our work, the presence of Ta may slightly alter the structure packing. Therefore, it explains the minor discrepancy in the structure trend observed against the reported structure evolution of non-doped $SrFeO_{3-\delta}$ family.[26] The elemental mappings displayed in **Figure 6.2(c-h)** further evidence the uniform distribution of Ta in these analyzed powders.
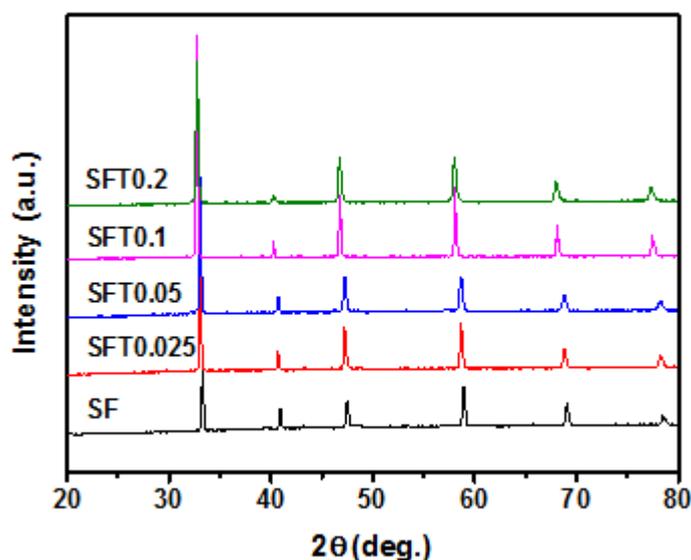
Figure 6.1 Room-temperature powder X-ray diffraction patterns of $SrFe_{1-x}Ta_xO_{3-\delta}$ (x = 0−0.2) disk membranes.
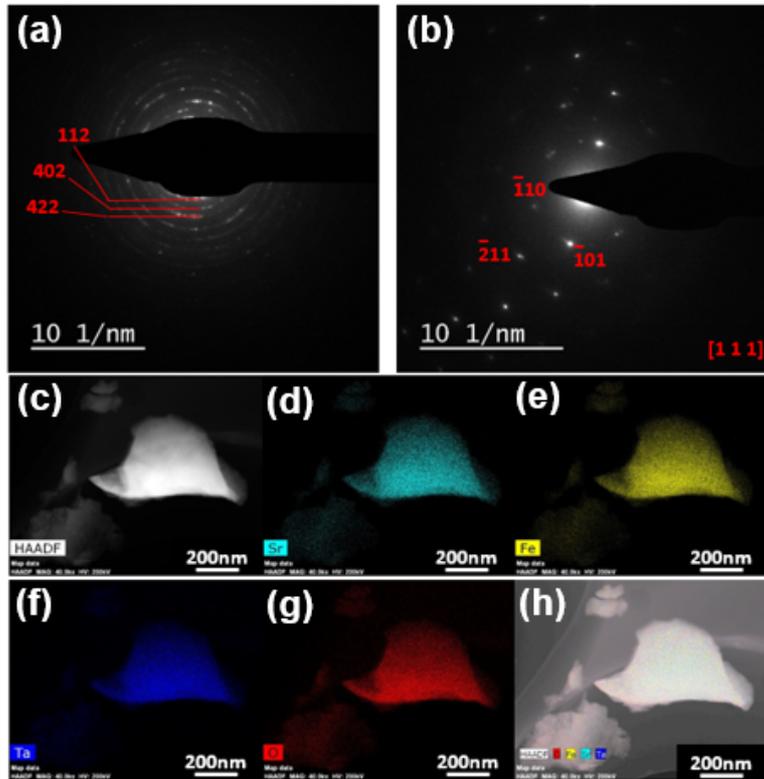
Figure 6.2 Selected area electron diffraction (SAED) patterns of (a) SF and (b) SFT0.05; and elemental identification by scanning transmission electron microscopy-energy dispersive X-ray analysis (STEM-EDX) of SFT0.05; (c) STEM image showing the area of EDX mapping; (d-g) EDX elemental mapping under high-angle annular dark field (HAADF) mode for Sr, Fe, Ta and O, respectively; and (h) the combined EDX signals.
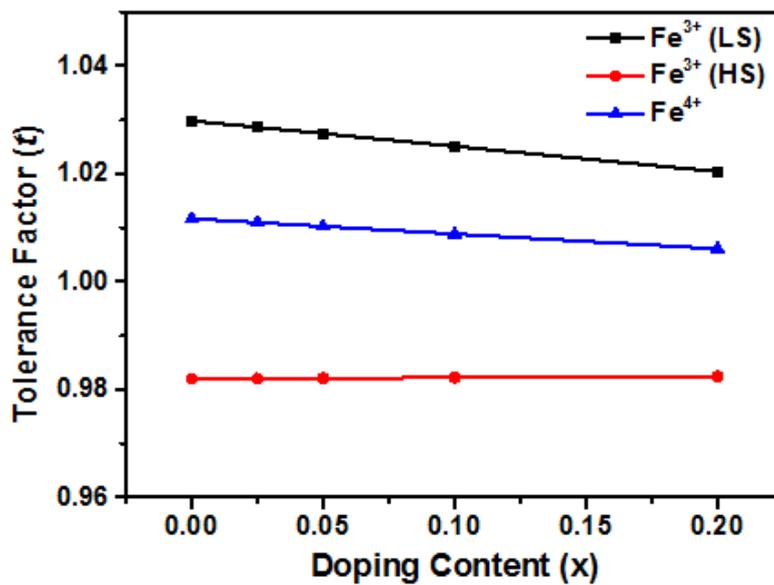
Figure 6.3 Goldschmidt tolerance factors of $SrFe_{1-x}Ta_xO_{3-\delta}$ (x = 0−0.2) for three different Fe scenarios, i.e., Fe^{3+} (LS), Fe^{3+} (HS) and Fe^{4+}.

171

For $ABO_{3-\delta}$ perovskite compound to have a cubic structure, the Goldschmidt tolerance factor given in Eq. (6.1) should ideally be between 0.8 and 1:[27]

$$t = \frac{R_A + R_O}{\sqrt{2}(R_B + R_O)} \qquad \text{(Eq. 6.1)}$$

Where R_A, R_B and R_O are the ionic radius of (12 coordinated) A-site cation, (6 coordinated) B–site cation and oxygen anion, respectively. The ionic radius of six-coordinated Ta^{5+}, Fe^{2+} (LS), Fe^{2+} (HS), Fe^{3+} (LS), Fe^{3+} (HS) and Fe^{4+} is 0.64, 0.61, 0.78, 0.55, 0.645 and 0.585 Å, respectively.[16] The results of the Goldschmidt tolerance factor calculations (**Figure 6.3**) together with the room temperature iodometric titration results and charge balance calculations (**Table 6.1**) as well as the weak ligand field in perovskite oxide indicate that the most possible oxidation states of Fe are +3 (HS) and +4, i.e., Fe co-exists as a mixture of Fe^{3+} (HS) and Fe^{4+} in these compounds. The relative amount of Fe^{4+} at room temperature also appears to increase in conjunction with the increased Ta doping amount (**Table 6.1**). This is consistent with the smaller ionic radius of Fe^{4+} and the tendency to preserve the cubic structure. Our calculations (accounting both Fe^{3+} (HS) and Fe^{4+} – not shown here) indicate the obtainment of tolerance factor approaching much closer to 1 for compositions containing higher relative amount of Fe^{4+}.

Table 6.1 Room temperature oxygen non-stoichiometry (δ), average Fe valence, amount of Fe^{3+} (HS) and Fe^{4+}, and Goldschmidt tolerance factor (t) of $SrFe_{1-x}Ta_xO_{3-\delta}$

| x	0	0.025	0.05	0.1	0.2
δ	0.392	0.234	0.184	0.127	0.031
Fe valence	3.21	3.49	3.56	3.61	3.67
Fe^{3+} amount	0.78	0.51	0.44	0.39	0.33
Fe^{4+} amount	0.22	0.49	0.56	0.64	0.67
t	0.988	0.996	0.997	0.998	0.998

Increased amount of Ta doping also leads to the decreased room temperature oxygen non-stoichiometry and the expected subsequent lowered ionic conductivity.[7] Thermogravimetric analysis (TGA) was then performed to evaluate the effect of Ta doping on the weight loss profile with temperature change; the results of which are shown in **Figure 6.4**. All compounds provide negligible weight loss below 350 °C. It is interesting to note that SF and SFT0.025 exhibit noticeable weight gain which was started at 350 °C. This phenomenon was likely caused by the onset of phase transition

from orthorhombic to cubic structure as reported by other researchers.[26] This weight gain nonetheless disappears on the SFT0.05, SFT0.1 and SFT0.2 profiles in agreement with the absence of phase transition particularly for these compounds with cubic structure which were retained even at room temperature.

The typical scanning electron microscopy (SEM) images of the fractured cross-section and surface views of the sintered disk membranes are presented in **Figure 6.5**. To achieve a dense structure, it is necessary to increase the sintering temperature progressively as a function of Ta content, i.e., 1200, 1230, 1250, 1300 and 1400 $^{\circ}$C for SF, SFT0.025, SFT0.05, SFT0.1 and SFT0.2, respectively. Noteworthy is that the melting point for Ta_2O_5 of 1872 $^{\circ}$C is higher than Fe_2O_3 (1566 $^{\circ}$C). **Figure 6.5(a-e)** shows the formation of dense body with isolated pores as evidenced by the negligible leakage from oxygen permeation testing. Moreover, the number of pores also appears to increase at larger Ta content, most likely due to the aforementioned reduced sinterability as well as the decreased oxygen non-stoichiometry which hinders the oxygen diffusion (**Table 6.1**). A typical surface morphology of the disk membrane, represented by SFT0.05, is shown in **Figure 6.5(f)**, where grains with size of ~2–3 μm are visible.
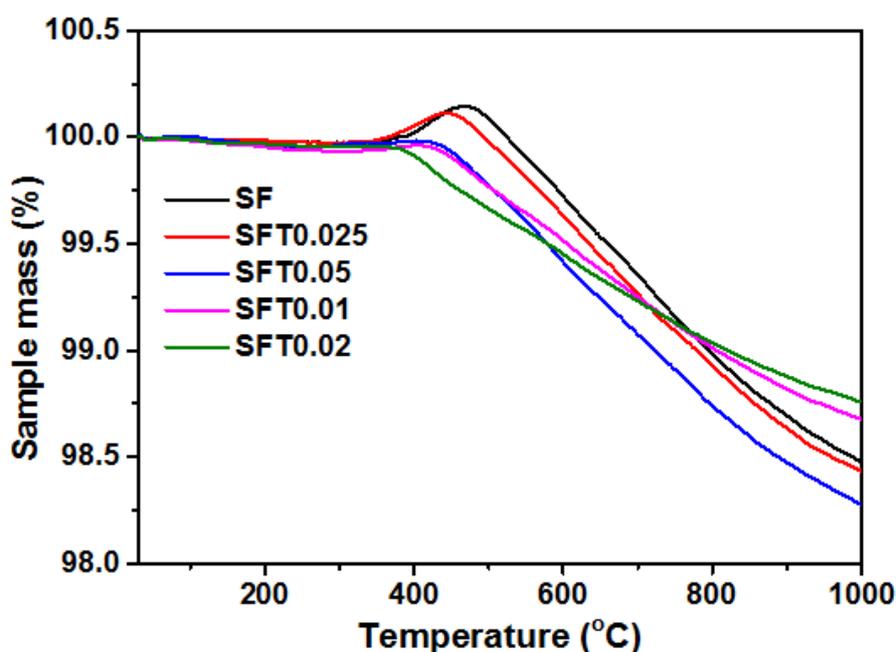
Figure 6.4 Thermal weight loss evolution profiles of $SrFe_{1-x}Ta_xO_{3-\delta}$ (x = 0−0.2) powders.
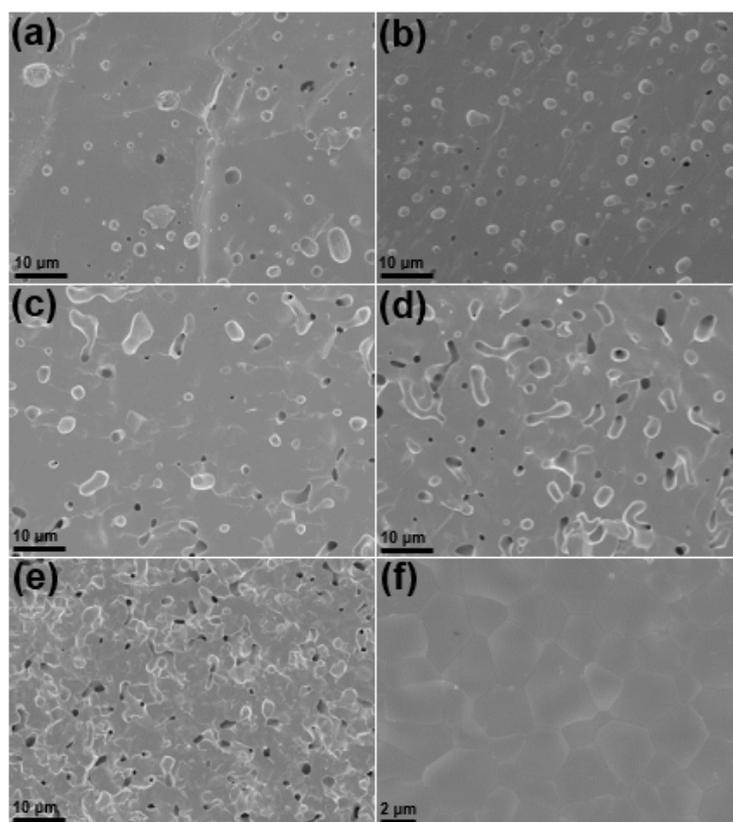
Figure 6.5 Scanning electron microscopy images of the cross-section of $SrFe_{1-x}Ta_xO_{3-\delta}$ ($x = 0$ − 0.2) disk membranes: (a) SF; (b) SFT0.025; (c) SFT0.05; (d) SFT0.1; (e) SFT0.2; and (f) the typical surface view of SFT0.05.

6.3.2 Permeation tests

Figure 6.6(a) displays the temperature-dependent oxygen permeation fluxes of 1-mm-thick membranes between 750–950 $^{\circ}$C. SF has the lowest oxygen fluxes with a maximum value of 0.26 mL min^{-1} cm^{-2} at 950 °C as anticipated from the low redox activity of Fe. Upon doping with 2.5 mol.% of Ta, the fluxes at these temperatures were increased by a factor of 2 relative to the non-doped compound. Increasing the dopant amount to 5 mol.% leads to the achievement of optimum oxygen fluxes reaching 0.85 mL min^{-1} cm^{-2} at 950 °C. Such flux improvements have previously been reported in the case of partial substitution of Fe in $SrFeO_{3-\delta}$ with Nb and Sc, which is attributed to the improved ionic and electronic conductivities and structure stability.[28,29] Likewise, Ta doping promotes the oxygen ionic transport by suppressing the formation of oxygen vacancy-ordered orthorhombic structure down to room temperature. The significant rise in flux appears on the profiles for SF and SFT0.025 during the temperature rise from 750 $^{\circ}$C to 800 $^{\circ}$C (**Figure 6.6(a)**) which may indicate the occurrence of partial

phase transition. Incorporating more Ta beyond 5 mol.% as is the case of SFT0.1 and SFT0.2 membranes lowered the oxygen fluxes, e.g., the maximum fluxes of only 0.59 mL min^{-1} cm^{-2} and 0.38 mL min^{-1} cm^{-2}, respectively at 950 ^{o}C. This is consistent with the reduced oxygen non-stoichiometry and the higher metal-oxygen bond strength (given the higher Ta-O bond strength relative to Fe-O bond strength) for compounds with higher Ta content (Table 1) which may lower the oxygen ionic conductivity.[28-30] It is well-known that the oxygen permeability is strongly influenced by the concentration of oxygen vacancies and the mobility of oxygen ions.[31] The concentration of oxygen vacancies is normally proportional to its oxygen non-stoichiometry while the mobility of oxygen ions is reflected by the bond strength of the metal-oxygen.[32]

Applying the Arrhenius equation, the activation energies for oxygen permeation between 800 and 950 ^{o}C were 114.85, 82.97, 67.47, 71.18 and 95.82 kJ mol^{-1} for SF, SFT0.025, SFT0.05, SFT0.1 and SFT0.2, respectively. For permeation through SF and SFT0.025, substantially larger activation energies of 232.89 and 167.02 kJ mol^{-1} nevertheless were indicated upon rising the temperature from 750 to 800 ^{o}C. As such, structure stability appeared to facilitate less thermally activated permeation and higher fluxes at lower temperatures.[20,22]

For bulk-diffusion limited process, Wagner equation states that the oxygen flux J_{O2} is inversely related to the thickness L.[33,34] **Figure 6.7** displays the thickness dependent oxygen fluxes of the best membrane composition (SFT0.05) between 750 and 950 ^{o}C. The oxygen permeation through mixed ionic-electronic conducting (MIEC) membrane consists of surface exchange reactions and bulk-diffusion steps.[7] At 950 ^{o}C, decreasing the membrane thickness from 1.5 to 1.0 or 0.5 mm led to the flux increase from 0.56 to 0.85 or 1.39 mL min^{-1} cm^{-2}, respectively. In order to clarify the controlling steps for oxygen transport through such membranes, a particular constant ($K_{d1/d2}$) was defined to determine a proportional relation whether or not exists between the membrane thickness and oxygen flux.[20] Here d_1 and d_2 represent two different membrane thickness. If the surface exchange reaction becomes the rate limiting step, this constant would be equal to the value of d_1/d_2. It would however be close to 1 if the bulk-diffusion is the rate limiting step. The calculation of $K_{d1/d2}$ based on **Figure 6.7** reveals $K_{d1/d2}$ values approaching to 1; implying the domination of bulk-diffusion step on the oxygen permeation of SFT0.05, in particular for the membrane thickness over 0.5 mm.
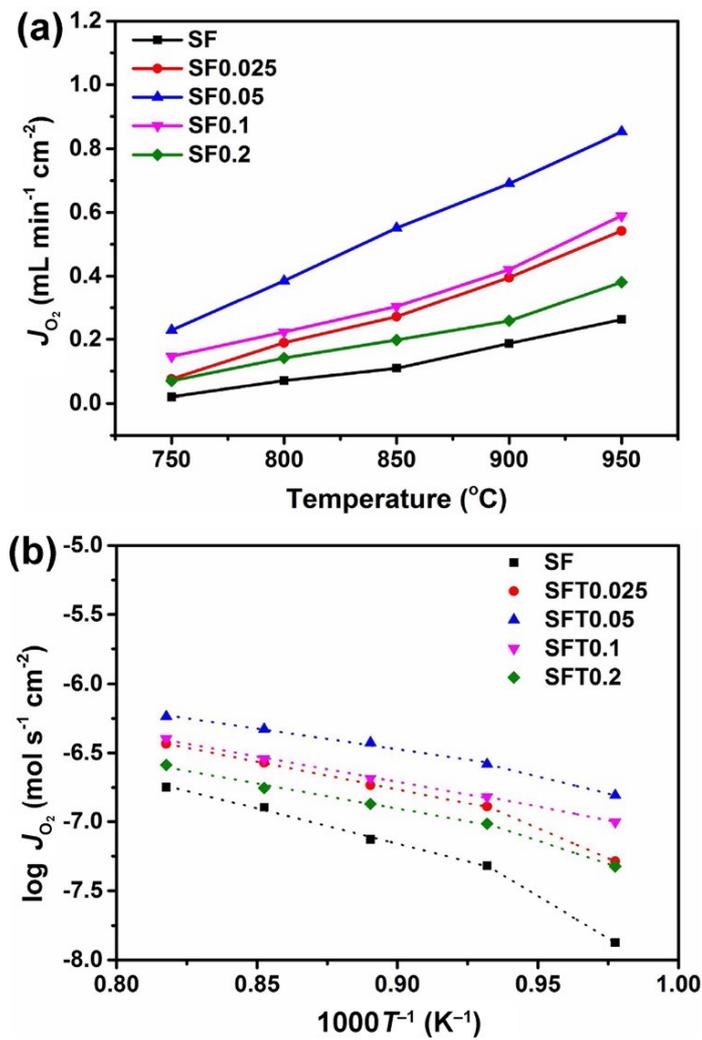
Figure 6.6 (a) Temperature dependent oxygen permeation fluxes of SrFe$_{1-x}$Ta$_x$O$_{3-\delta}$ (x = 0−0.2) disk membranes; and (b) the respective Arrhenius plots.
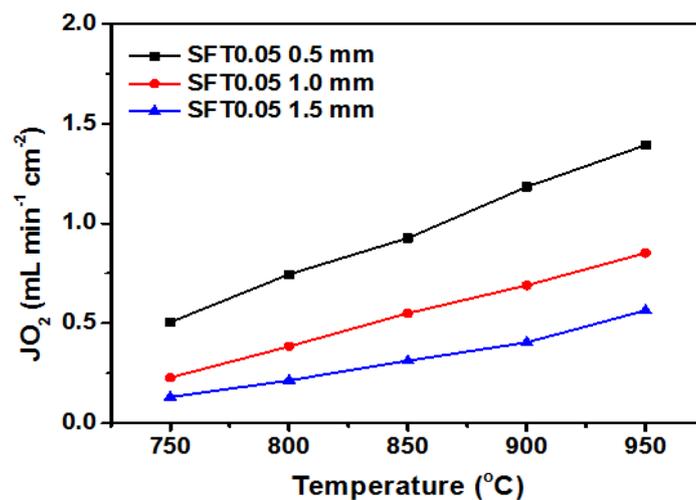
Figure 6.7 Temperature dependent oxygen permeation fluxes of SFT0.05 disk membranes with different thickness.
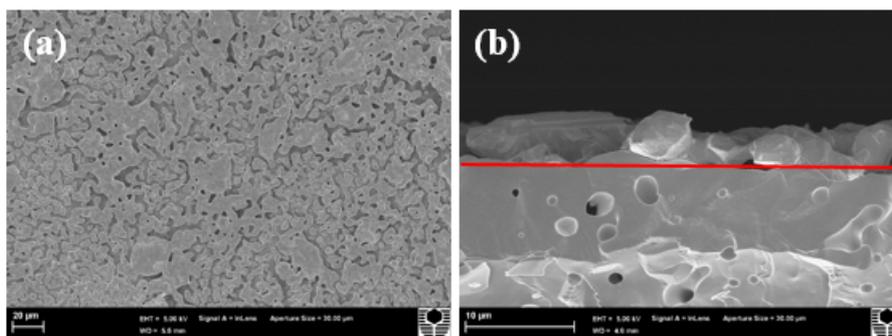
Figure 6.8 Scanning electron microscopy images of (a) the surface and (b) the upper cross-section of SFT0.05 membrane decorated with a porous silver layer.

We further examined the effects of enhancing the surface reaction rate and the electronic conductivity of the membrane (i.e., through external electronic short circuit) by applying surface decoration and conductive sealing. These engineering approaches have recently become an attractive approach to improve the performance of highly stable ionic conductor membranes. As the surface decorations, coatings of precious metals, perovskite, fluorite and metal-fluorite dual-phase compound have been attempted.[35-41] Here, silver paste was applied as both the decoration catalyst and the conductive sealing layer. A typical porous silver decoration layer with a thickness of ~4 mm on the SFT0.05 membrane surface is shown on **Figure 6.8**. **Figure 6.9(a)** illustrates the oxygen permeation fluxes for three different scenarios: the first (base) case where non-conductive ceramic sealing was applied with no surface decoration, the second case where non-conductive ceramic sealing was applied with surface decoration and the third case where both conductive silver sealing and surface decoration were applied. Here, surface decoration appears to be more efficient towards improving the oxygen fluxes than electronically short-circuiting the membrane given the overwhelmingly higher electronic conductivity of perovskite MIEC relative to its ionic conductivity.[7,31] As a reference, the electronic conductivities of SF and its doped compounds are generally 30–90 S cm^{-1} at 700–850 $^\circ$C.[42,43] Such values rationalize the marginal effect of electronic short circuit imparted on the oxygen permeability, in agreement with the observations from other researchers.[44] The activation energies obtained from the respective Arrhenius plots shown in **Figure 6.9(b)** for the second and third cases are 57.84 and 57.69 kJ mol^{-1}, which compares favorably against the first case showing 67.47 kJ mol^{-1} activation energy.
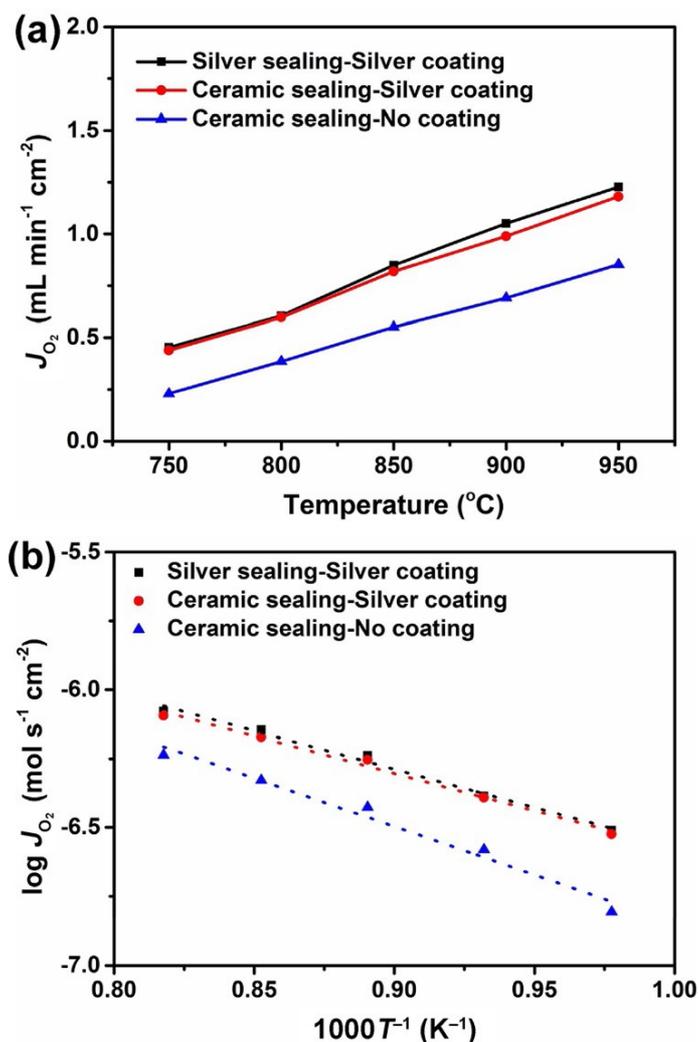
Figure 6.9 (a) Temperature dependent oxygen permeation fluxes of SFT0.05 disk membranes with different sealing and decoration; and (b) the respective Arrhenius plots.

6.3.3 CO_2 resistance and chemical analysis

The stability of SFT0.05 to CO_2 is an important consideration for its practical application as an oxygen selective membrane in oxy-fuel process or high temperature membrane reactors. Fourier-Transform Infra-Red spectra (FTIR) analysis was used to probe its stability and identify the possible chemical bonds formed by the reaction with CO_2 in SFT0.05 and SF powders after heat treatment at 850 ^{o}C for 10 h in 100 % CO_2 atmosphere (treated samples denoted as SFT0.05-CO_2 and SF-CO_2 in **Figure 6.10**). The appearance of three characteristic bands at 860, 1445 and 1771 cm^{-1} for CO_2-treated SF signifies the presence of carbonates anions (CO_3^{2-}) from $SrCO_3$ which formed during the CO_2 exposure. For comparison purpose, the inset of **Figure 6.10** also shows

FT-IR spectrum of SrCO₃. However, such SrCO₃-associated characteristic bands is absent from the spectrum of CO_2-treated SFT0.05. It is instead identical to the fresh SFT0.05; highlighting enhancement in CO_2 resistance for SFT0.05 relative to SF.
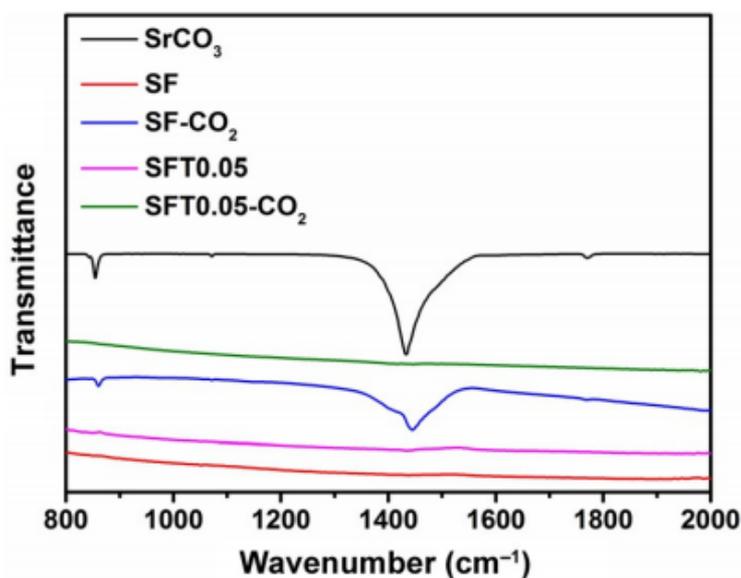
Figure 6.10 Fourier-Transform Infra-Red (FTIR) spectra of fresh and CO_2-treated SF and SFT0.05 powders (SF, SF-CO_2, SFT0.05 and SFT0.05-CO_2), including commercial SrCO₃ powder as a reference.

The observed CO_2 resistance of SFT0.05 can be explained by Lewis acid-base theory where CO_2 is the acid gas while SFT0.05 is the solid base.[4,9,45] Within this context, O1s binding energy (O1s BE) has often been used as a parameter representing the basicity of perovskite oxides with a higher O1s BE implies lower tendency for the perovskite oxide to donate electrons to CO_2 to participate in the reaction and therefore reflects the lower basicity.[4,9] Here, O1s BE of SF and SFT0.05 were quantified using X-ray photoelectron spectroscopy (XPS) as shown in **Figure 6.11**. The peaks at ~533.6 eV represent absorbed water which are identical for both SF and SFT0.05. Likewise, the peaks at ~531.0 eV are assigned to the absorbed oxygen on both spectra. The peak for the lattice oxygen however emerged at higher O1s BE (528.7 eV) for SFT0.05 compared to that for SF (528.3 eV). This higher O1s BE value (0.4 eV) from SFT0.05 verifies its lower basicity than that from SF. It is interesting to note that the difference in O1s BE for lattice oxygen observed here between SFT0.05 and SF exactly matches the previous comparative observation between $Sr(Co_{0.8}Fe_{0.2})_{0.9}Ta_{0.1}O_{3-\delta}$ and $SrCo_{0.8}Fe_{0.2}O_{3-\delta}$.[9]
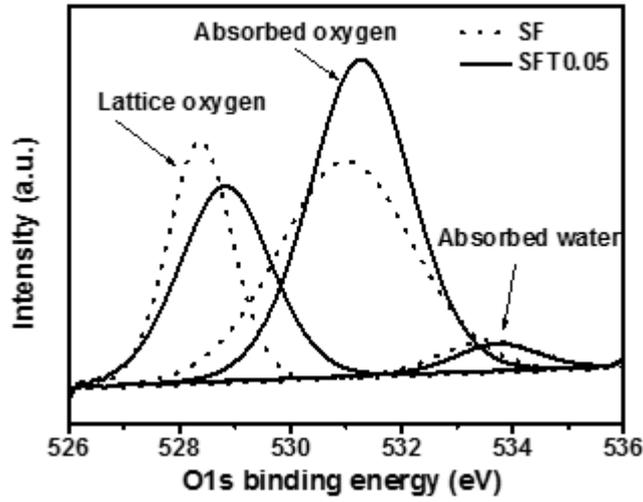
Figure 6.11 X-ray photoelectron spectroscopy spectra of oxygen species on fresh SF and SFT0.05 powders.
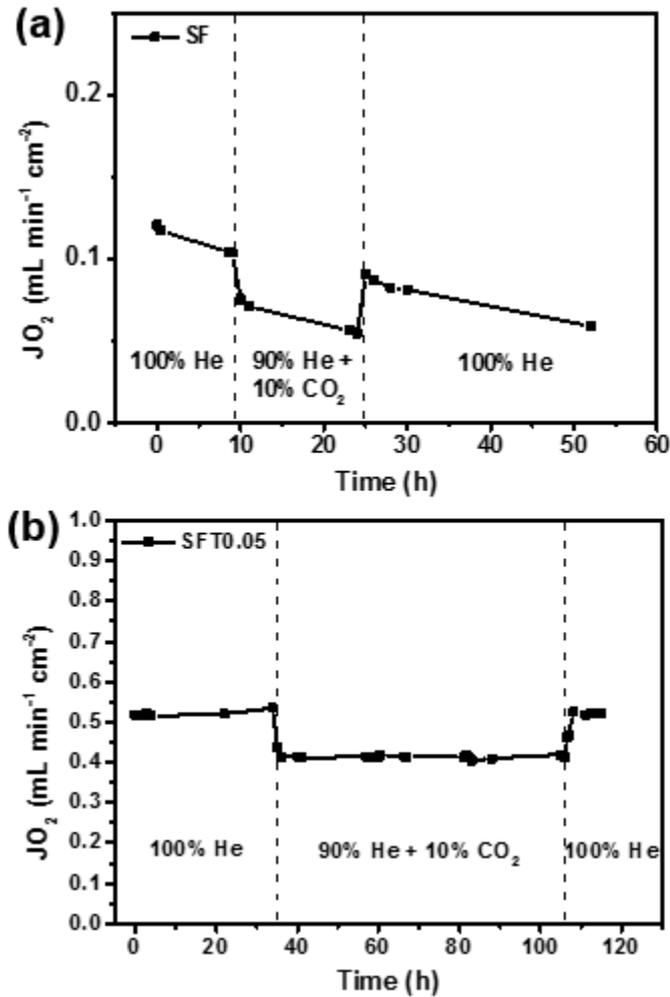
Figure 6.12 Long-term permeation tests of (a) SF and (b) SFT0.05 disk membranes in CO_2-containing atmosphere.

The CO_2 resistance of SFT0.05 in long term permeation testing (in the presence of 10 vol.% of CO_2 in helium) at 850 ^oC against SF is presented in **Figure 6.12**. For SF (**Figure 6.12(a)**), during the first 10-hour period where 100 % helium was used as the sweep gas, the fluxes decreased from 0.12 to 0.10 mL min^{-1} cm^{-2}, which is likely due to the phase instability of SF. After the introduction of CO_2 for 1 hour, the flux rates were substantially reduced to 0.075 mL min^{-1} cm^{-2}; most likely due to the CO_2 absorption on the membrane surface.[39,46] During the next 15-hour period, the oxygen fluxes decreased further by 27 % (from 0.075 to 0.055 mL min^{-1} cm^{-2}). Upon changing the atmosphere back to 100 % helium, the fluxes continued to drop to lower values, reaching 0.59 mL min^{-1} cm^{-2} after 52 hour. The degradation of O_2 fluxes after the introduction of CO_2 is likely caused by both phase instability and chemical reaction with CO_2. Our calculations on O_2 degradation rates prior to, during and after introducing CO_2 (not shown here) indicate that the degradation rate became faster under CO_2-containing atmosphere. Due to the relatively high chemical stability of the cobalt-free SF oxide and low CO_2 concentration here, the contribution from CO_2 reaction becomes less apparent although it does exist as we will show below. Unlike SF, SFT0.05 (**Figure 6.12(b)**) shows much higher initial fluxes which varies around 0.51 mL min^{-1} cm^{-2} during the initial 34-hour period of permeation using 100 % helium. When CO_2 was introduced on the 34th hour, the fluxes dropped slightly to 0.42 mL min^{-1} cm^{-2}; translating into 18 % reduction only. This flux was maintained over the next 71-hour period of testing. As observed, the initial fluxes could be recovered upon switching the atmosphere back to 100 % helium. SFT0.05 therefore showed superior performance in comparison with SF, in pure helium and 10 vol.% CO_2-containing helium atmospheres; highlighting enhanced structural and chemical stability from Ta doping. We also characterized the phases on the sweep side of the SF and SFT0.05 membranes subjected to long term test using powder X-ray diffraction (**Figure 6.13**). The powder XRD pattern for SF reveals the formation of $SrCO_3$ (PDF #05–0418) which is not observed in SFT0.05 sample.[23] It is worth noting that a trade-off exists between the performance and stability. Our focus on SFT0.05 is to balance the high oxygen flux with the relatively improved chemical stability. The highest Ta doping composition we developed here, i.e., SFT0.2 is anticipated to have the best chemical stability as is demonstrated for its Nb doped $SrFeO_{3-\delta}$ analogue, $SrFe_{0.8}Nb_{0.2}O_{3-\delta}$ perovskite membrane.[47] Accordingly, the additional permeation tests at 850 ^oC we performed

using 100 % CO_2 sweep gas confirmed this hypothesis (**Figure 6.14**). SFT0.2 delivered the lowest oxygen fluxes deterioration rate (21.9 % between 0-32 h) followed by SFT0.05 (33.9 % between 0-26 h) and SF (46.0 % between 0-9 h). Sudden drops in fluxes were also noticed upon switching the sweep gas from helium to CO_2 at 0 h. Approximately 60 % reduction from the initial fluxes (in helium) were obtained consistently for the three tested compositions which is indicative of significant CO_2 adsorption on the membrane surface.
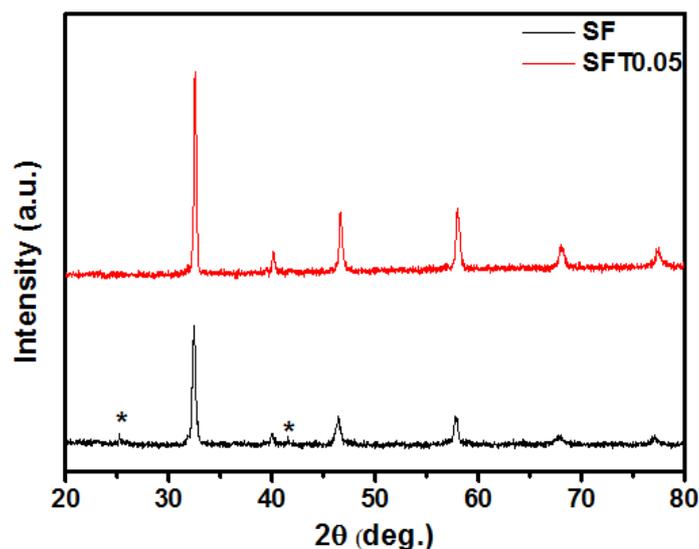
Figure 6.13 Room-temperature powder X-ray diffraction patterns of SF and SFT0.05 disk membranes (sweep side) after long-term test under CO_2-containing atmosphere (*: $SrCO_3$ PDF #05-0418).
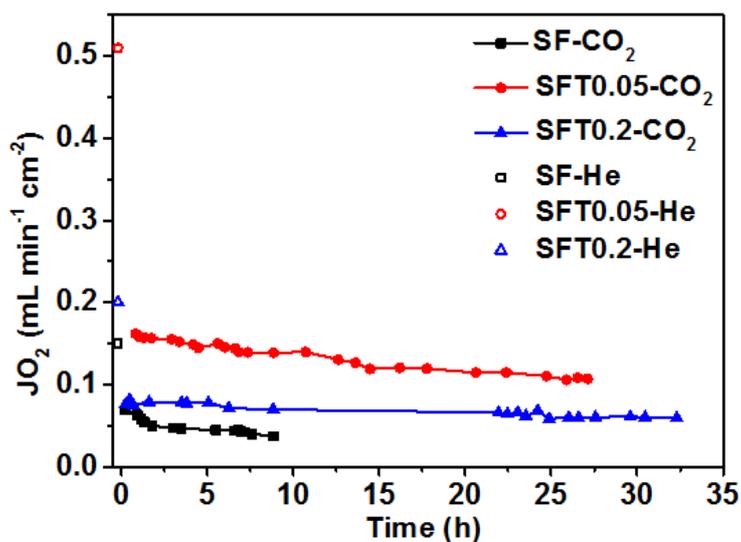
Figure 6.14 Long-term permeation tests of SF, SFT0.05 and SFT0.2 disk membranes in 100 % CO_2 sweep gas (The first points are the fluxes under 100 % helium).

6.4 Conclusions

$SrFe_{1-x}Ta_xO_{3-\delta}$ (x = 0−0.2) perovskite oxide membranes were synthesized using solid-state reaction route and characterized in terms of their structure, morphology and oxygen permeation flux rates. Composition optimization indicates that the incorporation of 5 mol. % Ta within the $SrFeO_{3-\delta}$ perovskite framework can stabilize the cubic structure and maximize the oxygen permeation fluxes. The oxygen permeation through $SrFe_{0.95}Ta_{0.05}O_{3-\delta}$ membrane with thickness over 0.5 mm was mainly limited by bulk-diffusion. Catalyst surface decoration is more effective than using the external electronic short circuit to improve the oxygen fluxes. The results from FT-IR spectroscopy, XPS analysis and long-term permeation test confirmed the enhanced CO_2 resistance of $SrFe_{0.95}Ta_{0.05}O_{3-\delta}$ than $SrFeO_{3-\delta}$ and highlight the potential of Ta-doped $SrFeO_{3-\delta}$ perovskites for applications in clean energy project like oxy-fuel combustion to further reduce the oxygen production cost and in high temperature membrane reactors for greener chemical synthesis like the syngas production from partial methane oxidation.

6.5 References

1. M. Czyperek, P. Zapp, H. J. M. Bouwmeester, M. Modigell, K. V. Peinemann, I. Voigt, W. A. Meulenberg, L. Singheiser, D. Stöver, Energy Procedia, 2009, 1, 303–310.

2. M. Czyperek, P. Zapp, H. J. M. Bouwmeester, M. Modigell, K. Ebert, I. Voigt, W. A. Meulenberg, L. Singheiser, D. Stöver, J. Membr. Sci., 2010, 359, 149–159.

3. J. Yi, T. E. Weirich, M. Schroeder, J. Membr. Sci., 2013, 437, 49–56.

4. W. Chen, C. Chen, H. J. M. Bouwmeester, A. Nijmeijer, L. Winnubst, J. Membr. Sci., 2014, 463, 166–172.

5. A. Leo, S. Liu, J. C. Diniz da Costa, Int. J. Greenhouse Gas Control, 2009, 3, 357–367.

6. J. Repasky, D. McCarthy, P. Armstrong, M. Carolan, ITM Technology for Carbon Capture on Natural Gas and Hybrid Power Systems, Workshop on Technology Pathways Forward for Carbon Capture & Storage on Natural Gas Power Systems, Air

Products and Chemicals, Inc. Washington DC, 2014.

7. J. Sunarso, S. Baumann, J. M. Serra, W. A. Meulenberg, S. Liu, Y. Lin, J. C. Diniz da Costa, J. Membr. Sci., 2008, 320, 13–41.

8. H. D. Megaw, Crystal structures: a working approach, W.B. Saunders Company, Philadelphia, 1973.

9. W. Chen, C. Chen, L. Winnubst, Solid State Ionics, 2011, 196, 30–33.

10. K. Efimov, T. Klande, N. Juditzki, A. Feldhoff, J. Membr. Sci., 2012, 389, 205–215; 11. Y. Wei, O. Ravkina, T. Klande, H. Wang, A. Feldhoff, J. Membr. Sci., 2013, 429, 147–154.

12. T. Klande, O. Ravkina, A. Feldhoff, J. Membr. Sci., 2013, 437, 122–130.

13. K. Partovi, F. Liang, O. Ravkina, J. Caro, ACS Appl. Mater. Interfaces, 2014, 6, 10274–10282.

14. Ø. F. Lohne, J. Gurauskis, T. N. Phung, M. A. Einarsrud, T. Grande, H. J. M. Bouwmeester, K. Wiik, Solid State Ionics, 2012, 225, 186–189.

15. H. Luo, Y. Wei, H. Jiang, W. Yuan, Y. Lv, J. Caro, H. Wang, J. Membr. Sci. 2010, 350, 154–160.

16. R. D. Shannon, C. T. Prewitt, Acta. Cryst., 1968, B25, 925–946.

17. I. Kagomiya, Y. Shimono, K.–i. Kakimoto, Solid State Ionics, 2014, 262, 664–667.

18. A. A. Markov, E. V. Shalaeva, A. P. Tyutyunnik, V. V. Kuchin, M. V. Patrakeev, I. A. Leonidov, V. L. Kozhevnikov, J. Solid State Chem., 2013, 197, 191–197.

19. M. Arnold, Q. Xu, F. D. Tichelaar, A. Feldhoff, Chem. Mater., 2009, 21, 635–640.

20. K. Zhang, R. Ran, L. Ge, Z. Shao, W. Jin, N. Xu, J. Membr. Sci., 2008, 323, 436–443.

21. J. Sunarso, S. Liu, Y. Lin, J. C. Diniz da Costa, J. Membr. Sci., 2009, 344, 281–287.

22. Z. Shao, W. Yang, Y. Cong, H. Dong, J. Tong, G. Xiong, J. Membr. Sci., 2000, 172, 177–188.

23. ICDD PDF-2, Joint Committee on Powder Diffraction Standards (JCPDS)-International Centre for Diffraction Data (ICDD), Pennsylvania, 2004, Powder Diffraction File (PDF) database.

24. H. Falcon, J. A. Barbero, J. A. Alonso, M. J. Martinez–Lope, J. L. G. Fierro, Chem. Mater., 2002, 14, 2325–2333.

25. J. P. Hodges, S. Short, J. D. Jorgensen, X. Xiong, B. Dabrowski, S. M. Mini, C. W. Kimball, J. Solid State Chem., 2000, 151, 190–209.

26. Y. Takeda, K. Kanno, T. Takada, O. Yamamoto, J. Solid State Chem., 1986, 63, 237–249.

27. V. M. Goldschmidt, Geochemische Verterlungsgesetze der Elemente, Norske Videnskap, Oslo, 1927.

28. M. Patrakeev, A. Markov, I. Leonidov, V. Kozhevnikov, V. Kharton, Solid State Ionics, 2006, 177, 1757–1760.

29. P. V. Anikina, A. A. Markov, M. V. Patrakeev, I. A. Leonidov, V. L. Kozhevnikov, Solid State Sci., 2009, 11, 1156–1162.

30. M. J. Akhtar, Z. N. Akhtar, J. P. Dragun, C. R. A. Catlow, Solid State Ionics, 1997, 104, 147–158.

31. K. Zhang, J. Sunarso, Z. Shao, W. Zhou, C. Sun, S. Wang, S. Liu, RSC Adv., 2011, 1, 1661–1676.

32. A. F. Sammells, R. L. Cook, J. H. White, J. J. Osborne, R. C. MacDuff, Solid State Ionics, 1992, 52, 111–123.

33. C. Wagner, W. Schottky, Z. Phys. Chem., 1930, B11, 163–210.

34. C. Chen, H. Kruidhof, H. J. M. Bouwmeester, H. Verweij, A. J. Burggraaf, Solid State Ionics, 1997, 99, 215–219.

35. A. Leo, S. Liu, J. C. Diniz da Costa, J. Membr. Sci., 2009, 340, 148–153.

36. K. Zhang, Z. Shao, C. Li, S. Liu, Energy Environ. Sci., 2012, 5, 5257–5264.

37. S. Imashuku, L. Wang, K. Mezghani, M. A. Habib, S.-H. Yang, J. Electrochem. Soc., 2013, 160, E148–E153.

38. L. Wang, S. Imashuku, A. Grimaud, D. Lee, K. Mezghani, M. A. Habib, S. -H. Yang, ECS Electrochem. Lett., 2013, 2, F77–F81.

39. C. Zhang, X. Meng, J. Sunarso, L. Liu, R. Xu, Z. Shao, S. Liu, J. Mater. Chem. A, 2015, 3, 19033–19041.

40. C. Zhang, R. Ran, G. H. Pham, K. Zhang, J. Liu, S. Liu, RSC Adv., 2015, 5, 5379–5386.

41. B. He, K. Zhang, Y. Ling, J. Xu, L. Zhao, J. Membr. Sci., 2014, 464, 55–60.

42. A. A. Markov, M. V. Patrakeev, O. A. Savinskaya, A. P. Nemudry, I. A. Leonidov, O. N. Leonidova, V. L. Kozhevnikov, Solid State Ionics, 2008, 179, 99–103.

43. G. Xiao, Q. Liu, S. Wang, V. G. Komvokis, M. D. Amiridis, A. Heyden, S. Ma, F. Chen, J. Power Sources, 2012, 202, 63–69.

44. Y. Chen, B. Qian, Y. Hao, S. Liu, M. O. Tade, Z. Shao, J. Membr. Sci., 2014, 470, 102–111.

45. Q. Zeng, Y. Zuo, C. Fan, C. Chen, J. Membr. Sci., 2009, 335, 140–144.

46. P. F. Haworth, S. Smart, J. M. Serra, J. C. Diniz da Costa, Phys. Chem. Chem. Phys., 2012, 14, 9104–9111.

47. J. Yi, M. Schroeder, M. Martin, Chem. Mater., 2013, 25, 815-817.

Chapter 7: Conclusions and Perspectives

7.1 Conclusions

In this thesis, novel CO_2-resistant ceramic membranes with several different configurations have been designed and investigated for oxygen permeation. We aimed to develop CO_2-resistance ceramic membranes for clean energy delivery applications such as oxyfuel combustion, coal gasification, green chemical synthesis and single chamber solid oxide fuel cells. Excellent CO_2-resistance and good oxygen permeation flux are the essential factors in these applications. We explored various methods in this thesis, *i.e.*, by using external short-circuit design on traditional GDC membrane, applying transition metal sintering aid in GDC membrane, and doping the tantalum into a $SrFeO_{3-\delta}$ membrane to enhance the overall O_2 permeability and CO_2-resistance. The following general conclusions have been derived from these studies.

7.1.1 $Ce_{0.9}Gd_{0.1}O_{2-\delta}$ membrane coated with porous $Ba_{0.5}Sr_{0.5}Co_{0.8}Fe_{0.2}O_{3-\delta}$ for oxygen separation

- A cheaper mixed ionic-electronic conducting BSCF was decorated on an ion conducting ceramic membrane GDC to realize the external short-circuit concept. The as-decorated GDC membrane showed enhanced oxygen permeation flux, compared with the membrane coated with silver.
- The BSCF coating improved the surface oxygen-exchange reaction kinetics by increasing the triple-phase boundary (TBP) area.
- The GDC membrane with a BSCF coating on the feed side and Ag coating on the sweep side facing to CO_2-containing atmosphere was stable during the long-term test.

7.1.2 Oxygen permeation behaviour through $Ce_{0.9}Gd_{0.1}O_{2-\delta}$ membranes electronically short-circuited by dual-phase $Ce_{0.9}Gd_{0.1}O_{2-\delta}$-Ag decoration

- The dual-phase membrane idea was successfully extended to surface coating to decorate GDC-Ag mixture on a fluorite GDC membrane.

- A continuous electronic conducing network could be formed on the surface with GDC-Ag (50 : 50 wt.%) coating, and a maximum oxygen flux of 0.128 mL min^{-1} cm^{-2} was achieved using the as-prepared membrane.
- The short-circuited membrane with GDC-Ag (50 : 50 wt.%) coating maintained stable performance in a CO_2-containing atmosphere for minimum 130 h.

7.1.3 Enhanced oxygen permeability and electronic conductivity of $Ce_{0.8}Gd_{0.2}O_{2-\delta}$ membrane via the addition of transition metal oxide sintering aids

- Cobalt incorporated into GDC membrane as a sintering aid could improve the sinterability and the electronic conductivity of GDC membranes.
- The sintering temperature was decreased by 300 °C with 2 mol. % Co (2Co-GDC) compared with that from a pure GDC membrane.
- The 2Co-GDC membrane showed the highest oxygen flux of 0.112 mL min^{-1} cm^{-2} under Air/He gradient at 900 °C, which was twice that of pure GDC membrane.
- The electronic conductivity was enhanced between 750-900 °C with the Co sintering aid, and the ionic transference numbers achieved from modified EMF method were lower, compared with pure GDC membrane.
- Long term (120 h) stability oxygen permeation test using 100 % CO_2 as the sweep gas demonstrated the enhanced CO_2-resistance of 2Co-GDC, indicating its potentials in clean energy delivery.

7.1.4 Enhanced CO_2 resistance for robust oxygen separation through tantalum-doped perovskite membranes

- Tantalum (Ta) was doped into $SrFeO_{3-\delta}$ to form $SrFe_{1-x}Ta_xO_{3-\delta}$ (x = 0-0.2) through a solid-state reaction method.
- Incorporation of 5 mol.% Ta could stabilize the cubic structure and enhance the CO_2-resistance by increasing the O1s binding energy.
- The long-term oxygen permeation test under CO2 atmosphere further demonstrate the potential of using Ta-doped perovskite in a clean energy delivery such as oxy-fuel combustion and high temperature membrane reactors.

In conclusion, above strategies provide alternatives to fabricate novel CO_2-

resistant membranes that are potentially to be used in oxygen production, oxyfuel combustion and membrane reactors. Compared with other CO_2-resistant membranes (as shown in Literature review chapter), the resultant membranes in this thesis showed comparable maximum O_2 flux, *i.e.*, higher than 0.1 mL min^{-1} cm^{-2} and can be remained stable during long-term operation. Although the O_2 fluxes through short-circuited membrane and sintering aid-doped membrane is one or two order(s) of magnitude lower compared with perovskite membranes, the key advantage of the membranes in this thesis is their robust and stable properties. The resultant membranes in this thesis can be designed as permeation unit in oxyfuel combustion factory and membrane reactors such as syngas production from methane due to the high stability. Moreover, under the reaction conditions, the oxygen concentration gradient through the membranes will be much larger than that employed in our permeation experiments, *i.e.*, 0.21 atm (air)/10^{-8} to 10^{-16} atm as opposed to 0.21 atm (air)/10^{-3} atm (sweep), thus resulting in much higher oxygen fluxes. Therefore, the short-circuit GDC membranes and those with sintering aid have better opportunity to be commercialized in the future.

7.2 Perspectives

1. The surface decoration method in this thesis was exemplified based on a single-phase fluorite GDC membrane. In the future, dual-phase membranes can be applied. Thus, the triple-phase boundary areas are extended and even quadruple-phase boundary can be formed. The oxygen permeation flux will be enhanced due to the increased surface oxygen exchange kinetics. Moreover, the use of dual-phase membrane instead of single GDC phase may further increase the oxygen permeability due to faster bulk diffusion rate.

2. Dual-phase coating has been frequently applied in the field of solid oxide fuel cells but seldom applied in the membranes for oxygen separation. In Chapter 4, we used GDC-Ag mixtures to demonstrate the applicability. In the future, different types of dual-phase coatings can be further developed for different applications. For example, the silver phase can be replaced by a robust electronic ceramic conductor (e.g., $La_{0.8}Sr_{0.2}CoO_{3-\delta}$, $La_{0.7}Sr_{0.3}MnO_{3-\delta}$ and spinel-structured oxide) or mixed ionic-electronic ceramic conductors. The

absence of noble metal can further reduce the cost and improve the compatibility between two phases.

3. The use of transition metal sintering aid was proved to decrease the sintering temperature and enhance the oxygen permeation flux. In addition to these transition metals, other materials such as perovskite oxide with lower melting-point may be a suitable sintering aid. In such a case, the sintering aid itself can permeate oxygen. For example, GDC powders can be soaked and stirred in BSCF gel to form BSCF-encapsulated GDC. The as-prepared GDC may be densified at lower temperature and the existence of BSCF on the GDC grain boundary can facilitate the oxygen transport.

4. The CO_2-resistant membranes involved in this thesis were targeted at applications in clean energy delivery such as oxyfuel combustion and membrane reactors. However, in this thesis we only demonstrated the oxygen permeability and CO_2-resistance of these membranes. In future work, these membranes should be tested under real industrial processes, e.g., oxyfuel combustion and green chemical synthesis.

Appendix: Permission of Reproduction from the Copyright Owner

Copyright Clearance Center   **RightsLink®**   Home | Account Info | Help | ✉

SOLID STATE IONICS	

Title: Guidelines for improving resistance to CO2 of materials for solid state electrochemical systems

Author: A. Brandão,J.F. Monteiro,A.V. Kovalevsky,D.P. Fagg,V.V. Kharton,J.R. Frade

Publication: Solid State Ionics

Publisher: Elsevier

Date: 16 June 2011

Copyright © 2010 Elsevier B.V. All rights reserved.

Logged in as:
Chi Zhang
Account #:
3001096626

LOGOUT

Order Completed

Thank you for your order.

This Agreement between Chi Zhang ("You") and Elsevier ("Elsevier") consists of your license details and the terms and conditions provided by Elsevier and Copyright Clearance Center.

Your confirmation email will contain your order number for future reference.

Printable details.

License Number	4046250438464
License date	Feb 11, 2017
Licensed Content Publisher	Elsevier
Licensed Content Publication	Solid State Ionics
Licensed Content Title	Guidelines for improving resistance to CO2 of materials for solid state electrochemical systems
Licensed Content Author	A. Brandão,J.F. Monteiro,A.V. Kovalevsky,D.P. Fagg,V.V. Kharton,J.R. Frade
Licensed Content Date	16 June 2011
Licensed Content Volume	192
Licensed Content Issue	1
Licensed Content Pages	5
Type of Use	reuse in a thesis/dissertation
Portion	figures/tables/illustrations
Number of figures/tables/illustrations	4
Format	both print and electronic
Are you the author of this Elsevier article?	No
Will you be translating?	No
Order reference number	
Original figure numbers	Figure 1, 2, 3, 5
Title of your thesis/dissertation	Novel ceramic membranes for gas separation in enabling the clean energy delivery
Expected completion date	Feb 2017
Estimated size (number of pages)	207
Elsevier VAT number	GB 494 6272 12
Requestor Location	Chi Zhang 4/31 Nottingham Street East Victoria Park Perth, WA 6101 Australia Attn: Chi Zhang
Total	0.00 AUD

RightsLink®

Home	Account Info	Help	✉

Title: Thermodynamic stabilities of perovskite oxides for electrodes and other electrochemical materials

Author: Harumi Yokokawa,Natsuko Sakai,Tatsuya Kawada,Masayuki Dokiya

Publication: Solid State Ionics

Publisher: Elsevier

Date: May 1992

Copyright © 1992 Published by Elsevier B.V.

Logged in as:
Chi Zhang
Account #:
3001096626

LOGOUT

Order Completed

Thank you for your order.

This Agreement between Chi Zhang ("You") and Elsevier ("Elsevier") consists of your license details and the terms and conditions provided by Elsevier and Copyright Clearance Center.

Your confirmation email will contain your order number for future reference.

Printable details.

License Number	4046250741512
License date	Feb 11, 2017
Licensed Content Publisher	Elsevier
Licensed Content Publication	Solid State Ionics
Licensed Content Title	Thermodynamic stabilities of perovskite oxides for electrodes and other electrochemical materials
Licensed Content Author	Harumi Yokokawa,Natsuko Sakai,Tatsuya Kawada,Masayuki Dokiya
Licensed Content Date	May 1992
Licensed Content Volume	52
Licensed Content Issue	1-3
Licensed Content Pages	14
Type of Use	reuse in a thesis/dissertation
Portion	figures/tables/illustrations
Number of figures/tables/illustrations	1
Format	both print and electronic
Are you the author of this Elsevier article?	No
Will you be translating?	No
Order reference number	
Original figure numbers	Figure 5
Title of your thesis/dissertation	Novel ceramic membranes for gas separation in enabling the clean energy delivery
Expected completion date	Feb 2017
Estimated size (number of pages)	207
Elsevier VAT number	GB 494 6272 12
Requestor Location	Chi Zhang
4/31 Nottingham Street
East Victoria Park

Perth, WA 6101
Australia
Attn: Chi Zhang |

192

RightsLink®

Home Account Info Help

Title: Effect of CO2 and SO2 on oxygen permeation and microstructure of (Pr0.9La0.1)2(Ni0.74Cu0.21Ga0.05)O4+δ membranes

Author: Yanying Wei,Olga Ravkina,Tobias Klande,Haihui Wang,Armin Feldhoff

Publication: Journal of Membrane Science

Publisher: Elsevier

Date: 15 February 2013

Order Completed

Thank you for your order.

This Agreement between Chi Zhang ("You") and Elsevier ("Elsevier") consists of your license details and the terms and conditions provided by Elsevier and Copyright Clearance Center.

Your confirmation email will contain your order number for future reference.

Printable details.

License Number	4046250929776
License date	Feb 11, 2017
Licensed Content Publisher	Elsevier
Licensed Content Publication	Journal of Membrane Science
Licensed Content Title	Effect of CO2 and SO2 on oxygen permeation and microstructure of (Pr0.9La0.1)2(Ni0.74Cu0.21Ga0.05)O4+δ membranes
Licensed Content Author	Yanying Wei,Olga Ravkina,Tobias Klande,Haihui Wang,Armin Feldhoff
Licensed Content Date	15 February 2013
Licensed Content Volume	429
Licensed Content Issue	n/a
Licensed Content Pages	8
Type of Use	reuse in a thesis/dissertation
Portion	figures/tables/illustrations
Number of figures/tables/illustrations	1
Format	both print and electronic
Are you the author of this Elsevier article?	No
Will you be translating?	No
Order reference number	
Original figure numbers	Figure 1
Title of your thesis/dissertation	Novel ceramic membranes for gas separation in enabling the clean energy delivery
Expected completion date	Feb 2017
Estimated size (number of pages)	207
Elsevier VAT number	GB 494 6272 12
Requestor Location	Chi Zhang 4/31 Nottingham Street East Victoria Park Perth, WA 6101 Australia Attn: Chi Zhang
Total	0.00 AUD

Copyright Clearance Center

RightsLink®

Title:	Acidity Scale for Metal Oxides and Sanderson's Electronegativities of Lanthanide Elements
Author:	Nak Cheon Jeong,Ji Sun Lee,Eunju Lee Tae,Young Ju Lee,Kyung Byung Yoon
Publication:	Angewandte Chemie International Edition
Publisher:	John Wiley and Sons
Date:	Nov 21, 2008

Copyright © 2008 WILEY-VCH Verlag GmbH & Co. KGaA, Weinheim

Order Completed

Thank you for your order.

This Agreement between Chi Zhang ("You") and John Wiley and Sons ("John Wiley and Sons") consists of your license details and the terms and conditions provided by John Wiley and Sons and Copyright Clearance Center.

Your confirmation email will contain your order number for future reference.

Printable details.

License Number	4046261135155
License date	Feb 11, 2017
Licensed Content Publisher	John Wiley and Sons
Licensed Content Publication	Angewandte Chemie International Edition
Licensed Content Title	Acidity Scale for Metal Oxides and Sanderson's Electronegativities of Lanthanide Elements
Licensed Content Author	Nak Cheon Jeong,Ji Sun Lee,Eunju Lee Tae,Young Ju Lee,Kyung Byung Yoon
Licensed Content Date	Nov 21, 2008
Licensed Content Pages	5
Type of use	Dissertation/Thesis
Requestor type	University/Academic
Format	Print and electronic
Portion	Figure/table
Number of figures/tables	1
Original Wiley figure/table number(s)	Figure 3
Will you be translating?	No
Title of your thesis / dissertation	Novel ceramic membranes for gas separation in enabling the clean energy delivery
Expected completion date	Feb 2017
Expected size (number of pages)	207
Requestor Location	Chi Zhang 4/31 Nottingham Street East Victoria Park Perth, WA 6101 Australia Attn: Chi Zhang
Publisher Tax ID	EU826007151
Billing Type	Invoice

RightsLink®

Copyright Clearance Center

| Home | Account Info | Help | ✉ |

journal of MEMBRANE SCIENCE

Title:	CO2-tolerant oxygen separation membranes targeting CO2 capture application
Author:	Qing Zeng,Yan-bo Zuo,Chuan-gang Fan,Chu-sheng Chen
Publication:	Journal of Membrane Science
Publisher:	Elsevier
Date:	15 June 2009

Copyright © 2009 Elsevier B.V. All rights reserved.

Logged in as:
Chi Zhang
Account #:
3001096626

LOGOUT

Order Completed

Thank you for your order.

This Agreement between Chi Zhang ("You") and Elsevier ("Elsevier") consists of your license details and the terms and conditions provided by Elsevier and Copyright Clearance Center.

Your confirmation email will contain your order number for future reference.

Printable details.

License Number	4046260130733
License date	Feb 11, 2017
Licensed Content Publisher	Elsevier
Licensed Content Publication	Journal of Membrane Science
Licensed Content Title	CO2-tolerant oxygen separation membranes targeting CO2 capture application
Licensed Content Author	Qing Zeng,Yan-bo Zuo,Chuan-gang Fan,Chu-sheng Chen
Licensed Content Date	15 June 2009
Licensed Content Volume	335
Licensed Content Issue	1-2
Licensed Content Pages	5
Type of Use	reuse in a thesis/dissertation
Portion	figures/tables/illustrations
Number of figures/tables/illustrations	2
Format	both print and electronic
Are you the author of this Elsevier article?	No
Will you be translating?	No
Order reference number	
Original figure numbers	Figure 1, 2
Title of your thesis/dissertation	Novel ceramic membranes for gas separation in enabling the clean energy delivery
Expected completion date	Feb 2017
Estimated size (number of pages)	207
Elsevier VAT number	GB 494 6272 12
Requestor Location	Chi Zhang 4/31 Nottingham Street East Victoria Park
	Perth, WA 6101 Australia Attn: Chi Zhang
Total	0.00 AUD

ORDER MORE   CLOSE WINDOW

Copyright
Clearance
Center

RightsLink®

Home   Account Info   Help   ✉

SOLID STATE IONICS
DIFFUSION & REACTIONS

Title: Ta-doped SrCo0.8Fe0.2O3-δ membranes: Phase stability and oxygen permeation in CO2 atmosphere

Author: Wei Chen,Chu-sheng Chen,Louis Winnubst

Publication: Solid State Ionics

Publisher: Elsevier

Date: 11 August 2011

Copyright © 2011 Elsevier B.V. All rights reserved.

Logged in as:
Chi Zhang
Account #:
3001096626

LOGOUT

Order Completed

Thank you for your order.

This Agreement between Chi Zhang ("You") and Elsevier ("Elsevier") consists of your license details and the terms and conditions provided by Elsevier and Copyright Clearance Center.

Your confirmation email will contain your order number for future reference.

Printable details.

License Number	4046260320000
License date	Feb 11, 2017
Licensed Content Publisher	Elsevier
Licensed Content Publication	Solid State Ionics
Licensed Content Title	Ta-doped SrCo0.8Fe0.2O3-δ membranes: Phase stability and oxygen permeation in CO2 atmosphere
Licensed Content Author	Wei Chen,Chu-sheng Chen,Louis Winnubst
Licensed Content Date	11 August 2011
Licensed Content Volume	196
Licensed Content Issue	1
Licensed Content Pages	4
Type of Use	reuse in a thesis/dissertation
Portion	figures/tables/illustrations
Number of figures/tables/illustrations	1
Format	both print and electronic
Are you the author of this Elsevier article?	No
Will you be translating?	No
Order reference number	
Original figure numbers	Figure 6
Title of your thesis/dissertation	Novel ceramic membranes for gas separation in enabling the clean energy delivery
Expected completion date	Feb 2017
Estimated size (number of pages)	207
Elsevier VAT number	GB 494 6272 12
Requestor Location	Chi Zhang 4/31 Nottingham Street East Victoria Park Perth, WA 6101 Australia Attn: Chi Zhang
Total	0.00 USD

RightsLink®

Copyright Clearance Center

	Home	Account Info	Help	✉

journal of MEMBRANE SCIENCE

Title: Oxygen-selective membranes integrated with oxy-fuel combustion

Author: Wei Chen,Chu-sheng Chen,Henny J.M. Bouwmeester,Arian Nijmeijer,Louis Winnubst

Publication: Journal of Membrane Science

Publisher: Elsevier

Date: 1 August 2014

Copyright © 2014 Elsevier B.V. All rights reserved.

Logged in as:
Chi Zhang
Account #:
3001096626

LOGOUT

Order Completed

Thank you for your order.

This Agreement between Chi Zhang ("You") and Elsevier ("Elsevier") consists of your license details and the terms and conditions provided by Elsevier and Copyright Clearance Center.

Your confirmation email will contain your order number for future reference.

Printable details.

License Number	4046260465594
License date	Feb 11, 2017
Licensed Content Publisher	Elsevier
Licensed Content Publication	Journal of Membrane Science
Licensed Content Title	Oxygen-selective membranes integrated with oxy-fuel combustion
Licensed Content Author	Wei Chen,Chu-sheng Chen,Henny J.M. Bouwmeester,Arian Nijmeijer,Louis Winnubst
Licensed Content Date	1 August 2014
Licensed Content Volume	463
Licensed Content Issue	n/a
Licensed Content Pages	7
Type of Use	reuse in a thesis/dissertation
Portion	figures/tables/illustrations
Number of figures/tables/illustrations	1
Format	both print and electronic
Are you the author of this Elsevier article?	No
Will you be translating?	No
Order reference number	
Original figure numbers	Figure 5
Title of your thesis/dissertation	Novel ceramic membranes for gas separation in enabling the clean energy delivery
Expected completion date	Feb 2017
Estimated size (number of pages)	207
Elsevier VAT number	GB 494 6272 12
Requestor Location	Chi Zhang 4/31 Nottingham Street East Victoria Park Perth, WA 6101 Australia Attn: Chi Zhang
Total	0.00 USD

RightsLink®

| Home | Account Info | Help | ✉ |

Title: A Mixed Ionic and Electronic Conducting Dual-Phase Membrane with High Oxygen Permeability

Author: Wei Fang,Fangyi Liang,Zhengwen Cao,Frank Steinbach,Armin Feldhoff

Publication: Angewandte Chemie International Edition

Publisher: John Wiley and Sons

Date: Feb 23, 2015

© 2015 WILEY-VCH Verlag GmbH & Co. KGaA, Weinheim

Order Completed

Thank you for your order.

This Agreement between Chi Zhang ("You") and John Wiley and Sons ("John Wiley and Sons") consists of your license details and the terms and conditions provided by John Wiley and Sons and Copyright Clearance Center.

Your confirmation email will contain your order number for future reference.

Printable details.

License Number	4046260967918
License date	Feb 11, 2017
Licensed Content Publisher	John Wiley and Sons
Licensed Content Publication	Angewandte Chemie International Edition
Licensed Content Title	A Mixed Ionic and Electronic Conducting Dual-Phase Membrane with High Oxygen Permeability
Licensed Content Author	Wei Fang,Fangyi Liang,Zhengwen Cao,Frank Steinbach,Armin Feldhoff
Licensed Content Date	Feb 23, 2015
Licensed Content Pages	4
Type of use	Dissertation/Thesis
Requestor type	University/Academic
Format	Print and electronic
Portion	Figure/table
Number of figures/tables	1
Original Wiley figure/table number(s)	Figure 1
Will you be translating?	No
Title of your thesis / dissertation	Novel ceramic membranes for gas separation in enabling the clean energy delivery
Expected completion date	Feb 2017
Expected size (number of pages)	207
Requestor Location	Chi Zhang 4/31 Nottingham Street East Victoria Park Perth, WA 6101 Australia Attn: Chi Zhang

Title: Crystal Structure–Ionic Conductivity Relationships in Doped Ceria Systems

Author: Shobit Omar, Eric D. Wachsman, Jacob L. Jones, Juan C. Nino

Publication: Journal of the American Ceramic Society

Publisher: John Wiley and Sons

Date: Sep 9, 2009

© 2009 The American Ceramic Society

Logged in as:
Chi Zhang
Account #:
3001096626

LOGOUT

Order Completed

Thank you for your order.

This Agreement between Chi Zhang ("You") and John Wiley and Sons ("John Wiley and Sons") consists of your license details and the terms and conditions provided by John Wiley and Sons and Copyright Clearance Center.

Your confirmation email will contain your order number for future reference.

Printable details.

License Number	4046261366840
License date	Feb 11, 2017
Licensed Content Publisher	John Wiley and Sons
Licensed Content Publication	Journal of the American Ceramic Society
Licensed Content Title	Crystal Structure–Ionic Conductivity Relationships in Doped Ceria Systems
Licensed Content Author	Shobit Omar, Eric D. Wachsman, Jacob L. Jones, Juan C. Nino
Licensed Content Date	Sep 9, 2009
Licensed Content Pages	8
Type of use	Dissertation/Thesis
Requestor type	University/Academic
Format	Print and electronic
Portion	Figure/table
Number of figures/tables	1
Original Wiley figure/table number(s)	Figure 6
Will you be translating?	No
Title of your thesis / dissertation	Novel ceramic membranes for gas separation in enabling the clean energy delivery
Expected completion date	Feb 2017
Expected size (number of pages)	207
Requestor Location	Chi Zhang 4/31 Nottingham Street East Victoria Park Perth, WA 6101 Australia Attn: Chi Zhang
Publisher Tax ID	EU826007151
Billing Type	Invoice

AIChE JOURNAL

WILEY   AIChE

Title:	Influence of the preparation methods on the microstructure and oxygen permeability of a CO2-stable dual phase membrane
Author:	Huixia Luo,Heqing Jiang,Konstantin Efimov,Jürgen Caro,Haihui Wang
Publication:	AIChE Journal
Publisher:	John Wiley and Sons
Date:	Dec 17, 2010

Copyright © 2010 American Institute of Chemical Engineers (AIChE)

Order Completed

Thank you for your order.

This Agreement between Chi Zhang ("You") and John Wiley and Sons ("John Wiley and Sons") consists of your license details and the terms and conditions provided by John Wiley and Sons and Copyright Clearance Center.

Your confirmation email will contain your order number for future reference.

Printable details.

License Number	4046270357780
License date	Feb 11, 2017
Licensed Content Publisher	John Wiley and Sons
Licensed Content Publication	AIChE Journal
Licensed Content Title	Influence of the preparation methods on the microstructure and oxygen permeability of a CO2-stable dual phase membrane
Licensed Content Author	Huixia Luo,Heqing Jiang,Konstantin Efimov,Jürgen Caro,Haihui Wang
Licensed Content Date	Dec 17, 2010
Licensed Content Pages	8
Type of use	Dissertation/Thesis
Requestor type	University/Academic
Format	Print and electronic
Portion	Figure/table
Number of figures/tables	1
Original Wiley figure/table number(s)	Figure 3
Will you be translating?	No
Title of your thesis / dissertation	Novel ceramic membranes for gas separation in enabling the clean energy delivery
Expected completion date	Feb 2017
Expected size (number of pages)	207
Requestor Location	Chi Zhang 4/31 Nottingham Street East Victoria Park

Perth, WA 6101 Australia Attn: Chi Zhang |

RightsLink®

Home   Account Info   Help

Title: Effect of doping, microstructure, and CO2 on La2NiO4+δ-based oxygen-transporting materials

Author: Tobias Klande,Konstantin Efimov,Salvatore Cusenza,Klaus-Dieter Becker,Armin Feldhoff

Publication: Journal of Solid State Chemistry

Publisher: Elsevier

Date: December 2011

Order Completed

Thank you for your order.

This Agreement between Chi Zhang ("You") and Elsevier ("Elsevier") consists of your license details and the terms and conditions provided by Elsevier and Copyright Clearance Center.

Your confirmation email will contain your order number for future reference.

Printable details.

License Number	4046271226961
License date	Feb 11, 2017
Licensed Content Publisher	Elsevier
Licensed Content Publication	Journal of Solid State Chemistry
Licensed Content Title	Effect of doping, microstructure, and CO2 on La2NiO4+δ-based oxygen-transporting materials
Licensed Content Author	Tobias Klande,Konstantin Efimov,Salvatore Cusenza,Klaus-Dieter Becker,Armin Feldhoff
Licensed Content Date	December 2011
Licensed Content Volume	184
Licensed Content Issue	12
Licensed Content Pages	9
Type of Use	reuse in a thesis/dissertation
Portion	figures/tables/illustrations
Number of figures/tables/illustrations	1
Format	both print and electronic
Are you the author of this Elsevier article?	No
Will you be translating?	No
Order reference number	
Original figure numbers	Figure 2
Title of your thesis/dissertation	Novel ceramic membranes for gas separation in enabling the clean energy delivery
Expected completion date	Feb 2017
Estimated size (number of pages)	207
Elsevier VAT number	GB 494 6272 12
Requestor Location	Chi Zhang 4/31 Nottingham Street East Victoria Park Perth, WA 6101 Australia Attn: Chi Zhang
Total	0.00 USD

ACS Publications
Most Trusted. Most Cited. Most Read.

Title: Behavior of Ba(Co, Fe, Nb)O3-δ Perovskite in CO2-Containing Atmospheres: Degradation Mechanism and Materials Design

Author: Jianxin Yi, Michael Schroeder, Thomas Weirich, et al

Publication: Chemistry of Materials

Publisher: American Chemical Society

Date: Dec 1, 2010

Copyright © 2010, American Chemical Society

PERMISSION/LICENSE IS GRANTED FOR YOUR ORDER AT NO CHARGE

This type of permission/license, instead of the standard Terms & Conditions, is sent to you because no fee is being charged for your order. Please note the following:

- Permission is granted for your request in both print and electronic formats, and translations.
- If figures and/or tables were requested, they may be adapted or used in part.
- Please print this page for your records and send a copy of it to your publisher/graduate school.
- Appropriate credit for the requested material should be given as follows: "Reprinted (adapted) with permission from (COMPLETE REFERENCE CITATION). Copyright (YEAR) American Chemical Society." Insert appropriate information in place of the capitalized words.
- One-time permission is granted only for the use specified in your request. No additional uses are granted (such as derivative works or other editions). For any other uses, please submit a new request.

If credit is given to another source for the material you requested, permission must be obtained from that source.

BACK | CLOSE WINDOW

Copyright Clearance Center

RightsLink®

Home | Account Info | Help | ✉

Title:	Investigation of carbonates in oxygen-transporting membrane ceramics	Logged in as: Chi Zhang
Author:	Olga Ravkina,Tobias Klande,Armin Feldhoff	Account #: 3001096626
Publication:	Journal of Membrane Science	LOGOUT
Publisher:	Elsevier	
Date:	15 April 2015	

journal of MEMBRANE SCIENCE

Copyright © 2015 Elsevier B.V. All rights reserved.

Order Completed

Thank you for your order.

This Agreement between Chi Zhang ("You") and Elsevier ("Elsevier") consists of your license details and the terms and conditions provided by Elsevier and Copyright Clearance Center.

Your confirmation email will contain your order number for future reference.

Printable details.

License Number	4046280598437
License date	Feb 11, 2017
Licensed Content Publisher	Elsevier
Licensed Content Publication	Journal of Membrane Science
Licensed Content Title	Investigation of carbonates in oxygen-transporting membrane ceramics
Licensed Content Author	Olga Ravkina,Tobias Klande,Armin Feldhoff
Licensed Content Date	15 April 2015
Licensed Content Volume	480
Licensed Content Issue	n/a
Licensed Content Pages	8
Type of Use	reuse in a thesis/dissertation
Portion	figures/tables/illustrations
Number of figures/tables/illustrations	3
Format	both print and electronic
Are you the author of this Elsevier article?	No
Will you be translating?	No
Order reference number	
Original figure numbers	Figure 2, 4, 7
Title of your thesis/dissertation	Novel ceramic membranes for gas separation in enabling the clean energy delivery
Expected completion date	Feb 2017
Estimated size (number of pages)	207
Elsevier VAT number	GB 494 6272 12
Requestor Location	Chi Zhang 4/31 Nottingham Street East Victoria Park Perth, WA 6101 Australia Attn: Chi Zhang
Total	0.00 USD

ORDER MORE | CLOSE WINDOW

203

Request for Permission to Reproduce or Re-Publish ECS Material

Please fax this form to: The Electrochemical Society (ECS), Attn: Permissions Requests, 1.609.730.0629. You may also e-mail your request to: copyright@electrochem.org. Include all the information as required on this form. Please allow 3-7 days for your request to be processed.

I am preparing a (choose one): ☐ paper   ☐ chapter   ☐ book   ☑ thesis

entitled: Novel ceramic membranes for gas separation in enabling the clean energy delivery

to be published by: Curtin University

in an upcoming publication entitled: _____

I request permission to use the following material in the publication noted above, and request nonexclusive rights for all subsequent editions and in all foreign language translations for distribution throughout the world.

Description of material to be used—Indicate what material you wish to use (figures, tables, text, etc.) and give the full bibliographic reference for the source publication. You may attach a separate list, organized by ECS title.

S.J. Benson, D. Waller, J.A. Kilner, Degradation of La0.6Sr0.4Fe0.8Co0.2O3-d in carbon dioxide

and water atmospheres, Journal of the Electrochemical Society 146(4) 1305-1309 (1999)

Figure 1, 2, 4 and 5.

Signature: _____   Date: 2/12/2017

Name: Chi Zhang

Address: Department of Chemical Engineering, Curtin University, Perth, Western Australia 6845, Australia.

Telephone: _____   Fax: _____

E-mail: 17233411@student.curtin.edu.au

Permission is granted to reproduce the above-referenced material. Please acknowledge the author(s) and publication data of the original material, and include the words: "Reproduced by permission of The Electrochemical Society."

FEB 13 2017
Date

_____
Annie Goedkoop, Director of Publications Production
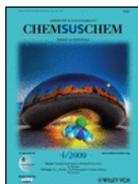
204

Copyright Clearance Center

RightsLink®

Home Account Info Help ✉

CHEMSUSCHEM
4/2009

Title: Enhanced CO2 Resistance for Robust Oxygen Separation Through Tantalum-doped Perovskite Membranes

Author: Chi Zhang,Hao Tian,Dong Yang,Jaka Sunarso,Jian Liu,Shaomin Liu

Publication: ChemSusChem

Publisher: John Wiley and Sons

Date: Jan 27, 2016

© 2016 WILEY-VCH Verlag GmbH & Co. KGaA, Weinheim

Order Completed

Thank you for your order.

This Agreement between Chi Zhang ("You") and John Wiley and Sons ("John Wiley and Sons") consists of your license details and the terms and conditions provided by John Wiley and Sons and Copyright Clearance Center.

Your confirmation email will contain your order number for future reference.

Printable details.

License Number	4046401151777
License date	Feb 12, 2017
Licensed Content Publisher	John Wiley and Sons
Licensed Content Publication	ChemSusChem
Licensed Content Title	Enhanced CO2 Resistance for Robust Oxygen Separation Through Tantalum-doped Perovskite Membranes
Licensed Content Author	Chi Zhang,Hao Tian,Dong Yang,Jaka Sunarso,Jian Liu,Shaomin Liu
Licensed Content Date	Jan 27, 2016
Licensed Content Pages	8
Type of use	Dissertation/Thesis
Requestor type	Author of this Wiley article
Format	Print and electronic
Portion	Full article
Will you be translating?	No
Title of your thesis / dissertation	Novel ceramic membranes for gas separation in enabling the clean energy delivery
Expected completion date	Feb 2017
Expected size (number of pages)	207
Requestor Location	Chi Zhang 4/31 Nottingham Street East Victoria Park Perth, WA 6101 Australia Attn: Chi Zhang
Publisher Tax ID	EU826007151
Billing Type	Invoice
Billing address	Chi Zhang 4/31 Nottingham Street